FACULDADE DE ENGENHARIA DA UNIVERSIDADE DO PORTO

Monitoring and optimization of 5 axis CNC milling

Beatriz Alexandra Alves Cardoso



Master's in Mechanical Engineering

FEUP Supervisor: Prof. Dr. Abílio de Jesus

FEUP Co-Supervisor: Prof. Dr. Ana Reis

SISMA Co-Supervisor: Eng. Pedro Sá Couto

July 22, 2025

This page was intentionally left blank

Monitoring and optimization of 5 axis CNC milling

Beatriz Alexandra Alves Cardoso

Master's in Mechanical Engineering

July 22, 2025

This page was intentionally left blank

Abstract

With the evolution of multi-axis machining, there is an increasing demand for dimensional accuracy and surface quality. This requires controlled and stable processes, that can be achieved and enhanced through process monitoring and optimization. CNC milling is widely versatile and used in several industries, including medical, sports and aerospace. In addition, the production of complex products requires careful planning, quality control, sophisticated tool path strategies and a continuous quality control of the machined parts.

This work investigates the use of sensor-based monitoring, focusing on electrical current and vibration signals, as a mean to evaluate process dynamics and energy consumption during 5-axis CNC milling. In addition, a machining strategy was developed to attend the demanding requirements of a product of the sport's field, exploring the world of machining and cutting tools. Three machining operations were monitored under varying cutting parameters, in which electric current and vibration signals were obtained using current clamps and a MEMS accelerometer, respectively. Both type of signals were processed by the Root Mean Square (RMS) method, in order to understand what can be concluded by this type of information and study the impact of cutting parameters on process efficiency. In addition, each produced workpiece was submitted to quality control to verify the dimensional accuracy and geometric tolerances.

The results showed that the electric current signal can be used as an indicator of energy consumption and cutting forces, with high linear correlation with Material Removal Rates (MRR) and cutting power. Vibration measurements were capable of reflecting dynamic oscillations, particularly in the tool radial X-axis direction. Both signals can be used together, but are not related as they provide distinct informations of process behaviour. Some limitations were also highlighted, such as the current measurement's inability to distinguish finishing passes and the malfunctions of the accelerometer that resulted in the disregard of two trials and needed additional signal processing steps (offset). Due to the absence of repeated trials, the statistical meaning is limited and the detection of outliers is challenging. Nevertheless, this study serves as a foundation for further developments in the theme of machining monitoring and optimization.

Keywords: CNC machining, Process Optimization, Sensor-based monitoring, Signal Acquisition, Vibrations, Electric currents

This page was intentionally left blank

Resumo

A evolução da maquinação CNC de múltiplos eixos gerou uma necessidade crescente de obter produtos com elevada precisão dimensional e qualidade superficial. Estes atributos requerem processos estáveis e controlados, que podem ser promovidos e melhorados com uma monitorização e otimização constante. O processo de fresagem é muito versátil e utilizado em diversos setores, como a indústria médica, desportiva e aeroespacial. Além disso, a produção de peças complexas exige um planeamento cuidadoso, ccontrolo de qualidade, estratégias de corte avançadas e um controlo de qualidade rigoroso.

Este trabalho investiga a monitorização de processos através da implementação de sensores, com foco em sinais de corrente elétrica e vibração, como meio de avaliar a estabilidade da fresagem e o consumo de energia associado. Além disso, foi desenvolvida uma estratégia de maquinação para responder aos requisitos de um produto do setor desportivo, permitindo explorar o mundo da maquinação e ferramentas de corte. Três operações de fresagem foram monitorizadas e foram realizados vários testes com diferentes parâmetros de corte. Os sinais de corrente elétrica e vibração foram captados através de pinças amperimétricas e um acelerómetro, respetivamente. O método RMS (valor quadrático médio ou valor eficaz) foi utilizado no processamento de sinais com o intuito de perceber que tipo de informação pode ser retirada destes sinais e o impacto dos parâmetros de corte na eficiência do processo. Além disso, cada peça foi submetida a um controlo de qualidade para verificar a precisão dimensional e as tolerâncias geométricas.

Os resultados mostraram que o sinal de corrente pode ser usado como indicador do consumo de energia e das forças de corte, apresentando uma correlação linear elevada com a taxa de remoção de material e a potência de corte. As medições de vibração refletiram oscilações dinâmicas, especialmente na direção radial da ferramenta (eixo X). Ambos os sinais podem ser usados em conjnto, mas de forma independente, pois fornecem informações distintas sobre o comportamento do processo. Também se destacaram algumas limitações, como a incapacidade da corrente detetar de forma distinta passos de acabamento e o mau funcionamento do acelerómetro que resultou na desconsideração de dois ensaios e necessitou de um passo adicional no seu processamento. Devido à ausência de repetição de ensaios, a robustez estatística é limitada e a deteção de outliers torna-se mais díficil. No entanto, este estudo serve como base para futuros desenvolvimentos no âmbito da monitorização e otimização de maquinação.

Palavras-Chave: Maquinação CNC, Otimização de processos, Monitorização de processos, Aquisição de sinais, Vibrações, Corrente elétrica

This page was intentionally left blank

Acknowledgements

First of all, I would like to express my deep gratitude to my supervisors at FEUP. To Prof.Dr.Abílio de Jesus, for his continuous guidance, technical insight and support throughout the development of this work. For being unconditionally available to help me and for all his interest in this project. To Prof. Dr. Ana Reis, for all the trust and opportunities she has given me during the last months, that allowed me to grow and learn. I am very grateful for having had the opportunity to work with them and increase my knowledge and skills.

To Prof. Dr. António Mendes Lopes, for his encouragement and advices that deeply contributed for this work. To José Ferreira for his guidance in the implementation of sensors.

To the team at SISMA- Sá Couto & Monteiro and my supervisor at SISMA, Eng. Pedro Sá Couto, my sincere gratitude for giving me the opportunity to develop my thesis in an industrial environment. I would like to highlight my gratitude for the constant interest shown and advice that helped me grow both as a person and as a professional- lessons I will carry with me into the future. To Eng. Pedro Nogueira, Eng. André Guimarães and Eng. Nuno Duro, for having been tireless in following, daily, this work. For passing on their vast knowledge on machining that made the experimental part possible. To all the other collaborators and staff at the company, for their kindness and availability that made this last months easier.

To my friends, for all the support and patience during this work and all the incredible memories made during these last years.

To David, for all the love, for always being by my side and encouraging me to achieve my goals.

To my parents and my sister, for their unconditional love and support. I own every opportunity I had to them and words will never be enough to express my gratitude.

This page was intentionally left blank

Industrial Acknowledgements

The author gratefully acknowledges the funding from Project “SNEXT“, with nr. 14419 and operation code at the Funds Platform COMPETE2030-FEDER-00582100, funded by FEDER and FSE+ through the COMPETE 2030 Program.



This page was intentionally left blank

Contents

1 Introduction **1**
- 1.1 Framework and motivation . . . 1
- 1.2 Project development at SISMA | Sá Couto & Monteiro . . . 2
- 1.3 Objectives . . . 2
- 1.4 Methodology . . . 3
- 1.5 Structure . . . 3

2 Literature Review **5**
- 2.1 Milling . . . 5
  - 2.1.1 CNC machinning . . . 7
  - 2.1.2 Process parameters . . . 8
  - 2.1.3 Cutting tools . . . 11
- 2.2 Characterization of 42CrMo4 Steel . . . 16
  - 2.2.1 Machining of 42CrMo4 Steel . . . 18
- 2.3 Monitoring techniques in machining . . . 20
  - 2.3.1 Signal Acquisition . . . 21
  - 2.3.2 Signal Processing . . . 25

3 Methodology **29**
- 3.1 Materials and Equipment . . . 29
- 3.2 Product Design . . . 31
- 3.3 Machining strategies . . . 33
  - 3.3.1 Initial Approaches . . . 34
  - 3.3.2 Final Strategy and CAM Validation . . . 36
- 3.4 Workpiece Production . . . 53
  - 3.4.1 Process monitoring . . . 54
  - 3.4.2 Quality control . . . 58

4 Results and Discussion **61**
- 4.1 Electrical Current Monitoring . . . 62
  - 4.1.1 Operation 1 . . . 63
  - 4.1.2 Operation 13 . . . 79
  - 4.1.3 Operation 15 . . . 88
  - 4.1.4 Comparison between operations . . . 99
- 4.2 Vibration Analysis . . . 103
  - 4.2.1 Operation 1 . . . 104
  - 4.2.2 Operation 13 . . . 109
  - 4.2.3 Operation 15 . . . 113
  - 4.2.4 Comparison between operations . . . 116

4.3 Quality Control 117

5 Conclusion and Future Works **121**
5.1 Conclusion 121
5.2 Future Works 122

A Cutting tools and tool holders nomenclature **123**

B Cutting parameters comparison **127**

C Current clamps technical data **129**

D RMS Current values over time **131**

E RMS acceleration plots of X, Y and Z axes **135**

F RMS acceleration plots of the Resultant **139**

G Quality Control Reports **141**

References **149**

List of Figures

Figure 1.1. Dissertation work plan. 3

Figure 2.1. Face milling operations [61]. 6
Figure 2.2. Feed direction in down-milling (left) and up-milling (right) [61]. 6
Figure 2.3. End milling operations using solid carbide tools [66]. 7
Figure 2.4. Feed per tooth during milling [9]. 9
Figure 2.5. Axial and radial depth of cut in end (left side) and ball-end milling (right side) [9]. 10
Figure 2.6. Influence of the number of flutes on machining [10]. 13
Figure 2.7. Tool pitch [10]. 13
Figure 2.8. Influence of the helix angle on chip evacuation [53]. 14
Figure 2.9. Influence of the depth of cut on cutting forces [8]. 15
Figure 2.10. Entering angle of an insert [8]. 15
Figure 2.11. Different types of chips observed in drilling [45]. 16
Figure 2.12. Impact of the alloying elements in the material's properties and machining [67]. 17
Figure 2.13. ISO material groups classification [64]. 18
Figure 2.14. Example of an experimental setup using a dynamometer for cutting forces estimation [72]. 22
Figure 2.15. Chatter effect on the machined surface [71]. 23
Figure 2.16. Example of experimental setups for vibration testing. 23
Figure 2.17. Example of an experimental setup for the estimation of both cutting forces and vibrations [28]. 24
Figure 2.18. Chatter prediction using Fast Fourier Transform method [72]. 26
Figure 2.19. Processing of vibration signals using a time waveform [85] 27

Figure 3.1. Axes movements of U500Xd2 Brother machine. 31
Figure 3.2. Technical drawing of the part. 32
Figure 3.3. Different views of the 3D model (following the European projection method). 33
Figure 3.4. Isometric view of the 3D model from different angles. 33
Figure 3.5. First setup (AP1). 37
Figure 3.6. Tool path visualisation for AP1. 37
Figure 3.7. Setup sheet for AP1. 38
Figure 3.8. Second setup (AP2). 38
Figure 3.9. Recommended coolant pressure and flow rate for RT 100 T drills from Guhring, for internal lubrication purposes [20]. 39
Figure 3.10. Peck drilling cycle. 39
Figure 3.11. Deep hole strategy using the *Advanced Drill* command. 40
Figure 3.12. Helical interpolation technique. 41
Figure 3.13. Tool entry configurations. 41

Figure 3.14. *Multi Passes* configuration. . . . 42
Figure 3.15. *Depth cuts* configuration. . . . 42
Figure 3.16. *Linking Parameters* configuration. . . . 43
Figure 3.17. Combined strategy with *Depth cuts* and *Multipasses* (Operation 15). . . . 43
Figure 3.18. Peck cycle of the main drill for the D4.04 hole. . . . 44
Figure 3.19. Tool path visualisation for AP2 from different perspectives. . . . 44
Figure 3.20. Setup sheet of AP2. . . . 45
Figure 3.21. End mills used in the machining strategy from Hoffmann. . . . 46
Figure 3.22. Chamfer mill used in machining from Hoffmann. . . . 47
Figure 3.23. Short end mill of 5 mm used in machining from Hoffmann. . . . 47
Figure 3.24. Drill of 4.04 mm and 5xD used in the machining of the deep hole from Guhring. . . . 48
Figure 3.25. Drills of 3.2 mm used in machining from Guhring. . . . 48
Figure 3.26. Face mill with inserts used in machining from Walter. . . . 49
Figure 3.27. Reamer of 3.28 mm used in machining from DIXI. . . . 49
Figure 3.28. Relationship between the height of the profile (R_t) and the feed per tooth (f_z) [63]. . . . 52
Figure 3.29. Total produced workpieces. . . . 53
Figure 3.30. Machining steps. . . . 54
Figure 3.31. Mechanical stop used for AP1. . . . 54
Figure 3.32. Monitoring setup for current signals. . . . 55
Figure 3.33. Accelerometer used for vibration monitoring. . . . 56
Figure 3.34. Placement of the accelerometer at the spindle. . . . 56
Figure 3.35. NC code that allows sensor positioning and activation of the *Load Monitoring* function. . . . 57
Figure 3.36. Load Monitoring Function of the Brother U500Xd2 5AX CNC machine. . . . 57
Figure 3.37. Comparison between Average and Peak Monitoring Methods of the *Machining Load Monitoring* function of the CNC machine. . . . 58
Figure 3.38. Quality control of the workpiece using a CMM Hexagon machine. . . . 59
Figure 3.39. Dimensional inspection using the Garant MM1200 profile projector. . . . 59
Figure 3.40. Surface roughness assessment using a Mitutoyo surface roughness tester. . . . 60
Figure 3.41. Dimensional inspection of the holes using a Go/No-Go gauge. . . . 60

Figure 4.1. Raw data from the .csv file of the current. . . . 63
Figure 4.2. Tool path of Operation 1. . . . 63
Figure 4.3. Current signal and corresponding RMS segmentation of Test 5 of OP1. . . . 64
Figure 4.4. Effective current value of each test of OP1. . . . 65
Figure 4.5. Average chip thickness, h_m, calculation in peripheral milling (left side) and face milling (right side) [2]. . . . 66
Figure 4.6. Progressive engagement of the tool with the workpiece during OP1. . . . 67
Figure 4.7. Variation of the current with each tool pass- OP1. . . . 68
Figure 4.8. Current vs Axial depth of cut - Test 1 (OP1). . . . 68
Figure 4.9. Current vs Material Removal Rate (MRR)- OP1. . . . 69
Figure 4.10. Specific cutting pressure of the workpiece material [64]. . . . 71
Figure 4.11. Current (RMS) vs Cutting Power of OP1. . . . 72
Figure 4.12. Current (RMS) vs Cutting Power of OP1 considering $K_c = k_{c1}$. . . . 73
Figure 4.13. Global Current (RMS) vs Average Torque- OP1 . . . 75
Figure 4.14. Global current (RMS) vs Torque-derived Power of OP1. . . . 76
Figure 4.15. Cutting Power vs Torque-derived Power of OP1. . . . 77

Figure 4.16. Idle current of each test of OP1. 78
Figure 4.17. Spindle speed vs Idle current of OP1. 78
Figure 4.18. Comparison of the idle current and current during cutting of OP1. 79
Figure 4.19. Tool path of Operation 13. 79
Figure 4.20. Segmentation of the tool path to determine the average a_e of OP13. 80
Figure 4.21. Raw and RMS current signals of Test 1 during OP13. 81
Figure 4.22. Comparison between the effective value of current (RMS) of each test of OP13. 82
Figure 4.23. Variation of the current with each tool pass- OP13. 82
Figure 4.24. Illustration of the tool intersecting a pre-drilled hole during OP13. 83
Figure 4.25. Current vs Material Removal Rate (MRR)- OP13 84
Figure 4.26. Current (RMS) vs Cutting Power- OP13. 85
Figure 4.27. Global current (RMS) vs Torque-derived Power- OP13. 86
Figure 4.28. Global current (RMS) vs Torque-derived Power- OP13. 86
Figure 4.29. Cutting Power vs Torque-derived Power- OP13. 87
Figure 4.30. Idle current of each test of OP13. 87
Figure 4.31. Spindle speed vs idle current of OP13. 88
Figure 4.32. Comparison of the idle current and current during cutting of OP13. 88
Figure 4.33. Tool path of Operation 15. 89
Figure 4.34. Radial depth of cut of the roughing passes of each segment in OP15 89
Figure 4.35. Radial depth of cut of the finishing passes in OP15. 89
Figure 4.36. Raw and RMS current signals of Test 1 during OP15. 90
Figure 4.37. Tool engagement of the tool intersecting a pre-drilled hole during OP15. . 91
Figure 4.38. Variation of the current with each tool pass- OP15. 91
Figure 4.39. Effective RMS current value of each test of OP15. 92
Figure 4.40. Current vs Material Removal Rate (MRR) during roughing of OP15. . . . 93
Figure 4.41. Comparison between MRRs of roughing and finishing passes- OP15. . . . 94
Figure 4.42. Current vs Cutting Power during roughing operations in OP15. 95
Figure 4.43. Comparison of the cutting power between roughing and finishing operations in OP15. 95
Figure 4.44. Global current (RMS) vs Average Torque- OP15. 97
Figure 4.45. Global Current (RMS) vs Torque-derived Power- OP15. 97
Figure 4.46. Cutting Power vs Torque-derived Power- OP15. 98
Figure 4.47. Idle current of each test of OP15. 98
Figure 4.48. Spindle speed vs Idle current of OP15. 99
Figure 4.49. Comparison of the idle current and current during cutting of OP15. 99
Figure 4.50. Comparison of the RMS current values. 100
Figure 4.51. Comparison of the average torque. 101
Figure 4.52. Comparison of the linear correlation of the current with the material removal rate of all tests. 101
Figure 4.53. Comparison of the linear correlation of the current with cutting power of all tests. 102
Figure 4.54. Comparison of the linear correlation of the global current with torque-derived power of all tests. 102
Figure 4.55. Comparison of the idle current of all operations. 103
Figure 4.56. Raw data of the acceleration from the .CSV file. 104
Figure 4.57. Vibration signal and corresponding RMS profile during OP1 of test 1. . . . 105
Figure 4.58. Acceleration values in each individual axis- OP1. 106

Figure 4.59. Acceleration values of each tool pass of the three axes of OP1. 106
Figure 4.60. Acceleration values of the resultant of OP1. 107
Figure 4.61. Example of a chatter stability lobe [82]. 108
Figure 4.62. Variation of the resultant acceleration values for each tool pass and for all tests- OP1. 108
Figure 4.63. Comparison of the RMS acceleration values of the scalar X + Y with the Z axis- OP1. 109
Figure 4.64. Acceleration values in each individual axis- OP13. 110
Figure 4.65. Acceleration values of each tool pass of the three axes of OP13. 111
Figure 4.66. Acceleration values of each tool pass of the three axes of OP13. 111
Figure 4.67. Variation of the resultant acceleration values for each tool pass and for all tests-OP13. 112
Figure 4.68. Comparison of the RMS acceleration values of the scalar X + Y with the Z axis-OP13. 112
Figure 4.69. Acceleration values in each individual axis- OP15. 114
Figure 4.70. Acceleration values of each tool pass of the three axes of OP13. 114
Figure 4.71. Acceleration values of the resultant of OP15. 115
Figure 4.72. Variation of the resultant acceleration for each tool pass and for all tests-OP15. 115
Figure 4.73. Comparison of the RMS acceleration values of the scalar X + Y with the Z axis- OP15. 116
Figure 4.74. Comparison of the resultant acceleration values of all operations. 117

Figure C.1. E27 Current clamp from Chauvin Arnoux. 129

Figure D.1. RMS current values over time from tests 1 to 4 of OP1. 131
Figure D.2. RMS current values over time from tests 5 to 7 of OP1. 132
Figure D.3. RMS current values over time from tests 1 to 4 of OP13. 132
Figure D.4. RMS current values over time from tests 5 to 7 of OP13. 133
Figure D.5. RMS current values over time from tests 1 to 4 of OP15. 133
Figure D.6. RMS current values over time from tests 5 to 7 of OP15. 134

Figure E.1. RMS acceleration values from tests 1 to 3 of OP1. 135
Figure E.2. RMS acceleration values from tests 4 and 5 of OP1. 136
Figure E.3. RMS acceleration values from tests 1 to 3 of OP13. 136
Figure E.4. RMS acceleration values from tests 4 and 5 of OP13. 137
Figure E.5. RMS acceleration values from tests 1 and 2 of OP15. 137
Figure E.6. RMS acceleration values from tests 3 and 4 of OP15. 138

Figure F.1. RMS acceleration Resultant values of OP1. 139
Figure F.2. RMS acceleration Resultant values of OP13. 140
Figure F.3. RMS acceleration Resultant values of OP15. 140

Figure G.1. Inspection report of workpiece number 1. 142
Figure G.2. Inspection report of workpiece number 2. 143
Figure G.3. Inspection report of workpiece number 3. 144
Figure G.4. Inspection report of workpiece number 4. 145
Figure G.5. Inspection report of workpiece number 5. 146
Figure G.6. Inspection report of workpiece number 6. 147

List of Tables

Table 2.1. Influence of cutting parameters on surface roughness, tool wear, and material removal rate (MRR) based on various studies. 11
Table 2.2. CVD and PVD coatings properties. 12
Table 2.3. Summary of studies on machining parameters for 42CrMo4 steel. 20
Table 2.4. Summary of sensor applications in machining monitoring. 25
Table 2.5. Summary of relevant studies on signal processing in vibration monitoring during milling. 28

Table 3.1. Chemical composition of the 42CrMo4 steel (% mass). 29
Table 3.2. Mechanical Properties of the material 42CrMo4 steel. 30
Table 3.3. First setup (AP1) of the initial machining strategy. 35
Table 3.4. Second setup (AP2) of the initial machining strategy. 35
Table 3.5. Comparison between programmed and catalogue cutting parameters – drilling operations. 51
Table 3.6. Comparison between programmed and catalogue cutting parameters – AP2 (Operations 13–20). 52
Table 3.7. Selected operations for monitoring. 54

Table 4.1. Cutting conditions used in each test of OP1. 62
Table 4.2. Cutting conditions used in each test of OP13. 62
Table 4.3. Cutting conditions used in each test of OP15. 62
Table 4.4. Mean RMS current value and percentage variation of each test during OP1. 65
Table 4.5. Mean RMS current values (A) for each cutting pass in OP1. 67
Table 4.6. RMS current and axial depth of cut (a_p) for each cutting pass of test 1- OP1. 68
Table 4.7. Material removal rate (MRR) for each test in OP1. 69
Table 4.8. Average chip thickness and specific cutting force for each test – OP1. . . . 71
Table 4.9. Estimated cutting power, considering the chip thickness, for each test in OP1. 72
Table 4.10. Estimated cutting power for each test in OP1, considering $K_c = k_{c1}$. 73
Table 4.11. Maximum and average spindle torque measured using the *Load Monitoring* Function- OP1. 74
Table 4.12. Rotational frequency and power estimated from spindle torque in OP1. . . 75
Table 4.13. Global current (RMS) measured during OP1 tests. 75
Table 4.14. Mean RMS current value and percentage variation for each test during OP13. 81
Table 4.15. Mean RMS current values (A) for each cutting pass of each test in OP13. . 82
Table 4.16. Material Removal Rate (MRR) for each test in OP13. 83
Table 4.17. Cutting power for each test of OP13. 84
Table 4.18. Maximum and average spindle torque, frequency of rotation and corresponding power- OP13. 85
Table 4.19. Global current (RMS) measured during OP13 tests. 86
Table 4.20. Mean RMS current values (A) for each cutting pass in OP15. 91

Table 4.21. Mean RMS current values and percentage variation for each test in OP15. . 92
Table 4.22. Material removal rate (MRR) for roughing and finishing in each test of OP15. 93
Table 4.23. Cutting power (P_c) for roughing and finishing operations in OP15. 94
Table 4.24. Maximum and average spindle torque and corresponding cutting power-OP15. 96
Table 4.25. Global RMS current value for each test of OP15. 96
Table 4.26. Acceleration RMS values and corresponding percentage variation in X, Y and Z axes for each test of OP1. 105
Table 4.27. Acceleration RMS values and corresponding percentage variation in X, Y and Z axes for each test of OP13. 110
Table 4.28. Acceleration RMS values and corresponding percentage variation in X, Y and Z axes for each test of OP15. 113
Table 4.29. Dimensional deviation values (μm) for each test and corresponding statistical metrics. 119
Table 4.30. Dimensional and geometric deviations measured at entry and exit sides of the D4,04 hole. 119

Table A.1. End mill nomenclature. 123
Table A.2. Chamfer mill nomenclature. 123
Table A.3. Drill code nomenclature. 124
Table A.4. Face mill nomenclature. 124
Table A.5. Reamer nomenclature. 124
Table A.6. Tool holders nomenclature. 125

Table B.1. Comparison between programmed and catalogue cutting parameters – Setup AP1. 127
Table B.2. Comparison between programmed and catalogue cutting parameters – Setup AP2. 127

List of symbols and abbreviations

a_e	Radial depth of cut
a_p	Axial depth of cut
D	Diameter
f_r	Feed per revolution
f_z	Feed per tooth
K_r	Entering angle
R_a	Roughness
v_c	Cutting speed
v_f	Feed rate
AE	Acoustic Emission
CBN	Cubic Boron Nitride
CCW	Counter Clockwise
CNC	Computer Numerical Control
CNN	Convolutional Neural Networks
CVD	Chemical Vapour Deposition
CW	Clockwise
FIR	Finite Impulse Response
FFT	Fast Fourier Transform
HHT	Hilbert-Huang Transform
HSS	High Speed Steels
ISO	International Organization for Standardization
MRR	Material Removal Rate
PLC	Programmable Logic Controller
PVD	Physical Vapour Deposition
RMS	Root Mean Square
SFTF	Short-Time Fourier Transform
SPRT	Self-propelled Rotary Tools
WPT	Wavelet Packet Transform
WT	Wavelet Transform

This page was intentionally left blank

Chapter 1

Introduction

1.1 Framework and motivation

5-axis CNC milling is essential in several manufacturing sectors such as mould industry, aerospace and medical devices and other applications where it is required to produce complex geometries and tight tolerances. This technology offers high flexibility since it has the ability to continuously orientate the tool or workpiece along 5 axes. This facilitates the machining of complex features, reduces the need of multiple setups and improves accessibility to difficult areas. However, it also introduces challenges that include process stability, vibration control, higher costs, the need of advanced tool path strategies and sophisticated monitoring.

In this context, monitoring techniques have gained increased importance. The acquisition of signals such as cutting forces, vibration, current and temperature provides valuable information about machining performance. The signals enable fault detection, tool wear monitoring and process optimization. Ultimately, these contribute to an increase of reliability and productivity.

In addition to the constant need to monitor and improve 5-axis CNC manufacturing in today's industries, the present work was also motivated by a real need identified at SISMA | Sá Couto & Monteiro, where the machining of a sports equipment component revealed challenges related to the high hardness of the material, requirement to meet tight dimensional tolerances and accelerated tool wear. This led to the need for a optimised machining strategy. At the same time, the company aims to develop internal monitoring capabilities to gain a deeper understanding of their processes and establish a methodology applicable to other workpieces and setups. By testing different sensors in real machining conditions, it becomes possible to evaluate which type of signals are most informative and which analyses are more suitable for future integration.

Therefore, this study aims to responds to an industrial challenge and contribute to the academic study of sensor-based monitoring and optimisation in 5-axis CNC milling.

1.2 Project development at SISMA | Sá Couto & Monteiro

This investigation was conducted at SISMA | Sá Couto & Monteiro. This company is specialized in CNC machining of high precision components for the medical, aerospace, optical and general mechanical industries. It combines an extensive know-how in machining technologies and responds to demanding tolerances and surface finish requirements.

This dissertation project was developed in direct collaboration with the company, within the context of a real production need. The focus was placed on the machining of a component from the sports sector in order to optimise the cutting process and explore the implementation of monitoring solutions. The practical outcome of this collaboration is expected to bring benefits to the company, that include improved machining efficiency and process traceability through data acquisition.

1.3 Objectives

The main objective of this investigation is to develop and validate a strategy that enables the monitoring and optimisation of a 5-axis CNC milling- by employing an efficient machining strategy, integrating sensors and applying signal analysis techniques- and establish correlations between the signals and machining quantities such as the cutting parameters and surface finish quality. To achieve this goal, the following questions are addressed throughout the dissertation:

- Can the acquired signals be used to estimate machining quantities such as cutting forces, stability or energy consumption?
- How do variations in cutting parameters influence the acquired signals?
- What is the impact of cutting parameters on dimensional accuracy?

1.4 Methodology

The dissertation work plan is represented in a Grantt chart, displayed in Figure 1.1. This chart exhibits the main tasks performed over the time.

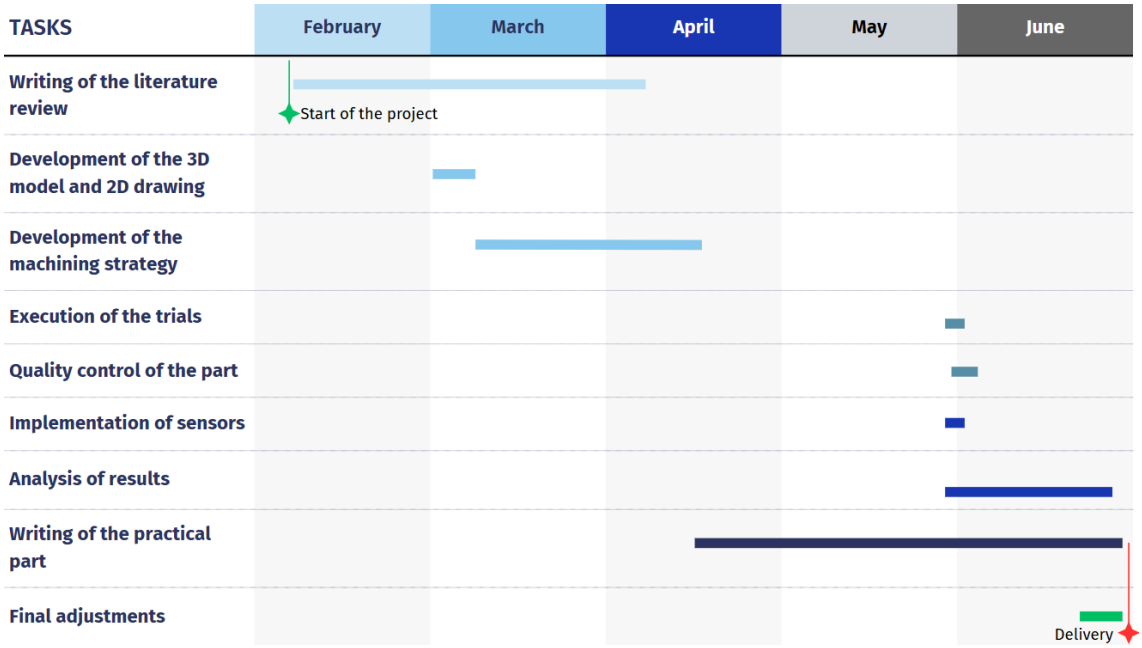


Figure 1.1: Dissertation work plan.

1.5 Structure

This dissertation is divided into five chapters. Chapter 1 corresponds to the introduction. It presents the industrial and academic framework of the project, the motivation behind the study, its main objectives and work plan.

Chapter 2 exposes the literature review. It provides the theoretical background required for the work development. The chapter includes a detailed review of 5-axis CNC milling, cutting tools, cutting parameters, material machinability and fundamentals of process monitoring.

Chapter 3 presents the material and equipments of this project. It also exhibits the 3D model and 2D drawing developed, the CAM-based machining strategy and selected tools. Throughout this chapter, all the decisions made are explained.

Chapter 4 is dedicated to the results and discussion. It presents the outcomes of the machining trials and signal acquisition. A comparative discussion is provided between different operations.

Finally, Chapter 5 summarises the most important conclusions and proposes future works, considering the goals of this study and aspects that can be improved to further enrich this work.

This page was intentionally left blank

Chapter 2

Literature Review

This chapter presents a critical review of the key concepts, technologies, and methods that support the monitoring and optimisation of CNC milling processes, with a particular focus on 5-axis machining. The discussion begins with the fundamentals of milling and CNC machines, followed by analysis of cutting tools and process parameters. The material used in this project is also explored, with an emphasis on its machinability. Finally, sensor-based monitoring strategies are also presented, with focus on the most relevant techniques for practical implementation and signal analysis applied in this work.

2.1 Milling

Milling is a machining process that consists of a rotating cutting tool with multiple edges to eliminate material from a workpiece [9], [22]. The cutting tool features several cutting edges known as teeth that can make programmed feed movements in nearly any direction, allowing for the creation of flat surfaces and complex shapes [9], [22]. This ability makes milling more versatile than other machining methods, including drilling, turning or slotting [9]. It is characterized as an intermittent cutting process, in which the tool's teeth enter and exit the workpiece with every revolution. Due to this interrupted cutting action, the teeth experience a cycle of impact force and thermal shock with each rotation [22], [73].

The first milling machine was developed by Eli Whitney around 1818, followed by Joseph A. Brown's universal milling machine, which introduced the knee-and-column design [22]. Today, modern CNC-controlled milling centres enable the production of highly complex components with high precision, featuring several numbers of axis that improve process flexibility [9].

There is a variety of milling operations but the most common are face milling (Figure 2.1), where the tool axis is perpendicular to the main surface, and peripheral milling, where the tool axis is parallel to the surface [22], [66].



Figure 2.1: Face milling operations [61].

Peripheral milling includes two main variants: up milling (conventional) and down-milling (climb) [43], [66]. In up-milling, the workpiece feed direction is opposite to the rotation of the tool, as exemplified in Figure 2.2. This results in higher cutting forces, since the chip starts with a minimal thickness and gradually increases as the cut progresses. Therefore, it is necessary to guarantee a good clamping/fixturing system due to the tendency of the forces to lift the part. In contrast, in down-milling (Figure 2.2), the feed direction is the same as the tool's rotation, leading to lower cutting forces and vibrations. In this case, at the beginning of the cut, the chip is wider and becomes thinner, reaching zero at the end of cut. Overall, down-milling is generally preferred, as it provides a more stable cut and typically results in better surface finish [8], [43], [66].

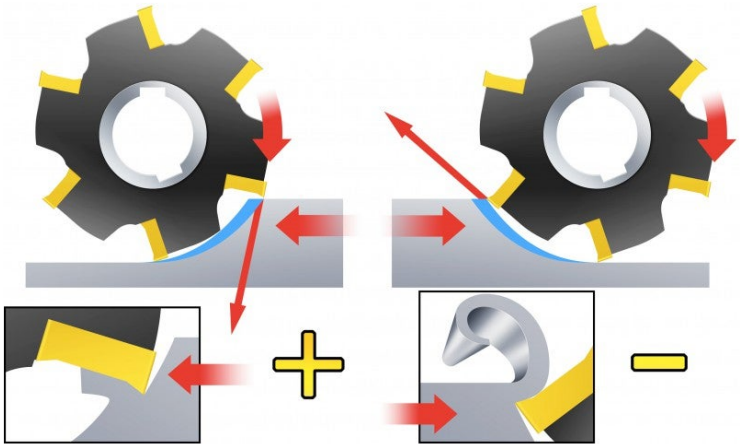


Figure 2.2: Feed direction in down-milling (left) and up-milling (right) [61].

Other operations include end milling, which is highly versatile, suitable for pockets, contours and slots (Figure 2.3). Thread and profile milling are used for specific geometrical features [22], [66].

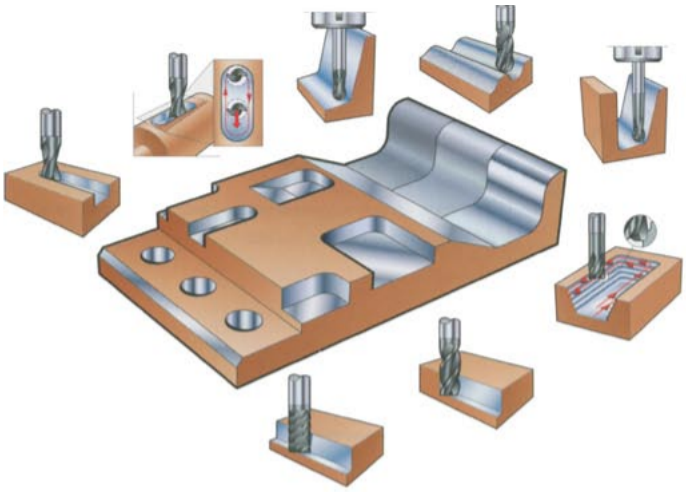


Figure 2.3: End milling operations using solid carbide tools [66].

Milling can be performed on vertical or horizontal machines, depending on the type of operation. While vertical machines are usually used for detailed parts, horizontal configuration allows higher material removal rates.

This process has a wide range of applications, specially highly complex components, for different industries. Turbine components, such as disks and blades, plastic injection moulding parts and electronic components are some examples [22]. The medical industry is another dominant area of milling industrial applications, with the manufacturing of prosthetics, typically made of titanium.

2.1.1 CNC machinning

Initially, milling machines were operated manually, which required operators with a high level of skill and understanding of the process. With the advancement of technology and computational control, CNC (Computer Numerical Control) machines became vital to the industry. The machine tools are controlled through programmed instructions, improving repeatability, accuracy and productivity compared to conventional machines. These interpret G-code to execute precise movements, adjusting speed, feed and tool changes autonomously [9].

A CNC machining centre is constituted by several components, such as guideways and drives, motors, ball screws and spindle. Linear guideways, including friction, ball bearing or hydrostatic types, improve damping capacity and positioning precision [22]. Servo motors, assisted by feedback loops, ensure accurate movements, while stepper motors provide simpler, open loop control. The rotational movement of electrical motors is converted into displacement motion of machine tools by ball screws and the spindle can be connected to the motor by different systems- timing belts, flexible coupling or integrated electrospindles, depending on the required speed and torque transmission [22].

CNC milling machines can also incorporate tool changers and tool length compensation systems. Automatic tool magazines reduce setup time by providing fast and precise tool changes [9].

In addition, the machine uses different coordinate systems (machine, workpiece, reference) to ensure positioning and motion accuracy. Generally, in CNC milling machines the Z-axis is positive in an upward direction and away from the workpiece [9].

Modern machines are equipped with user-friendly interfaces that allow operators to load and edit programs and visualize machining parameters. Furthermore, auxiliary functions such as coolant control, tool changes and safety interlocks are managed by PLCs (Programmable Logic Controllers), through M-codes [22]. These controllers can interact with sensors, allowing real time decision-making.

The number of axes defines the machine's capabilities. While 3-axis milling covers movements in the basic axes (X,Y and Z), 5-axis machining introduces two rotational axes, typically A and C that allow the table's rotation and tilting. This ability improves access to complex features, minimizes errors and its versatility allows the creation of highly complex geometries.

Finally, proper fixturing of the workpiece is crucial to ensure stability, accessibility and accuracy. Clamping systems, such as vises, jigs or custom fixtures, must be adapted to the part geometry and the operations required [6].

CNC machining can be further improved with simulation software that allows visualization of tool paths, detection of collisions, cycle time estimation and NC code generation [6].

All these systems and functions enable high accuracy and repeatability of the CNC machines. Compared to conventional milling machines, it is possible to obtain lower production times, including less time for machine setup. Moreover, there is high process flexibility since the program can be easily modified with the user interface, as the machine enhances intuitive interaction and ease of programming. As such, high skilled operators are not required, on contrary to conventional milling. By integrating sensors and control systems, there is reduction of errors and increased safety.

2.1.2 Process parameters

To optimize process performance, it is vital to establish suitable cutting parameters, since these have direct impact on the quality of the machined component, tool longevity and process efficiency. The main parameters that define a milling operation are cutting speed, v_c, feed per tooth, f_z, axial, a_p, and radial depth of cut, a_e [9].

Cutting speed refers to the linear speed at the cutting edges [9], [22]. It can be calculated by Equation 2.1, where D is the diameter of the tool (mm) and N is the rotational speed of the spindle (rpm).

$$v_c = \frac{\pi \cdot D \cdot N}{1000} [\text{m/min}] \tag{2.1}$$

The choice of cutting speed value for an operation depends on different factors that include tool material, the material being machined, type of operation and economic aspects of the tool [6]. For example, roughing operations usually operate at higher depth of cuts and lower cutting speeds than finishing operations. However, it is also crucial to account for tool wear and replacement

costs. If an excessive cutting speed leads to accelerated tool wear, adjustments must be made to balance productivity with tool life and overall cost-effectiveness.

The feed per tooth corresponds to the distance the tool travels in one rotation, as illustrated in Figure 2.4 , divided by the number of teeth [9], [27].

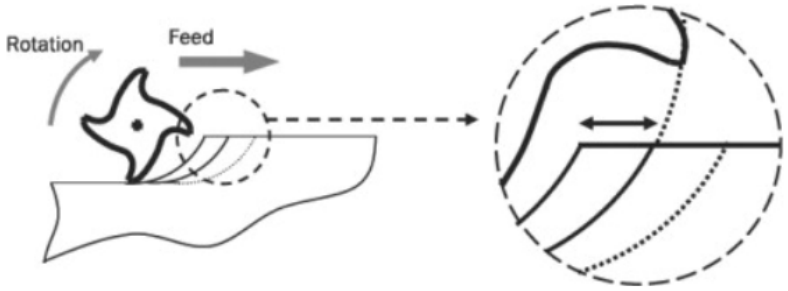


Figure 2.4: Feed per tooth during milling [9].

It can be related to the feed rate, v_f, spindle speed and number of teeth, z, resulting in Equation 2.2. The feed per tooth is usually expressed as mm/tooth and is an important parameter to determine the cutting time [27]. The definition of feed rate for a milling operation must be developed considering the type of tool, surface roughness, machine's rigidity and workpiece properties [6]. For example, in face milling it is usually suggested to use higher feeds because more teeth are in contact with the part. For finishing operations, where typically a small amount of material is removed, the feed rate can be increased [6].

$$v_f = f_z \cdot z \cdot N[\text{mm/min}] \tag{2.2}$$

It is also possible to obtain the feed per revolution, f_r, that corresponds to the product of the feed per tooth with the number of teeth (Equation 2.3) [9], [22], [27].

$$f_r = f_z \cdot z[\text{mm/rev}] \tag{2.3}$$

The depth of cut can be separated into axial and radial directions due to the milling tools' numerous edges [9], [27]. The axial depth of cut, a_p, is measured parallel to the tool rotation axis, while the radial depth, a_e, is measured over the tool's diameter [27]. This is due to the direction of feed in milling, being perpendicular to the tool rotation axis. These two variables are represented in Figure 2.5.

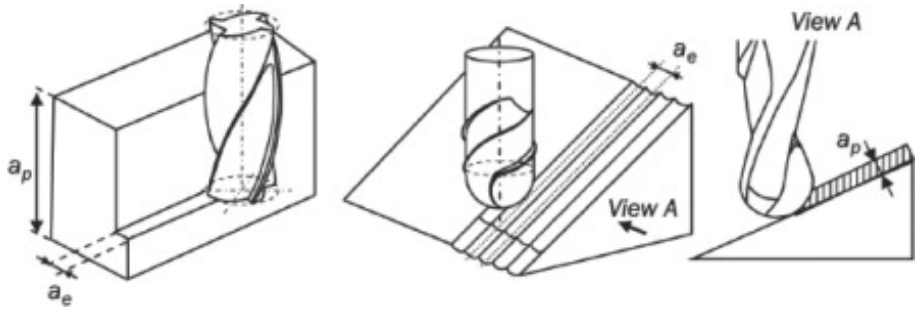


Figure 2.5: Axial and radial depth of cut in end (left side) and ball-end milling (right side) [9].

These parameters are crucial in determining cutting performance, product quality, tool life, and surface roughness. The optimization of these parameters is essential to improve production time, reduce costs, and enhance the final product [5].

Cutting speed influences both the thermal and mechanical loads during machining. According to Nguyen et al. [48], increasing cutting speed can reduce built-up edge (BUE) formation and shorten tool–workpiece contact times, which in turn may lead to smoother surfaces. However, higher cutting speeds are also associated with increased tool wear due to intensified thermal and tribological stresses.

Feed per tooth directly affects the tool engagement and chip load. Imad et al. [24] reported that higher feed values increase surface roughness and cutting forces, contributing to more pronounced feed marks and tool wear.

Axial and Radial Depths of Cut (a_p and a_e) define the cross-sectional area of material removed per pass and are critical for material removal rate (MRR). Vivancos et al. [75] demonstrated that increasing depth of cut enhances MRR but leads to higher cutting forces, greater flank wear and degraded surface finish- particularly in finishing operations where fine tolerances are required.

Cutting tool geometry, specifically the cutting edge radius, also plays a significant role in process performance. A study by Imad et al. [24] showed that larger edge radius result in increased cutting forces and feed marks, leading to higher surface roughness and micro hardness, especially in hardened steels.

The ideal is to achieve a balance between productivity and surface quality. While high values of v_c, f_z, and depths of cut can increase material removal rates, they also intensify mechanical and thermal loads, thereby accelerating tool wear and compromising surface finish. In contrast, lower values improve dimensional and surface quality, but reduce process efficiency. Table 2.1 summarises the influence of each parameter, based on the cited literature.

Table 2.1: Influence of cutting parameters on surface roughness, tool wear, and material removal rate (MRR) based on various studies.

Cutting Parameter	Effect on Surface Roughness	Effect on Tool Wear	Effect on Material Removal Rate (MRR)	References
Cutting Speed, (v_c)	Influence on surface roughness is non-linear; may improve or degrade surface finish depending on cutting conditions (e.g., AISI 4140).	Generally increases tool wear due to higher forces.	Tends to increase MRR with higher speeds.	[32], [48], [75]
Feed per Tooth, (f_z)	Higher feed rates generally lead to higher surface roughness and can cause feed marks. In certain conditions, feed rate can reduce roughness.	Increases tool wear, especially due to increased cutting forces.	Increases MRR.	[48], [68], [75]
Radial Depth of Cut, (a_e)	Has a significant impact on surface roughness. Higher a_e generally increases roughness due to higher cutting forces.	Variable impact depending on tool stiffness and cutting conditions.	Increases MRR.	[68], [75]
Axial Depth of Cut, (a_p)	Larger a_p increases surface roughness, especially due to increased cutting forces.	Larger a_p increases flank wear.	Increases MRR but also increases tool wear and roughness.	[48], [75]
Cutting Edge Radius	Larger radius generate more feed marks and higher micro hardness, affecting surface quality.	Can increase cutting forces and tool wear.	Less significant impact on MRR.	[24]

2.1.3 Cutting tools

In CNC milling, tool selection depends primarily on the geometry and size of the workpiece, as well as on the specific cutting operation. Effective chip evacuation is also critical to ensure process stability and surface integrity [73]. Finishing operations typically require tools with smaller teeth, high cutting speeds and low feed rates, while for robust roughing tools, lower speeds and higher feed rates are preferred [22].

The most relevant tool types in multi-axis CNC milling are face mills and end mills. Face mills are used to produce flat surfaces using cutting edges located on the tool's face. End mills combine peripheral and frontal cutting edges and are widely employed in operations such as pocketing, contouring, and slotting. Their versatility makes them essential in complex parts machining, particularly in five-axis machining [22], [43].

Gear hobs and convex or concave cutters are examples of form tools that can be used for specialized profiles, however their application is limited in CNC machining [22]. Because end mills and indexable cutters are more flexible, make changing tools easier, and work better with adaptive machining techniques, they are usually preferred.

Cutting tools can be made from various materials including high speed steels (HSS) and hard metals (carbides). HSS have a good combination of wear resistance and toughness, but it performs

less favourably compared to carbides. Additionally, the cutting speeds and feeds allowed for HSS are lower [8], [27].

Hard metals, typically composed of tungsten carbide (WC) and cobalt (Co), are produced via powder metallurgy. The carbides provide hot hardness and wear resistance, while the binder has a metallic matrix, responsible for the toughness of the metal. The composition of carbides depends on the type of application, where cobalt content can vary between 5% and 20%. Lower binder content increases hardness but reduces toughness [8], [27].

Carbide tools are often coated to improve mechanical properties, reduce friction and increase cutting speed [27]. Coatings can be applied through Chemical Vapour Deposition (CVD) or Physical Vapour Deposition (PVD). CVD is performed at 700–1050°C and produces strong adhesion and wear resistance. PVD, applied at 400–600°C, offers great cutting edge toughness and resistance to thermal cracking [8]. Table 2.2 summarises common coating types and their properties.

Table 2.2: CVD and PVD coatings properties.

Coating Type	**CVD**	**PVD**
Titanium Nitride (TiN)	Improves wear resistance and it is used for wear detection (gold colour) [8].	Used for general purposes and wear detection [8].
Titanium Carbonitride (TiCN)	Resistance to wear by abrasion and reduction of flank wear [8].	Flank wear resistance and high hardness [8].
Titanium Aluminium Nitride (TiAlN or AlTiN)	-	Higher hardness combined with oxidation resistance. Improves overall wear resistance [8].
Aluminium Oxide (Al_2O_3)	Low thermal conductivity and crater wear resistance. Improves plastic deformation resistance [8].	-
Aluminium Chromium Nitride (AlCrN)	-	High fracture resistance and low thermal conductivity at elevated temperatures. Good oxidation resistance and superior wear resistance [40], [80].

Uncoated carbides suffer significant and accelerated tool wear. Cermets, made of titanium-based carbides, exhibit self-sharpening wear, low cutting forces, and improved tool life, ideal for stainless steels and nodular cast irons [8].

The grain size is one of the most important aspects to understand the relationship between hardness and toughness. While toughness is enhanced by coarser grains, hardness is increased by finer grains. PVD produces finer, sharper layers, while CVD produces thicker, rounded ones. Additionally, thinner layers are more capable of maintaining sharpness for finishing. Thicker coatings provide heat protection but round the edge [8].

Key tool parameters include number of cutting edges, pitch, length of cut, tool fixation and refrigeration systems. Shorter tools with large diameters offer more stability and stiffness. While

fewer flutes promote evacuation and lower forces, more flutes increase stiffness and surface quality while limiting chip evacuation, as displayed in Figure 2.6. Four-flute tools are frequently used for steel [10].

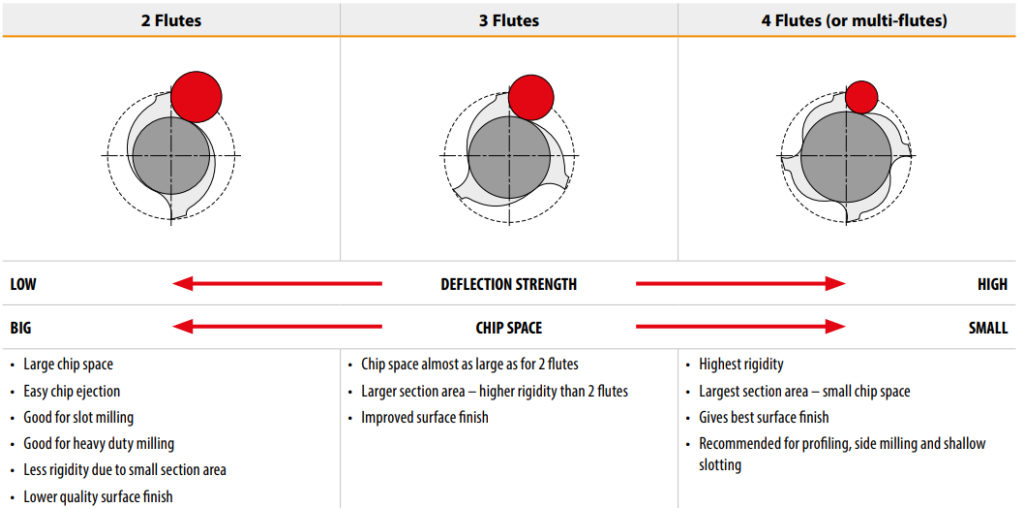


Figure 2.6: Influence of the number of flutes on machining [10].

Tooth pitch also impacts vibrations. A comparison with even pitch can be observed in Figure 2.7, concluding that an uneven configuration is preferred in vibration-prone operations because it reduces harmonic oscillation and increases stability [10].



Figure 2.7: Tool pitch [10].

When machining, it is essential to understand the interaction between the tool and the workpiece to predict and prevent potential errors. As discussed in Chapter 2.1, milling is characterized by an intermittent cutting process, which can impose significant stress on the tools. As axial depth of cut (a_p) increases, more flutes engage the workpiece, raising axial forces and tool deflection, compromising accuracy and finish. Higher radial depth (a_e) similarly increases forces. Additionally, for finishing, tool radius should be smaller than the part radius to avoid simultaneous multi-edge engagement, which is aggressive on the tool.

The entrance of the cutting tool is also critical. When the tool is programmed to enter in a straight line, thick chips are produced until the cutting edge has full contact. This reduces tool life and can lead to vibrations. It is preferable to enter the piece with a smaller feed and rolling entry. When milling corners, the contact area increases and the cutting edge is subjected to more unstable cutting forces. With this, there is a higher probability of vibrations and marks on the surface. As such, reducing tool diameter or applying a programmed corner radius can mitigate this effect [8].

Another important aspect is the helix angle, that influences the evacuation and cutting forces. Higher angles produce radial evacuation and higher axial forces, as illustrated by Figure 2.8 [53]. Therefore, for hard materials, lower helix angles (30º–45º) are preferred to reduce spindle load and vibration [10].

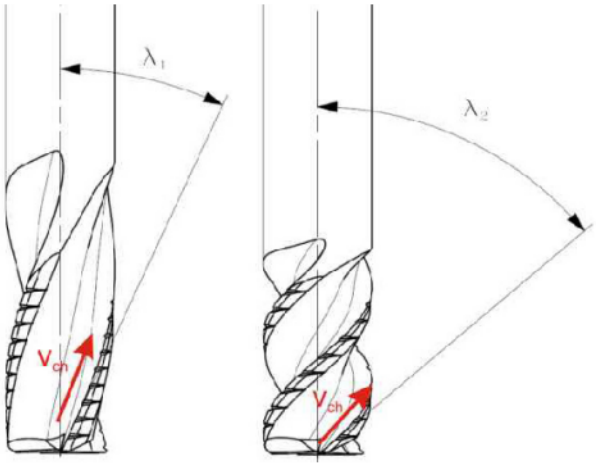


Figure 2.8: Influence of the helix angle on chip evacuation [53].

The existence of chamfers is also important since they distribute cutting forces over a higher area, increasing edge strength and reducing stress. Tools with 45º chamfers are standard in hard material applications, protecting the tool.

Regarding inserts, it is necessary to consider its shape, clearance angle, nose radius and angle. High entering angles reduce edge load but raise radial forces, while low angles do the opposite. Larger nose radius increases strength and depth of cut, while smaller radius improve chip breakage and reduce vibration. The relationship between depth of cut, a_p, and nose radius also impacts vibrations- radial forces become axial with the increase of depth of cut, as observed in Figure 2.9. As such, the nose radius should be lower or equal to the depth of cut [8].

Insert geometry also affects performance. The inserts can be negative, with 0º clearance angle, or positive (around 3º-7º). Negative inserts have higher cutting edge resistance and are more suitable for heavy cuts. On the other hand, positive inserts result in lower cutting forces.

The entering or lead angle, K_r, corresponds to the angle between the main cutting edge and material surface- Figure 2.10. Larger position angles increase cutting force but reduce vibration. Smaller angles produce thinner chips and less wear but are more prone to vibration [8].

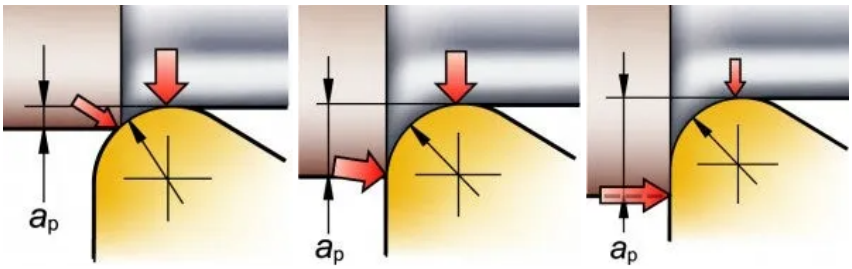


Figure 2.9: Influence of the depth of cut on cutting forces [8].

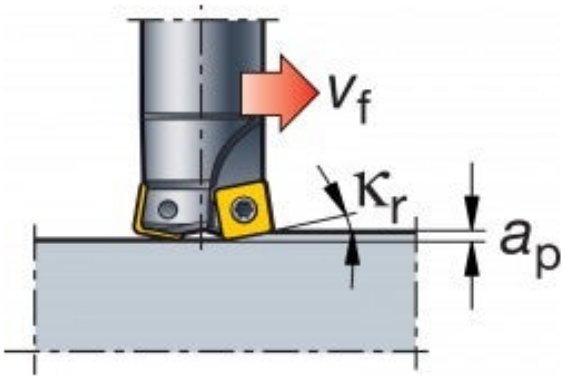


Figure 2.10: Entering angle of an insert [8].

Drilling is another common CNC operation. Drills are made from HSS or carbide. Carbide is preferred for small diameters, tight tolerances and regrind purposes [8]. Point angles vary from 118º (HSS) to 130–140º (carbide), with higher angles lowering axial force and shortening chips [45]. The clearance angle between the flank and hole wall prevents friction. Lower angles support the edge but raise heat. Higher angles reduce friction but may promote vibration [45].

The web is the main element of the drill because it withstands torsional and compressive loads and is responsible for its alignment. Its thickness increases from the point to the shank of the tool and impacts stiffness. Thick webs have higher stiffness, unlike thin webs that reduce the required axial force [45].

Chip shape reflects process efficiency, as Figure 2.11 indicates. Continuous chips are harder to evacuate and may indicate issues [45]. Drills typically evacuate chips upward, risking build-up and breakage. To help with chip evacuation, peck drilling is usually employed. However, it increases wear, so internal coolant is a mandatory addition, enhancing evacuation and tool life.

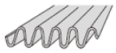
Types of Chips	Shape	Features and Ease of Raking
Conical Spiral		Fan-shaped chips cut by the cutting edge are curved by the flute. Chips of this type are produced when the feeding rate of ductile material is small. If the chip breaks after several turns, the chip raking performance is satisfactory.
Long Pitch		The generated chip comes out without coiling. It will easily coil around the drill.
Fan		This is a chip broken by the restraint caused by the drill flute and the wall of a drilled hole. It is generated when the feed rate is high.
Segment		A conical spiral chip that is broken before the chip grows into the long-pitch shape by the restraint caused by the wall of the drilled hole due to the insufficiency of ductility. Excellent chip disposal and chip discharge.
Zigzag		A chip that is buckled and folded because of the shape of flute and the characteristics of the material. It easily causes chip packing at the flute.
Needle		Chips broken by vibration or broken when brittle material is curled with a small radius. The raking performance is satisfactory, but these chips can pack closely creating.

Figure 2.11: Different types of chips observed in drilling [45].

Cutting fluids aid in chip removal and temperature control [10]. Tools with larger diameters require lower pressure but higher flow. Cooling options include high-pressure (around 70bar) for long-chip materials, Minimum Quantity Lubrication (MQL) for aluminium, and dry cutting for short chips and shallow depths. Emulsions, composed of a mixture of water and oil are typically preferred for CNC machining [8]. They offer higher specific heat capacity and thermal conductivity than straight oils, can be used in high pressure systems and are more affordable.

Regarding tool holders, they must ensure concentricity, gripping force and balance. Common systems include collets, hydraulic chucks, shrink-fit holders and Weldon/Whistle Notch. Collets offer precision and rigidity. Hydraulic chucks provide excellent concentricity, but may cause imbalance. Shrink-fit holders offer the best rigidity–precision combination. Weldon systems are simpler but less accurate due to asymmetry [10].

In summary, the selection of cutting tools in multi-axis CNC milling must consider not only the tool type and material, but also geometric features, coating technologies, chip evacuation efficiency and tool holding systems. These factors have a direct impact on machining forces, tool life, surface quality and process stability. The practical application of these concepts, used in the experimental approach, will be covered in Chapter 3.

2.2 Characterization of 42CrMo4 Steel

The focus of this chapter is on the specific material used in the machining case study- steel 42CrMo4. The workpiece was specifically investigated for this steel, therefore understanding its properties is essential to adjust cutting parameters, select appropriate tools and develop a suitable machining strategy.

Steel 42CrMo4 is a low-alloy, medium carbon steel, known for its high strength, high fatigue strength and wear resistance [54], [83], [87]. The presence of chromium (Cr) and molybdenum (Mo) in its composition significantly enhances its mechanical properties, making it suitable for demanding applications [4], [54], [83], [87].

Alloying elements are added to steel in order to obtain the desired properties. When combined with other elements, alloying elements can produce properties that differ slightly from those they would have if used alone, which can either be beneficial or incompatible. Chromium and molybdenum enhance tensile strength, wear resistance, high-temperature performance, hot wear resistance and corrosion resistance. Additionally, they contribute to maintaining hardness at elevated temperatures and extending tool life. Chromium increases tensile strength while reducing thermal and electrical conductivity, whereas molybdenum enhances the elastic limit [67]. In general, each alloying element has an impact on the mechanical, thermal and machining abilities of a material. Figure 2.12 illustrates the influence of these elements on material characteristics and machinability.

Elemento de liga		C	Si	Mn (1)	Mn (2)	Cr	Ni (1)	Ni (3)	Al	W	V	Co	Mo	Cu	P	S
Propriedades mecânicas	Dureza	↑↑↑	↑	↑	↓↓↓	↑↑	↑	↓↓	–	↑	↑	↑	↑	↑	↑	–
	Resistência à tracção	↑↑↑	↑	↑	↑	↑↑	↑	↑	–	↑	↑	↑	↑	↑	↑	–
	Limite de elasticidade	↑↑↑	↑↑	↑	↓	↑↑	↑	↓	–	↑	↑	↑	↑	↑↑	↑	–
	Alongamento	↓	↓	~	↑↑↑	↓	~	↑↑↑	–	↓	~	↓	↓	~	↓	↓
	Estricção	~	~	~	~	↓	~	↑↑	↓	↓	~	↓	↓	~	↓	↓
	Resistência ao impacto	↓	↓	~	–	↓	~	↑↑↑	↓	~	↑	↓	↑	~	↓↓↓	↓
	Elasticidade	↓	↑↑↑	↑	–	↑	–	–	–	–	↑	–	–	–	–	–
	Estabilidade a quente	↓	↑	~	–	↑	↑	↑↑↑	–	↑↑↑	↑↑	↑↑	↑↑	↑	–	–
Velocidade Crítica			↓	↓	↓↓	↓↓↓	↓↓	↓↓	–	↓↓	↓↓	↑↑	↓↓	–	–	–
Formação de carbonetos			↓	~	–	↑↑	–	–	–	↑↑	↑↑↑↑	–	↑↑↑	–	–	–
Resistência ao desgaste			↓↓↓	↓↓	–	↑	↓↓	–	–	↑↑↑	↑↑	↑↑↑	↑↑	–	–	–
Forjabilidade			↓	↑	–	↓	↓	↓↓↓	↓↓	↓↓	↑	↓	↓	↓↓↓	↓	↓↓↓
Maquinabilidade		↓	↓	↓	↓↓↓	–	↓	↓↓↓	–	↓↓	–	~	↓	~	↑↑	↑↑↑
Oxidação a quente		↓	↓	~	↓↓	↓↓↓	↓	↓↓	↓↓	↓↓	↓	↓	↑↑	~	–	–
Aptidão à Nitruração			↓	~	–	↑↑	–	–	↑↑↑	↑	↑	–	↑↑	–	–	–
Resistência à corrosão		~	–	–	–	↑↑↑	–	↑↑	–	–	↑	–	–	↑	–	↓

Figure 2.12: Impact of the alloying elements in the material's properties and machining [67].

Due to its high strength, 42CrMo4 is commonly used in applications where static and dynamic stresses are significant, such as automotive components, bolted assemblies, cranks, forged parts, injection moulding and pressure vessels [3], [54], [87]. It is also widely used in industries that require heat treatment and plastic deformation [83]. However, like other high-strength steels, 42CrMo4 is prone to hydrogen embrittlement, a risk that increases with material strength. To mitigate this and enhance properties such as tensile strength, hardness and fatigue resistance, the material is typically subjected to quenching and tempering treatments [21], [54], [83], [87].

For machining purposes, it is important to classify the material into an ISO (International Organization for Standardization) group. According to the ISO 513 standard, there are six main ma-

terial groups, as displayed by Figure 2.13, categorised by physical and machining characteristics. These are identified by letters and colours, with additional sub-groups. Materials not explicitly included in the ISO standards can be classified in an additional group, O.



Figure 2.13: ISO material groups classification [64].

As a steel alloy, 42CrMo4 is placed within ISO group P (steels). While it may reach relatively high hardness levels, it typically does not reach the levels of hardness required for group H, making group P the most appropriate classification.

In summary, steel 42CrMo4 is a highly versatile alloy that offers an excellent combination of strength, toughness and wear resistance, making it suitable for a wide range of industrial applications. Its properties can be further improved through appropriate heat treatments, such as quenching and tempering, to optimize mechanical performance and durability. However, selecting the optimal heat treatment process depends on specific application requirements.

2.2.1 Machining of 42CrMo4 Steel

Machining processes can alter material's properties and performances through mechanical, chemical, thermal and physical effects [68]. Steel alloys, like 42CrMo4, require quality tool materials, coatings and cooling methods for effective machining. Surface integrity, influenced by micro geometry, subsurface alterations and residual stresses, plays a critical role in product quality [42].

Numerous researches have studied the optimal cutting parameters for 42CrMo4 to enhance tool performance and final product quality. Van-Hai Nguyen et al. [48] studied the milling of AISI 4140 steel, which is equivalent to 42CrMo4, and found that the optimal milling parameters included a cutting speed of 428.46 m/min, a feed rate of 0.285 mm/tooth and a depth of cut of 0.208 mm, with a tool radius of 0.4 mm. Regarding the tool material, PVD-coated Nano-TiAlN coating resulted in more controlled wear and cutting forces.

Further research by Van-Hai Nguyen et al. [47] explored different cutting tools, including TiCN/Al2O3 MT-CVD-coated, TiAlN PVD-coated and uncoated carbide tools. Nano-TiAlN PVD-coated tools demonstrated superior thermal resistance, wear performance and tool life. The best results were observed with cutting speeds from 228.41 to 449.82 m/min, feed per tooth between 0.1 and 0.24 mm/tooth and depths of cut between 0.16 and 0.23 mm.

Marco Stipkovic et al. [68] investigated the surface integrity of quenched and tempered 42CrMo4 using cubic boron nitride (CBN) inserts, without cutting fluids. Their research revealed

that higher feed per tooth and cutting depth increased surface roughness, while cutting speed had a minimal effect. Regarding cutting stresses, the feed and cutting speed were the most influential parameters. Milling with CBN inserts resulted in low surface roughness and compressive residual stresses, which makes it suitable for fatigue loading applications. The optimal cutting parameters identified were a cutting speed of 344.9 m/min, a feed per tooth of 0.17 mm/tooth and a depth of cut of 0.21 mm.

Advanced machining techniques have also been explored. Marcin Płodziet et al. [56] compared high-feed (HF) milling with conventional face milling for 42CrMo4. HF milling resulted in higher removal rates but also generated higher cutting forces, particularly in the axial direction, along with increased vibrations and surface roughness, making it suitable for high-stiffness machines.

W. Ahmed et al. [1] investigated self-propelled rotary tools (SPRT), which rotate due to cutting forces. These tools reduced wear by 22–37% compared to fixed tools. However, surface roughness was improved with conventional round inserts. Optimal parameters varied depending on the objective: high MRR (240 m/min, 0.25 mm/rev), better finish (235 m/min, 0.19 mm/rev, 19° inclination) or balanced operation (98 m/min, 0.23 mm/rev, 7° inclination).

Cooling techniques also play a crucial role in machining. Cutting fluids enhance tool life and surface quality by providing cooling and lubrication. However, environmental concerns and disposal costs have led research into alternative techniques such as dry cutting and Minimum Quantity Lubrication (MQL) [14]. Dry cutting reduces fluid use but can lead to increased wear and heat. MQL offers a compromise, reducing fluid consumption while maintaining machining quality and tool life. Sales et al. [60] demonstrated that MQL improved both tool life and surface roughness in AISI 4140. The best results were obtained with fluid flows of 100–150 ml/h, confirming MQL's potential.

In summary, machining of 42CrMo4 steel demands careful optimisation of tool materials, coatings and cutting parameters. Table 2.3 summarises the key findings of the discussed studies, which consistently point to TiAlN-coated carbide tools, cutting speeds between 220 and 450 m/min, feed rates from 0.1 to 0.28 mm/tooth and depths of cut ranging from 0.15 to 0.25 mm. Despite the guidance offered by literature, parameters must always be adapted to the specific part geometry, machining strategy and equipment constraints.

Table 2.3: Summary of studies on machining parameters for 42CrMo4 steel.

Cutting Parameters	Tools	Conclusions	Reference
Cutting speed: 428.46 m/min; **Feed per tooth**: 0.285 mm/tooth; **Depth of cut**: 0.208 mm	High-strength fine carbides with nano-TiAlN PVD coating.	Higher cutting speed and feed improved MRR but increased tool wear.	[48]
Cutting speed: 228.41–449.82 m/min; **Feed per tooth**: 0.1–0.24 mm/tooth; **Depth of cut**: 0.16–0.23 mm	Cemented carbide with nano-TiAlN PVD coating.	Speed and feed improved MRR; TiAlN coating reduced tool wear.	[47]
Cutting speed: 344.9 m/min; **Feed per tooth**: 0.17 mm/tooth; **Depth of cut**: 0.21 mm	Cubic boron nitride (CBN) inserts.	Feed and depth increased roughness; optimised parameters improved fatigue resistance.	[68]
Variable in each test	Conventional carbide tools and high-feed (HF) milling tools.	HF milling increased MRR but also cutting forces and roughness.	[56]
Cutting speed: 240 m/min & **feed per rev.**: 0.25 mm/rev (high productivity); **Cutting speed**: 235 m/min & **feed per rev.**: 0.19 mm/rev (better surface finish); **Cutting speed**: 98 m/min & **feed per rev.**: 0.23 mm/rev (balanced approach)	Self-propelled rotary tools (SPRT).	SPRT reduced tool wear; fixed tools gave better surface finish.	[1]
Cutting speed: 250 m/min; **Feed per rev.**: 0.1 mm/rev; **Depth of cut**: 1 mm; cutting fluid flow variations	TiAlN-coated cemented carbide inserts.	MQL improved tool life and reduced surface roughness.	[60]

2.3 Monitoring techniques in machining

Reliable, efficient and safe machining operations require strong monitoring strategies [35]. The early identification of errors, optimisation of cutting conditions and prevention of failures depend on the acquisition, processing and interpretation of signals from the machining system. Monitoring systems enable adaptive control and predictive maintenance by evaluating important variables such as cutting force, vibrations and temperature [17], [35]. This contributes to reduced waste, increased productivity and enhanced process stability.

Monitoring techniques are typically classified as either *direct* or *indirect* [35]. Direct monitoring involves the measurement of physical parameters such as tool wear using equipment like high-resolution cameras, laser sensors or electrical resistance probes [70]. While this approach offers high accuracy, its complexity and limits in industrial settings makes it impractical in industrial environments, in most cases. In contrast, indirect measurement estimates the machining conditions based on cutting forces, vibrations, acoustic emissions or temperature using correlations that have been empirically determined [35], [41], [70], [74]. This method allows for continuous process monitoring without interfering with operations and is more flexible for real-time industrial applications.

The integration of sensors with advanced signal processing algorithms enables predictive maintenance and improves process control [35]. Digital Signal Processing (DSP) techniques are crucial in the refinement and extraction of relevant features from acquired signals [17]. Frequency-domain methods, such as the Fast Fourier Transform (FFT), reveal periodic components, while time-domain methods detect rapid shifts. Since most machining signals are non-stationary, it takes more complex methods to identify significant patterns in them, like the Hilbert-Huang Transform (HHT), Wavelet Transform (WT) and Short-Time Fourier Transform (STFT), that offer a more localized analysis [17]. However, computational and interpretational complexity are major limitations.

To achieve optimal monitoring, three components should be considered: appropriate sensor selection, effective signal processing and the application of predictive models with high reliability [35]. The following sections review commonly monitored parameters in machining, particularly in milling, and explore typical sensor technologies and experimental setups.

2.3.1 Signal Acquisition

The acquisition of signals during machining operations is mainly accomplished using sensor technologies, enabling constant monitoring of key process variables. This leads to enhanced process stability, monitoring of tool conditions and optimization of the process. There is a variety of options for sensors, including force, vibration and electric current sensors, thermocouples and infrared sensors for temperature monitoring ([36], [37]), acoustic emission (AE) systems ([74], [78]), sound analysis ([7], [52]) and wireless approaches ([13]).

2.3.1.1 Force and Torque sensors

The study of cutting forces in metal cutting processes is essential for tool design, energy efficiency, tool wear estimation and surface finish prediction. These forces are very sensitive to tool wear and process alterations, which makes it a great indicator of performance [35], [70]. Cutting forces can be divided into two categories: static forces, which are average values, and dynamic forces, that are variations during cutting [35]. Typically, a dynamometer is used to measure these forces directly but strain-gauges, current signals from motors or machine behaviours can also be used to measure them indirectly [35].

Force sensors use piezoelectric or strain-based sensing devices to convert force into measurable electrical signals. Torque sensors operate in a similar manner but detect rotational loads instead. Since these sensors are frequently built into machine spindles or tool holders, special signal transmission techniques are needed. Overall, force and torque sensors are very useful for real-time process monitoring and tool wear detection because of their high reactivity [70].

Several studies highlight the use of dynamometers for measuring cutting forces. H. Saglam and A. Unuvar [59] monitored milling forces using a dynamometer to register the forces in all directions (X,Y and Z) and three strain-gauges that register the strain, which in turn can be used to estimate forces. L.N. L'opez de Lacalle et al. [33] employed a KISTLER quartz dynamometer

to measure forces and torques in three directions (X, Y, Z). Similarly, Wei-Kang Wang et al. [79] combined a fixed dynamometer on the workpiece and a rotational dynamometer on the spindle to monitor cutting forces and predict chatter. M. Q. Tran et al. [72] placed a KISTLER dynamometer between the workpiece and the machine table, as demonstrated by Figure 2.14, to estimate cutting forces.

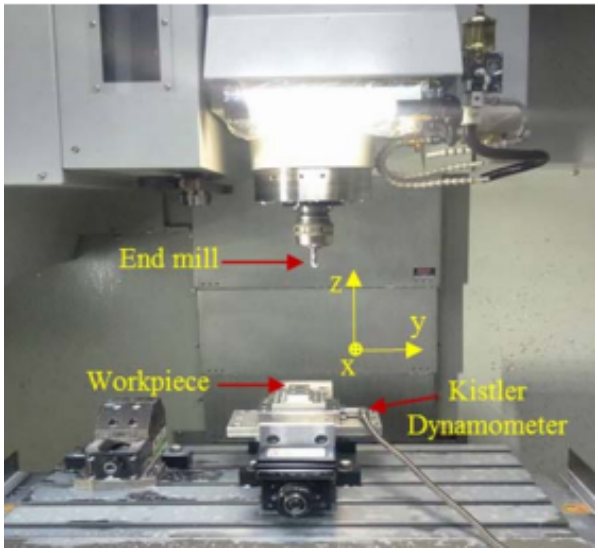


Figure 2.14: Example of an experimental setup using a dynamometer for cutting forces estimation [72].

2.3.1.2 Vibration Monitoring

Vibration is a fundamental dynamic phenomenon in machining processes. It can significantly impact dimensional accuracy, surface finish, tool life and overall process stability [13], [35], [57]. L. Pejryd et al. [52] demonstrated that cutting pressures also increase and that the machine tool is damaged due to vibrations between the tool and the workpiece.

Vibrations in machining are typically categorised into three main types [13], [52], [57]:

- **Free vibration**: happens when a system is disrupted and given the freedom to oscillate without constant external stimulation. Usually, sudden impact is the primary cause.
- **Forced vibration**: typically caused by an imbalance between spindles, bearings, gears and other machine tools.
- **Self-excited vibration (chatter)**: results from regenerative effects at the tool-workpiece interface.

Chatter, in particular, is considered the most critical and common vibration type in milling [79]. According to G. Quintana et al. [57], it can be classified as primary or secondary. Primary chatter is induced by friction or thermal effects. Secondary chatter occurs due to waviness regeneration, especially in overlapping tool paths. When the cutter vibrates, it causes a wave on

the surface that will, in turn, interact with the subsequent tooth as it cuts and produce a new one. This effect can be observed in Figure 2.15. The difference between waves is what causes the chip thickness and cutting force to change and, ultimately, result in vibrations [57].

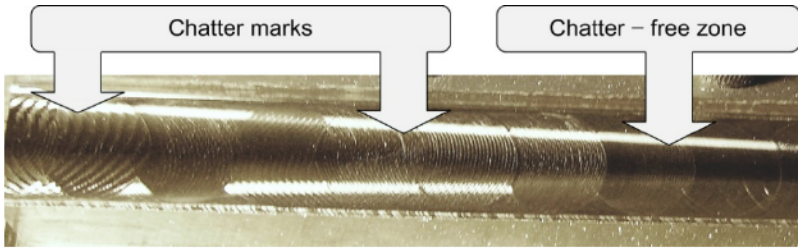
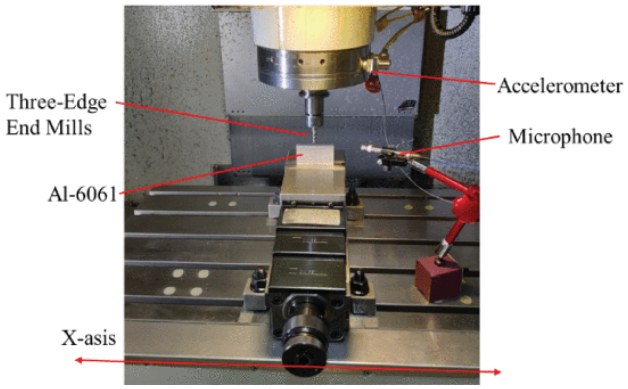


Figure 2.15: Chatter effect on the machined surface [71].

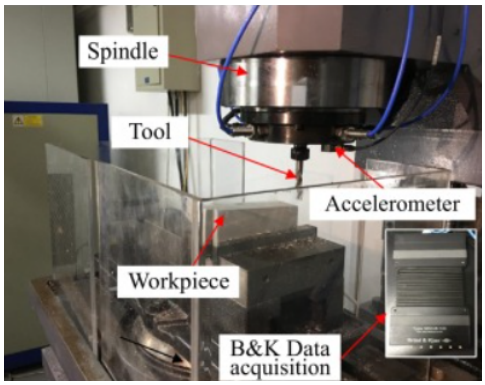
Accelerometers are the most widely used sensors for vibration monitoring. Typically mounted on the spindle or machine body, they record acceleration and can detect oscillations along different axes [30]. Proximity and eddy-current sensors may also be employed to measure relative displacements [26].

Li et al. [38] points out the advantage of spindle-integrated sensors, since vibration monitoring at the tool tip is not as sensitive. They proposed embedding piezoelectric actuators and sensors into the tool holder for real-time chatter control. Hao Jiang et al. [26] installed proximity sensors on the spindle head and workpiece, along with accelerometers, to quantify vibrational displacement in X and Y directions using eddy current sensors. There are several other studies that use accelerometers for vibration detection during machining [34], [55], [81].

Given the challenges of placing sensors near the cutting tool due to chip removal and coolant presence, accelerometers are usually installed on the spindle [55]. Because the spindle is directly attached to the tool, vibrations are reflected on the sensor more precisely. Additionally, the sensor is more stable due to the body being stationary. Examples of other experimental setups using accelerometers and microphones are illustrated in Figures 2.16a and 2.16b.



(a) Experimental setup using an accelerometer and microphone [7].



(b) Experimental setup using an accelerometer [79].

Figure 2.16: Example of experimental setups for vibration testing.

It is also very common to use both an accelerometer and dynamometer to obtain information about vibrations and cutting forces at the same time. Typically, the accelerometer is placed at the spindle and the dynamometer at the workbench/table. For instance, T. Kalvoda et al. [28] used a three-axis accelerometer to obtain accelerations in the three conventional axis (X,Y,Z) and a three-axis piezoelectric dynamometer. The experimental setup can be observed in Figure 2.17. This configuration is usually standard for this type of sensors and readings.



Figure 2.17: Example of an experimental setup for the estimation of both cutting forces and vibrations [28].

Optimizing fixture design to reduce excessive vibrations and increase machining precision is other way to achieve vibration management [35]. Reducing the speed and/or depth of cut is a popular solution on the production floor. However, this strategy lowers production. As alternative, identifying the system's transfer functions, with the help of an impact hammer and a force transducer can help evaluate vibration risks [52].

2.3.1.3 Power and current monitoring

Monitoring motor power and current can also be used as a form to evaluate machining performance and identifying irregularities since it does not interfere with operations. These monitoring methods are included into the controls of CNC systems, allowing control algorithms to make real-time process modifications. However, external factors such as temperature variations, friction, and the general condition of the machine can compromise the accuracy of sensor readings, potentially leading to misleading interpretations [70].

Despite these limitations, current monitoring has proved to be practical and non-invasive method for evaluation of tool condition during milling operations. It is possible to indirectly estimate the cutting load without requiring physical modification of the machine structure by correlating the increase in spindle motor current with progressive tool wear. This method has shown to

be appropriate for industrial applications because of its affordability, simple implementation, and ability to work with real-time monitoring systems. Y. Zhou at al. [86] concluded that current-based monitoring methods can have similar performance to direct cutting force measurement techniques, particularly when combined with advanced signal processing techniques.

2.3.1.4 Summary of sensors approach

To conclude, there is a wide number of options and techniques to monitor different aspects of a machining process. In this ambit, most studies, summarized in Table 2.4, focus on vibration and cutting forces monitoring because these factors have a great impact on tool life, surface roughness and overall process and product's quality. For this measurements, piezoelectric sensors are usually used and quartz crystals are preferred for their high rigidity and frequency response.

Table 2.4: Summary of sensor applications in machining monitoring.

Sensors Used	Objective	Variables Monitored	Reference
Dynamometer, strain gauges	Force monitoring	Cutting forces (X, Y, Z)	[59]
Quartz dynamometer, torque sensor	Force and torque monitoring	Cutting forces, torque	[33]
Fixed + rotating dynamometer	Chatter prediction	Cutting forces, vibration	[79]
Dynamometer under workpiece	Force estimation	Cutting forces (X, Y, Z)	[72]
Piezo actuators, sensors	Chatter control	Vibration signals	[38]
Eddy current, accelerometers	Displacement/vibration	Vibration	[26]
Microphone (mobile), software	Acoustic chatter detection	Sound frequency	[52]
Accelerometer + microphone	Vibration and acoustic monitoring	Acceleration, sound	[7]
Piezo-film sensor, XBee module	Wireless vibration monitoring	Vibration	[13]
Accelerometer + dynamometer	Force and vibration analysis	Forces, acceleration	[28]
AE sensors (tool/workpiece)	Tool wear detection	AE frequency spectra	[74], [78]
Thermocouples, IR camera	Temperature evaluation	Heat distribution	[36], [37]
Spindle current sensors	Indirect force estimation	Power/current signals	[70], [79], [86]

2.3.2 Signal Processing

To effectively monitor machining operations, it is essential to not only acquire signals but also to process them in order to extract relevant information from noisy and complex signals [79]. The raw output from sensors like accelerometers, dynamometers and current clamps is often not suitable for direct analysis and, therefore, requires pre-processing and transformation techniques. Signal processing in machining monitoring is commonly divided into three stages: pre-processing, domain transformation, and feature extraction and classification.

Pre-processing involves signal amplification, filtering, and segmentation. Piezoelectric sensors, such as accelerometers or force sensors, typically cannot be directly connected to the A/D converter. For this purpose, an amplifier is employed to transform the electrical charge into a voltage signal that aligns with the input range of the converter [70].

Filtering is applied to remove irrelevant frequency bands, typically using Finite Impulse Response (FIR) filters or Kalman filters. Additionally, spectral windowing functions such as the Hamming window are often applied before FFT to reduce spectral leakage [29], [7]. Signal segmentation isolates the cutting phase from idle time, ensuring that only relevant data is processed [70].

Signal processing methods are typically performed in the time, frequency, or time-frequency domains [35], [79]. In the time domain, statistical indicators such as the Root Mean Square (RMS), peak-to-peak amplitude and standard deviation provide information on signal intensity [85], [23].

Frequency domain methods identify the frequencies that result from signals [79]. Fast Fourier Transform (FFT) is a common technique to detect chatter, as it has the capacity to transform time domain signals into the frequency domain [79]. The main limitation of this method is that it does not have the ability to provide the moment the frequency occurred, which limits its applicability to non-stationary signals, like chatter [72].

Time-frequency methods overcome these limitations by combining both domains. Examples of techniques include Wavelet Transform (WT), that overcomes the limitation of monitoring non-stationary signals of the FFT. Although it has a higher computational cost, it can combine time and frequency analysis. The Hilbert-Huang Transform (HHT) is suitable for non-stationary and non-linear signals [35], [79]. The Short-Time Fourier Transform (STFT), an extension of the FFT, applies the transform to consecutive time windows, allowing for time–frequency localisation [79].

Several studies demonstrate the performance of these techniques. M. Q. Tran et al. [72] applied Fast Fourier Transform (FFT), Short-time Fourier Transform (STFT) and Continuous Wavelet Transform (CWT) to cutting force signals under varying conditions to detect chatter. CWT was found to be the most effective, as it offers both time and frequency resolution. STFT has a limited time resolution, so it is not appropriate for real time chatter monitoring. At last, FFT was able to identify chatter occurrence, around 4000 Hz, as it can observed in Figure 2.18, but it is limited to stationary signals.

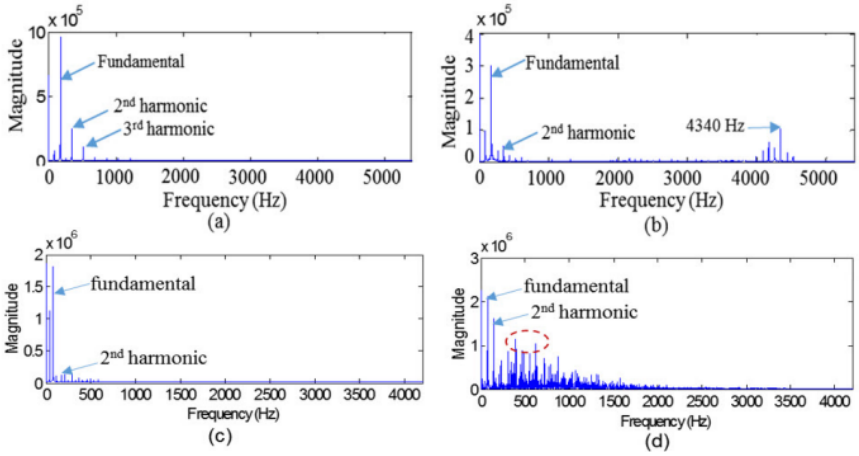


Figure 2.18: Chatter prediction using Fast Fourier Transform method [72].

Huang et al. [23] analysed cutting force signals in milling of Ti–6Al–4V using a sampling

rate of 7,000 Hz, which enabled a frequency analysis up to 3,500 Hz. Chatter was identified through FFT as non-harmonic peaks between 700 and 2,400 Hz, confirming the need for high-resolution sampling. In addition, the standard deviation of cutting force increased by over 80% during unstable cutting, supporting its use as a vibration indicator.

Sun et al. [69] monitored vibrations during thin-walled milling by measuring dynamic clamping force using embedded piezoelectric sensors sampled at 20 kHz. FFT revealed chatter frequency components around 600 Hz under unstable conditions. Zhou C et al. [86] observed chatter occurrence around 850 Hz and additional energy from 800 Hz.

W. Zhong et al. [85] studied the effect of cutting fluid based on vibration signals of the milling process, using time waveform, FFT and Wavelet Packet Transform (WPT). The waveform plots (Figure 2.19) revealed a close to periodic pattern (with small variations in time), typical of dynamic systems and intermittent cutting. The RMS (Root Mean Sqaure) value was used as a key indicator of vibration intensity, revealing that higher spindle speeds and fluid flow rates lead to increased dynamic excitation. FFT and WPT results showed that cutting fluid affects not only the amplitude but also the spectral distribution of vibration energy.

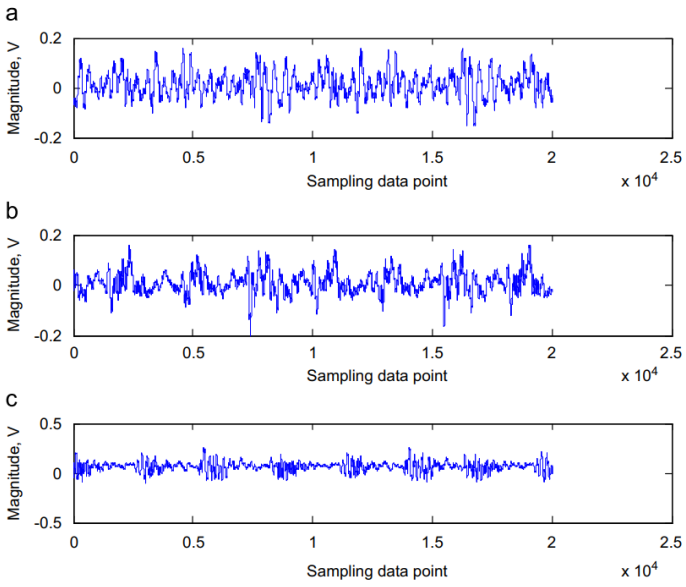


Figure 2.19: Processing of vibration signals using a time waveform [85] .

Although not applied in this work, other studies have explored alternative signal processing techniques. X. Li et al. [39] applied Wavelet-based De-noising and Permutation Entropy to analyse motor current signals, using a Median filter to reduce noise. Kalvoda et al. [28] employed the Hilbert-Huang Transform (HHT) with Empirical Mode Decomposition (EMD) to extract real-time amplitude, phase and frequency data. Kim et al. [29] used a Kalman Filter on servo motor currents, which improved force estimation.

After the signal is processed, it is necessary to identify the causes that are causing the phenomenon being evaluated. Statistical indicators (e.g., Root Mean Square (RMS), peak-to-peak,

entropy) help detect changes in the process, providing an overview of the process behaviour. Methods like power spectral entropy and fractal dimensions can identify more complex and specific patterns [79].

In a systematic review of over a hundred studies, Ghazali and Rahiman [15] identified RMS and FFT as the most used techniques in vibration analysis for machining. RMS is distinguished for its ease of use and efficiency in measuring vibration intensity, particularly under stationary conditions. The identification of frequency components associated with mechanical failures, such as chatter is possible with FFT. Although methods like Wavelet Transform can overcome certain limitations, the authors reinforce that RMS and FFT are essential due to their lower computational cost and robustness.

In recent developments, machine learning models such as Support Vector Machines (SVM), Convolutional Neural Networks (CNN) and fuzzy logic systems have been used for classification and condition recognition, particularly when combined with time–frequency features [7], [79], [70].

In summary, signal processing plays a critical role in the detection and interpretation of machining conditions. While advanced methods offer higher accuracy in complex scenarios, FFT and RMS remain the most practical tools for vibration-based monitoring, due to their simplicity and compatibility with industrial applications. Table 2.5 summarises several key studies on signal processing in machining.

Table 2.5: Summary of relevant studies on signal processing in vibration monitoring during milling.

Method(s) Used	**Analysis Parameters**	**Conclusion**	**Reference**
FFT, STFT, CWT	Cutting force signals	CWT most effective for chatter; FFT detected chatter but limited to stationary signals.	[72]
FFT, Std. deviation	Cutting force	Chatter between 700–2400 Hz; standard deviation increased >80% under instability.	[23]
FFT, RMS, WPT	Vibration under different lubrication	RMS increased with speed and flow; high flow rates shifted spectral energy to higher bands.	[85]
FFT	Clamping force	Chatter at 600 Hz; PVDF-based sensing effective for non-intrusive monitoring.	[69]
FFT	Cutting force signals	Chatter observed at 850 Hz; non-harmonic components related to instability.	[86]
ApEn, STFT, CNN	Vibration and sound signals	STFT images with CNN achieved 95.5% classification accuracy.	[7]
RMS, FFT	Review (105 studies)	RMS and FFT most used- robust, low-cost and suited for real-time use.	[15]
Wavelet de-noising, Permutation Entropy	Motor current signals	Effective for detecting tool breakage; entropy varied with cutting conditions.	[39]
HHT, EMD	Real-time vibration	Extracted instantaneous amplitude, phase, frequency; suited for non-stationary signals.	[28]
Kalman Filter	Servo motor current	Improved force estimation; accuracy limited by non-linear friction.	[29]

Chapter 3

Methodology

This chapter describes the methodology used to perform experimental tests and emphasizes the most critical parts of the machining process. Each section approaches the important parts of an experimental setup, providing the properties of the used material, machine characteristics, product's design, the explored approaches, cutting tools and plans for machining along with the technical decisions and, finally, the production of the part.

3.1 Materials and Equipment

In this case study, the material used was 42CrMo4 steel, introduced in Chapter 2.2. This is a challenging material because of its high strength and hardness, which causes accelerated wear in the tools.

The steel was supplied in the cold drawn condition, meaning it was plastically deformed at room temperature through a die, resulting in improved dimensional precision and enhanced mechanical strength. However, this process reduces ductility, making the material more susceptible to cracking under certain cutting conditions [31], [84].

The nominal diameter of the bar was 40 mm and its chemical composition is detailed in Table 3.1. According to the ISO classification, this material belongs to group P. Based on the total content of alloying elements (3.04%) and carbon content below 0.5%, it can be further classified as a low alloyed steel- subgroup P2 [67].

Table 3.1: Chemical composition of the 42CrMo4 steel (% mass).

C	Mn	Si	S	P	Cr	Ni	Mo	Al	Cu	B
0.428	0.870	0.280	0.0200	0.012	1.050	0.100	0.150	0.020	0.110	0.0001

From its alloy elements, it is also possible to obtain some prespective of its machinability. For instance, Cr and Mo are carbide formers that increase abrasive wear. The material also exhibits a

high manganese, Mn, content which improves the stability, yield strength and tensile strength [67]. The percentage of carbon is relatively high, suggesting higher abrasive wear. Sulphur, S, is known for its positive impact on machinability, but in this material its value is very small, suggesting low influence when milling [67]. Although most of the alloying elements have both positive and negative aspects, the low percentage of sulphur and higher content of carbon, indicates that this material is going to promote tool wear.

The material exhibits a tensile strength of 744 MPa and a proof stress of 593 MPa, measured at 0.2% plastic strain. Other mechanical properties can be found in Table 3.2.

Table 3.2: Mechanical Properties of the material 42CrMo4 steel.

Tensile Strength, Rm [MPa]	**Proof stress, Rp (0,2) [MPa]**	**Elongation (%)**	**Hardness (HBW)**
744.0	593.0	14.7	220.0

Its hardness was obtained by the Hardness Brinell Wolfram carbide test, where a tungsten carbide ball is used instead of a steel ball. The material's elongation of 14.7% suggests good ductility, compared to most steels. However, the balance between high strength and low sulphur results in a material with low machinability, promoting tool wear and increased cutting forces.

The results of a Jominy hardenability test were also presented in the material's technical file, where the hardness began around 58 HRC and decreased to 35 HRC at 50 mm. As such, even though the material demonstrates good surface hardening behaviour, the hardenability rapidly decreases with increasing depth.

In conclusion, the chemical and mechanical characteristics of 42CrMo4 make it a difficult-to-machine material. This material requires careful tool selection and machining strategies to minimise wear and maintain process stability.

The experimental work was conducted on a Brother U500Xd2 5AX five-axis CNC machine. The spindle is capable of delivering a maximum power of 15.4 kW, with a maximum torque of 27 Nm and rotational speed of 16000 rpm. Furthermore, the spindle is driven by a three-phase motor that functions on alternating current (AC) with 200 to 230 V. This high spindle speed is combined with a BT30 tool interface, which is suitable for high-speed machining operations due to its low mass and good balance.

In addition to the traditional three axes (X,Y,Z), it features two more axes- A and C- that allow the table to tilt and rotate, as illustrated in Figure 3.1. This configuration enables complex part productions and simultaneous 5-axis machining.

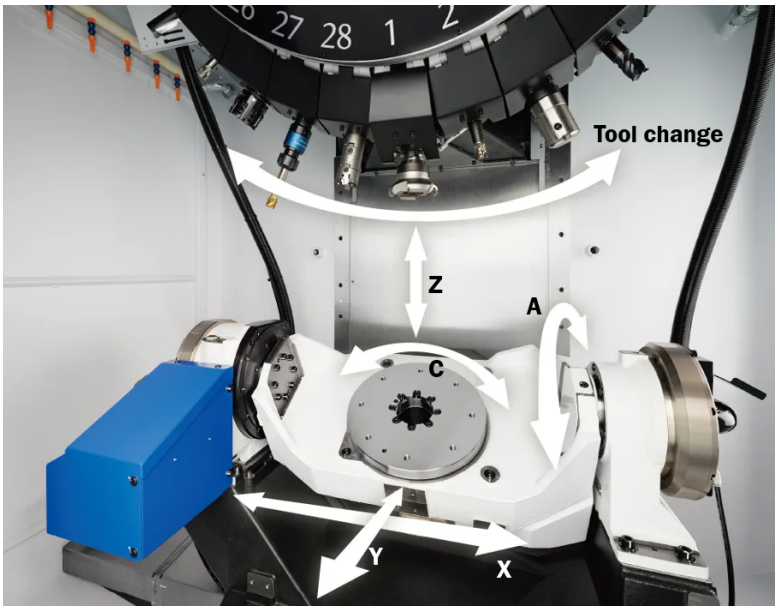


Figure 3.1: Axes movements of U500Xd2 Brother machine.

The cutting fluid is also a critical aspect as it helps with chip breakage, lubricates the cutting zone and helps control the temperature. In this study the coolant used is Ecocool Global 1000, an oil and water emulsion supplied by FUCHS. The emulsion exhibits a density of 0.99 g/cm^3 at 15ºC and a pH value of 9.4. The recommended concentration in water goes from 6% to 8%.

Advanced functions are also available, such as Machining Load Monitor function. This feature provides information about the maximum and medium values of the spindle load for each tool. Through a pre-defined value introduced in the machine, when this function is activated, if the load surpasses the pre-set threshold, the alarm goes off. This facilitates process monitoring and can help indicate tool wear.

Overall, the U500Xd2 machine is suitable for high performance cutting, capable of producing complex products with elevated accuracy. Its advanced functions contribute to a stable cutting process and its monitoring.

3.2 Product Design

For this project, a test part was designed and produced since the original part could not be disclosed due to confidentiality restrictions. The workpiece was based on the key features of the original component, which was produced for the sports industry.

The 2D drawing was established according to the requirements discussed with the engineers at SISMA and can be observed in Figure 3.2. It was developed in the SolidWorks software.

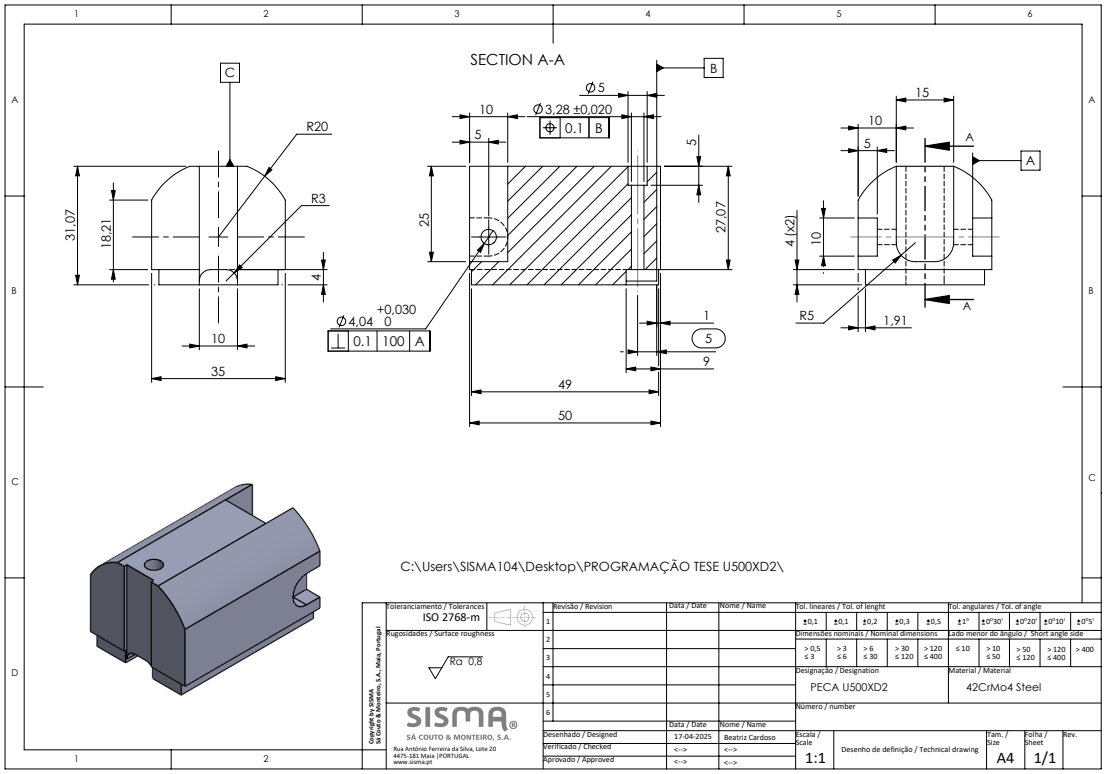


Figure 3.2: Technical drawing of the part.

This technical drawing highlights the most important aspects that affect the machining strategies and selection of cutting tools. The most demanding requirements are the perpendicularity and position tolerances.

The position tolerance of the D3.28 hole informs that its axis must be inside a theoretical cylinder of 0.1 mm of diameter [46]. This tolerance is ensured by the inspection dimension of 5 mm and the datum B. The machining of this hole is also demanding because the height is around seven times the diameter (7xD). This requires long tools, which are more prone to deflection and vibrations. Additionally, chip evacuation becomes harder when drilling deep holes.

Regarding the perpendicularity tolerance, it is necessary to guarantee that the axis of the D4.04 hole, is inside a theoretical cylinder of 0.1 mm, along 100 mm and perpendicular to the face of datum A [46]. Datum C is the secondary reference for this tolerance. This is difficult to obtain because, when drilling, it is difficult to guarantee that there are no tool axis deviation.

Another interesting aspect of this part is the two straight vertical lateral surfaces, with a height of 18.21 mm, that were designed for quality control purposes. These serve as references to measure the D3.28 hole position and ensure repeatability. The bottom 90 degree corners (1.91 x 4 mm) were implemented to facilitate the fixture of the part. Both of these additions are common practice in machining, but only implemented if there is no interference with the functional parts of the piece.

The 3D model of the part was also designed, with SolidWorks, providing a deeper understanding of the geometry and serves as base to program the machining strategy in CAM software.

Figures 3.3 and 3.4 illustrate the 3D views of the part to be machined.

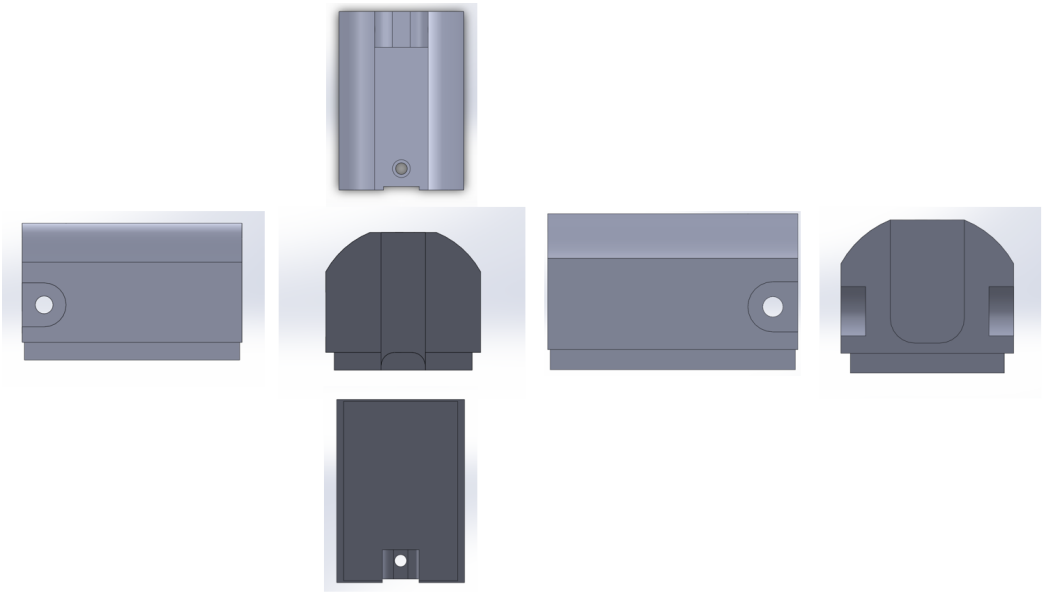
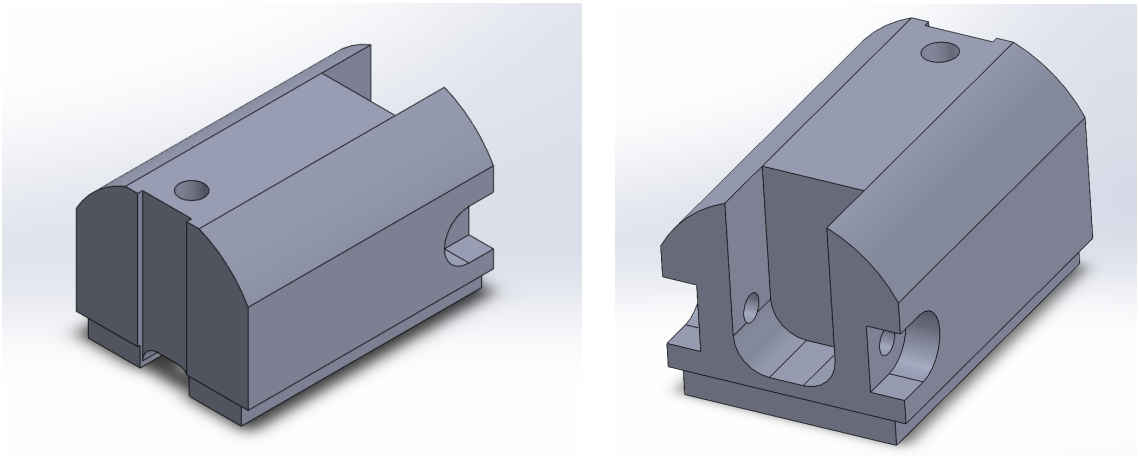


Figure 3.3: Different views of the 3D model (following the European projection method).



(a) View 1. (b) View 2.

Figure 3.4: Isometric view of the 3D model from different angles.

3.3 Machining strategies

This subsection describes the development and refinement of the machining strategy for the experimental part. It includes the definition of clamping setups, tool selection, parameter adjustment and strategies that combine practical decisions with CAM-based validation.

3.3.1 Initial Approaches

The development of a machining strategy is not only guided by theoretical principles, but also by practical experience. In this context, the guidance and expertise of the company's engineers were essential to establish a solid strategy.

From the experience of engineers, some practical rules were considered. For instance, in roughing, it is important to try to maximize material removal to minimise load impact on finishing tools. If there is excess material left, the finishing tool will have to work in overload, resulting in accelerated tool wear and vibrations. Additionally, it is usual to select tool diameters around 70–80% of the feature size.

In finishing operations, smaller tools are preferred to ensure that final dimensions are reached and match the shape of the part with more precision. Surface roughness is a critical factor in finishing and is mainly affected by the feed per tooth, f_z. Higher feed per tooth generally produces ribbed finishes, so it is important to find a balance between desired surface roughness and productivity.

A first analysis of the part geometry led to the identification of three main types of operations: face milling to produce plain/flat faces, end milling to produce perpendicular faces and profiles with radius, and drilling for the holes.

Drilling operations require careful consideration due to the significant depth of the holes and the tight tolerances involved. Regarding the 4.04 mm diameter hole, because it is difficult to guarantee that the tool cuts in the same exact point, when changing the cutting plane, it is better to drill in a single pass through the full width of the part, rather than performing two drilling operations in each side.

The sequence of operations involving the oblong feature, adjacent to this hole, was also considered. Drilling into a machined oblong may lead to deviation as a result of lack of material support. Although machining this feature after is likely to push chips into the hole, it can be solved by either a chamfer mill- capable of cleaning and removing sharp edges- or by manual removal of chips using, for example, a ball nose end mill.

In addition, to reduce the effective drilling depth, it was also considered to machine the two surrounding boxes of 5 mm diameter. In summary, for this particular hole, both boxes can be machined first, followed by drilling and finally milling of the oblong.

Clamping configuration of the part was also critical at this point. Because of the cylindrical shape of the raw material and limited access to the top and bottom surfaces in a single setup, two distinct clamping configurations, or setups, were considered. After evaluation of the available fixturing devices at SISMA and consulting with the technical team, it was possible to select the most suitable options. This led to two different configurations, designated as AP1 and AP2.

At this stage, the value of diameters, type of operations, sequence and clamping modes were defined. The initial machining strategy can be visualized in Tables 3.3 and 3.4, corresponding, respectively, to the first and second clamping configuration.

Table 3.3: First setup (AP1) of the initial machining strategy.

Operation Number	Type of tool	Diameter (mm)	Comments
1	face mill	40	Roughing – Top
2	face mill	40	Finishing – Top
3	end mill	12 or 8	Roughing – Lateral recess
4	end mill	12 or 8	Finishing – Lateral recess

Table 3.4: Second setup (AP2) of the initial machining strategy.

Operation Number	Tool	Diameter (mm)	Comments
1	face mill	40	Roughing – Top
2	face mill	40	Finishing – Top
3	face mill	40	Roughing – Front face
4	face mill	40	Finishing – Front face
5	face mill	40	Roughing – Back face
6	face mill	40	Finishing – Back face
7	end mill	12	Roughing – Lateral 1
8	end mill	12	Finishing – Lateral 1
9	end mill	12	Roughing – Lateral 2
10	end mill	12	Finishing – Lateral 2
11	end mill	8	Roughing – Oblong Right
12	end mill	8	Finishing – Oblong Right
13	end mill	8	Roughing – Oblong Left
14	end mill	8	Finishing – Oblong Left
15	drill	4	Drilling – Hole D4.04
16	end mill	8	Roughing – Oblong Back
17	end mill	8	Finishing – Oblong Back
18	reamer	4.04	Reaming – Hole D4.04
19	end mill	8	Roughing – Slot Front
20	end mill	8	Finishing – Slot Front
21	end mill	6	Roughing – Slot Access Hole D3.28
22	end mill	5	Finishing – Slot Access Hole D3.28
23	end mill	3	Roughing – Counterbore D5 Top
24	end mill	3	Finishing – Counterbore D5 Top
25	drill	3.2	Drilling – Hole D3.28
26	reamer	3.28	Reaming – Hole D3.28
27	chamfer end mill	4	Chamfer – Hole 4.04 – 1
28	chamfer end mill	4	Chamfer – Hole 4.04 – 2
29	chamfer end mill	3	Chamfer – Hole 3.28

The tool selection process began by consulting catalogues from the main suppliers of the company, such as Guhring, Hoffman, Sandvik Coromant and ISCAR. After analysing this approach and conducting further research on machining methods, it was concluded that for the two drilling operations, it would be better to consider deep hole strategies, such as pilot drill and peck drilling [8], [10], [18].

A pilot drill is responsible for providing accuracy of drill location and preventing eccentricities. The pilot tool should be shorter and only enter a depth up until 3xD [8], [18]. Peck drilling involves intermittent retraction of the tool in order to facilitate chip evacuation in deep holes [8].

Chip evacuation, cooling and lubrication directly affect tool life. Therefore, another critical aspect when drilling long lengths is the availability of internal cooling supply and its pressure. Although external cooling also helps with surface lubrication and chip removal, it is often insufficient at greater depths than 3xD [8]. As such, to effectively remove chips, internal cooling systems must provide sufficient pressure and flow rate. According to tool manufacturers, a minimum pressure of 10-15 bar is recommended at high depths [8], [10]. However, the required pressure also depends on the diameter of the tool, where smaller diameters typically require higher pressure values and lower flow rates [8].

The pressure available at the U500Xd2 internal cooling system is around 15 bar, which is at the lower limit of the recommended range. Considering the application conditions- narrow diameters, depths of 6-7xD and a medium-hard material that tends to form long and continuous chips- concerns rise about its capability to evacuate chips and provide proper lubrication. As a result, the incorporation of pilot drilling and peck cycles are important to reduce tool misalignment, improve chip evacuation and surpass the limitation imposed by coolant pressure.

The choice of diameters was also modified, replacing the end mill of 12 mm of diameter for 10 mm, since it is capable of performing the same operations and has shorter length, making it less prone to deflection. To break sharp edges, it is more economical and time-efficient to use a single chamfer mill with 4 mm diameter, rather than two different tools with varying diameters. This approach simplifies tool management, cuts down cycle time and eliminates unnecessary tool changes.

The final tool selection and refinement of the machining strategy was carried out in parallel with the CAM simulation. These points will be addressed in the following section 3.3.2.

3.3.2 Final Strategy and CAM Validation

After considering some preliminary approaches, the implementation and tuning of the final strategy was supported by MasterCAM software. This CAM program allows the definition of tools and their respective paths, parameters and simulation of the operations. It is an essential step in the production planning of a product as it allows the detection of collisions and errors, in addition to automatically generating the G-code for the machine.

3.3.2.1 Setup AP1 Strategy and Operations

Following the correct modelling of the part and fixturing, the simulation of the AP1 setup was conducted. It is represented in Figure 3.5 and corresponds to the production of the surfaces that allow the next configuration- AP2.

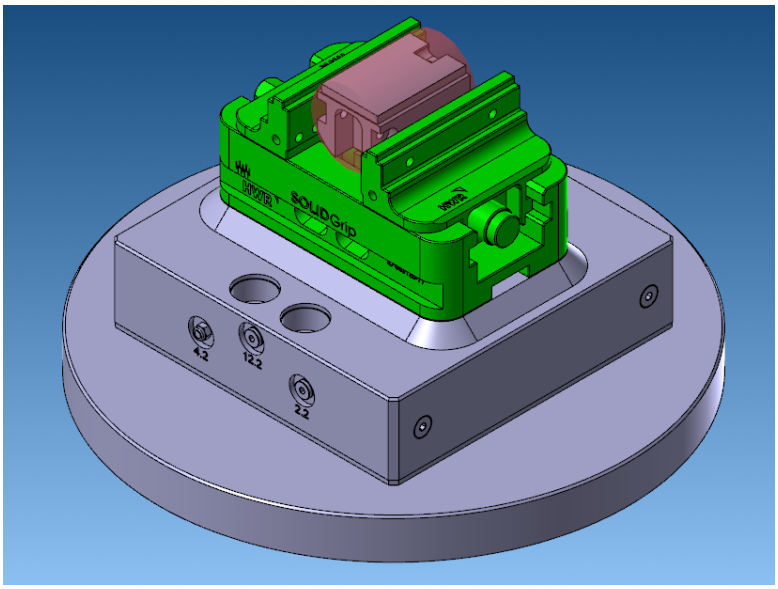


Figure 3.5: First setup (AP1).

The roughing of the top surface was performed with a 10 mm diameter end mill instead of a face mill. Face mills generate higher axial forces and, since the part is a cylindrical bar placed in a vice, there is an increased risk of part slippage during the operation. The usage of an end mill reduces the axial loads and increases stability under less rigid clamping. Moreover, this tool was already planned for the next roughing operations, thus reducing the number of tool changes. For this operation, the tool performs several passes and cuts with the lateral and end faces, increasing stability.

The top is finished with the face milling cutter in just one pass. The roughing and finishing of the lateral recess are executed with an end mill of 10 mm of diameter, consistent with the initial strategy defined. Chamfers of 0.02 mm were added using a 4 mm chamfer mill. All the tool paths programmed for AP1 are represented in Figure 3.6.

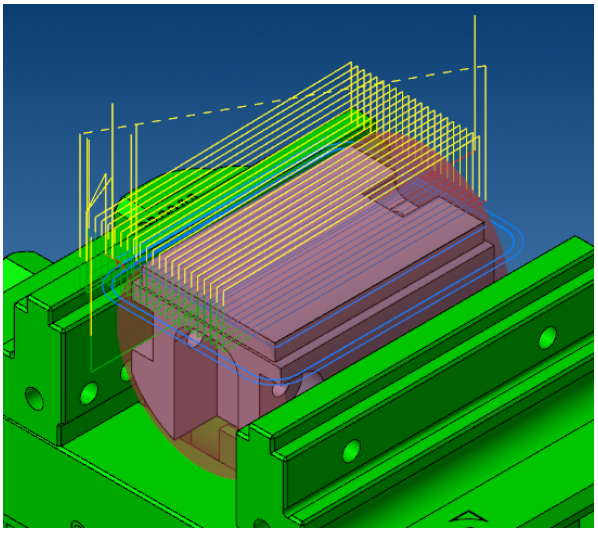
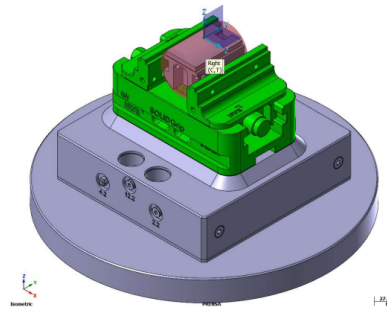


Figure 3.6: Tool path visualisation for AP1.

The respective setup sheet can be observed in Figure 3.7. This document provides essential information about the machining plan, including operations sequence, tools and tool holders used, time of each operation, spindle speed and feed rate and other important notes. The sheet serves as reference for both the technical and shop floor team, promoting traceability and consistency between planning and execution stages.



Lista de Programas Mastercam

Tempo total
0H 2M

Programa	No	Cone	Ferramenta	T	Ø	Comp. Ferram.	Plano	Stock XY	Stock Z	Inc Z	S	F	Z Max	Z Min	H:M:S	Top of Stock	Comentario
PECA US00XD2-AP1	1	BBT30 PP CP25 A=75 D IR	FCH0.2 D10 Z4 2.5XD DE 10 REV AD30-203015 10	1	10	32	Top	0	0,1	NA	5730	1030	20	-7,37	00:01:30	0	ROUGHING TOP
	2	BBT30 PP CP25 A=75 D IR	FCH0.2 D10 Z4 2.5XD DE 10 REV AD30-203015 10	1	10	32	Top	0,05	0,05	NA	5730	1030	20	-11,42	00:00:41	-7,47	ROUGHING LATERAL RECESS
	3	BBT30 PP ER20 A=60 D IR	FCH0.2 D10 Z4 2.5XD DE 10 REV AD30-203015 10	4	10	32	Top	0	0	NA	5730	1030	20	-11,47	00:00:12	-7,47	FINISHING LATERAL RECESS
	4	BBT30 PR d16 D40 A=39 REF	FPA D40 R0.4 Z4 AP8 90	2	40	40	Top	0	0	NA	1950	400	20	-7,47	00:00:13	-7,47	FACE MILLING TOP
	5	BBT30 PP CP11M A=10 0 ANG	FC D4 Z4 90 DE4 REV MD	3	4	18	Top	0	0	NA	16000	750	20	-8,07	00:00:13	-7,47	CHAMFER EXT.

Figure 3.7: Setup sheet for AP1.

3.3.2.2 Setup AP2 Strategy and Operations

The reposition of the part- AP2- allowed full access to the remaining features including front and back faces, as illustrated in Figure 3.8.

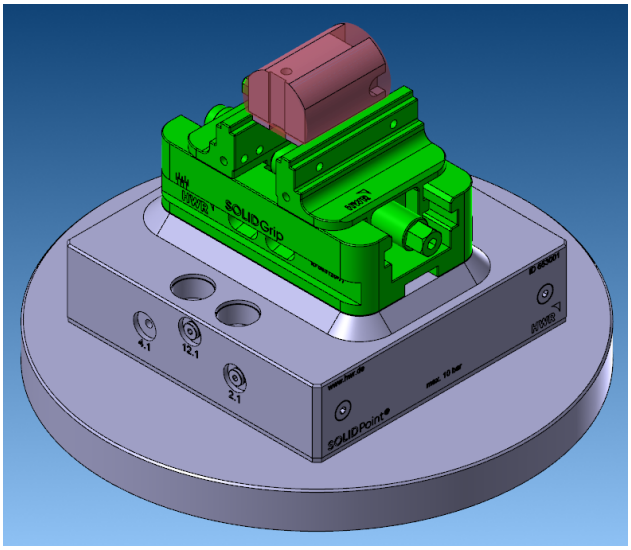


Figure 3.8: Second setup (AP2).

Drilling strategies were refined because of coolant system pressure limitations (15bar). According to Figure 3.9 this value is significantly below the minimum recommended pressure of the tool manufacturer [20]. Therefore, it is necessary to implement a peck cycle, in addition to the usage of a pilot drill.

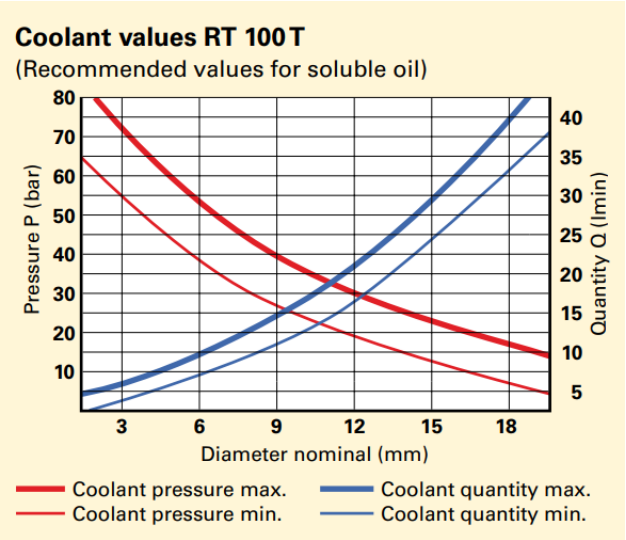


Figure 3.9: Recommended coolant pressure and flow rate for RT 100 T drills from Guhring, for internal lubrication purposes [20].

This strategy was followed for both holes. Initially, a pilot drill was employed to ensure precise positioning and centring- Figure 3.10- followed by the main drill to complete the full hole depth. For the D3.28 hole a reamer operation was also performed to ensure that the final dimensions were reached and given the unavailability of drills with 3.28 mm of diameter. On the other hand, the 4.04 mm hole was drilled to the final diameter. It is important to mention that the same strategy was not used for the holes due to tool stock limitations.



Figure 3.10: Peck drilling cycle.

The main drills were first programmed counter-clockwise (CCW) to prevent marking during positioning, a common approach in gun drilling [16]. Although the supplier only considers this necessary with depths of 40xD, a more conservative approach was adopted to ensure process

stability. Furthermore, supplier guidelines tend to consider ideal conditions that do not always reflect the limitations of real-world setups.

The internal coolant was also, initially, deactivated to avoid deflection due to coolant pressure. When the pressure of the system is turned on it can cause slight movements at the tip of the drill. This effect can be understood by analogy with a garden tap at full pressure- if the hose is let go of, it starts to move around due to the sudden force of the water. Similarly, the pressure can cause the tool to vibrate or shift slightly before the tool is stabilised or guided in the material.

Once the drill is fully guided, the rotation is switched to the standard clockwise (CW) direction and internal coolant flow is initiated, ensuring that the drill entered the material smoothly. This configuration was simulated using the command *Advanced Drill* in MasterCAM, as exhibited in Figure 3.11.

Depth	Feed	Spindle	RPM
-6.0	100.0	CCW	500
-6.0	100.0	CW	500
-26.0	350.0	CW	3500
-6.0	500.0	CW	3500
-6.0	500.0	CW	3500
0.0	100.0	CW	500
Retract	5000.0	CCW	500

Figure 3.11: Deep hole strategy using the *Advanced Drill* command.

Regarding the D4,04 hole strategy, the final approach involved machining only the front side oblong prior to the hole rather than both of them. Exiting a solid carbide drill into an open cavity increases the risk of tool breakage. As such, allowing the drill to cut through a solid wall ensures a more controlled process, reducing the probability of deviation.

For the D5 top box, a helical interpolation strategy (Figure 3.12) was adopted instead of conventional plunging, that would cause the milling cutter to behave like a drill. This technique is more advantageous because it enables constant contact of the tool with the material and is performed with lower feeds that result in smooth changes of direction and reduced workload. In addition, it produces a good surface finish [8]. Shorter tools should be used with this procedure, hence the choice of an extra short cutter length.

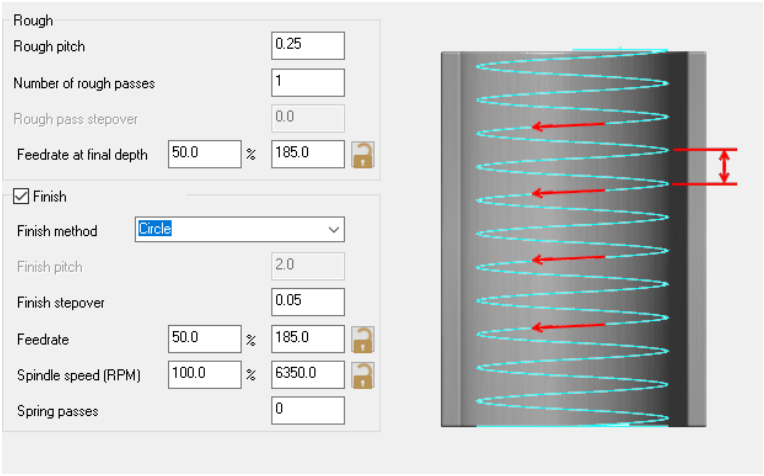


Figure 3.12: Helical interpolation technique.

The chamfers were performed with the same tool as AP1, to remove the remaining sharp edges. As common practice, the chamfers were performed at the end. The remaining operations followed the logic that was initially planned.

In both setup configurations it is important to program a smooth entry, as discussed in Chapter 2.1.3. Typically, a tangent path is preferred, as observed in Figure 3.13, in order to decrease vibrations and cutting forces at the cutting edges. Depending on the operation and available space for the tool, different configurations for the tool entry and exit can be employed- for example entering with radius.

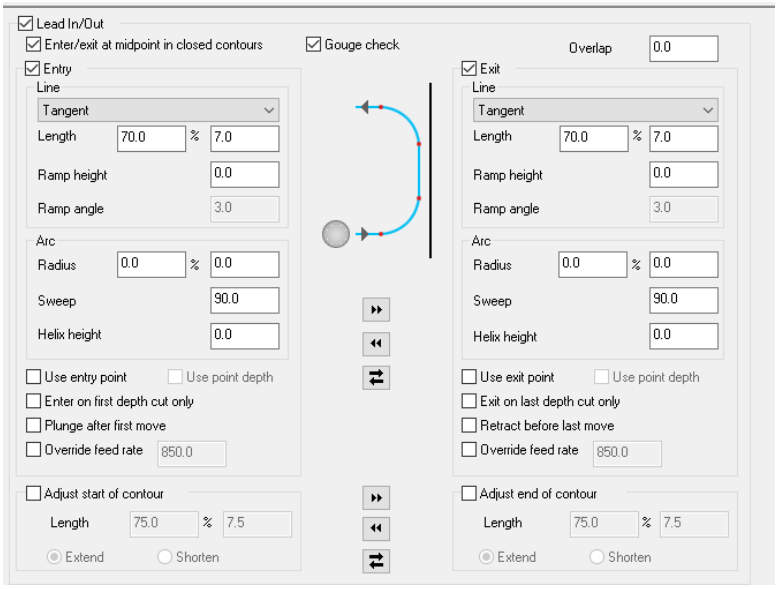


Figure 3.13: Tool entry configurations.

Two main strategies were used during AP1 and AP2- *Multi Passes* and *Depth cuts*. The first is used when there is mainly a lateral increment of the tool. This technique enables several passes and smoother cuts, as exemplified in Figure 3.14. The *Spacing* value is selected by the user and

corresponds to the increment of the tool in each pass. The number of passes is then automatically calculated based on that value and on the length to be machined. In the example bellow, 15% of the tool diameter is being used in each increment, resulting in a total of 22 passes.

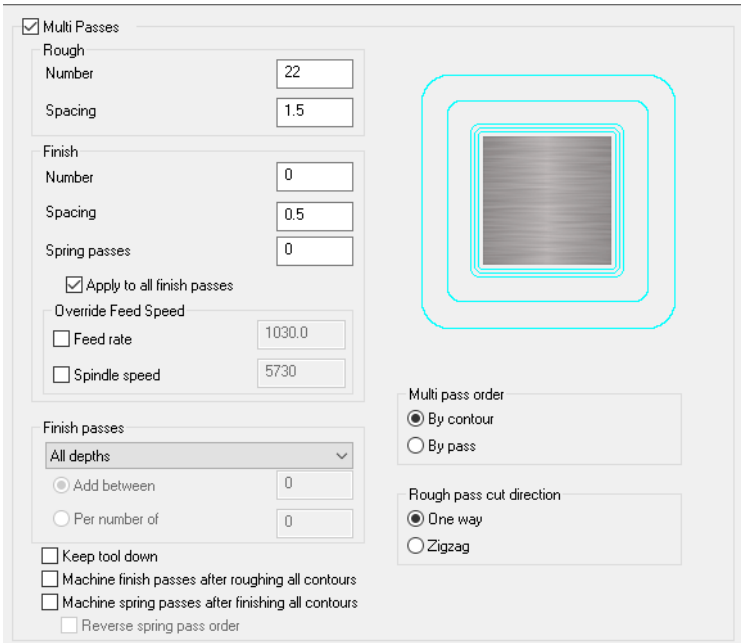


Figure 3.14: *Multi Passes* configuration.

The *Depth cuts* configuration is used when the diameter of the tool is fully engaged with the material. In these situations, it is not necessary to perform multiple radial passes. Instead, a deeper axial step is applied, improving productivity. The strategy is exemplified in Figure 3.15, where the tool performs increments of 1 mm.

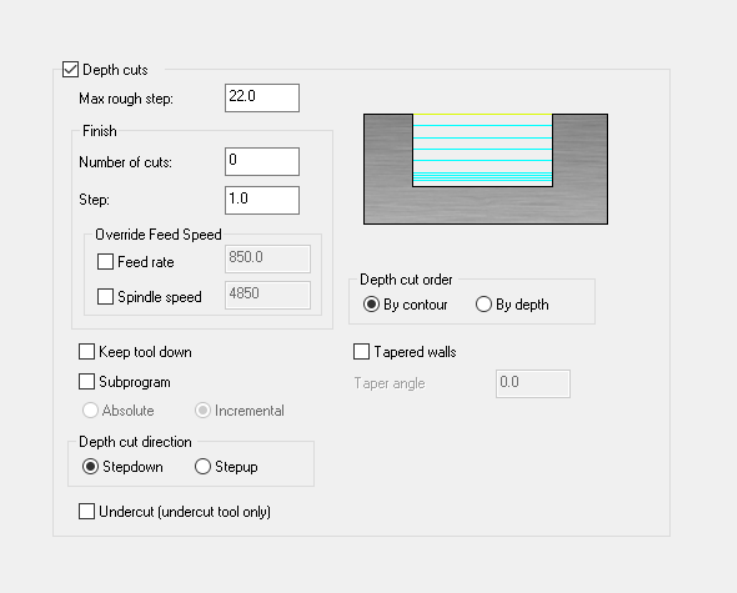


Figure 3.15: *Depth cuts* configuration.

These values are automatically calculated based on the top of stock and final depth of the material in each operation. These parameters are defined by the user in the *Linking Parameters* window, as illustrated in Figure 3.16. The number of passes is determined by subtracting the *Top of stock* and *Depth* values. In this case, the tool performs five passes.

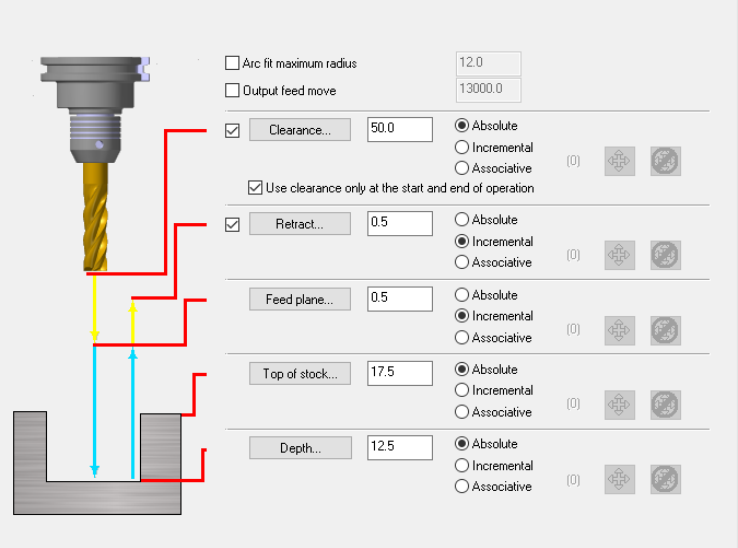


Figure 3.16: *Linking Parameters* configuration.

It is also possible to combine these two strategies to perform roughing and finishing in the same operation. This was employed in the oblong that has access to the slot with two radius of 3 mm (operation 15), as exhibited in Figure 3.17. With the *depths of cut*, the tool performs thirteen passes that perform the roughing with a maximum increment of 0.7 mm. With the multipasses feature, the tool path widens by 0.03 mm and makes two finishing passes in other to reach the final dimension. With this approach, it is not necessary to finish with multiple passes, thus avoiding marks. Since the tool has sufficient cutting length the final dimension and shape of the feature are obtained in fewer steps.

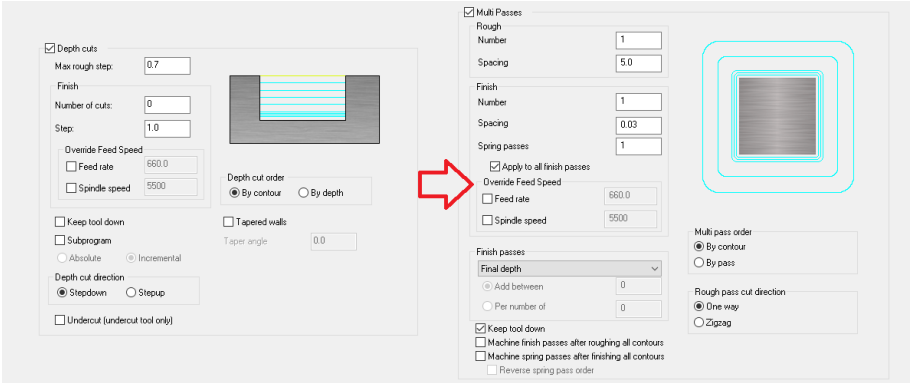


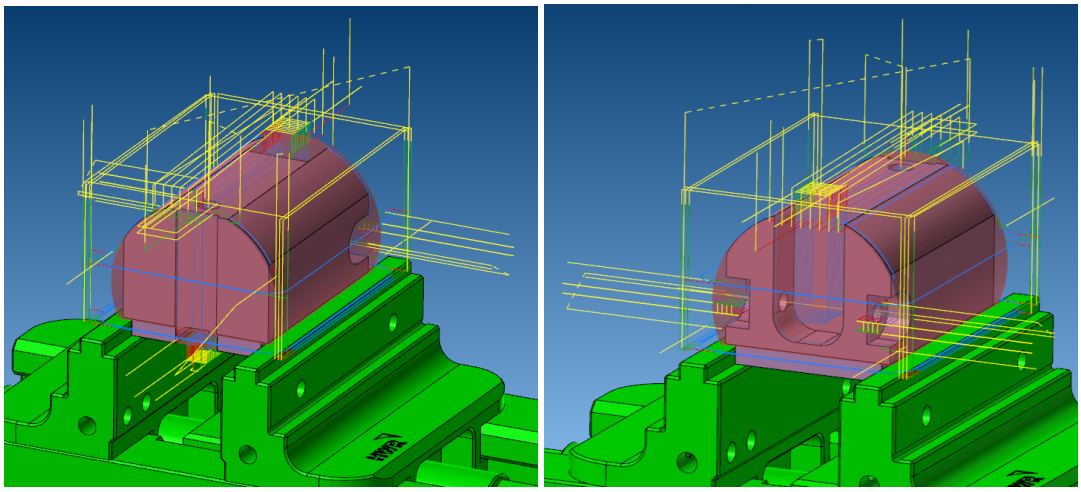
Figure 3.17: Combined strategy with *Depth cuts* and *Multipasses* (Operation 15).

After the results of the quality control regarding the first machined part, it was found that the D4.04 hole was outside tolerance limits. As such, it was decided to remove the operation with the pilot drill for reasons discussed in Chapter 4.3. The final peck cycle was adopted, as observed in Figure 3.18, performing fewer steps and with the drill cutting in the CW direction at the start, because there was no previous point guiding it. The gun drilling inspired strategy remained the same for the D3.28 hole operation.

Depth	Feed	Spindle	RPM
-0.7	50.0	CW	1500
-0.5	500.0	CW	3500
-26.0	250.0	CW	3500
0.0	500.0	CW	3500
Retract	5000.0	CCW	3500

Figure 3.18: Peck cycle of the main drill for the D4.04 hole.

In addition, the chamfers were also increased because a lot of burr was observed. The trajectories of all tools during AP2 is also illustrated in Figure 3.19.

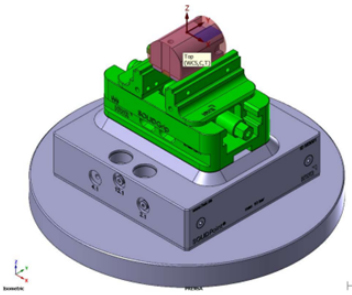


(a) Tool paths of AP2- view 1.

(b) Tool paths of AP2- view 2.

Figure 3.19: Tool path visualisation for AP2 from different perspectives.

The final setup sheet of AP2 is exhibited in Figure 3.20, where all the operations, tools and other relevant informations are listed.



Lista de Programas Mastercam

Tempo total
0H 7M

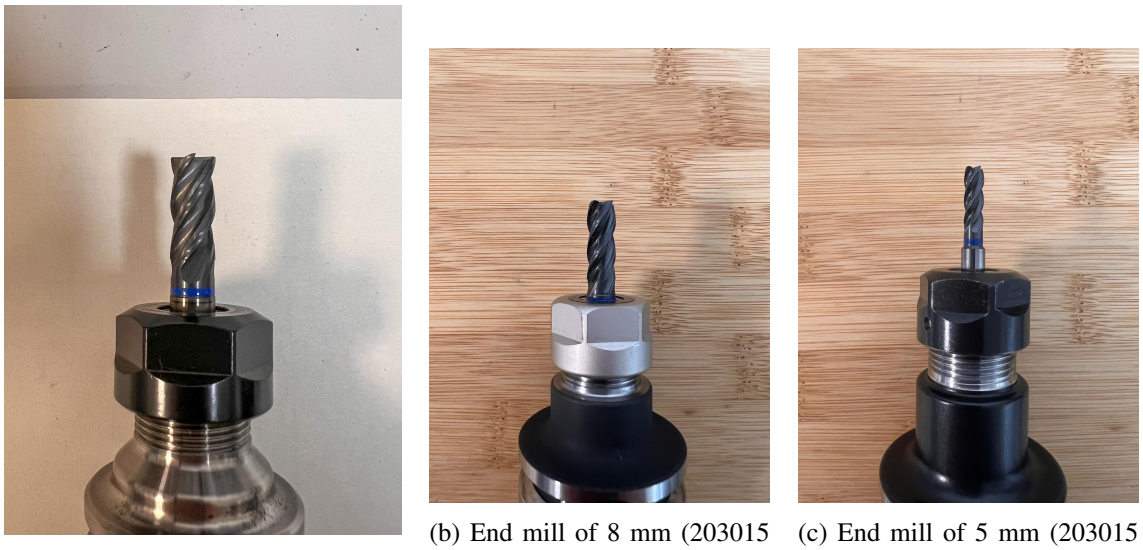
Programa	No	Cone	Ferramenta	T	Ø	Comp. Ferram.	Plano	Stock XY	Stock Z	Inc Z	S	F	Z Max	Z Min	H:M:S	Top of Stock	Comentario
PECA US00XD2-AP2	1	BBT30 PP CP25 A=75 D IR	FCH0.2 D10 Z4 2.5XD DE 10 REV AD30-203015 10	1	10	32	Top	0,05	0	NA	4850	850	20	-27,5	00:00:32	0	ROUGHING LATERAL-1
	2	BBT30 PP CP25 A=75 D IR	FCH0.2 D10 Z4 2.5XD DE 10 REV AD30-203015 10	1	10	32	Top	0,05	0	22	4850	850	20	-27,5	00:00:16	0	ROUGHING LATERAL-2
	3	BBT30 PP CP25 A=75 D IR	FCH0.2 D10 Z4 2.5XD DE 10 REV AD30-203015 10	1	10	32	Top	0	0,1	NA	5730	1030	20	0,1	00:00:28	1	ROUGHING TOP
	4	BBT30 PP ER20 A=60 D IR	FCH0.2 D10 Z4 2.5XD DE 10 REV AD30-203015 10	4	10	32	Top	0	0	22	4000	400	20	-27,3	00:01:04	0	FINISHING LATERAL
	5	BBT30 PR d16 D40 A=3 9 REF	FPA D40 R0.4 Z4 AP8 9 0	2	40	40	Top	0	0	NA	1950	400	20	0	00:00:15	0	FACE MILLING TOP
	6	BBT30 PP ER16 A=63 D IR	FCH0.2 D8 Z4 2.5XD D E8 REV AD25-203015 8	5	8	27	Right	0,05	0,05	1	5800	580	50	12,55	00:00:12	17,5	ROUGHING OBLONG-RIGHT
	7	BBT30 PP ER16 A=63 D IR	FCH0.03 D3 Z3 2XD DE 6 REV-202295 3	10	3	15	Top	0	0	NA	6350	370	20	-5	00:00:25	0	ROUGHING D5 BOX TOP
	8	BBT30 PP ER16 A=70 D IR	B D4.04 5XD 140 DE6 REV MD REF	7	4,04	40	Right	0	0	NA	1500	350	30	-13,5	00:00:33	0	HOLE D4.04 RIGHT
	9	BBT30 PP ER16 A=63 D IR	B D3.2 3XD 140 DE6 REV MD	8	3,2	25	Top	0	0	NA	3500	250	20	-13	00:00:03	-5	PILOT HOLE D3.2 TOP
	10	BBT30 PP ER16 A=63 D IR	B D3.2 7XD 140 D6 REV MD REF	9	3,2	70	Top	0	0	NA	3000	100	30	-30	00:00:22	0	HOLE D3.2 TOP
	11	BBT30 PP ER16 A=63 D IR	M D3.28 CR DE3 NREV MD-321232	11	3,28	35	Top	0	0	NA	1905	150	20	-28	00:00:29	-5	REAMER D3.28 TOP
	12	BBT30 PP ER16 A=63 D IR	FCH0.2 D8 Z4 2.5XD D E8 REV AD25-203015 8	5	8	27	Left	0,05	0,05	1	5800	580	50	12,55	00:00:12	17,5	ROUGHING OBLONG-LEFT
	13	BBT30 PP ER16 A=63 D IR	FCH0.2 D8 Z4 2.5XD D E8 REV AD25-203015 8	5	8	27	Back	0,05	0,05	1	5800	580	50	15,05	00:01:00	25	ROUGHING OBLONG-BACK
	14	BBT30 PP ER16 A=63 D IR	FCH0.2 D8 Z4 2.5XD D E8 REV AD25-203015 8	5	8	27	Front	0,05	0,05	1	5800	580	50	24,05	00:00:08	25	ROUGHING SLOT- FRONT
	15	BBT30 PP ER16 A=70 D IR	FCH0.1 D5 2.5XD DE6 REV AD19-203015 5	12	5	25	Front	0	0	0,7	5500	660	50	16	00:00:20	24,5	ROUGHING FINISHING ACCESS SLOT D3.28- FRONT
	16	BBT30 PP CP16 A=75 D IR	FCH0.2 D8 Z4 2.5XD D E8 REV AD25-203015 8	13	8	27	Front	0	0	NA	5800	1200	50	24	00:00:04	25	FINISHING SLOT- FRONT
	17	BBT30 PP CP16 A=75 D IR	FCH0.2 D8 Z4 2.5XD D E8 REV AD25-203015 8	13	8	27	Back	0	0	NA	5800	1200	50	15	00:00:03	25	FINISHING SLOT- BACK
	18	BBT30 PP CP16 A=75 D IR	FCH0.2 D8 Z4 2.5XD D E8 REV AD25-203015 8	13	8	27	Right	0	0	NA	5800	1200	50	12,5	00:00:01	17,5	FINISHING SLOT- RIGHT
	19	BBT30 PP CP16 A=75 D IR	FCH0.2 D8 Z4 2.5XD D E8 REV AD25-203015 8	13	8	27	Left	0	0	NA	5800	1200	50	12,5	00:00:01	17,5	FINISHING SLOT- LEFT
	20	BBT30 PP ER16 A=63 D IR+EQ16/ER11ML	FC D4 Z4 90 DE4 REV MD	3	4	18	Top	0	0	NA	16000	350	20	-0,7	00:00:02	0	CHAMFER D5
	21	BBT30 PP ER16 A=63 D IR+EQ16/ER11ML	FC D4 Z4 90 DE4 REV MD	3	4	18	Top	0	0	NA	16000	350	20	-0,5	00:00:11	0	CHAMFER TOP EDGES
	22	BBT30 PP ER16 A=63 D IR+EQ16/ER11ML	FC D4 Z4 90 DE4 REV MD	3	4	18	Back	0	0	NA	16000	350	50	24,5	00:00:24	25	CHAMFER BACK EDGES
	23	BBT30 PP ER16 A=63 D IR+EQ16/ER11ML	FC D4 Z4 90 DE4 REV MD	3	4	18	Front	0	0	NA	16000	350	50	24,5	00:00:19	25	CHAMFER FRONT EDGES
	24	BBT30 PP ER16 A=63 D IR+EQ16/ER11ML	FC D4 Z4 90 DE4 REV MD	3	4	18	Right	0	0	NA	16000	350	50	17	00:00:05	17,5	CHAMFER RIGHT EDGES
	25	BBT30 PP ER16 A=63 D IR+EQ16/ER11ML	FC D4 Z4 90 DE4 REV MD	3	4	18	Right	0	0	NA	16000	350	50	11,8	00:00:02	12,5	CHAMFER HOLE- RIGHT
	26	BBT30 PP ER16 A=63 D IR+EQ16/ER11ML	FC D4 Z4 90 DE4 REV MD	3	4	18	Left	0	0	NA	16000	350	50	17	00:00:05	17,5	CHAMFER LEFT EDGES
	27	BBT30 PP ER16 A=63 D IR+EQ16/ER11ML	FC D4 Z4 90 DE4 REV MD	3	4	18	Left	0	0	NA	16000	350	50	11,8	00:00:02	12,5	CHAMFER HOLE- LEFT

Figure 3.20: Setup sheet of AP2.

3.3.2.3 Cutting tools and tool holders used

The final tools were selected using a combination of theoretical knowledge and the company's tool database. This database was also integrated into the CAM software, making it possible to choose among tools already present in the company's inventory. Subsequently, tool paths were created and adjustments were made to optimise machine performance and validate the process through the simulation. This allowed resource optimization and made possible to ensure tool availability would not constrain the experimental tests.

The selected end mills, supplied by Hoffmann (series 203015) are made of micrograin solid carbide and coated with Aluminium Chromium Nitride (AlCrN). Although AlCrN is more common on stainless steels, it has high thermal stability and fracture resistance at high temperatures, making it more than adequate for 42CrMo4 steel. The combination of a small grain size and a PVD coating indicates high wear resistance, hardness and a sharp cutting edge. Additionally, the unequal spacing between the four cutting edges promotes reduced vibrations. It also features a 35º helix angle, which ensures a good combination of cutting forces and stability. The 45º chamfer angle strengthens the cutting edge and eliminates sharp edges. Finally, the negative deviation of the tool, f8, compensates for eccentricities since the real dimensions of the cutter are slightly smaller than the nominal diameter [46]. Figure 3.21 illustrates all the end mills used.



(a) End mill of 10 mm (203015 10).

(b) End mill of 8 mm (203015 8).

(c) End mill of 5 mm (203015 5).

Figure 3.21: End mills used in the machining strategy from Hoffmann.

For chamfering operations, a chamfer mill from Hoffmann (series 208107) was selected. This tool is also made of micrograin solid carbide and features a TiAlN coating, which is typically used for medium-alloyed steels and is applied via PVD, resulting in a combination of high hardness and oxidation resistance. The 90º tip is ideal for creating accurate 45º chamfers that help eliminate sharp edges and allow for a more even distribution of cutting forces. The shank has a tolerance of h6, ensuring a tight fit and high concentricity, which is particularly important for smaller diameter features [46].



Figure 3.22: Chamfer mill used in machining from Hoffmann.

For the pocket feature of 5 mm that requires high stability, a compact three flute end mill from Hoffmann (series 202295) was selected (Figure 3.23). It is manufactured from fine-grain solid carbide and features a TiAlN coating. The 45° helix and 45º chamfer angle promote chip evacuation and reduces cutting forces, which is particularly advantageous in the milling of confined cavities. At last, its negative tolerance of e8 that compensates for eccentricities [46], improving process stability.



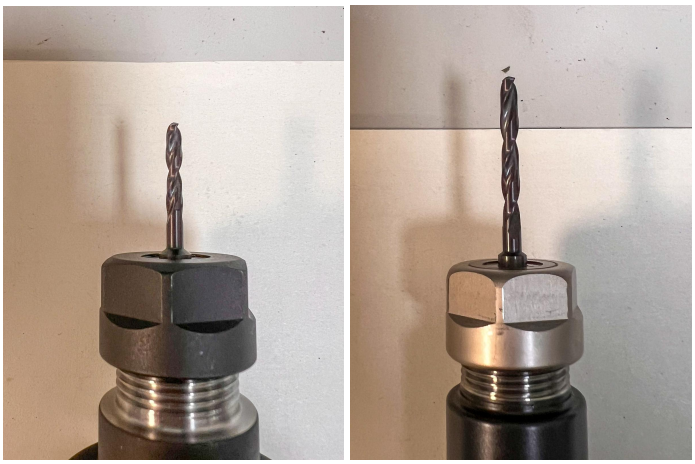
Figure 3.23: Short end mill of 5 mm used in machining from Hoffmann.

Drilling operations were performed using Guhring solid carbide drills from the 5111, 5512 and 5514 series. All the drills from Guhring (5111, 5512, 5514) have similar properties, deferring on the cutting length and internal cooling. The tools have a multilayer coating made from TiN and TiAlN [19], which results in high thermal stability, hardness and wear resistance. These also feature a 140º point angle that reduces axial forces, improves centring and reduces localized wear. Internal cooling is essential for deep drilling with thermal control and without chip clogging. The

pilot drill (5514) does not have internal coolant, as it will drill to a shallow depth. The different drills are represented in Figures 3.24 and 3.25, respectively.



Figure 3.24: Drill of 4.04 mm and 5xD used in the machining of the deep hole from Guhring.



(a) Drill of 3xD. (b) Drill of 7×D.

Figure 3.25: Drills of 3.2 mm used in machining from Guhring.

The face milling cutter, supplied by Walter (F5041.B16.040.704.08) accommodates four indexable inserts (LNMU090404R-L55T WKP35G), as demonstrated in Figure 3.26. The support possesses a robust structure that promotes stability. The inserts combine a negative geometry, suitable for harsh cuts and of high resistance, with a straightening edge that helps distribute the cutting forces. Additionally, it has a multi-layer coating of TiN and TiAlN, that combines high thermal stability and high wear resistance at elevated temperatures [77].



Figure 3.26: Face mill with inserts used in machining from Walter.

The 3.28 mm hole was finished using an uncoated solid carbide reamer from DIXI (321232)- Figure 3.27. It features six irregular cutting edges and through coolant capability, improving chip evacuation. The 0.03 tolerance ensures a tight tolerance with a precise hole diameter. In this application the absence of coating is not critical since dimensional accuracy and chip evacuation have priority over tool life. However, it is necessary to ensure internal cooling and reduce cutting speeds to prevent accelerated wear.



Figure 3.27: Reamer of 3.28 mm used in machining from DIXI.

All tools are listed in the setup sheets (Figures 3.7 and 3.20) in the form of different nomenclatures. Those codes contain the main characteristics of each tool, facilitates communication between the different teams involved in the machining process and improves traceability. An explanation of code elements is provided in Appendix A.

Another important aspect of the machining strategy is the usage of separate tools for roughing and finishing when using the 10 mm and 8 mm end mills, which are the most used and, thus, more prone to wear. This helps reduce wear and preserve edge sharpness for finishing in order to improve surface quality.

The selection of tool holders is also critical to ensure high quality machining. It is essential to achieve the best possible concentricity between the machine and tool axes, as well as to ensure the best clamping possible to prevent positional errors during the process. In addition, tool holders are generally calibrated to avoid the occurrence of vibrations [10].

The spindle taper is one of the most influential components in achieving concentricity [10]. In this case, for the Brother machine, BBT30 tapers are used. These are dual-contact cones, i.e., the flange of the tool holder is in contact with the spindle face in addition to the taper surface. This taper follows the JIS 6339 standard.

Moreover, tool holders are also identified through an internal company nomenclature, typically expressed as BBT30 PP CP25 A=75 DIR. This codes defines the geometry and functional characteristics of the holder and is explained in Appendix A. This type of designation improves traceability and allows for quick identification of the tool holder type used in each operation.

The code CP25 corresponds to the CentrolP series from Fahrion, which is a specific designation of the manufacturer [12]. It refers to the collet pocket geometry and defines which type of collet can be inserted. The CP series is compatible with ER collets, which are according to ISO 15488 standards [11]. For example, a CP25 is designed to accommodate and ER25 collet.

In this context, there are some important aspects that must be considered. For drilling operations, sealed collets are recommended as they force the coolant through the internal channels of the tool, ensuring sufficient pressure, lubrication and chip evacuation. In addition, their tighter tolerances contribute to improved concentricity, which is particularly important in this type of operation.

3.3.2.4 Cutting parameters selection and comparison

To determine the cutting parameters for each tool and operation, the initial step typically involves consulting the suppliers' catalogues. However, the recommended values are often based on ideal machining conditions, such as maximum machine rigidity, perfect clamping and optimal chip evacuation, which do not accurately reflect real conditions. As such, the catalogues serve as guidelines for estimating starting values.

Digital selection tools provided by suppliers, including Hoffmann's *ToolScout*, *Walter GPS* and Guhring cutting data calculator, were consulted. The reamer cutting data from DIXI can be consulted in the catalogue, considering the material group and tool diameter.

It is important to note that the material considered in these interfaces does not have the same properties as the one used in the experimental work. The machine properties are also an approximation of the real conditions. As the suppliers themselves reiterate, these cutting data suggestions are based on tests that do not take into account all real machining conditions and may vary depending on the needs of each operation. So, it is expectable for the values to suffer alterations in the real application.

After gathering the recommended cutting parameters from each supplier, a critical evaluation was carried out during the CAM simulation stage. Instead of applying the suggested values

directly, each operation was individually analysed and the parameters were adapted taking into account the specific machining conditions of the experimental setup.

The tool path and area of contact of the tool with the material have a significant impact on the choice of feed and speed. For instance, if a large amount of the tool diameter (radial engagement) is in contact with the material, lower feed rates should be used to prevent vibrations and maintain stability. Furthermore, operations involving helical interpolation or peck drilling require more conservative values.

The tool holder system and machine interface are also critical. Different stiffnesses impact the dynamic behaviour and require adaptations of feed and speed to avoid chatter and eccentricities. Additionally, the capabilities of the CNC milling machine itself, such as maximum spindle power and torque, produce physical constraints. In particular, torque limitations during heavy passes and power restrictions in high-speed finishing require adjusting feeds accordingly.

A comparison between the recommended and applied values can be observed in Appendix B.

Tables 3.5 and 3.6 highlight the most significant differences. Considering the previously discussed challenges of the drilling operations- tool deflection, eccentricities and chip evacuation- it is better to incorporate a more conservative approach.

Even though Guhring considers the material and tool diameter, there are several other aspects taking into account as optimal that, in reality, are not. So, the suggested values are significantly increased. In this case, the use of long and small diameter tools combined with deep drilling and the need for pilot holes and peck cycles, require a reduction in speeds and feed to ensure a stable cut (Table 3.5).

Table 3.5: Comparison between programmed and catalogue cutting parameters – drilling operations.

			Programmed values				**Catalog**			
Op.	**Tool**	**Tool #**	v_c (m/min)	f_z (mm/tooth)	v_f (mm/min)	n (rpm)	v_c (m/min)	f_z (mm/tooth)	v_f (mm/min)	n (rpm)
8	B D4.04 5×D 140 DE6 REV MD REF	7	44	0.0500	350	3500	120	0.0775	1466	9460
9	B 3.2 3×D 140 DE6 REV MD	8	35	0.0357	250	3500	105	0.1300	1359	10450
10	B 3.2 7×D 140 DE6 REV MD REF	9	30	0.0167	100	3000	120	0.0499	1194	11943
11	M D3.28 CR DE3 NREV MD	11	20	0.0132	150.39	1905	25	0.0149	219	2433

When milling features such as slots or oblongs, the tool often exhibits a large radial engagement with the material or is fully immersed in it (a_e = D), which increases the risk of vibrations and makes the reproduction of the radius harder. In order to improve stability and surface quality, it is necessary to reduce both the speed and feed. Reduced feed per tooth values were also applied to improve chip evacuation, minimise thermal stress and extend tool life.

This effect is even more pronounced when using small-diameter tools, such as the 5 mm end mill applied in Operation 15 (Table 3.6), where the tool's lower stiffness and the high contact area- particularly when interpolating a 3 mm radius- requires a more conservative set of parameters.

Moreover, it is preferable to perform a greater number of passes with reduced parameters, rather than attempting to achieve the full depth or contour in fewer, more aggressive cuts. This

approach distributes the load more evenly, reduces stress and vibrations.

Table 3.6: Comparison between programmed and catalogue cutting parameters – AP2 (Operations 13–20).

Op.	Tool	Tool #	Programmed values				Catalog			
			v_c (m/min)	f_z (mm/tooth)	v_f (mm/min)	n (rpm)	v_c (m/min)	f_z (mm/tooth)	v_f (mm/min)	n (rpm)
12	FCH0.2 D8 Z4 2.5×D DE8 REV AD25	5	146	0.0250	580	5800	180	0.0350	1000	7160
13	FCH0.2 D8 Z4 2.5×D DE8 REV AD25	5	146	0.0250	580	5800	180	0.0350	1000	7160
14	FCH0.2 D8 Z4 2.5×D DE8 REV AD25	5	146	0.0250	580	5800	180	0.0350	1000	7160
15	FCH0.1 D5 Z4 2.5×D DE6 REV AD19	12	86	0.0300	660	5500	180	0.0250	1150	11500
16	FCH0.2 D8 Z4 2.5×D DE8 REV AD25	13	146	0.0517	1200	5800	180	0.0350	1000	7160
17	FCH0.2 D8 Z4 2.5×D DE8 REV AD25	13	146	0.0517	1200	5800	180	0.0350	1000	7160
18	FCH0.2 D8 Z4 2.5×D DE8 REV AD25	13	146	0.0517	1200	5800	180	0.0350	1000	7160
19	FCH0.2 D8 Z4 2.5×D DE8 REV AD25	13	146	0.0517	1200	5800	180	0.0350	1000	7160

Unlike the remaining operations, chamfering is performed with significantly higher cutting speed and spindle speed. Because it is a non-critical finishing operation and small amounts of material are being removed, it is possible to apply more aggressive cutting data without compromising the functional aspects of the part and dimensional accuracy.

There are also differences between roughing and finishing operations, particularly regarding surface quality. In finishing, surface roughness- usually characterized by the arithmetical mean roughness of the profile, R_a- is a critical aspect. To achieve smoother finishes, it is common to reduce cutting parameters, especially the feed per tooth, f_z. The total height of the profile, R_t, is directly influenced by f_z, as it can be observed by Figure 3.28.

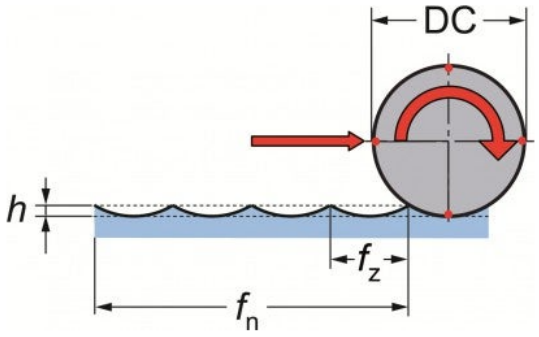


Figure 3.28: Relationship between the height of the profile (R_t) and the feed per tooth (f_z) [63].

This relationship is expressed by Equation 3.1, showing that increasing f_z leads to a higher profile height and, as a consequence, rougher surface finishes. Overall, lower f_z improves surface quality.

$$R_t = \frac{f_z^2}{4 \cdot D} \tag{3.1}$$

In contrast, roughing operations are typically performed with higher values of feed and depth of cut to maximise material removal rate (MRR) and improve overall productivity.

To sum up, the supplier recommendations were used as a starting point and the cutting parameters were adapted to suit the real machining conditions. This way, the applied data reflects the consideration of key aspects such as tool engagement, tool-holders stiffness and machining strategies to ensure part quality and tool preservation under real industrial conditions.

3.4 Workpiece Production

For this project and in order to validate, monitor and optimise the process, eight workpieces were produced as illustrated by Figure 3.29. Part number 0 validated the strategy and parts 1 to 7 were used for testing parameter variations and sensor-based monitoring.



Figure 3.29: Total produced workpieces.

Before machining, all cutting tools were measured using a Zoller smartCheck system, which provides high-precision dimensional data (e.g., overall length, cutting diameter, edge geometry and eccentricities). The tool offsets were then introduced in the CNC controller to avoid positioning errors or collisions. The workpiece zero was defined using a probe, ensuring correct alignment of the programmed tool paths.

The clamping strategy is illustrated in Figure 3.30, which shows the sequential positioning of the workpiece throughout the machining process. In the initial phase (AP1), the cylindrical stock was clamped using a mechanical stop (Figure 3.31) to prevent any potential displacement of the workpiece under cutting forces and ensure repeatability. After machining the first features, the part was re-clamped (AP2) by the lateral recess, using a vice with serrated jaws. These teeth provide additional grip and prevent slippage during machining. After all these steps, the production of the workpiece is completed.

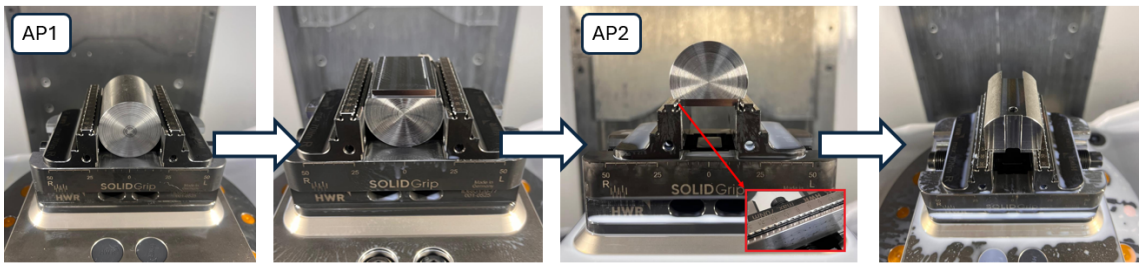


Figure 3.30: Machining steps.

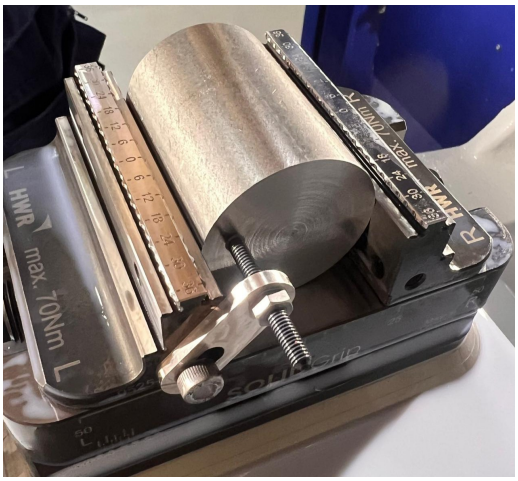


Figure 3.31: Mechanical stop used for AP1.

3.4.1 Process monitoring

Due to the large number of operations in this part (over 30), three milling operations were selected for monitoring to facilitate data acquisition and analysis. Although drilling is critical, the milling operations are more relevant to the study objectives. In particular, roughing operations were selected as they are usually more demanding and prone to vibration.

To assess tools with different diameters and lengths, three end mills were selected: diameter of 10.8 and 5 mm. These tools are the most used during the production and are expected to suffer more wear in shorter time, making them interesting choices for monitoring. The selected operations, all from AP2, are listed in Table 3.7.

Table 3.7: Selected operations for monitoring.

Operation	**Tool**	**Tool Number**	**Time**
OP1- Roughing Lateral-1	FCH0.2 D10 Z4 2.5XD DE10 REV AD30	1	00:00:32
OP13- Roughing Oblong Back	FCH0.2 D8 Z4 2.5XD DE8 REV AD25	5	00:01:00
OP15- Rough. Finish. Access Slot for Hole D3.28	FCH0.1 D5 2.5XD DE6 REV AD19	12	00:00:20

The chosen operations reflect different cutting strategies and geometric features. OP1 involves peripheral roughing and is one of the longest operations. OP13 corresponds to the roughing of an

oblong geometry, including machining of curved surfaces. At last, OP15 combines roughing and finishing stages allowing to obtain data from both regimes. This diversity in tool paths, engagement conditions and tool sizes provides a representative dataset for analysing vibration, load and current signals under different machining conditions.

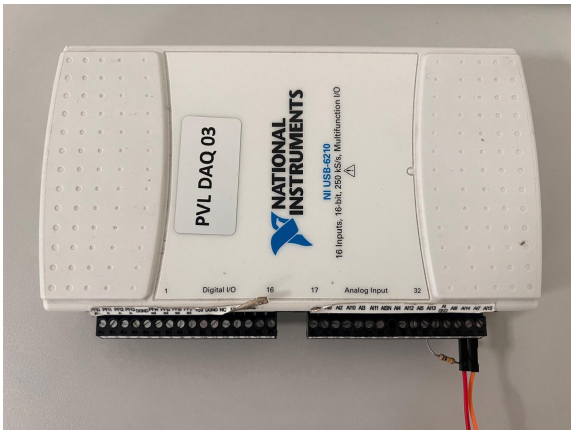
The acquisition of data involved two types of sensors: a MEMS accelerometer and a current clamp, both provided by FEUP/INEGI.

Current monitoring was performed at the spindle drive level, using an E27 AC/DC electric current clamp connected directly to the spindle cable, as seen in Figure 3.32a. In the Figure, it is possible to observe 3 cables (u,v and w) that correspond to the three phases of the spindle. The clamp was connected to one of them.

This sensor has a measuring range of 100 mA to 100 A and a bandwidth of 100 kHz. Further technical details can be consulted in Appendix C. The clamps were also connected to an NI USB-6210 data acquisition system (DAQ)- Figure 3.32b. A Python script was used to perform data collection and store it in a .CSV file. It is important to note that, since the clamp's bandwidth is significantly higher than the DAQ's, the sampling rate of this setup is limited by the acquisition system.



(a) Current clamps connected to the spindle drive cable.



(b) NI USB-6210 Data Acquisition System.

Figure 3.32: Monitoring setup for current signals.

To monitor vibrations, a wireless accelerometer, represented in Figure 3.33, was used. This device is still in the experimental phase and communicates with a web platform developed by Palbit, allowing real time visualization of acceleration data. Its implementation is easy, requiring no

wiring and using magnets for fixation. The 3-axis accelerometer, based on the MP4-6886 Motion-Tracking device from IvenSense, features configurable ranges up to ±16g and 16-bit resolution.

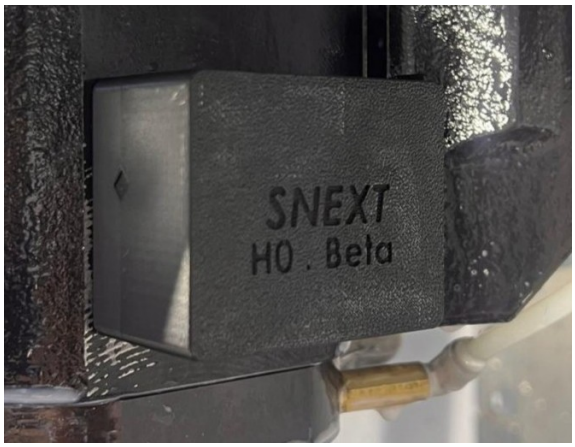


Figure 3.33: Accelerometer used for vibration monitoring.

This sensor was placed directly at the spindle, as demonstrated in Figure 3.34, because it is the most stable body and is the closest to the cutting zone, as discussed in Chapter 2.3.1.2.

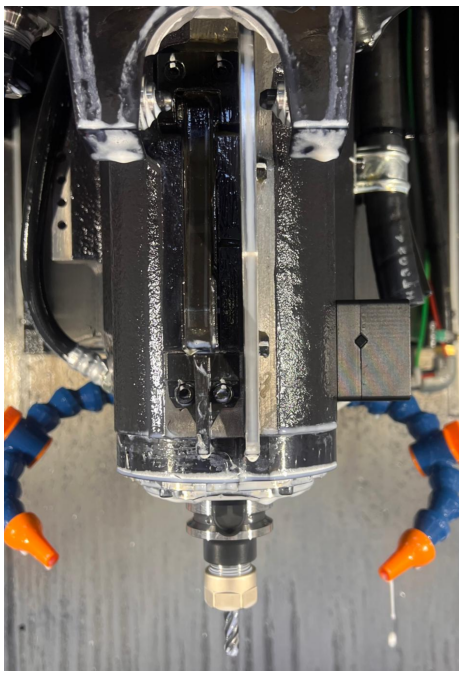


Figure 3.34: Placement of the accelerometer at the spindle.

Because of automatic tool changes, it was necessary to modify the G-code to add mandatory stops before and after the monitored operations. The code was adapted by inserting the M1 command at the start and end of each operation. Moreover, intermediate tool retractions movements were added to avoid collisions and position the sensor. This adaptation of the code can be observed in Figure 3.35.

```
G0 G43 H1 Z100. M8 M494

M0

(POSITION SENSOR)

G0 G43 H1 Z20. M8 M494
M280
M341 E1 (ACTIVATE LOAD READING)
Z2.
```

(a) Activation of function.

```
M289
M340 (DEACTIVATE LOAD READING)

M0
(REMOVE SENSOR)


( ROUGHING LATERAL-2 )
M280
```

(b) Deactivation of function.

Figure 3.35: NC code that allows sensor positioning and activation of the *Load Monitoring* function.

In parallel, the spindle torque was also registered using the *Machining Load Monitoring* function of the machine. It estimates the spindle torque based on internal servo signals and displays the relative load in Newton-metres (Nm).

This function is activated in the G-code using the command M341, where the maximum and average value of the spindle torque is displayed on the user interface, as it can be observed by Figure 3.36. Overall, while these values do not represent an absolute measurements, it offers a consistent indication for tool monitoring.

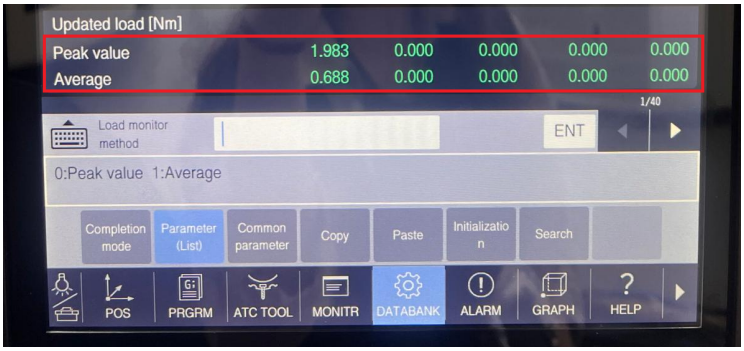


Figure 3.36: Load Monitoring Function of the Brother U500Xd2 5AX CNC machine.

Two monitoring modes are available. The peak mode uses a moving average over a defined time constant (100 ms in this case), ignoring acceleration and deceleration phases. On the other hand, the average mode computes the mean load including all phases. The time constant acts as a window that helps smooth fluctuations in the signal. Figure 3.37 illustrates both modes, highlighting how signal interpretation changes with each method.

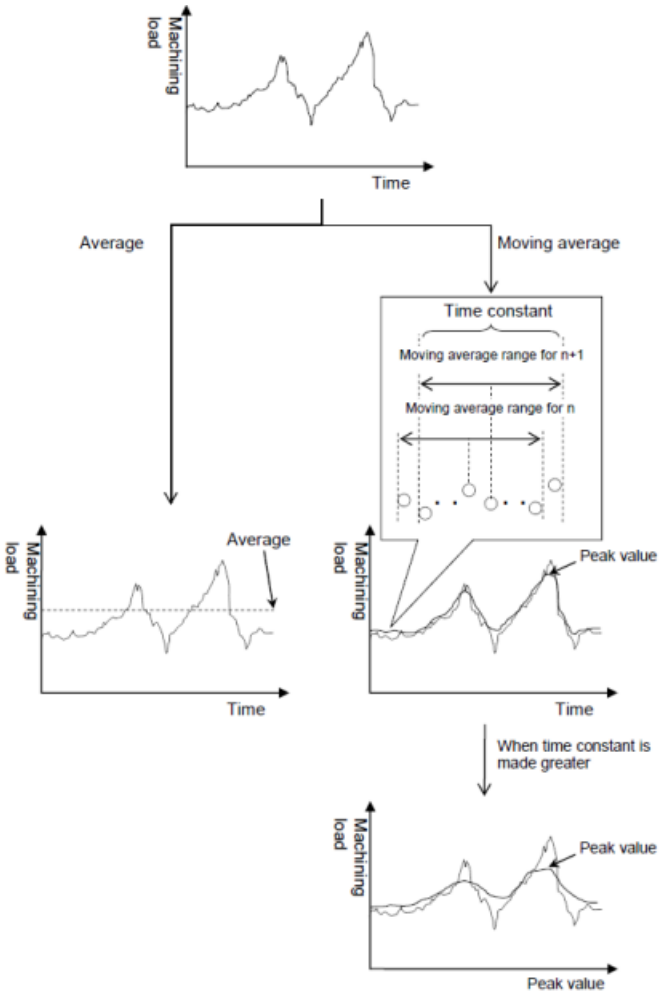


Figure 3.37: Comparison between Average and Peak Monitoring Methods of the *Machining Load Monitoring* function of the CNC machine.

In summary, three milling operations were monitored using current clamps, an accelerometer and the machine's integrated load monitoring function. This combination provides insight into energy consumption, vibratory behaviour, and mechanical load under different cutting conditions. The goal is to relate these signals with the cutting parameters variation and understand the viability of this type of hardware and signals for process monitoring and optimization.

3.4.2 Quality control

After machining, the quality control of the parts was performed to verify dimensional and geometric tolerances, as well as surface finish. This analysis is crucial to ensure part conformity with requirements and support process optimisation. All inspection procedures were systematically repeated for each machined part, ensuring dimensional consistency, process stability and full traceability. The corresponding inspection controls are going to be discussed in Chapter 4.

Based on the 3D model, a detailed inspection was carried out using a Hexagon Coordinate Measuring Machine (CMM)- Figure 3.38. The workpiece was clamped on the table and scanned

by a probe, generating a personalised inspection program and a complete report of all measured dimensions and geometric tolerances.



Figure 3.38: Quality control of the workpiece using a CMM Hexagon machine.

To complement the analysis, a Garant MM1200 optical projector. Figure 3.39a, was used. This equipment is particularly useful to analyse contours, radius and angular features that are difficult to measure with conventional contact instruments. The workpiece is displayed through optical magnification, as demonstrated by Figure 3.39b.



(a) Profile projector from Garant.

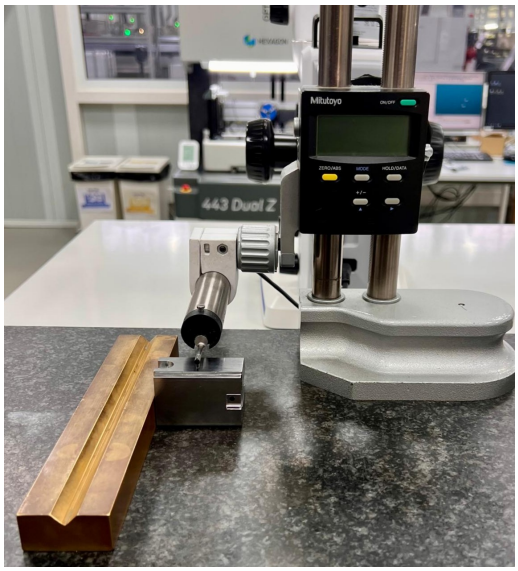


(b) Screen display of the projector.

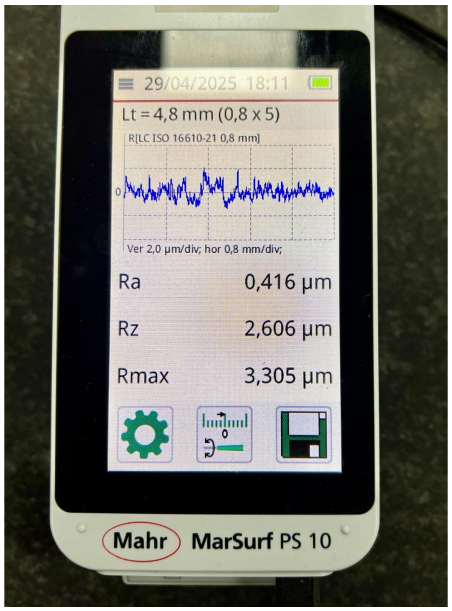
Figure 3.39: Dimensional inspection using the Garant MM1200 profile projector.

The most common method to evaluate surface roughness is using a surface profilometer [46].

The equipment used, represented in Figure 3.40a, is a surface roughness tester from Mitutoyo, equipped with a display from Mahr that shows the surface profile and values of Ra, Rz and $R_{(}max)$ as demonstrated by Figure 3.40b.



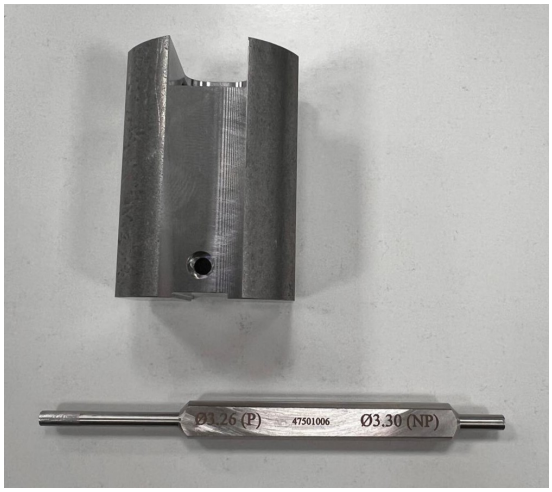
(a) Surface profilometer equipment.



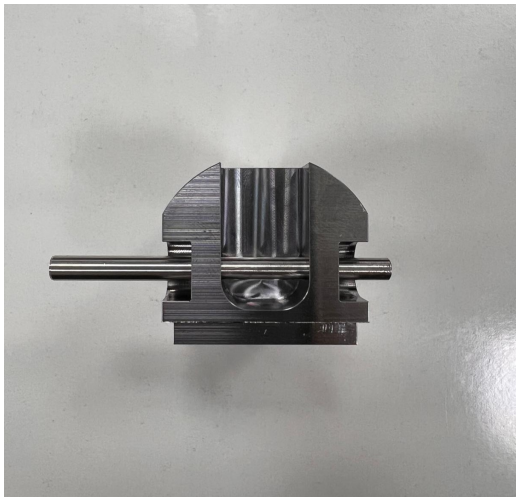
(b) Display of the profilometer.

Figure 3.40: Surface roughness assessment using a Mitutoyo surface roughness tester.

To quickly verify the dimensional tolerances of the drilled holes, a Go/No-Go gauge was used. It consists of two ends: one that must fit into the hole (Go side) and another that must not (No-Go side), allowing a fast pass/fail assessment of the specified tolerance limits [46], as shown in Figure 3.41



(a) Go/No-Go gauge used to verify the tolerance of the holes.



(b) Example of the gauge fitting into the hole during inspection.

Figure 3.41: Dimensional inspection of the holes using a Go/No-Go gauge.

Chapter 4

Results and Discussion

This chapter presents the experimental results obtained throughout the machining trials. A total of eight parts were manufactured, with monitoring conducted on seven of them. The analysis is structured into three main sections: electrical current signals acquired from current clamps, vibration data recorded using an accelerometer and quality control reports. For current and acceleration signals, the analysis is further divided by machining operation- OP1, OP13 and OP15.

Each section presents the collected data, the methods of analysis applied and discussion of the results with focus on identifying trends, find indicators of process instability and understand the impact of process parameters. Ultimately, this evaluation aims to determine whether this monitoring approach can reliably extract process information and be applied to other machining contexts.

The raw data from the current and vibration signals is processed using the Root Mean Squared (RMS) method. RMS is a statistical technique used to quantify the average magnitude of a signal. This method calculates the square root of the mean of the sum of squares of the signal, as expressed by Equation 4.1, in order to assess the signal amplitude and energy in the time domain [51]. RMS is commonly used in current and voltage calculations, as well as vibration data since it is more simple and direct to compute compared to other techniques.

$$RMS = \sqrt{\frac{1}{N}\sum_{t=1}^{N}(x(t))^2} \tag{4.1}$$

Since RMS calculates a global average value, that does not show local variations, it is common to divide the signal into smaller segments- windows- and calculate the RMS of each. This approach allows the identification of general trends while reducing noise.

To evaluate the influence of cutting parameters on process behaviour, the cutting speed, v_c, and feed per tooth, f_z, varied around the reference condition (test 1). From trials 2 to 5, v_c was increased or decreased around 30%, while f_z was kept constant and vice-versa. The final two trials involved simultaneous variation of both parameters. It is important to note that, in some cases, the adjustment percentage was limited to avoid exceeding the recommended values by the tool manufacturer. Tables 4.1, 4.2 and 4.3 summarizes the cutting conditions applied in each test of OP1, OP13 and OP15, respectively.

Table 4.1: Cutting conditions used in each test of OP1.

Test	v_c **(m/min)**	f_z **(mm/tooth)**	**Spindle speed, S (rpm)**	**Feed rate, F (mm/min)**	**Variation**
1	152	0.0438	4850	850	Reference
2	106.4	0.0438	3386.8	593.4	$\downarrow v_c$, f_z constant
3	152	0.031	4850	600	$\downarrow f_z$, v_c constant
4	180	0.0438	5729.6	1003.6	$\uparrow v_c$, f_z constant
5	152	0.057	4850	1103.1	$\uparrow f_z$, v_c constant
6	180	0.057	5729.6	1306.3	$\uparrow$ both v_c and f_z
7	106.4	0.031	3386.8	420	$\downarrow$ both v_c and f_z

Table 4.2: Cutting conditions used in each test of OP13.

Test	v_c **(m/min)**	f_z **(mm/tooth)**	**Spindle speed,** S **(rpm)**	**Feed rate,** F **(mm/min)**	**Variation**
1	146.0	0.0250	5800.0	580.0	Reference
2	96.2	0.0250	3827.7	382.8	$\downarrow v_c$, f_z constant
3	146.0	0.0175	5800.0	406.6	$\downarrow f_z$, v_c constant
4	180.0	0.0250	7161.0	716.0	$\uparrow v_c$, f_z constant
5	146.0	0.0330	5800.0	766.8	$\uparrow f_z$, v_c constant
6	180.0	0.0330	7162.0	945.4	$\uparrow$ both v_c and f_z
7	96.2	0.0175	3827.7	267.9	$\downarrow$ both v_c and f_z

Table 4.3: Cutting conditions used in each test of OP15.

Test	v_c **(m/min)**	f_z **(mm/tooth)**	**Spindle speed, S (rpm)**	**Feed rate, F (mm/min)**	**Variation**
1	86	0.030	5500	660.0	Reference
2	60.2	0.030	3832.5	383.3	$\downarrow v_c$, f_z constant
3	86	0.021	5500	459.9	$\downarrow f_z$, v_c constant
4	112	0.030	7130	855.6	$\uparrow v_c$, f_z constant
5	86	0.040	5500	876.0	$\uparrow f_z$, v_c constant
6	112	0.040	7130.1	1140.8	$\uparrow$ both v_c and f_z
7	60.2	0.021	3832.5	321.9	$\downarrow$ both v_c and f_z

It is also important to highlight that this study was conducted without repetition of tests, not guaranteeing statistical repeatability. This limitation makes the identification of outliers more challenging and restricts the robustness of statistical significance.

4.1 Electrical Current Monitoring

Electrical current signals were acquired from the main drive circuit of the spindle using clamp meters, as described in Section 3.4.1. The data was acquired at 1000 Hz and the raw data was

stored in a .csv format, with time stamped current values recorded for each monitored axis, as observed in Figure 4.1. The time column in the files does not reflect the real process time, however each recorded sample corresponds to a fixed increment of 1 ms, allowing relative time analysis.

Time	Batch_id	Cu*	Cu*_rms
1748959762	1,74896E+18	-3,828092771	0,775825499
1748959762	1,74896E+18	-2,972788174	0,907003077
1748959762	1,74896E+18	0,185259606	0,906092071
1748959762	1,74896E+18	3,441996443	1,05559363
1748959762	1,74896E+18	4,001234088	1,230176803

Figure 4.1: Raw data from the .csv file of the current.

Different RMS windows were explored to assess which segment best traduced the evolution of current. Additionally, the effect of applying different windows in the final RMS values was analysed and it was possible to conclude that there are no significant variations of results (maximum around 0.01 A). As such, the raw data was processed using the root mean square (RMS) method, applied over fixed time windows of 100 ms (i.e., 100 samples). The evaluation is structured by machining operation and for each, current profiles are elaborated.

4.1.1 Operation 1

Operation number one corresponds to the three lateral passes in each side of the part (right and left planes) performed with a 10 mm diameter end mill. In total, the tool performs six passes, as it is possible to see by its path represented in Figure 4.2.

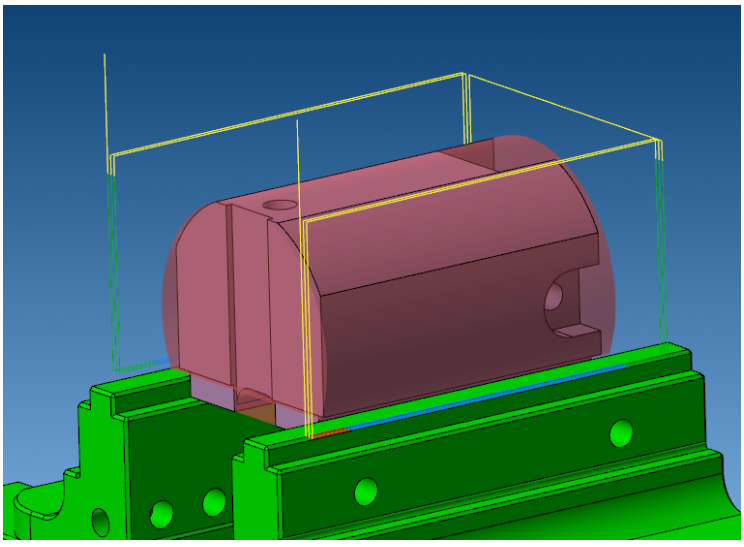
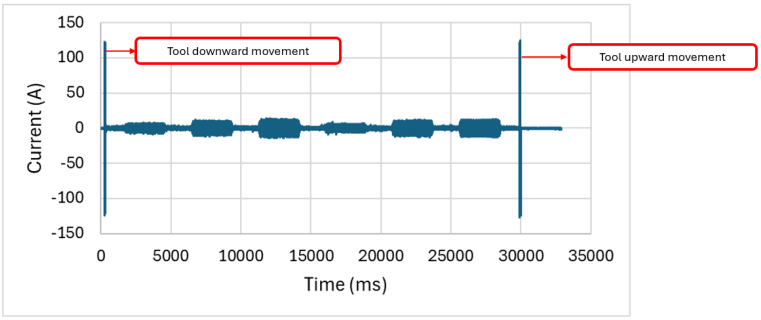


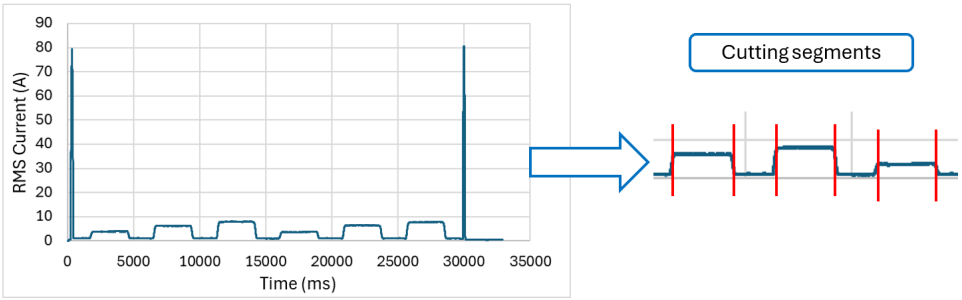
Figure 4.2: Tool path of Operation 1.

For each test, the current over time was plotted. The result is shown in Figure 4.3a, which corresponds to Test 5, but in general all the curves show similar behaviour. The RMS values were also plotted. Test 5 results are represented in Figure 4.3b. Similar to the first plot, it is

possible to observe the initial descent of the tool and the last ascent of the tool. Additionally, it is also possible to see that, for each side, the current increases in each pass. To estimate the energy demand during cutting, each current signal was segmented to isolate the effective cutting moments of the operation, as illustrated by Figure 4.3b. All the RMS current plots of all tests of OP1 can be seen in Appendix D.



(a) Current signal over time.



(b) RMS current profile and cutting segment identification.

Figure 4.3: Current signal and corresponding RMS segmentation of Test 5 of OP1.

The mean value was calculated over each segment and a global RMS value representative of the test was obtained by calculating the average of the six mean values. This approach enables both local estimation of energy consumption during each individual pass and a consistent comparison across different trials. Additionally, the impact of idle time is minimised.

To further investigate the impact of cutting parameters, the percentage variation of the current was calculated. Equation 4.2 was used, allowing for a quantification of the impact of each parameter adjustment. Each test is compared to the the test of reference, which corresponds to test 1.

$$\%Variation = \frac{I_i - I_{reference}}{I_{reference}} \cdot 100 \tag{4.2}$$

Table 4.4 presents the global average value of each test, along with the percentage of variation.

Table 4.4: Mean RMS current value and percentage variation of each test during OP1.

Test	Mean RMS current (A)	% Variation
1	5.055	0.00%
2	5.186	+2.59%
3	4.515	-10.68%
4	5.213	+3.12%
5	5.995	+18.58%
6	5.880	+16.30%
7	4.678	-7.47%

Figure 4.4 presents the effective current values obtained for each test, where it is noticeable the impact of cutting parameters. Test 5, which corresponds to an increase of f_z with v_c constant, showed the highest value of current. On the other hand, a decrease of only f_z (Test 3) resulted in the lowest value of the current.

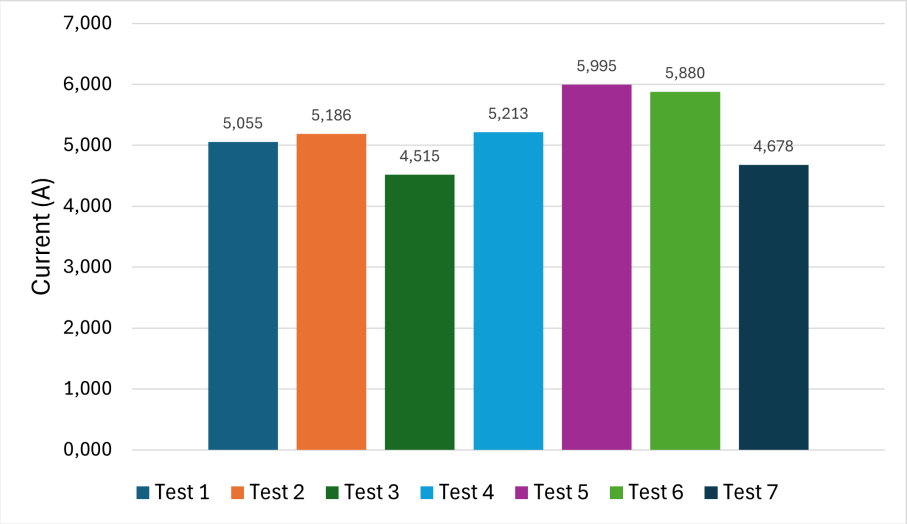


Figure 4.4: Effective current value of each test of OP1.

This graph, along with the percentage variation, indicate that the feed per tooth, f_z, has a more significant impact on the current than cutting speed, v_c. Tests where f_z changed led to larger variations in RMS current (-10.68% and 18.58%) suggesting a stronger correlation between feed and energy. In contrast, isolated variations in v_c produced smoother differences and similar results of current.

This influence is in accordance to theory, since the cutting power, P_c, is calculated using the feed rate, v_f, as expressed in Equation 4.3. In turn, the feed rate is influenced by the feed per tooth. As such, it is expected for the power to increase with the increase of f_z.

$$P_c = \frac{a_p \cdot a_e \cdot v_f \cdot K_c}{60 \cdot 10^6} [\text{kW}] \tag{4.3}$$

Furthermore, f_z also influences chip thickness, that varies during cutting. In milling, it is more common to consider the average chip thickness, h_m, describing the relationship between radial depth of cut, a_e, and tool diameter, D [2]. For simpler operations, this dimension is calculated through the feed per tooth, depth of cut, diameter and entering angle, as illustrated by Figure 4.5.

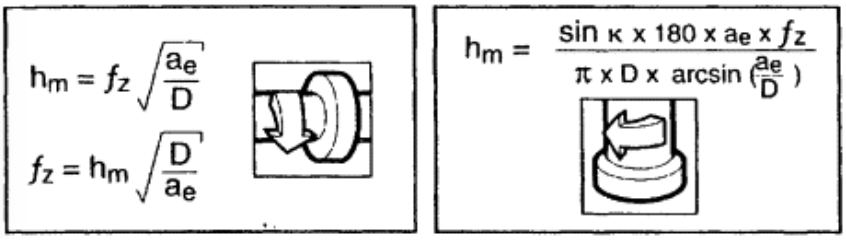


Figure 4.5: Average chip thickness, h_m, calculation in peripheral milling (left side) and face milling (right side) [2].

When f_z becomes smaller than the minimum chip thickness, h_{min}, the material does not form chips [49]. Instead of cutting material, ploughing occurs and the cut enters a friction dominated regime. So, even if f_Z is null, the cutting pressure is never equal to 0, as friction is present. This phenomenon is known as the size effect in machining, where the specific cutting pressure, K_c, experiences a non-linear increase with the decrease of the undeformed chip thickness, h_0 [2], [44], [76]. This means that part of the consumed energy is not associated to cut but to friction.

Regarding the cutting speed effect on the current, it would be expected that increasing speed would result in higher energy. However, this relationship is not necessarily linear. The cutting power also depends on the cutting force, which can decrease with the raise of v_c.

This can be explained by the material's yield strength, described by the Johnson-Cook constitutive model. This model captures the combined effects of strain hardening, strain rate and temperature, as expressed by Equation 4.4 [25], [65]:

$$\sigma = \left[A + B \cdot \varepsilon_p^n\right] \cdot \left[1 + C \cdot \ln\left(\frac{\dot{\varepsilon}}{\dot{\varepsilon}_0}\right)\right] \cdot \left[1 - \left(\frac{T - T_0}{T_m - T_0}\right)^m\right] \tag{4.4}$$

In this formula, ε_p is the plastic strain, $\dot{\varepsilon}$ is the effective strain rate and $\dot{\varepsilon}_0$ is the reference strain rate. T_m and T_0 are the melting and room temperature, respectively. The coefficients A, B and C are the yield stress at T_0, hardening modulus and strain rate hardening, respectively. Finally, n and m are the work-hardening and thermal softening coefficients [25]. This model enables the study of the impact of different factors on the material's deformation.

Cutting speed has an impact on the strain rate of the material, where higher values lead to higher strain rates. This increase of $\dot{\varepsilon}$ leads to hardening of the material and, thus, increase of the required load to remove material. On the other hand, higher v_c also result in more generated heat in the cutting zone, which leads to a reduction of the third term of the constitutive model. This phenomenon is called thermal softening, that lowers the cutting force required for cutting.

Therefore, an increase of v_c can result in two different material responses: strain hardening, by the increase of the strain rate, and thermal softening, due to temperature increase. Overall,

the relationship between cutting speed and current consumption is non-linear, since the material's response depends on the interaction between thermal and strain hardening effects.

In this operation, a_p increases in each tool pass, as illustrated by Figure 4.6. This is translated in the increase of current consumption with each tool engagement, as observed before.

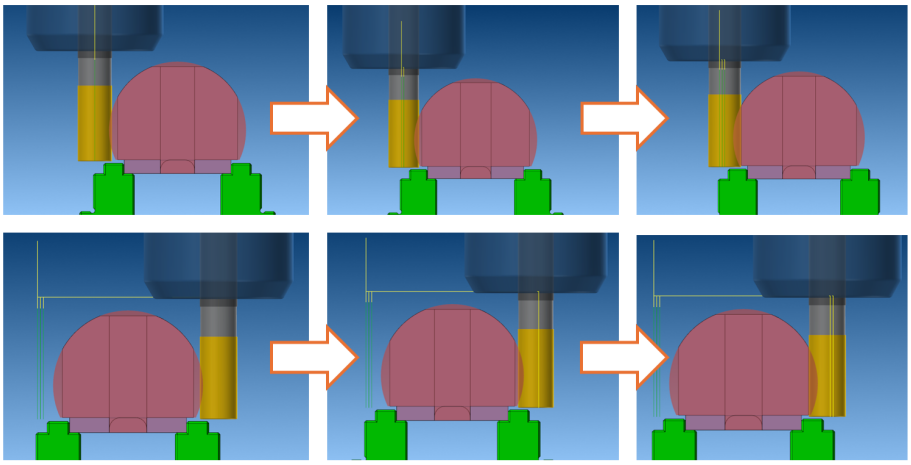


Figure 4.6: Progressive engagement of the tool with the workpiece during OP1.

The plot represented in Figure 4.7 corresponds to the evolution of the current with each tool pass during each test and helps reinforce this conclusion. The results are also listed in Table 4.5. In each pass, the axial depth of cut, a_p, increases leading to higher cutting forces with each pass translating into higher measured current. In addition, higher a_p means higher contact of the tool with the workpiece, i.e., larger amounts of material being removed.

Table 4.5: Mean RMS current values (A) for each cutting pass in OP1.

Test \ **Tool Pass**	1	2	3	4	5	6
1	3.340	5.322	6.730	3.171	5.150	6.619
2	3.154	5.350	6.760	3.465	5.591	6.797
3	3.043	4.773	5.793	3.033	4.785	5.665
4	3.559	5.433	6.819	3.334	5.426	6.706
5	3.900	6.223	7.946	3.665	6.457	7.776
6	3.832	6.109	7.714	3.861	6.161	7.600
7	3.132	4.969	5.831	3.163	5.013	5.959

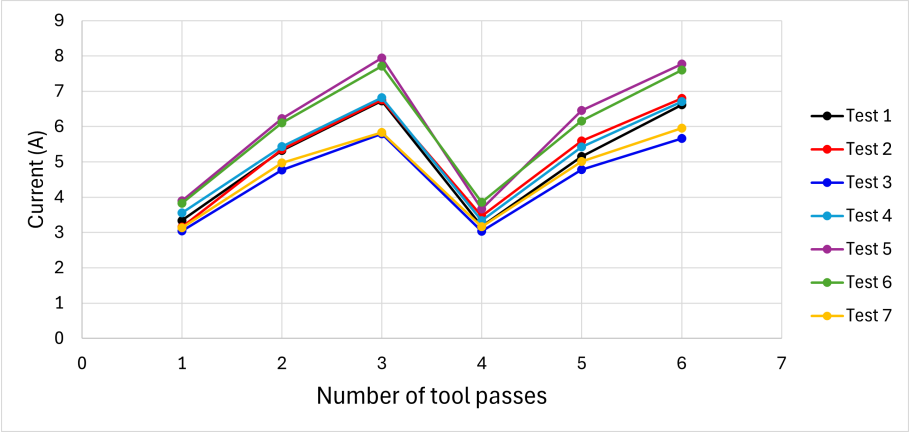


Figure 4.7: Variation of the current with each tool pass- OP1.

To further compute the relationship between depth of cut, a_p, and current, I, the values of a_p for each engagement were determined (Table 4.6) and the corresponding plot is represented in Figure 4.8, where it becomes clear that there is a linear response of the current with the increase of a_p. This indicates that the current is capable of detecting the response of energy consumption to different amounts of removed material.

Table 4.6: RMS current and axial depth of cut (a_p) for each cutting pass of test 1- OP1.

Pass	1	2	3	4	5	6
RMS (A)	3.340	5.322	6.730	3.171	5.150	6.619
a_p (mm)	11.20	15.68	18.21	11.20	15.68	18.21

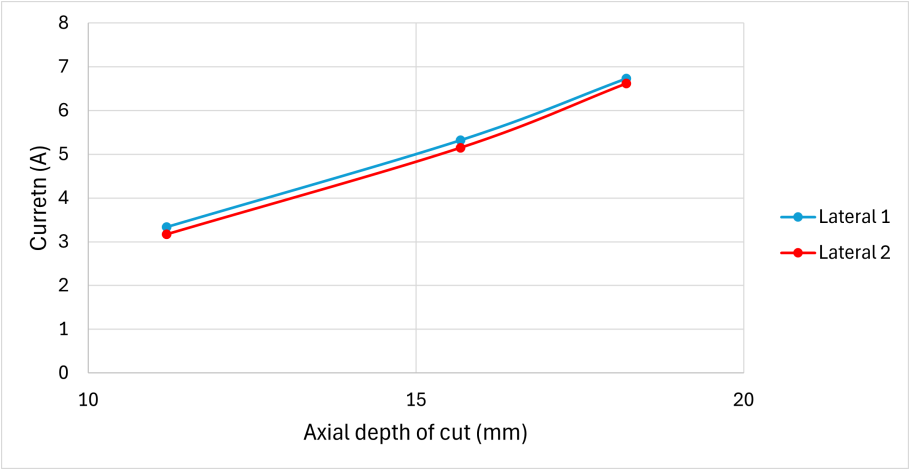


Figure 4.8: Current vs Axial depth of cut - Test 1 (OP1).

It is also possible to associate the current with the quantity of removed material (MRR). This variable is calculated by Equation 4.5, where it depends on the radial and axial depths of cut and the feed rate.

$$MRR = \frac{a_p \cdot a_e \cdot v_f}{1000} [cm^3/\text{min}] \tag{4.5}$$

For each test, the MRR was determined and is listed in Table 4.7. Test number 6, that corresponds to the increase of both f_z and v_c, has the highest MRR value, while test 7 has the lowest. This is expectable since this rate estimates the material removed along the time, so if the tool moves at lower pace and cuts less material per tooth, the MRR result will be lower.

Table 4.7: Material removal rate (MRR) for each test in OP1.

Test	MRR (cm^3/min)
1	10.220
2	7.135
3	7.214
4	12.070
5	13.264
6	15.707
7	5.050

The relationship of this rate with the current is plotted in Figure 4.9. The linear regression line describes the relationship between the two variables. R^2 measures the adjustment of the regression line to the experimental data, which means that it indicates the variability of the data that is explained by the model. The perfect determination coefficient of the linear regression is represented by 1.

In this case, the value of R^2 indicates that 74% of the current variation can be attributed to the variation of MRR. This is a strong value, however it suggests that the current does not have a perfect linear variability with the removal rate. MRR is a volumetric metric that does not consider mechanical, thermal and material behaviour interactions, while the current is more related with the load, which can cause deviation between both variables.

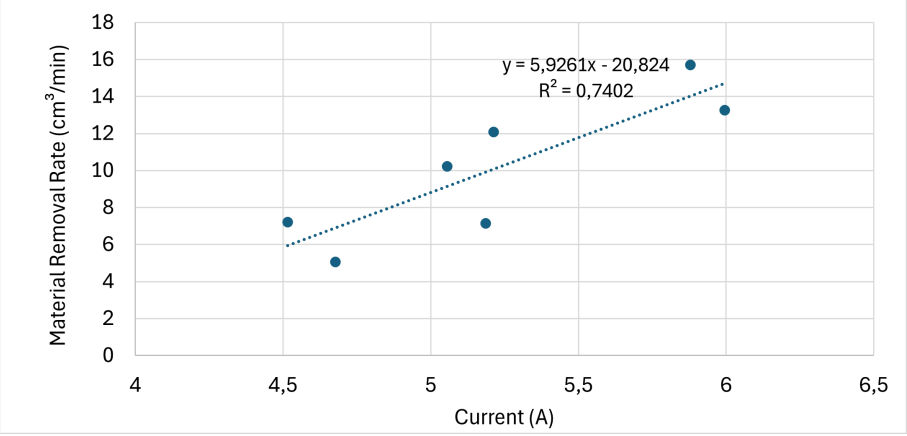


Figure 4.9: Current vs Material Removal Rate (MRR)- OP1.

Another important aspect is the impact of f_z in the MRR results, which is more significant compared to v_c. This is because the feed per tooth has a direct influence in the feed rate, v_f, and chip thickness, h_m. Higher f_z result in higher average chip thickness and, as consequence, the amount of material being removed per tooth also increases.

4.1.1.1 Current and Cutting Power

Cutting power reflects the mechanical load required to remove material. The motor current is also expected to reflect this load. Thus, it is important to evaluate if current measurements can represent the energy consumption under different machining conditions.

The spindle motor is a three-phase AC motor. As such, the electrical power can be estimated using Equation 4.6, where V_p is the voltage between phases, I_L is the current in one line and PF is the power factor [58].

$$P = \sqrt{3} \cdot V_p \cdot I_L \cdot PF \tag{4.6}$$

The power factor is a measure of how efficiently electrical energy is being converted into useful work in an AC circuit. It depends on the impedance angle of the circuit, θ, that represents the difference of phase between the voltage, V, and current, I [58]. The expression that translates this variable is Equation 4.7.

$$PF = cos(\theta) \tag{4.7}$$

The power factor varies with the motor load and this variable is not provided in the machine's manual. As consequence, without knowing the power factor, the line current and voltage are not sufficient to calculate an accurate value of the electrical power.

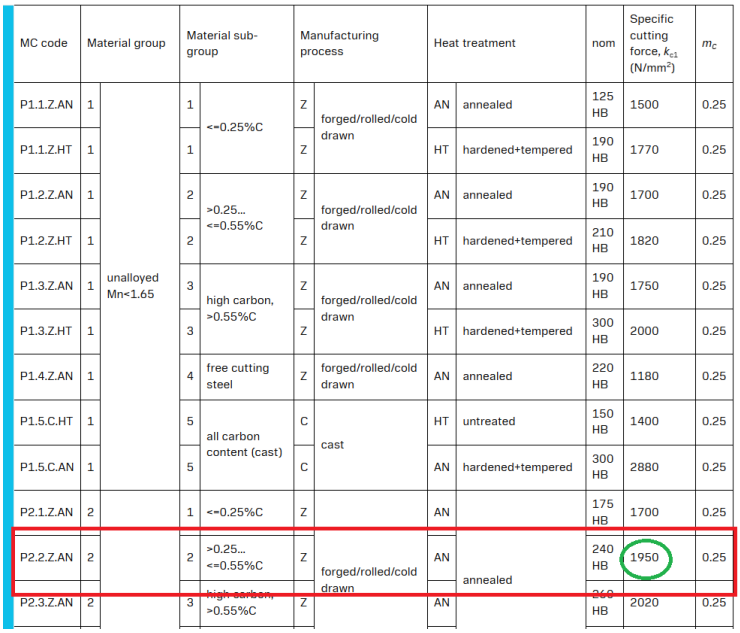
As an alternative, the cutting power, that depends on a_p, a_e, feed rate, v_f, and specific cutting pressure, K_c, was used to evaluate the relationship with the measured current. Its expression is represented in Equation 4.3. To determine the cutting power, P_c, of each trial it is necessary to find the value of K_c of the workpiece material- 42CrMo4 steel.

The specific cutting pressure is equivalent to the force in the cutting direction, required to remove a chip. Typically, the value provided by tool catalogues is K_{c1}, which corresponds to the force necessary to remove a chip with a thickness of 1 mm [62]. To estimate K_c, the value of chip thickness exponent, m_C, average chip thickness, h_m, and rake angle γ_o need to be determined [64]. This expression is represented in Equation 4.8.

$$K_c = k_{c1} \cdot h_m^{-m_c} \cdot \left(1 - \frac{\gamma_o}{100}\right) \tag{4.8}$$

The most similar material of the group P was found in the Sandvik catalogs (Figure 4.10) and the corresponding K_{c1}- 1950 N/mm^2- was used for the calculations of P_c. The value of m_c is also provided by the supplier- 0,25. It is important to remember this is an estimation of K_c and the

material of group P, although similar, has variations of hardness and thermal treatment compared to the 42CrMo4 steel.



MC code	Material group		Material sub-group		Manufacturing process		Heat treatment		nom	Specific cutting force, k_{c1} (N/mm²)	m_c
P1.1.Z.AN	1	unalloyed Mn<1.65	1	<=0.25%C	Z	forged/rolled/cold drawn	AN	annealed	125 HB	1500	0.25
P1.1.Z.HT	1		1		Z		HT	hardened+tempered	190 HB	1770	0.25
P1.2.Z.AN	1		2	>0.25... <=0.55%C	Z	forged/rolled/cold drawn	AN	annealed	190 HB	1700	0.25
P1.2.Z.HT	1		2		Z		HT	hardened+tempered	210 HB	1820	0.25
P1.3.Z.AN	1		3	high carbon, >0.55%C	Z	forged/rolled/cold drawn	AN	annealed	190 HB	1750	0.25
P1.3.Z.HT	1		3		Z		HT	hardened+tempered	300 HB	2000	0.25
P1.4.Z.AN	1		4	free cutting steel	Z	forged/rolled/cold drawn	AN	annealed	220 HB	1180	0.25
P1.5.C.HT	1		5	all carbon content (cast)	C	cast	HT	untreated	150 HB	1400	0.25
P1.5.C.AN	1		5		C		AN	hardened+tempered	300 HB	2880	0.25
P2.1.Z.AN	2		1	<=0.25%C	Z		AN		175 HB	1700	0.25
P2.2.Z.AN	2		2	>0.25... <=0.55%C	Z	forged/rolled/cold drawn	AN	annealed	240 HB	1950	0.25
P2.3.Z.AN	2		3	high carbon, >0.55%C	Z		AN		240 HB	2020	0.25

Figure 4.10: Specific cutting pressure of the workpiece material [64].

Given that this operation consists on peripheral milling, the expression present in the left side of Figure 4.5 can be used to determine h_m. A rake angle of 0º was considered in the calculations since it is not provided in tool data sheet. However, because the operation is executed by an end mill, it is possible to consider that the rake angle is approximately null. The results are listed in Table 4.8.

Table 4.8: Average chip thickness and specific cutting force for each test – OP1.

Test	f_z **(mm/tooth)**	h_m **(mm)**	k_c **(N/mm²)**
1	0.0438	0.01239	5844.94
2	0.0438	0.01239	5844.94
3	0.0310	0.00877	6372.47
4	0.0438	0.01239	5844.94
5	0.0570	0.01612	5472.42
6	0.0570	0.01612	5472.42
7	0.0310	0.00877	6372.47

In addition, a_p varies with each tool pass, so, in order to obtain a representative value of the operation for the cutting power calculation, the mean axial depth of cut was considered. This consideration takes into account the variation in material removal along the depth, while providing a global estimation of the power.

The values of P_c for each test of OP1 are listed in Table 4.9 and the linear regression between the current RMS values and power is represented in Figure 4.11. Because the analysis is made for specific operations, only a significant small percentage of the machine capacity is being monitored so it makes sense to find and discuss a linear relationship between current and cutting power.

Table 4.9: Estimated cutting power, considering the chip thickness, for each test in OP1.

Test	**Cutting Power (W)**
1	995.63
2	695.06
3	766.23
4	1175.78
5	1209.74
6	1432.58
7	536.36

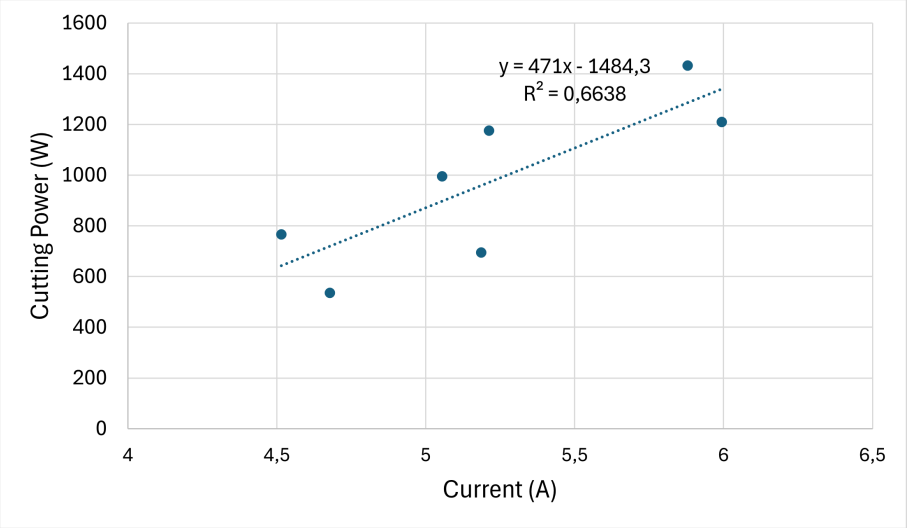


Figure 4.11: Current (RMS) vs Cutting Power of OP1.

The slope of the regression line represents the variability rate of P_c with the increase of current, I. Its value of 471 W/A suggests that, on average, each additional ampere of current corresponds to an increase of around 471 W in cutting power.

The coefficient R^2 indicates that about 66% of the variation in cutting power can be explained by the current. The remaining 34% can be attributed to other factors such as thermal and mechanical effects, material behaviour or tool engagement conditions. To sum up, this plot demonstrates that the current and estimated cutting power have a moderate linear relationship.

Because the other operations are more complex and the calculation of the average chip thickness involves more sophisticated modelling, it is important to understand if it is possible to consider $K_c \approx k_{c1}$. Therefore, the value of P_c was calculated considering K_c constant across the different tests and equal to 1950 N/mm^2. The results are represented in Table 4.10 and the plot between

current and cutting power is illustrated in Figure 4.12.

Table 4.10: Estimated cutting power for each test in OP1, considering $K_c = k_{c1}$.

Test	Cutting Power (W)
1	332.16
2	231.89
3	234.47
4	392.26
5	431.07
6	510.48
7	164.13

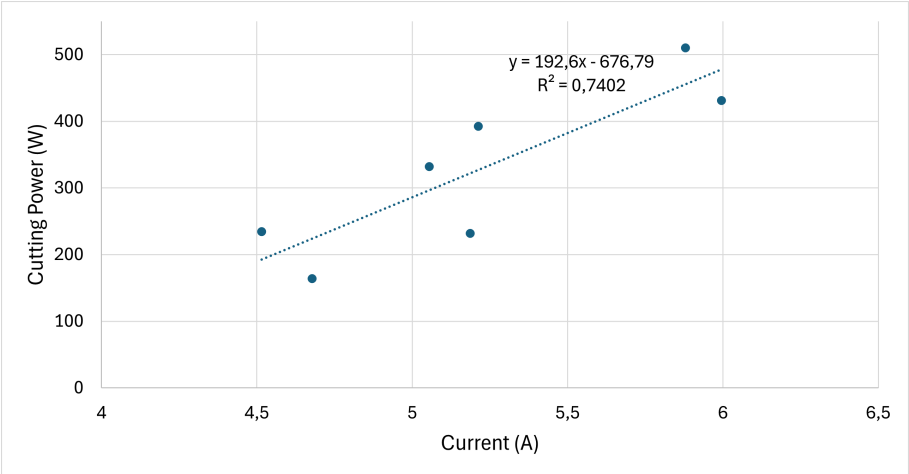


Figure 4.12: Current (RMS) vs Cutting Power of OP1 considering $K_c = k_{c1}$.

Although this simplification leads to significantly lower power values, it results in a stronger linear relationship between the two variables ($R^2 \approx 0.74$). On average, the ratio between the cutting power considering h_m and the simplified model is around 3. This indicates that neglecting the impact of h_m can lead to underestimations of cutting power, especially in operations where the chip thickness is really small.

However, the difference between the coefficients of determination is about 8%, suggesting that the simplified version is able to capture the relationship between current and P_c with reasonable accuracy. As such, in operations where estimating h_m is complex, the use of k_{c1} as an approximation of the specific cutting pressure can be justified, with its limitations acknowledged.

The combined increase of v_c and f_z led to the highest energy consumption during cutting, which is according to the current RMS values, and the decrease of both leads to the least amount of cutting power required. Once again, the feed per tooth has higher influence in the energy involved in cutting than the cutting speed.

Overall, the results demonstrate that while current can be used as a practical indicator of the cutting power, as it shows a positive correlation between RMS current and estimated power, it does

not fully capture the complexity of the power consumption during cutting and other factors can have weight in its value. However, all the plots demonstrate that the current is capable of detecting load variations and quantify the change in energy.

4.1.1.2 Torque and Power

The global power can also be estimated by the spindle torque, T, and frequency of rotation, f_{rot}. Both the maximum and average torque values during OP1 were recorded using the machine's *Load Monitoring* function, which is discussed in more detail in Section 3.4.1. The maximum torque does not consider the accelerations and decelerations of the spindle, while the average value translates all the movements.

The results obtained for each test are listed in Table 4.11. The test with the highest value of maximum torque is test 6, but the test with the highest average values is test 5. Although increasing v_c and f_z was expected to result in the highest global values of torque, as demonstrated before, f_z has direct impact in the chip thickness. This significantly impacts the cutting pressure and force. Therefore, the feed per tooth was shown to produce more significant variations in torque throughout the operation.

Table 4.11: Maximum and average spindle torque measured using the *Load Monitoring* Function-OP1.

Test	Maximum Torque (Nm)	Average Torque (Nm)
1	1.959	1.171
2	1.983	0.688
3	1.720	1.060
4	2.007	1.159
5	2.253	1.263
6	2.264	1.251
7	1.708	1.044

The average torque was used for power estimation, as it provides a global representation of the mechanical effort required throughout the operation (including both idle and cutting time). Based on the average values and the spindle speed, the cutting power was calculated. The frequency of rotation in rad/s was calculated by Equation 4.9, involving spindle speed values.

$$f_{rot} = \frac{2 \cdot \pi \cdot n}{60} [\text{rad/s}] \tag{4.9}$$

The power can then be calculated through Equation 4.10.

$$P = T \cdot f_{rot} [\text{W}] \tag{4.10}$$

The results for each trial of OP1 are represented in Table 4.12, along with the rotational frequency.

Table 4.12: Rotational frequency and power estimated from spindle torque in OP1.

Test	Rotational Frequency (rad/s)	Power (W)
1	507.891	594.74
2	354.665	244.01
3	507.891	538.36
4	600.002	695.40
5	507.891	641.47
6	600.002	750.60
7	354.665	370.27

In order to understand if the values of torque given by the machine can serve as indirect indicators of tool wear, it is important to assess its correlation to the measured current and estimated cutting power. In this sense, the global current, considering both moments where the tool is and is not cutting, was estimated through the RMS method and an average value was obtained for each test- Table 4.13. Then, the relationship between RMS global current and torque was plotted, as Figure 4.13 illustrates.

Table 4.13: Global current (RMS) measured during OP1 tests.

Test	Global Current (A)
1	5.792
2	4.222
3	4.993
4	5.624
5	7.715
6	6.460
7	5.377

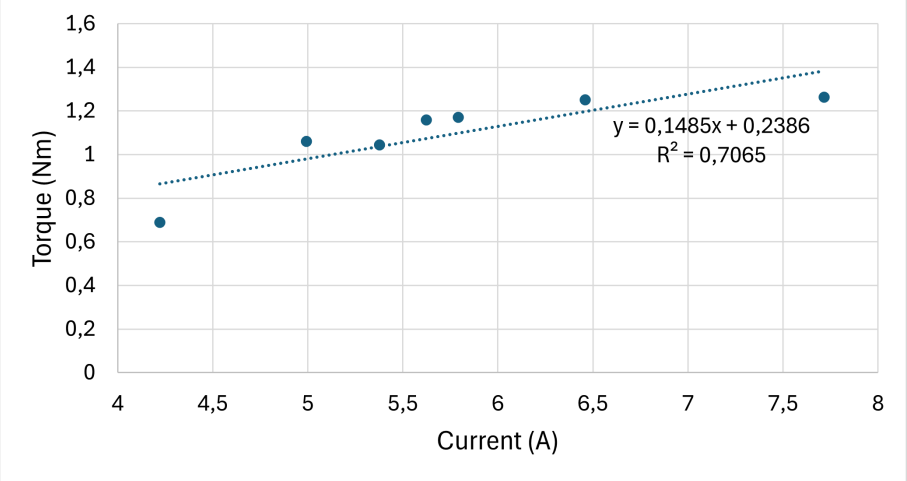


Figure 4.13: Global Current (RMS) vs Average Torque- OP1

This graph demonstrates that the measured current has a moderate linear relationship with the torque supplied by the machine- $R^2 \approx 0.71$. Hence, it can be affirmed that the torque measured by the servo motor is capable of indicating the electrical consumption of the operation.

The relationship between the current and the power calculated with the torque was also determined. As represented in Figure 4.14, there is a lower linear correlation between these two ($R^2 \approx 0.49$). This non-linearity can be justified by the variation of speed, that makes the relationship between current and power noisy. Small speed changes affect the power but not the torque directly and, because the power in question is a product of both, there is a tendency to amplify these variations. Overall, it is normal for the I to have a stronger linear relationship with the torque and less linear with the Power estimated from the torque.

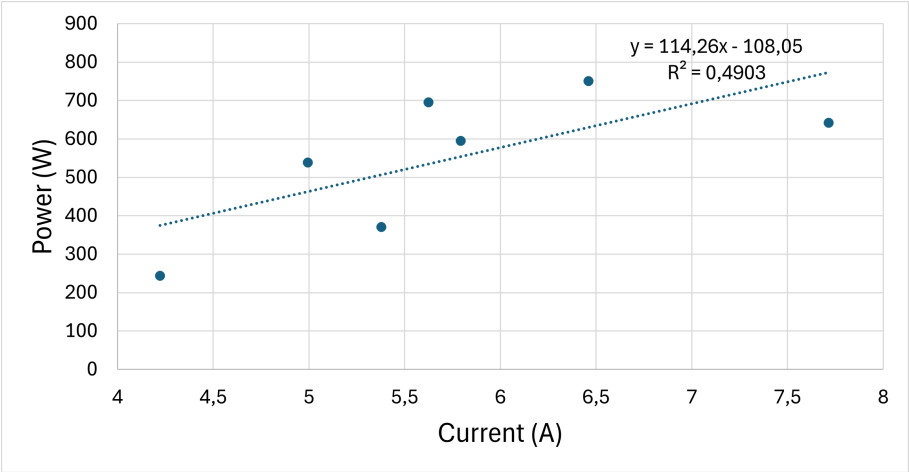


Figure 4.14: Global current (RMS) vs Torque-derived Power of OP1.

Regarding the torque's ability to indicate real cutting efforts, the linear correlation between the cutting power, P_c, and torque derived power was estimated as is represented in Figure 4.15. The average torque read by the machine considers several factors such as accelerations, decelerations, friction and load variations. In contrast, the cutting power estimated with the chip geometry and specific cutting pressure only accounts the ideal chip formation. For this reason the power estimated from the torque is, on average, approximately 60% higher than the theoretical cutting power calculated from chip geometry.

In addition, the correlation between these variables is relatively high $R^2 \approx 0.73$. Based on this results, it can be concluded that the torque estimated by the machine is suitable to reflect the real cutting efforts variation.

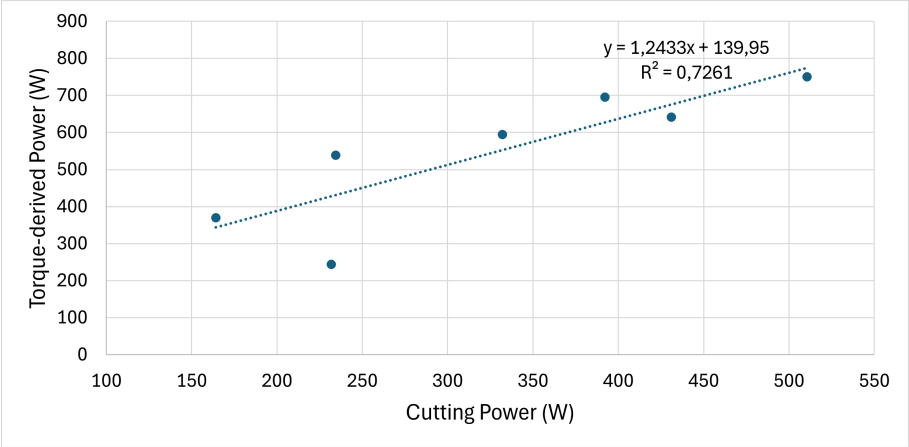


Figure 4.15: Cutting Power vs Torque-derived Power of OP1.

Furthermore, since tool wear is accelerated, typically, by the increase of cutting forces, which corresponds to an increase of cutting power, this machine function turns out to be a viable indirect indicator of tool wear. This is particularly important because this is a function already available at the machine that can easily be used in every process and give critical indications of tool life, which is one of the main problems when using hard steel.

4.1.1.3 Idle Current

To complement the analysis of the cutting moments, the current consumption during idle movements was also evaluated. The baseline or idle current corresponds to the moments when the spindle is rotating without engaging the material. This analysis is relevant to understand the effective contribution of material removal for the total energy consumption.

The RMS value of the idle current was calculated over the segments where no cutting occurred, excluding the initial descent and final ascent of the tool since it corresponds to a significant peak in the current but does not provide useful information. This baseline corresponds to the current consumed between tool passes, allowing for a comparison against active cutting values. The method employed is the same as the one used for the cutting segments.

The values of the effective current obtained from the RMS method for each test are represented in Figure 4.16.

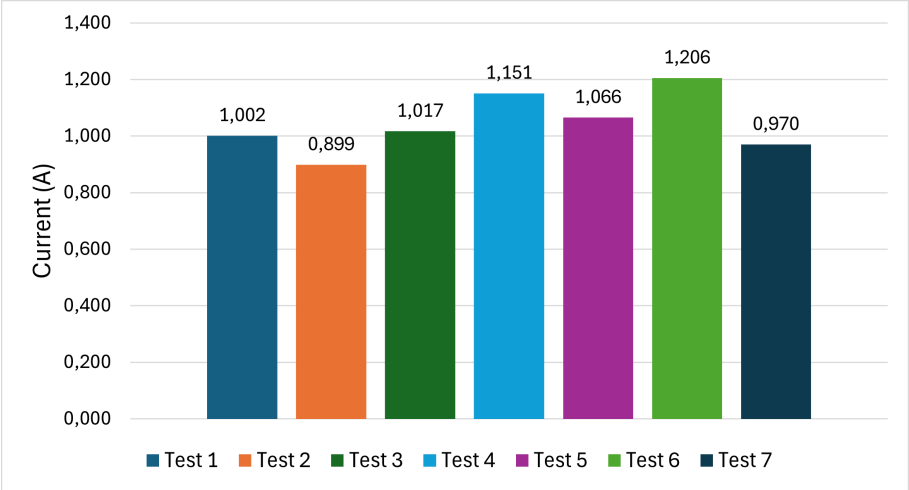


Figure 4.16: Idle current of each test of OP1.

The baseline current showed variations across tests, specially in test 4 and 6. This might be explained by the change of rotation speed with the variation of v_c. By increasing the speed, the tool requires higher energy to decelerate and win over friction between tool passes, resulting in small variations of baseline values. Since f_z does not directly impact spindle speed, it is expected that the values are similar between tests 3 and 5, where v_c remains constant.

To confirm this effect of the spindle speed, n, on the idle current, the linear correlation between them was drawn and is represented in Figure 4.17. As the linear regression indicates, both variables have a strong relationship ($R^2 \approx 0.82$), which confirms that the spindle speed has a significant impact on the variations of the current during idle time, justifying the difference between tests.

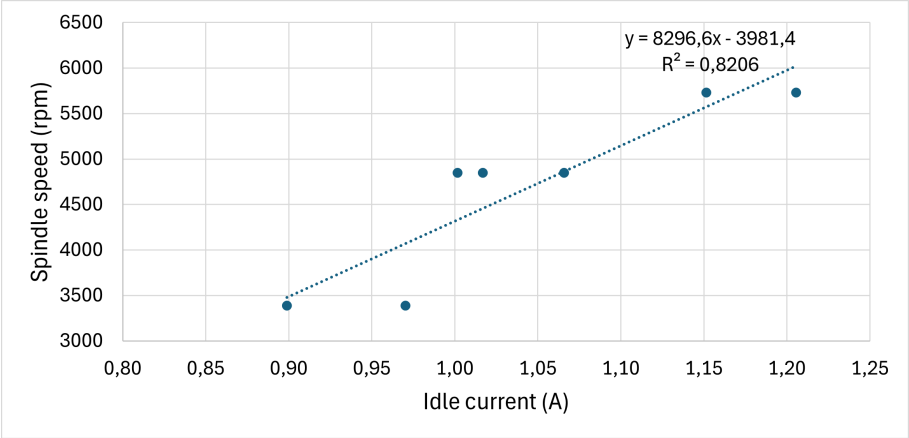


Figure 4.17: Spindle speed vs Idle current of OP1.

At last, Figure 4.18 shows the comparison of the RMS current measured during cutting and idle time. As expected, the current during cutting is significantly higher. This reinforces the idea that the current clamp is capable of capturing the additional load during engagement of the tool with the material and, thus, can be used as an indicator of process performance.

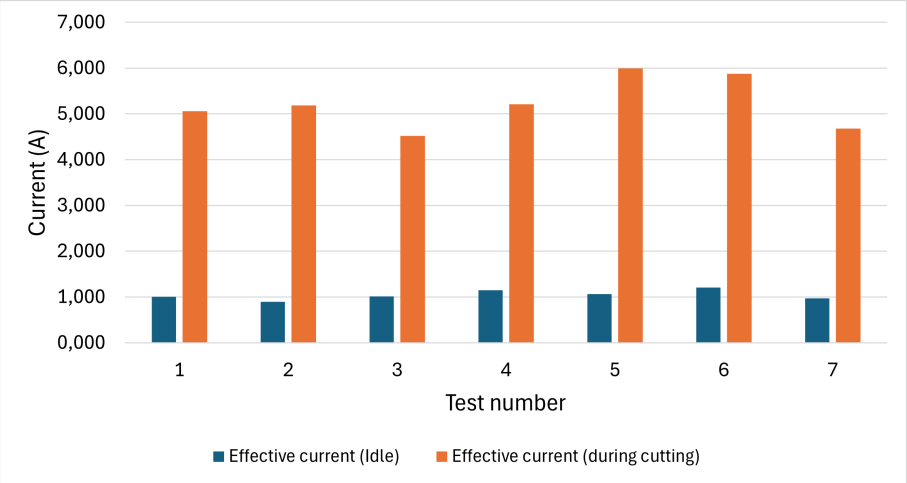


Figure 4.18: Comparison of the idle current and current during cutting of OP1.

4.1.2 Operation 13

Operation number thirteen corresponds to the roughing of the oblong in the back face of the workpiece. The tool is a 8 mm diameter end mill and performs a total of 10 passes, as observed by the tool path illustrated in Figure 4.19.

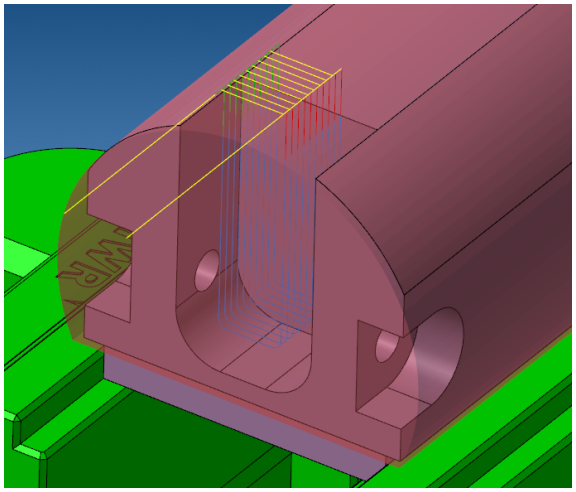


Figure 4.19: Tool path of Operation 13.

In this operation, a_e changes along each tool engagement and a_p remains constant. Therefore, an average value was estimated to represent a global radial depth for the operation. The depth of cut is constant, removing 1 mm in the axial direction.

To determine an average value of a_e, each pass was decomposed into three segments: two vertical movements (downward and upward) and one horizontal movement, as illustrated by Figure 4.20.

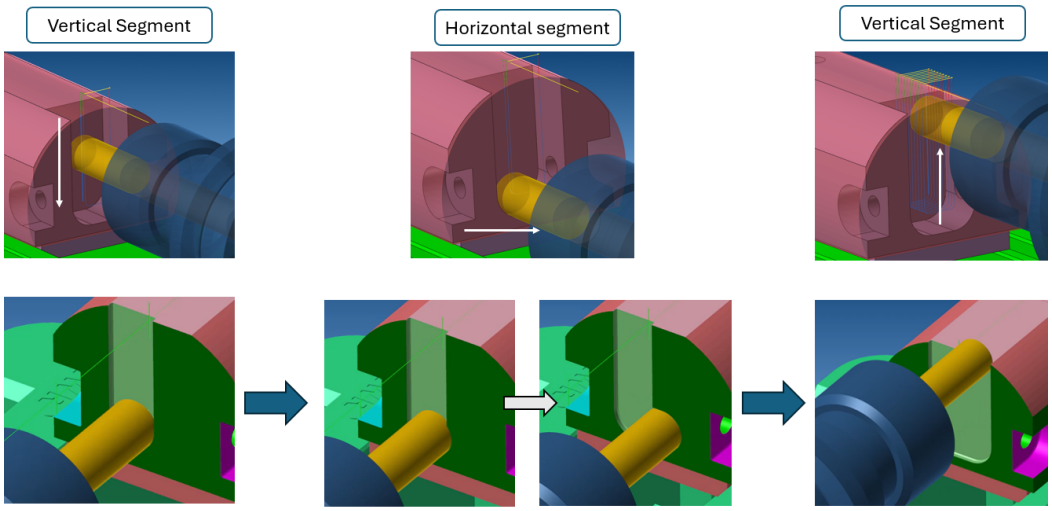


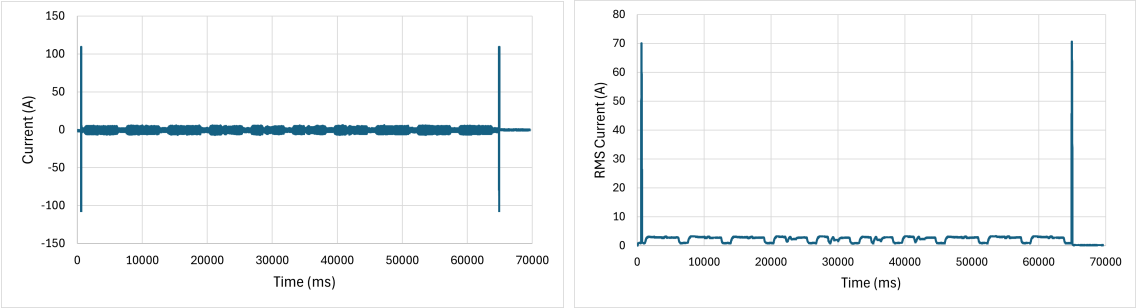
Figure 4.20: Segmentation of the tool path to determine the average a_e of OP13.

To understand this scheme, it is important to remember that in the CAM simulation is the tool that moves around the workpiece. However, in the machine the spindle remains fixed in a vertical position (Z-axis of the machine) and it is the workpiece that rotates and tilts. As such, the back surface of the part is oriented towards the spindle, meaning that the simulated Z-axis direction corresponds to the Y-axis in the machine coordinate system.

During the vertical segments, the value in the Y-axis of the machine varies, while X remains constant. In this movements the value of a_e is given by X, which corresponds to 100% of the tool diameter. During the horizontal segment, as X varies and Y remains constant, a_e is given by the value in Y which is also equivalent to 100% of the tool diameter. As such, the value of a_e in all segments is 8 mm, resulting in an average value of a_e= 8 mm.

This approach is a simplification of the real situation. In the first tool pass, the tool engages with 100% of its diameter, but in the following engagements, in the horizontal section, the effective radius of contact is smaller corresponding to a smaller real depth of cut. However, based on the geometry of the feature, the relative reduction in contact area is minimal. It is estimated that the effective width of cut varies by approximately 7%, as the maximum contact corresponds to the width of the part, 15 mm, over a 16 mm diameter tool, i.e., $\frac{15}{16} \approx 93\%$. The value of 16 mm was considered based on the full width of the geometry, which corresponds to the engagement of the 8 mm diameter tool along both sides of the slot ($2 \times 8 = 16$ mm). This small value allows the usage of a simplified average value of a_e for further calculations.

The current over time was plotted- Figure 4.21a- and the values after the application of RMS are also represented in Figure 4.21b. These graphics are an example of a typical curve of OP13 regarding current evolution. All the RMS current plots of all tests of OP13 can be seen in Appendix D.



(a) Raw current values over time.

(b) RMS current values over time.

Figure 4.21: Raw and RMS current signals of Test 1 during OP13.

In order to compare current consumption between tests, the mean RMS value of each was obtained, along with the percentage variation of each test relative to the reference value (test 1). These results can be found in Table 4.14.

Table 4.14: Mean RMS current value and percentage variation for each test during OP13.

Test	Mean RMS current (A)	% Variation
1	2.784	0.00%
2	2.474	-11.14%
3	2.295	-17.55%
4	2.861	+2.78%
5	2.924	+5.04%
6	3.167	+13.74%
7	2.115	-24.04%

The graphic represented in Figure 4.22 shows that test 6 experienced the highest current consumption, followed by test 4 and 5. This is expected since higher speed and feed are related to higher cutting forces and, hence, more energy. The decrease of parameters also lead to a decrease of current, which also agrees with what was expected based on theoretical knowledge.

From the percentage variation results, it is possible to conclude that, similar to OP1, the feed per tooth has a more pronounced influence on the measured current than the cutting speed. The average chip thickness, h_m, is directly affected by f_z, increasing the amount of removed material. Ultimately, this leads to higher cutting forces, resulting in significant impact in energy. In addition, as previously discussed, the impact of v_c in current is not linear and can be explained by the Johnson-Cook constitutive model.

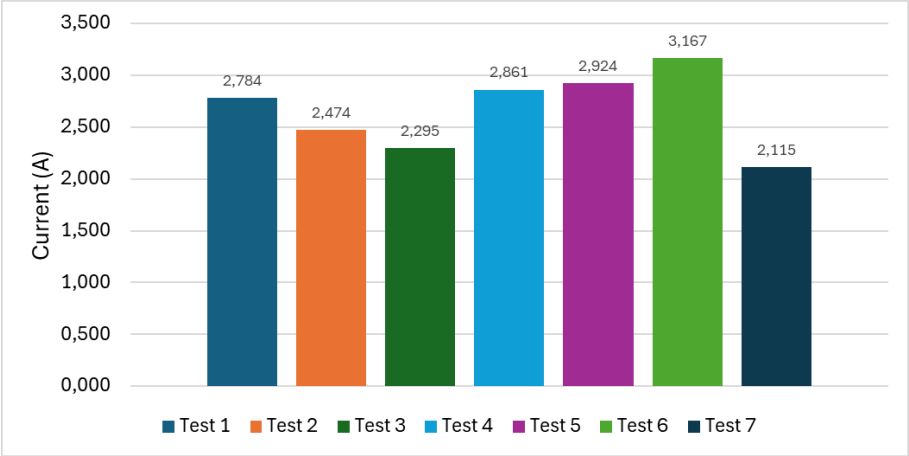


Figure 4.22: Comparison between the effective value of current (RMS) of each test of OP13.

Analysing the current values in each tool pass- Table 4.15- it is possible to observe more pronounced oscillation in passes four to seven compared to the others. The corresponding pattern plotted in Figure 4.23 confirms these irregular load conditions on the spindle during these intervals.

Table 4.15: Mean RMS current values (A) for each cutting pass of each test in OP13.

Test \ Tool Pass	1	2	3	4	5	6	7	8	9	10
1	2.960	2.937	2.914	2.660	2.381	2.428	2.578	2.961	3.025	2.995
2	2.496	2.540	2.607	2.345	2.153	2.286	2.318	2.733	2.587	2.674
3	2.468	2.392	2.463	2.168	2.052	2.059	2.213	2.347	2.419	2.373
4	3.036	3.076	3.064	2.609	2.451	2.711	2.567	3.039	3.124	2.936
5	3.130	3.130	3.005	2.821	2.626	2.459	2.727	3.168	3.133	3.044
6	3.487	3.362	3.275	2.920	2.799	2.656	2.919	3.404	3.475	3.369
7	2.221	2.288	2.248	1.963	1.911	1.864	1.989	2.182	2.264	2.216

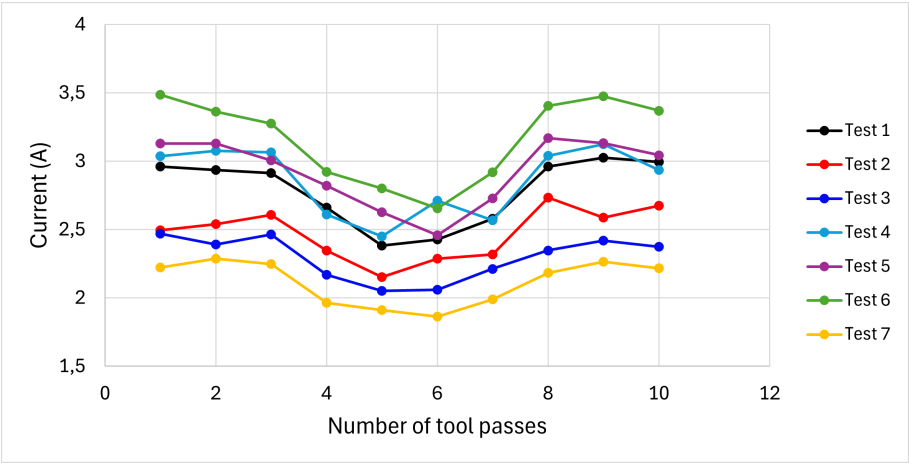


Figure 4.23: Variation of the current with each tool pass- OP13.

After analysing the operation, it was concluded that these passes coincide with the encounter of the tool and the pre-drilled D4.04 hole, as demonstrated by Figure 4.24. With continuous full engagement of the tool with the material surface, the cutting load is more uniform. In contrast, these transitions in and out of voids result in dynamic variations in force and, as consequence, in current consumption. Therefore, it is expected to observe a decrease of the current in the moments where the tool enters the empty space, since the load at the spindle is also lower. Capturing this phenomenon demonstrates that the clamps are capable of capturing dynamic changes and translating the tool's behaviour in a way that is faithful to what happens in reality.

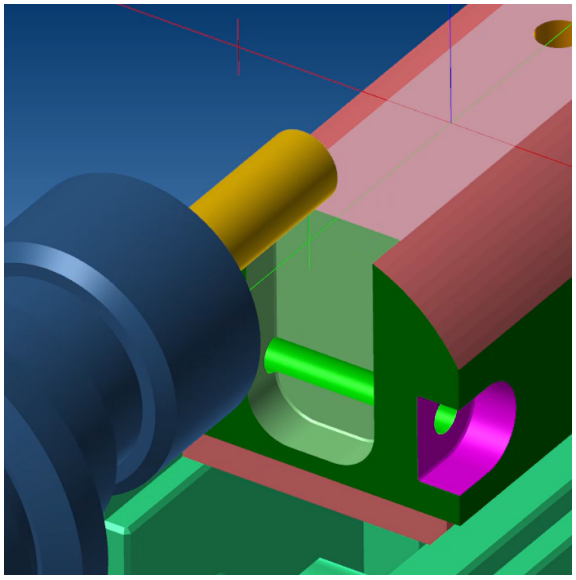


Figure 4.24: Illustration of the tool intersecting a pre-drilled hole during OP13.

The relationship of the current with the MRR was also estimated. The MRR values of each test are represented in Table 4.16 and the regression line between the two variables is drawn in Figure 4.25.

Table 4.16: Material Removal Rate (MRR) for each test in OP13.

Test	**MRR (cm^3/min)**
1	4.640
2	2.630
3	3.253
4	5.728
5	6.134
6	7.563
7	2.143

As expected, the tests where f_z is higher demonstrate increased MRRs. Regarding the relationship between current and MRR, the value of R^2- 0,92-shows a strong correlation between these

two, where the current serves as a reliable indication of material removal.

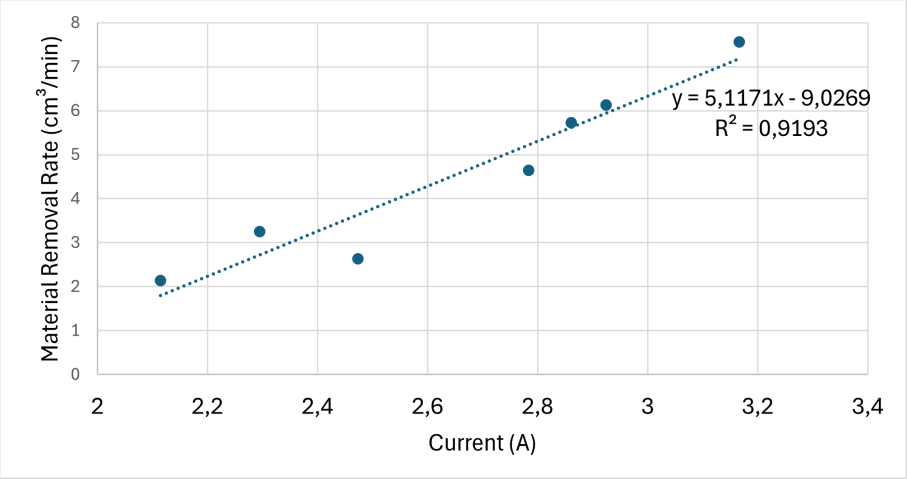


Figure 4.25: Current vs Material Removal Rate (MRR)- OP13

4.1.2.1 Current and Cutting Power

The cutting power was determined using Equation 4.3. As discussed in the previous section, given the complexity of this operation and respective determination of h_m, the cutting power was determined considering $K_c \approx k_{c1} \approx 1950 N/mm^2$. The results are listed in Table 4.17

Table 4.17: Cutting power for each test of OP13.

Test	Cutting Power (W)
1	150.80
2	85.49
3	105.72
4	186.16
5	199.37
6	245.80
7	69.65

The relationship between the RMS values of the current and the cutting power was plotted and is shown in Figure 4.26. As previously observed, the current does not vary in a perfectly linear manner with the cutting power. Yet, in this operation, the regression line shows a positive linear tendency with a high value of the coefficient- $R^2 \approx 0.92$. This result indicates that around 92% of the variation in power can be explained by the current. To conclude, this correlation and low dispersion of points reinforces the ability of the current to be used as an indicator of cutting power.

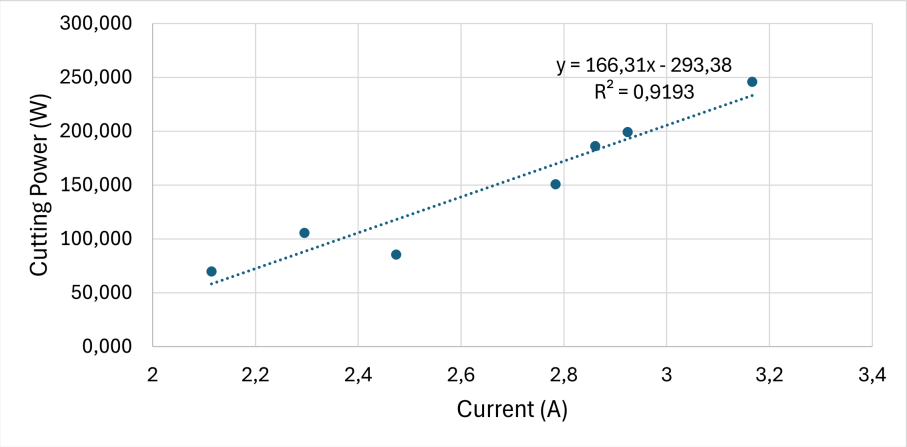


Figure 4.26: Current (RMS) vs Cutting Power- OP13.

4.1.2.2 Torque and Power

The overall power, estimated with the average torque given by the machine and spindle speed, was also determined and related to the RMS global value of current of each test.

The registered values of spindle torque are represented in Table 4.18, along with the results of power using the average torque and rotational frequency. Test number 4, corresponding to an increase of v_c, possesses in general the highest values of spindle torque, followed by test 5 (increase of f_z). Cutting speed impacts, mostly, the strain rate of the material that can lead to two different effects on cutting forces: an increase or decrease. In this case, it is possible to observe that the hardening response of the material was dominant as v_c increases torque. The feed per tooth directly impacts chip thickness and cutting forces, so this high result is expected.

Table 4.18: Maximum and average spindle torque, frequency of rotation and corresponding power- OP13.

Test	Maximum Torque (Nm)	Average Torque (Nm)	Frequency Rotation (rad/s)	Power (W)
1	0.999	0.752	607.375	456.75
2	0.833	0.635	400.836	254.53
3	0.806	0.640	607.375	388.72
4	1.011	0.783	749.793	587.09
5	1.041	0.780	607.375	473.75
6	1.014	0.760	750.003	570.00
7	0.712	0.554	400.836	222.06

The correlation between the spindle average torque and measured global current is expressed in Figure 4.27. The results of the RMS method for the global current are also listed in Table 4.19. The linear relationship between the two variables is strong ($R^2 \approx 0,83$), indicating that the torque measured by the servo motor is capable of representing the current consumption.

Table 4.19: Global current (RMS) measured during OP13 tests.

Test	Global Current (A)
1	4.530
2	3.234
3	3.603
4	6.259
5	5.909
6	5.131
7	3.263

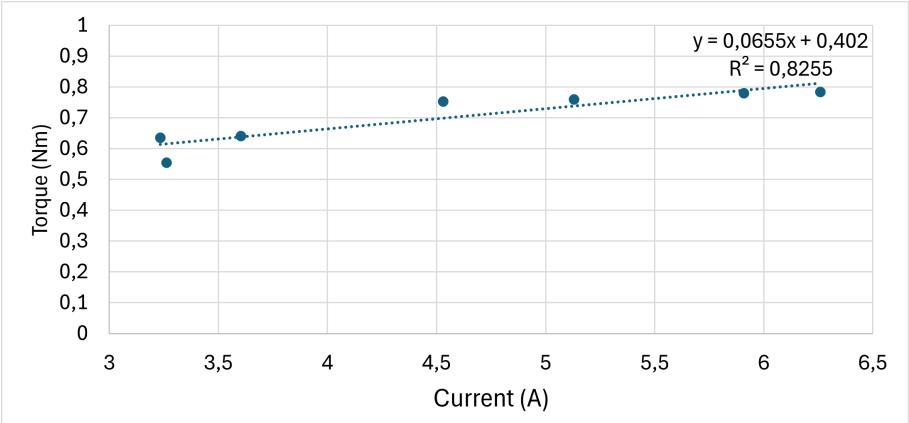


Figure 4.27: Global current (RMS) vs Torque-derived Power- OP13.

The relationship between current and the torque-derived power was also determined. As Figure 4.28 shows, there is a good linear correlation between both where 78% of the global current variations are explained by the power estimated from the spindle torque. These results indicate that the measured current is capable of reflecting mechanical efforts in the case of this operation.

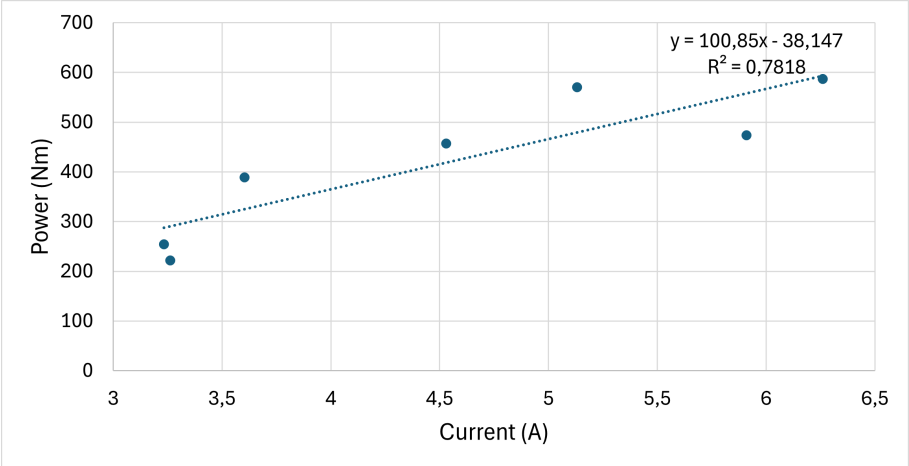


Figure 4.28: Global current (RMS) vs Torque-derived Power- OP13.

Finally, the high linear correlation between the cutting power and estimated power from the torque- Figure 4.29- demonstrates that the values given by the servo motor can serve as indirect indicators of the cutting effort during the operation ($R^2 \approx 0.84$). Because tool wear is mostly increased by the cutting force and, as consequence, cutting power required, it is possible to conclude that the *Machining Load Monitoring* function can be used as a tool wear indicator.

Additionally, the cutting power results are lower than the overall power because only the cutting moments are being considering, disregarding accelerations and decelerations of the tool when it is not cutting.

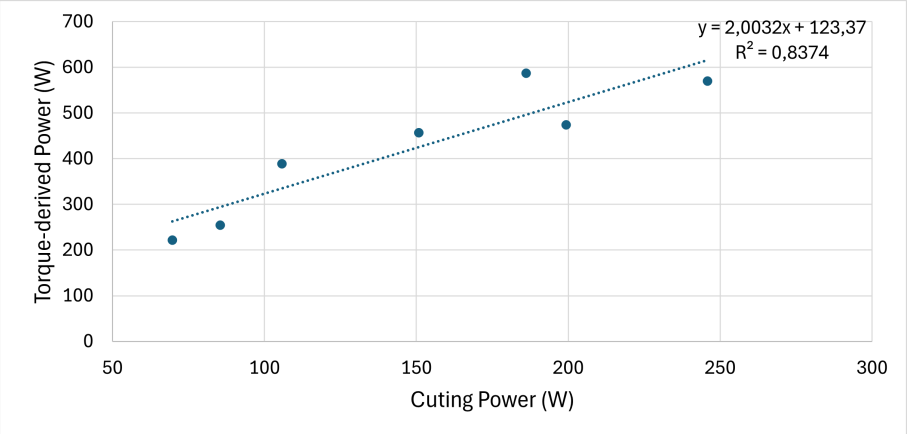


Figure 4.29: Cutting Power vs Torque-derived Power- OP13.

4.1.2.3 Idle Current

The idle or baseline current was also analysed in operation 13 and compared to the current consumption during cutting. The results are represented in Figure 4.30, in which variations of current occur. Once again, the cause of these differences can be attributed to spindle speed changes. The v_c has higher impact in the current consumption while the tool is not cutting than f_z, where tests 3 and 5 have similar results.

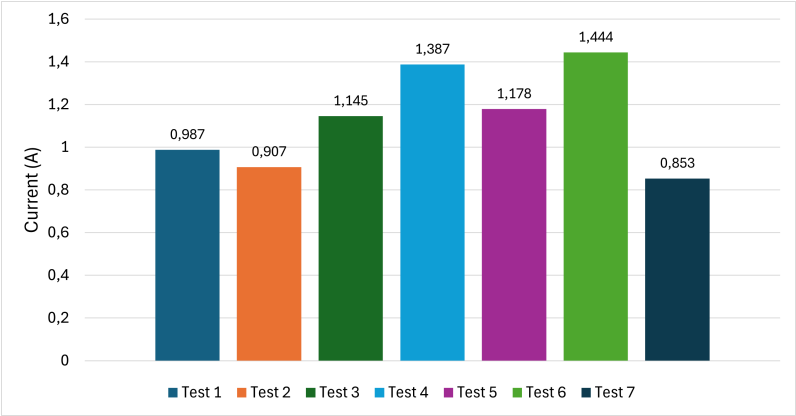


Figure 4.30: Idle current of each test of OP13.

To further confirm the impact of the spindle speed in the current, the linear relationship is represented in Figure 4.31. As the coefficient R^2 demonstrates, there is a strong correlation between these two variables (around 88%). As such, the differences observed between tests can be attributed to the different v_C applied.

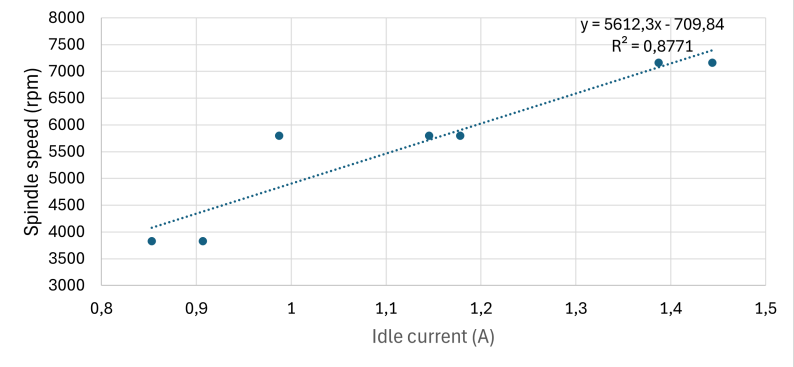


Figure 4.31: Spindle speed vs idle current of OP13.

The idle current is lower than the current while cutting, as expected, as demonstrated by Figure 4.32. The results show, once again, that the current sensor has the ability to record the load variations between cutting and idle rotation of the tool.

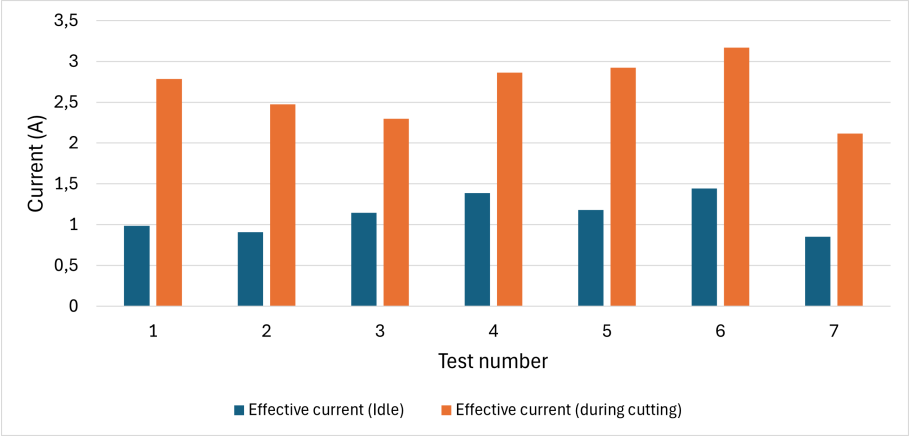


Figure 4.32: Comparison of the idle current and current during cutting of OP13.

4.1.3 Operation 15

Operation 15 consists on the roughing and finishing of the slot that accesses the D3.28 hole. The tool used was a 5 mm diameter end mill and it executed thirteen roughing passes plus two finishing steps. In total, the tool performs fifteen steps, as illustrated by Figure 4.33. This operation is also detailed in Section 3.3.2.

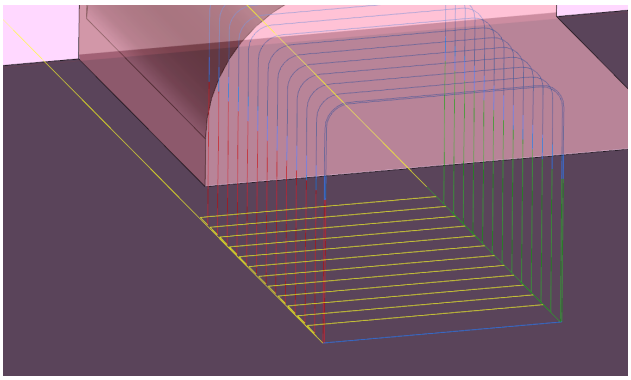


Figure 4.33: Tool path of Operation 15.

During the 13 roughing passes, the tool has a constant axial depth of cut equal to 0.7 mm, while the radial depth varies. For this operation, a segmentation of the path was employed to determine the average radial depth of cut. According to the scheme in Figure 4.34, the a_e of the vertical segments is equal to the tool diameter value (5 mm) and for the horizontal segment, a_e corresponds to the maximum height value of the feature- 4 mm. As such, the average value of a_e for this operation results in 4.67 mm ($\frac{5+4+5}{3} \approx 4.67$).

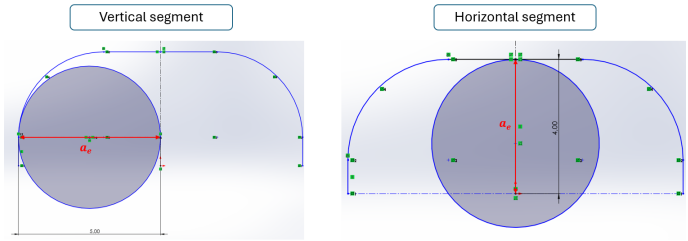


Figure 4.34: Radial depth of cut of the roughing passes of each segment in OP15

Regarding the finishing passes, the tool widens 0.03 mm, as illustrated by Figure 4.35, which corresponds to the radial depth of cut. a_p is the sum of the axial depths of each roughing operation- 9 mm.

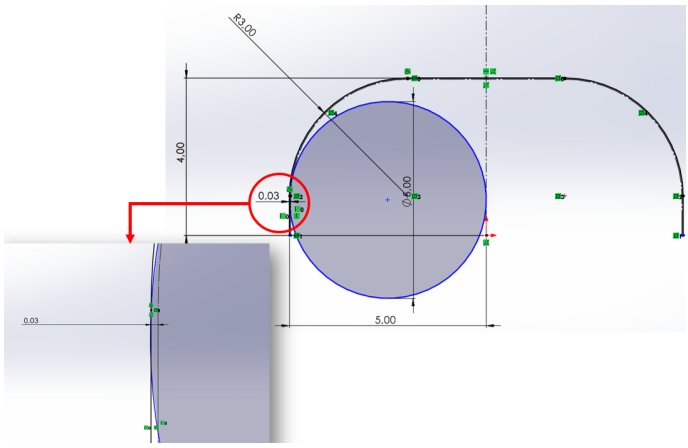
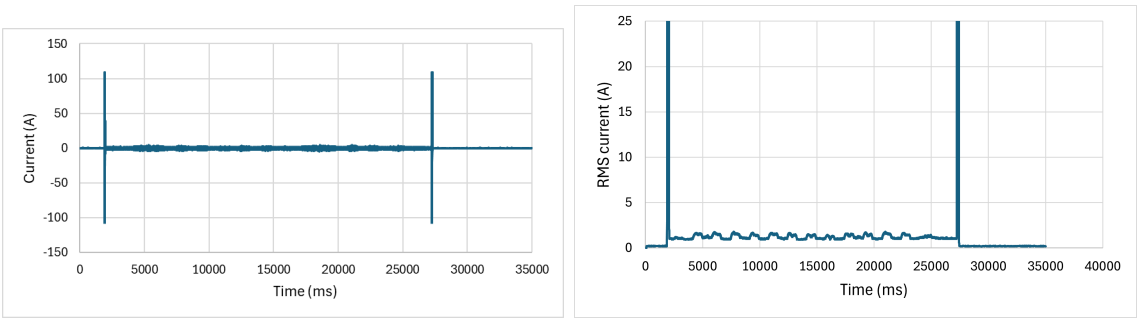


Figure 4.35: Radial depth of cut of the finishing passes in OP15.

The raw current values over time were obtained and Figure 4.36a exemplifies the plot of Test 1. The other tests have similar plots. Unlike the previous operations, this graph does not exhibit distinct current fluctuations associated with tool engagement. This suggests a significantly lower current demand during cutting, possibly closer to the baseline level.

After the application of the RMS method in a window of 100 ms, it became possible to distinguish individual tool passes, as the noise was reduced and a local analysis was promoted. However, only roughing passes exhibited distinct fluctuations, whereas finishing operations were not captured, as demonstrated by Figure 4.36b. In some tests, even the 13 step was difficult to identify. All the RMS current plots of all tests of OP15 can be seen in Appendix D.



(a) Raw current values over time.

(b) RMS current values over time.

Figure 4.36: Raw and RMS current signals of Test 1 during OP15.

In this case, finishing operations did not produce sufficient current variations most likely due to their lower cutting force and reduced material removal, which limits the detection of cutting activity based on current. The tool is only removing 0.03 mm of material, in which the final step is spring back that, in reality, takes away almost 0% of material. The removal of these minimum amounts of material is expected to produce a very small mechanical load that, in consequence, does not produce significant energy increase.

Despite the effectiveness of the RMS method in identifying cutting segments in roughing operations, its applicability to finishing operations is more limited. As such, it is important to be careful when using current based monitoring for low-load operations. Moreover, the distinguish of cutting segments on the tests where the cutting parameters are lower, which tends to lead to lower current consumption, was significantly harder and, since this is a manual selection, it is likely to observe more outliers and errors.

The further analysis will be focused on the roughing operations, but it is important to estimate the cutting power differences between finishing and large MRRs to confirm this theory, which will be discussed in the next section.

When analysing the current in each pass- Table 4.20- it becomes clear that there are tool engagements that consume less current.

Table 4.20: Mean RMS current values (A) for each cutting pass in OP15.

Test \ Tool Pass	1	2	3	4	5	6	7	8	9	10	11	12	13
1	1.510	1.596	1.608	1.354	1.566	1.488	1.336	1.230	1.398	1.480	1.573	1.524	1.333
2	1.411	1.464	1.424	1.344	1.415	1.458	1.202	1.200	1.247	1.464	1.440	1.358	1.146
3	1.426	1.377	1.532	1.189	1.343	1.294	1.367	1.292	1.225	1.337	1.547	1.459	1.163
4	1.917	1.695	1.450	1.787	1.802	1.734	1.697	1.323	1.387	1.436	1.739	1.709	1.604
5	1.376	1.677	1.468	1.715	1.446	1.210	1.641	1.330	1.406	1.520	1.436	1.269	1.725
6	1.227	1.279	1.486	1.710	1.682	1.725	1.785	1.778	1.766	1.535	1.612	1.723	1.589
7	1.182	1.393	1.254	1.268	1.326	1.157	1.214	1.203	1.127	1.176	1.201	1.266	1.035

As Figure 4.37 shows, from passes 6 to 10, the tool intersects the D3.28 pre-drilled hole. Similar to what happens in OP13, when the tool encounters a void the cutting force lowers. As a result, the required energy is lower, which means current consumption decreases.

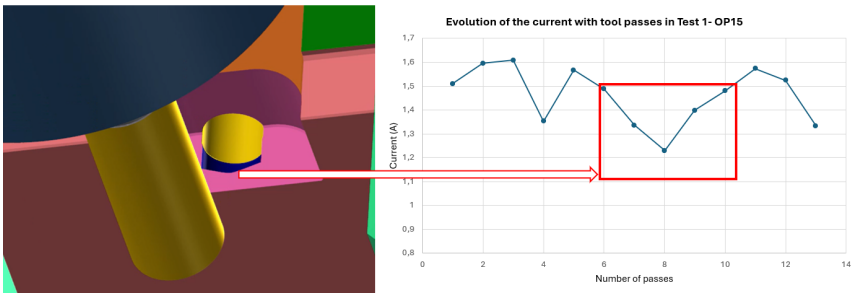


Figure 4.37: Tool engagement of the tool intersecting a pre-drilled hole during OP15.

Figure 4.38 shows the evolution of RMS current values in each tool pass for all tests. The pattern in this operation is not as similar as for the other operations, however, there is a general decrease of I from passes 6 to 10, representing the transition of the tool between support material and void. Tests number 4 and 5, that correspond to a decrease of v_c and f_z respectively, show higher current variations between tool engagements.

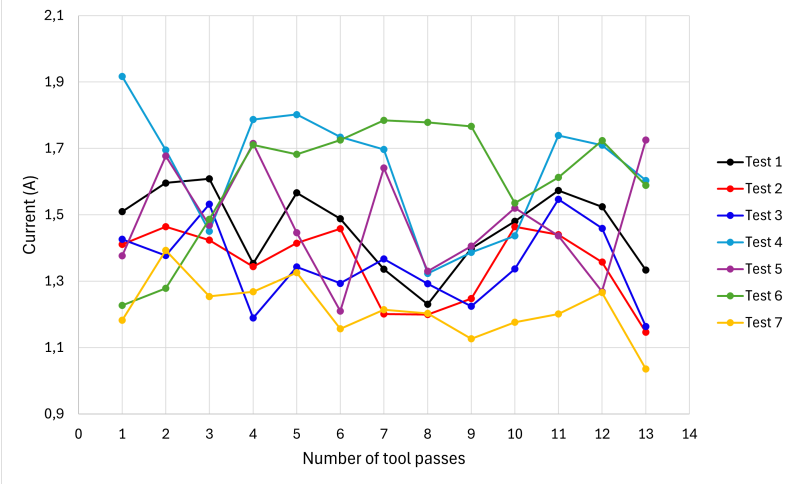


Figure 4.38: Variation of the current with each tool pass- OP15.

The overall current RMS value for each trial was also determined, using a window of 100 ms. The results are presented in Table 4.21, as well as the percentage variation of each trial relative to the first one (reference).

Table 4.21: Mean RMS current values and percentage variation for each test in OP15.

Test	Mean RMS Current (A)	% Variation
1	1.4720	0.00%
2	1.3689	-7.01%
3	1.3657	-7.22%
4	1.6396	+11.39%
5	1.4578	-0.96%
6	1.6091	+9.31%
7	1.2306	-16.40%

Observing Figure 4.39 it can be concluded that test 4 has the highest value of the current, which corresponds to an increase of v_c. The lowest value of current is observed in test 7, where there is a decrease of both v_c and f_z. In this operation, the impact of f_z is not as pronounced, with v_c producing larger differences in current consumption.

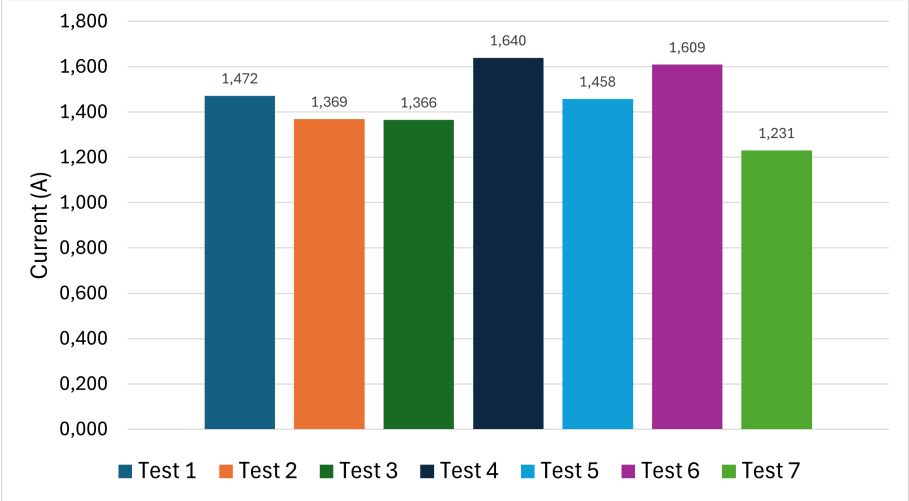


Figure 4.39: Effective RMS current value of each test of OP15.

The relationship between the current during roughing and the corresponding MRRs was also plotted- Figure 4.40. The regression line demonstrates, once again, that the current is a good indirect indicator of MRR, as the value of R^2 indicates a solid linear correlation, where 77.56% of MRRR variation can be explained by the variation of current. The tests where f_Z was increased corresponded, once more, to higher MRRs.

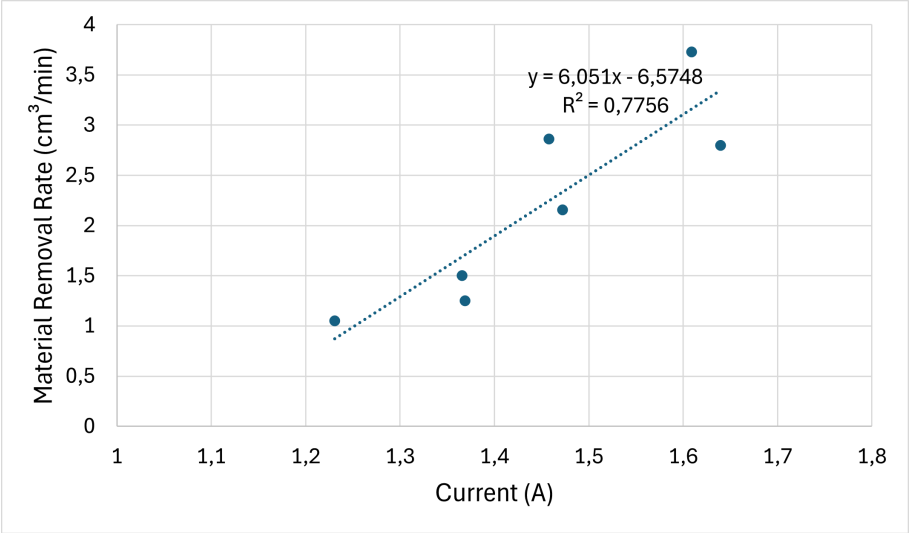


Figure 4.40: Current vs Material Removal Rate (MRR) during roughing of OP15.

After this, a comparison between the results of roughing and finishing passes took place to further understand the limitations of this hardware in the detection of current consumption in finishing operations. Both the roughing and finishing passes were evaluated using Equation 4.5 and the results are represented in Table 4.22. Figure 4.41 highlights the large difference between these two, where roughing passes can reach up to 3.7 cm^3/min and finishing operations remain below 0.3 cm^3/min.

Table 4.22: Material removal rate (MRR) for roughing and finishing in each test of OP15.

Test	**MRR roughing (cm^3/min)**	**MRR finishing (cm^3/min)**
1	2.158	0.166
2	1.253	0.097
3	1.503	0.116
4	2.797	0.216
5	2.864	0.221
6	3.729	0.287
7	1.052	0.081

Since the current is, among others, a result of spindle load and, hence, the amount of removed material, the low values of the last two finishing passes did not produce significant current variations. The current consumption in these were probably around the baseline values of the operation, leading to ineffective distinction of finishing tool engagements by the clamps. Overall, this data indicates that it is necessary to use a complementary or alternative sensor.

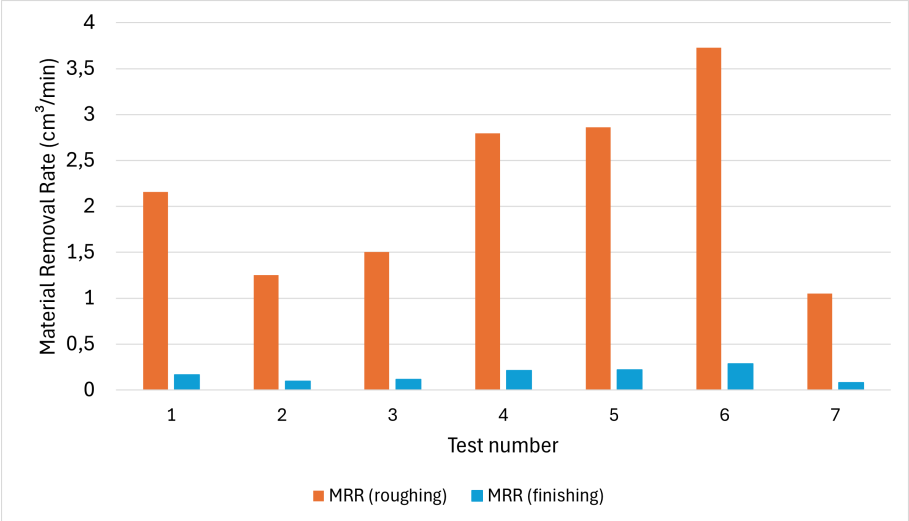


Figure 4.41: Comparison between MRRs of roughing and finishing passes- OP15.

4.1.3.1 Current and Cutting Power

The cutting power, P_c, for roughing and finishing passes were also estimated and compared to further justify the limited ability of the clamps to identify finishing operations. To calculate the cutting power of this operation, the simplification of $K_c \approx k_{c_1}$ was applied given the complexity of this operation. The values for roughing and finishing are listed in Table 4.23. It can be observed that there is a great difference between the cutting effort required in these two situations.

Table 4.23: Cutting power (P_c) for roughing and finishing operations in OP15.

Test	P_c **roughing (W)**	P_c **finishing (W)**
1	70.12	5.41
2	40.72	3.14
3	48.86	3.77
4	90.90	7.01
5	93.07	7.17
6	121.20	9.34
7	34.20	2.64

First of all, the relationship between the current and power, shown in Figure 4.42, was established to assess the ability of the current to express cutting efforts in this case. With an R^2 of around 78% it is possible to affirm that there is a good linear correlation between these two variables, with most of the variation in power being explained by the current. Once more, this demonstrates that the current is a good indirect measurement of cutting power.

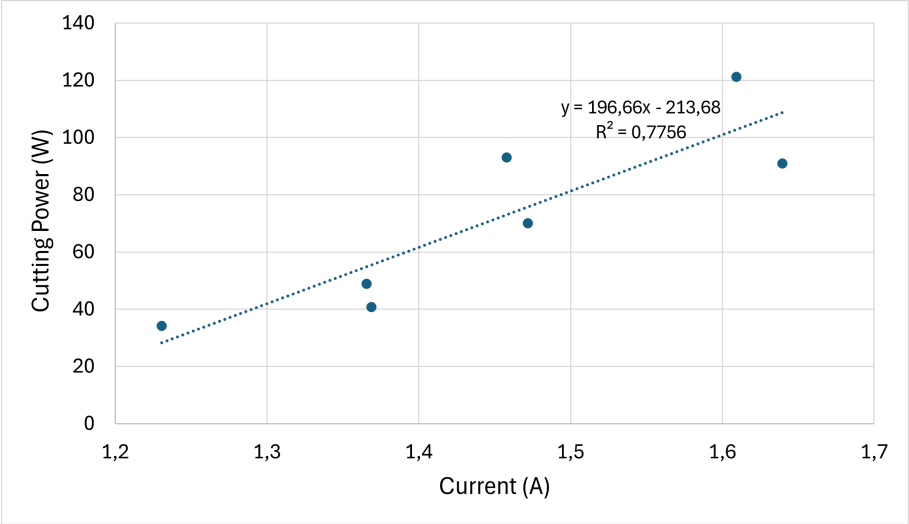


Figure 4.42: Current vs Cutting Power during roughing operations in OP15.

Now, it is important to compare the cutting power for roughing and finishing to reinforce the previous conclusion. This comparison is graphically represented in Figure 4.43. It is observable a large difference of energy consumption as it was expected. The power during finishing passes is, on average, 90% lower than in roughing, which reinforces the reason behind the insufficient response of the clamps. With small loads, the current becomes similar to the baseline values and, as consequence, the finishing operations are not distinguished.

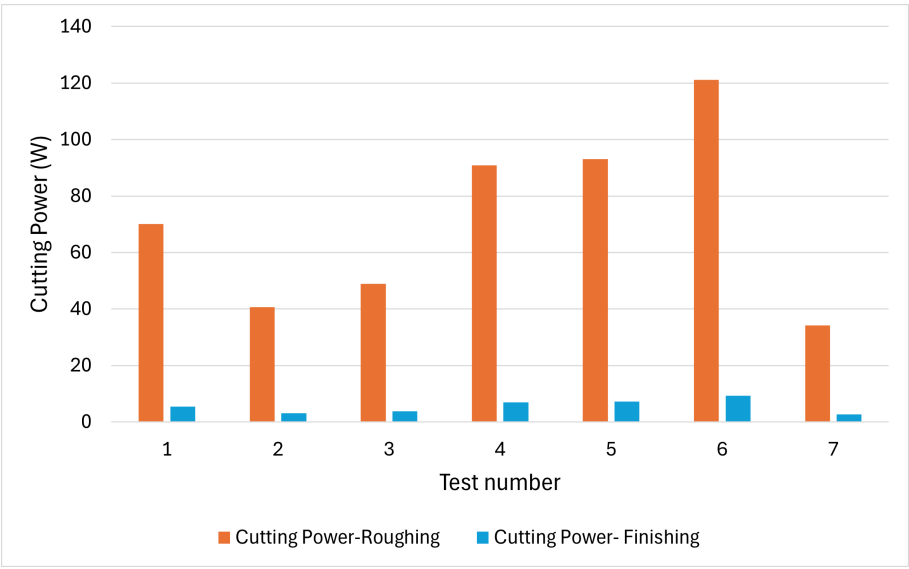


Figure 4.43: Comparison of the cutting power between roughing and finishing operations in OP15.

4.1.3.2 Torque and Power

The power estimated from the average torque, considering both cutting and idle time, was determined and the results can be found in Table 4.24. This value of torque also captures both the roughing and finishing loads of this operation.

Table 4.24: Maximum and average spindle torque and corresponding cutting power- OP15.

Test	Maximum Torque (Nm)	Average Torque (Nm)	Power (W)
1	0.548	0.332	191.22
2	0.444	0.287	115.18
3	0.478	0.343	197.55
4	0.603	0.424	316.58
5	0.595	0.367	211.38
6	1.114	0.843	629.43
7	0.415	0.274	109.97

To compare both signals of current and spindle torque, the global current of the operation in each test was determined- Table 4.25.

Table 4.25: Global RMS current value for each test of OP15.

Test	Global Current (A)
1	6.051
2	3.423
3	6.022
4	8.434
5	4.887
6	8.765
7	4.569

As demonstrated by Figure 4.44, approximately, 58% of current variations are explained by torque changes. With values of torque this low, the sensibility of current measurement might not be enough to capture small variations, hence this lower linear correlation. This can hint at a limitation of torque usage to indicate current consumption in operations with low cutting effort.

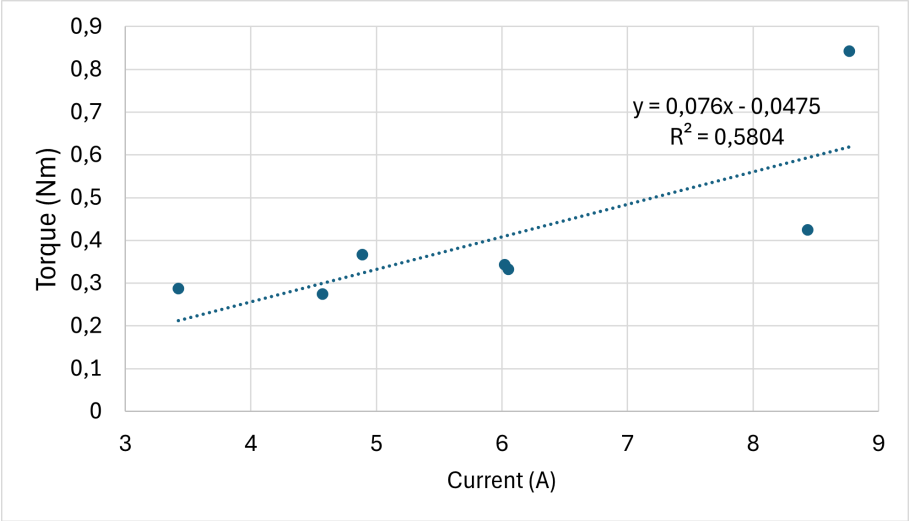


Figure 4.44: Global current (RMS) vs Average Torque- OP15.

Despite the lower correlation observed between RMS current and average torque ($R^2 \approx 0.58$), the relationship between current and torque-derived power was stronger ($R^2 \approx 0.71$), as Figure 4.45 illustrates. This discrepancy can be explained by the power equation, where the rotational speed influence can enhance the linear trend and lead to a stronger regression fit.

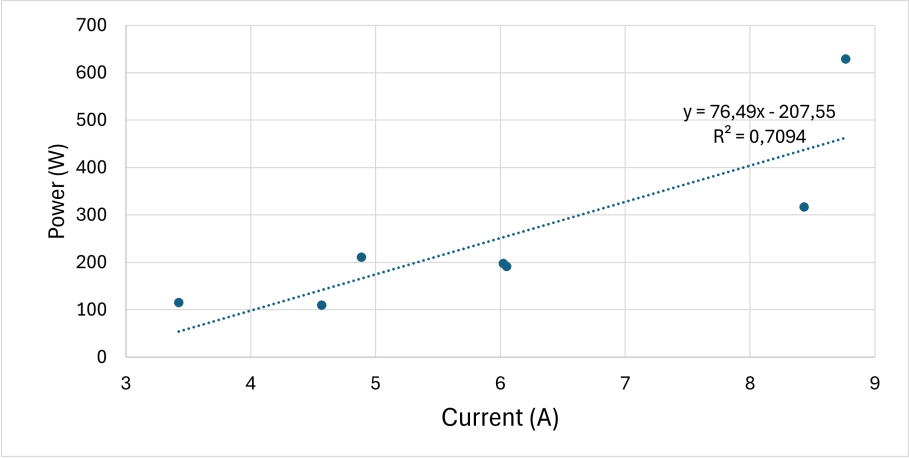


Figure 4.45: Global Current (RMS) vs Torque-derived Power- OP15.

At last, the relationship between cutting power and power determined with the torque was drawn. The good linear correlation present in Figure 4.46 demonstrates that most power variations can be explained by the cutting efforts ($R^2 \approx 0.75$). As such, the torque given by the machine is suitable to indicate cutting forces and, ultimately, tool wear.

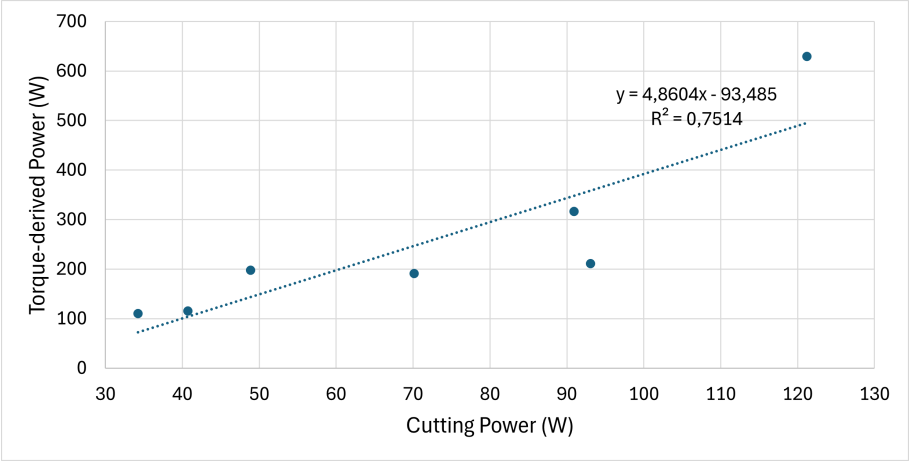


Figure 4.46: Cutting Power vs Torque-derived Power- OP15.

4.1.3.3 Idle Current

The idle current results of operation 15 are represented in Figure 4.49. Only the current between the roughing passes was considered as the final finishing steps are indistinguishable. Similar to the previous operations, there is variations between each test. These fluctuations might be due to spindle speed changes, caused by the variations of v_c. When the spindle moves at higher speed, it requires higher effort/energy to decelerate, hence the higher consumption of current.

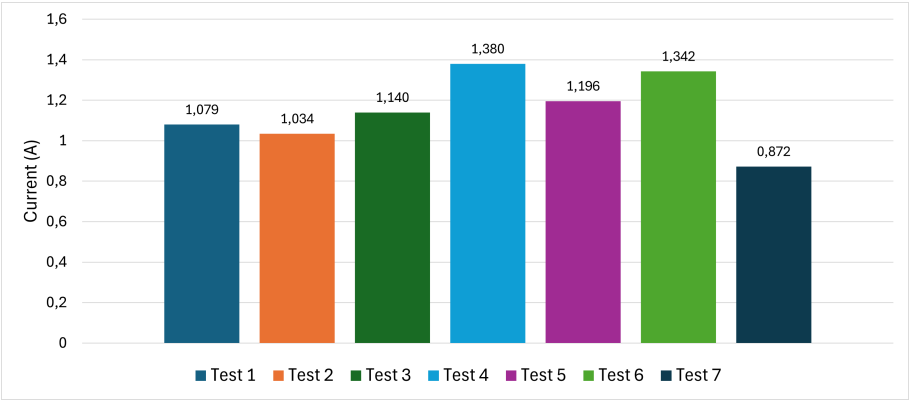


Figure 4.47: Idle current of each test of OP15.

The relationship between spindle speed and idle current was also obtained in order to understand if the differences observed between tests can be attributed to changes in v_c. As the plot shown in Figure 4.48 indicates, there is a strong linear correlation between these variables ($R^2 \approx 0.89$), reinforcing that the spindle speed has a significant impact in current consumption during idle time.

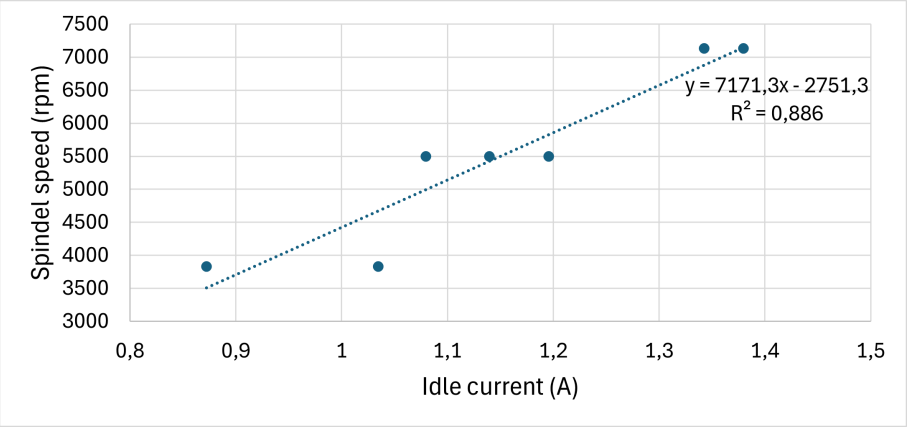


Figure 4.48: Spindle speed vs Idle current of OP15.

As Figure 4.49 indicates, the idle current is lower, but the difference between this and cutting current is smaller than what was observed for the other operations. Even though the tool experiences an increase in mechanical load during cutting, the overall current values are relatively small. The cutting strategy can also impact this moderate consumption of current since it involves multiple passes with continuous contact and smaller depths of cut. In addition, the finishing passes remove minimal material so the associated energy is similar to idle time. All these factors contribute to this lower difference between baseline current and current during cutting and help explain the inability of the clamps to capture finishing operations. Nevertheless, the increase of load is captured by the clamps, which reinforces the ability of the clamps to distinguish energy variation even though it is unable to capture finishing steps fluctuations.

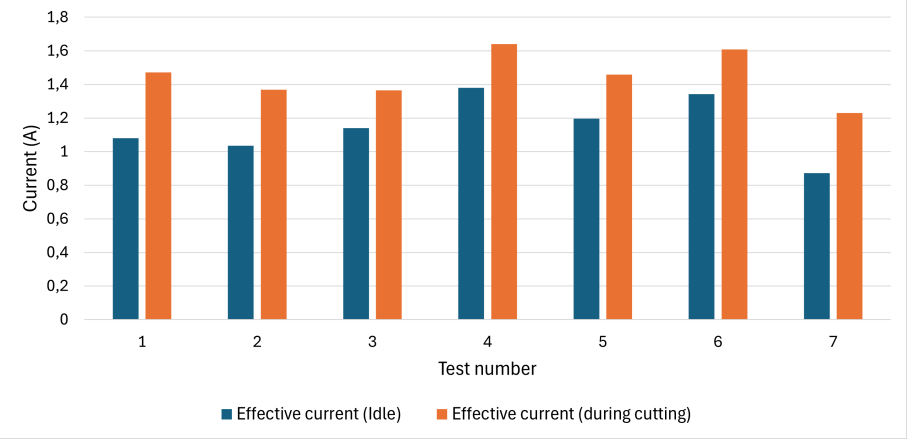


Figure 4.49: Comparison of the idle current and current during cutting of OP15.

4.1.4 Comparison between operations

This section presents a comparative analysis of the three selected operations in terms of electrical current measurements. The goal is to assess the viability of using current signals for process monitoring for different machining conditions.

Starting with the RMS current during cutting moments, expressed in Figure 4.50, OP1 stands out as the operation with the highest values. This reflects the aggressive cutting strategy and the usage of a larger diameter tool with variable depth of cuts. Larger and longer tools typically have higher contact areas, which results in higher cutting forces required to remove material. Moreover, the different a_p in each pass also increases the mechanical effort required.

Although the radial depth of cut changed within each pass for both OP13 and OP15, it did not produce as significant changes in force as the fluctuation of a_p. In addition, the lower diameter values also result in less required torque and the numerous tool steps enhance a uniform torque distribution which, in turn, results in lower current consumption. OP13 showed moderate current values, where the cutting parameters influence was well captured. In regards to OP15, performed with a 5 mm diameter tool, it presented the lowest results of current, as the material removed per pass was also lower. In general, tests 5 and 6 resulted in the highest values of current across all tests which is expected because of the increase of f_z and, consequently, the chip thickness.

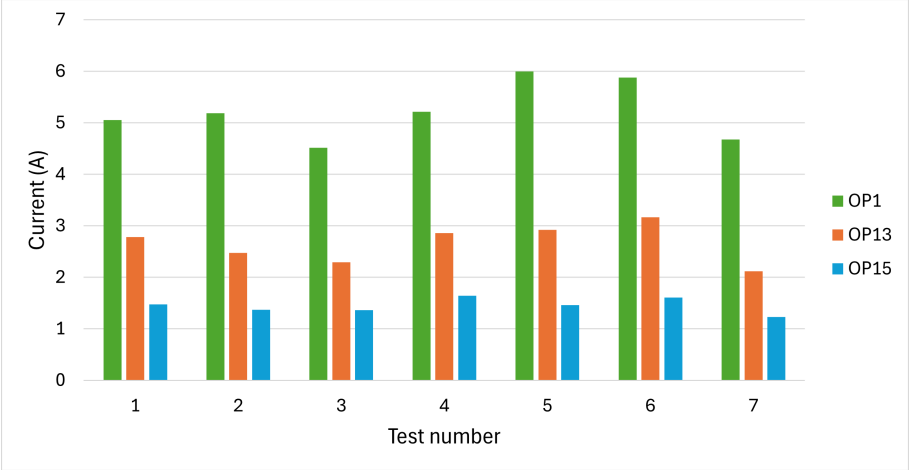


Figure 4.50: Comparison of the RMS current values.

In terms of average spindle torque- Figure 4.51- OP1 exhibited, once more, the highest values. The larger tool radius and robust constitution contribute to higher torque not only due to cutting forces but also due to the effort required to overcome rotational inertia. OP13 presented intermediate torque values, with good stability across tests, showing that torque followed the cutting load relatively well. This is also a consequence of increased number of tool passes that helps distribute load.

At last, OP15 recorded the lowest torque overall. In this operation, there is the consideration of two finishing passes that induce a really small load that contributes to the reduction of the average torque. Test 6 showed a significant increase, likely due to the influence of acceleration and deceleration effects rather than cutting force itself.

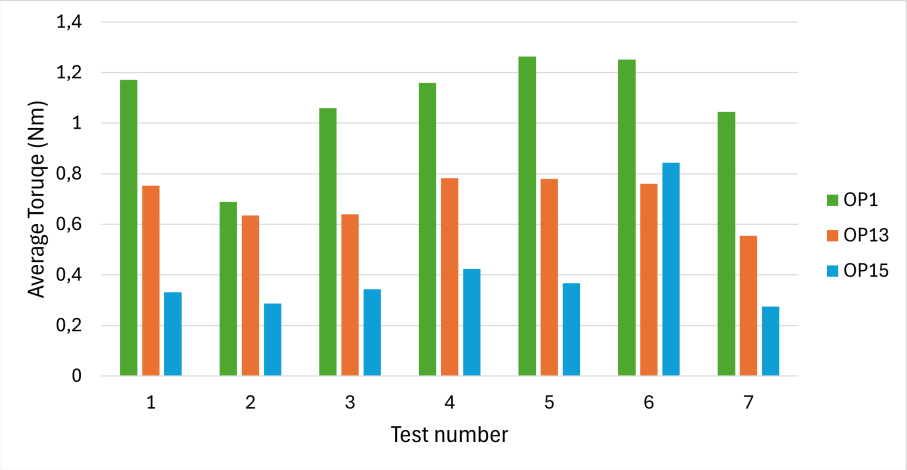


Figure 4.51: Comparison of the average torque.

When analysing the linear correlation of the current and the material removal rate, a linear trend was found in all three operations, as Figure 4.52 shows. OP13 has the strongest correlation ($R^2 \approx 0.91$). OP1 also demonstrated a good linear relationship, but more dispersion of data likely due to variable axial depth of cut. OP15 also indicated a solid response of the current signal of different MRRs. In general, these results indicate that the current signal obtained from the clamps is suitable to translate different volumes of removed material, which in turn is associated to the cutting loads involved. However, it is not possible to establish a single global relationship.

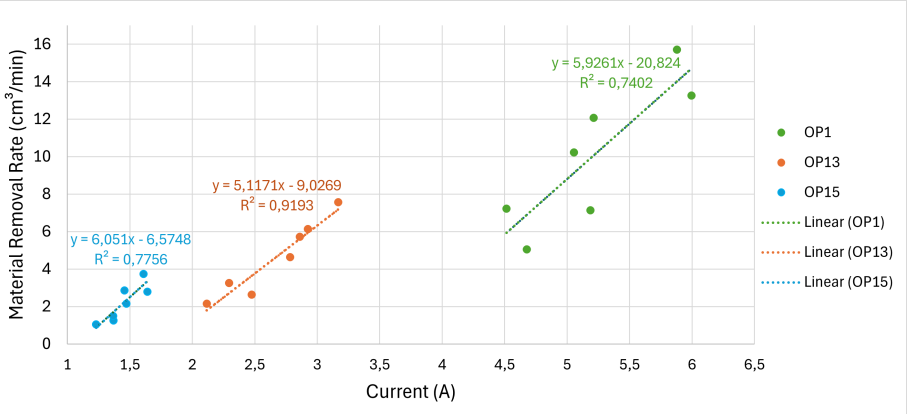


Figure 4.52: Comparison of the linear correlation of the current with the material removal rate of all tests.

Regarding the cutting power and measured current linear relationship, as Figure 4.53 indicates, OP13 has the strongest correlation. OP1 had the highest cutting power values, which is expected since it has the highest MRRs and torque, translating into higher cutting forces. OP15 also showed a solid relationship. In addition, despite the low range, OP15 showed a steeper slope, meaning that the current was responsive to smaller load variations. However, in this operation the limitation of distinguishing finishing passes is present.

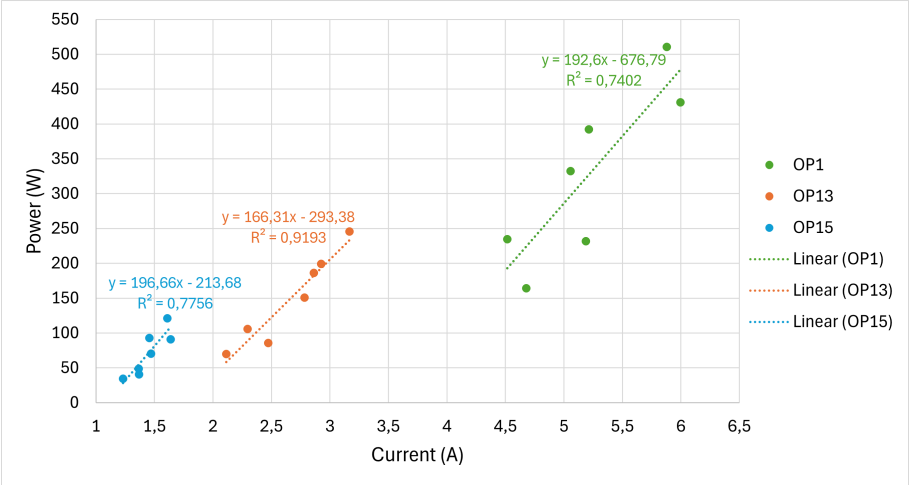


Figure 4.53: Comparison of the linear correlation of the current with cutting power of all tests.

When the power estimated form torque and spindle speed is compared with the cutting power, OP13 maintained a stronger correlation, while OP1 and OP15 have greater data dispersion. However, in general, the power estimated from the torque demonstrated that the machine's function is capable of indicating energy consumption during cutting, the corresponding cutting effort and, as consequence, can indicate tool wear in an indirect manner.

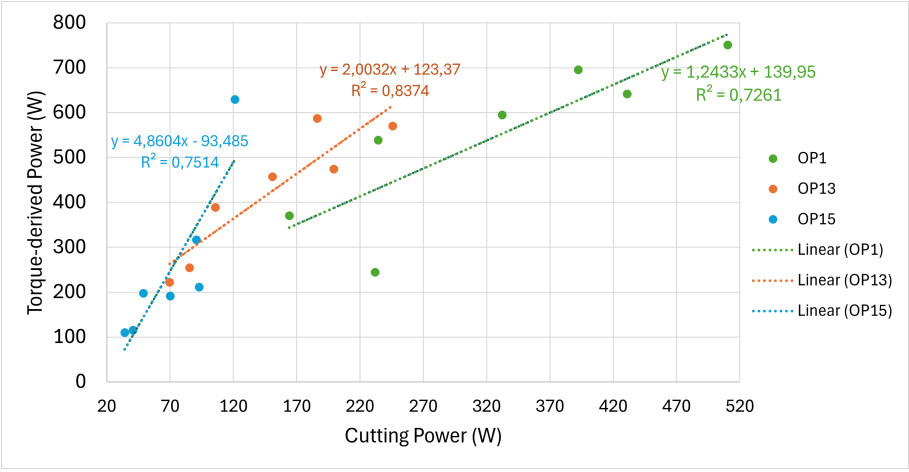


Figure 4.54: Comparison of the linear correlation of the global current with torque-derived power of all tests.

Finally, the idle current, represented in Figure 4.55, is relatively close between the three operations, which indicates that the machine conditions when not cutting are stable and the measurement system is consistent.

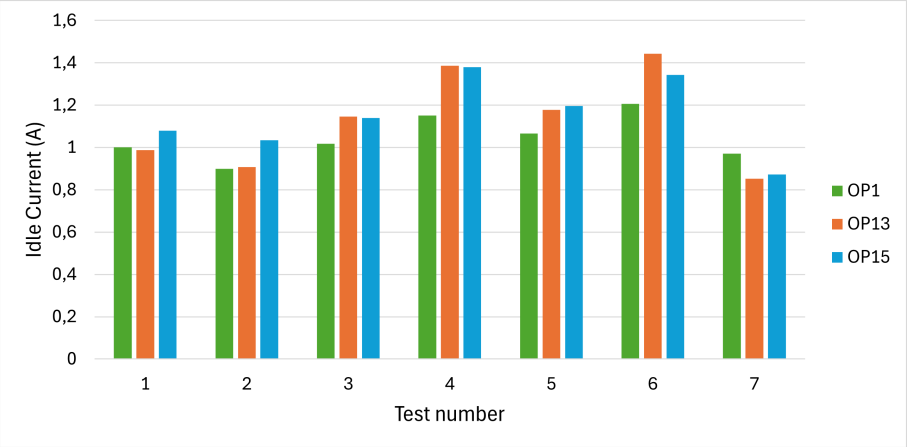


Figure 4.55: Comparison of the idle current of all operations.

When considering all the results together, there is a coherence between the different studied metrics. Operations that showed higher current consumption during cutting, also showed higher torque, cutting power and MRRs. OP1 demonstrates the capacity of current to reflect high-load conditions, though the influence of dynamic effects is more evident in the torque signal. OP13, in particular, maintained great linear correlations across all indicators, demonstrating that under stable cutting conditions, the current clamps reflect the process dynamics with efficiency. Finally, OP15, despite low absolute values, exhibits sensitivity in current response, but the close values between cutting and baseline current limits its applicability in process monitoring.

Overall, the trends observed across the different graphs support one another and reinforce the conclusion that the measured current is a reliable indicator of cutting performance. Torque data from the CNC spindle can be used to complement this information and be used as an indicator to predict tool wear.

4.2 Vibration Analysis

The study of vibration consisted on acceleration values acquired from an MEMS accelerometer. Then sensor's sampling rate was calculated for each operation and, in general, it resulted in 1500 Hz. This rate was calculated by, first, removing the repeated lines. Then, the time interval between consecutive points was determined and an average was applied to these intervals. The sampling rate is equal to the inverse of the average of times, as Equation 4.11 indicates.

$$\text{Acquisition rate} = \frac{1}{\Delta t}. \tag{4.11}$$

The raw data was stored in a .CSV file, registering the time, acceleration values in the three axes and acceleration of the resultant, as indicated by Figure 4.56.

Amplitude Y (m/s^2)	Amplitude Z (m/s^2)	Amplitude X (m/s^2	Resultant (m/s^2)	TimeStamp (us)	Time (s)
0,085738506	5,360092031	0,28527876	5,368363032	0	0
0,085738506	5,360092031	0,28527876	5,368363032	542	0,00054
0,16716917	5,125380117	0,23258833	5,133377466	1086	0,00109
0,16716917	5,125380117	0,23258833	5,133377466	2854	0,00285
0,358770732	4,55057543	0,012246533	4,564712823	3968	0,00397

Figure 4.56: Raw data of the acceleration from the .CSV file.

Similar to the current processing, the data was treated using the root mean square (RMS) method, applied over a window with fixed number of points. The number of points corresponds to a time interval. Additionally, different RMS windows were explored to find the one that best translated the signal with less noise. The best window corresponded to 500 points that corresponds, in all operations, to a time segment of, approximately, 0.33 seconds.

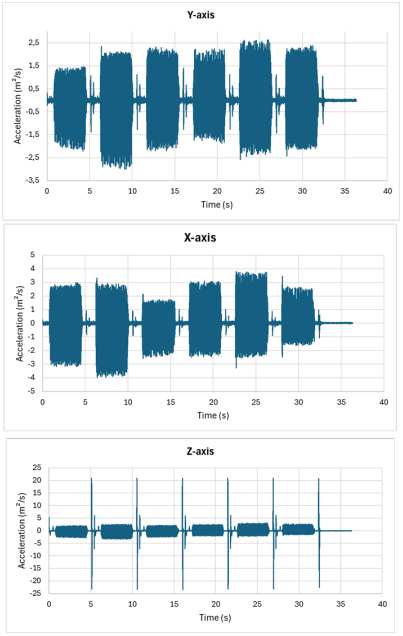
All the three axes and resultant were treated and analysed, obtaining the RMS average value for each. In addition, the impact of using different RMS windows in those results were also evaluated, but led to the conclusion that the values are very similar using different number of points.

During the trials, the sensor began to exhibit an increase of instability around the zero reference, despite repeated calibration attempts. This issue caused a drift effect, where the signal gradually deviates from the baseline. To mitigate this effect and compensate for the offset present in the acceleration signals, the mean value (offset) of each axis was determined and subtracted from the raw data.

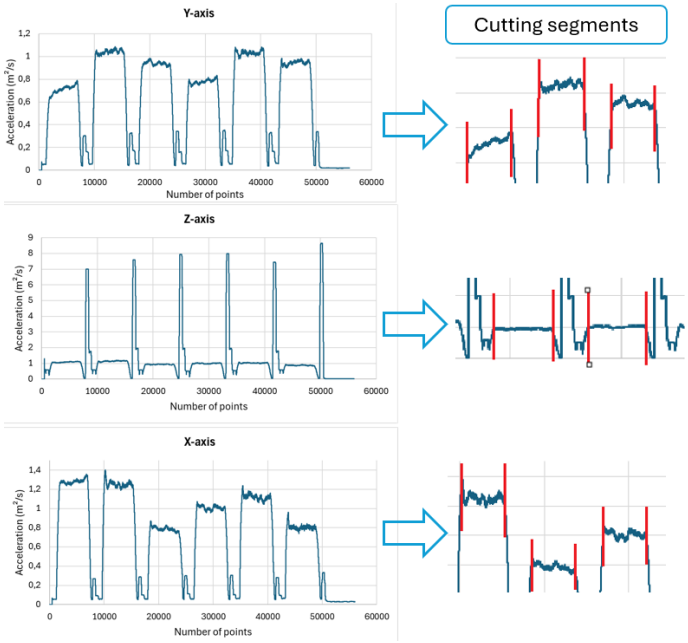
Moreover, in the last two tests, involving variations in both cutting speed and feed per tooth, the sensor froze intermittently. As a result, these two tests could not be evaluated and were excluded from the vibration analysis. The evaluation is structured by machining operation and, within each, all tests.

4.2.1 Operation 1

The acceleration values over time was plotted for each test and is shown in Figure 4.57a. The symmetry indicates that there is no data saturation. Then, the plots of the RMS method are also represented in Figure 4.57b, where the cutting segments are highlighted. In these graphs it is possible to observe the ascendant and descendant movement of the tools and each tool step executed. In this operation, 6 passes are distinguished. All the RMS acceleration plots, of all tests of OP1, can be found in Appendix E.



(a) Vibration signal over time of test 1-OP1.



(b) RMS acceleration values profile of test 1-OP1.

Figure 4.57: Vibration signal and corresponding RMS profile during OP1 of test 1.

To evaluate the vibration levels during cutting, the RMS value of each segment was calculated (Figure 4.57b) and a global representation of the operation was determined applying the average of the means of each segments. The results are expressed in Table 4.26 and Figure 4.58 illustrates the graph comparing the RMS current of each test of Operation 1.

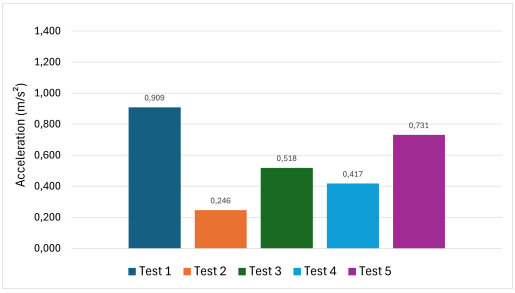
Table 4.26: Acceleration RMS values and corresponding percentage variation in X, Y and Z axes for each test of OP1.

Test	RMS Y-axis (m/s^2)	RMS Z-axis (m/s^2)	RMS X-axis (m/s^2)	% Variation Y-axis	% Variation Z-axis	% Variation X-axis
1	0.909	1.009	1.039	0%	0%	0%
2	0.246	0.327	1.151	-72.91%	-67.58%	+10.77%
3	0.518	0.554	0.555	-42.95%	-45.06%	-46.57%
4	0.417	0.568	0.740	-54.08%	-43.74%	-28.79%
5	0.731	0.631	0.736	-19.59%	-37.51%	-29.22%

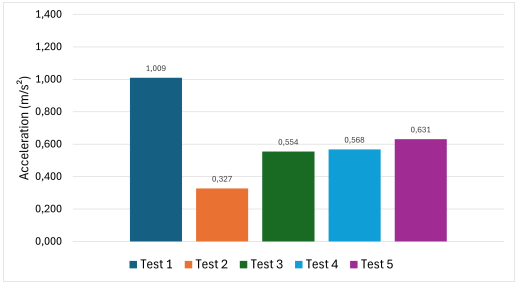
The X-axis (Figure 4.58c) is perpendicular to the tool axis and feed direction so, because this operation is a peripheral roughing, as expected, it presents the highest values of acceleration. The Y-axis (Figure 4.58a) is the same direction as the feed, where the stiffness of the tool dominates, observing the lowest results of vibration. At last, Z-axis (Figure 4.58b) corresponds to the tool axis, showcasing the most moderate values of all axes.

In general, all parameter variations resulted in decreased vibration in regards of the reference test (number 1), expect in test 2. The decrease of v_c increased acceleration values but only for the X-axis. Test 3 has a more uniform decrease of acceleration in all axes, highlighting good stability even though the cutting time increases. Test 4 demonstrated moderate and well-distributed

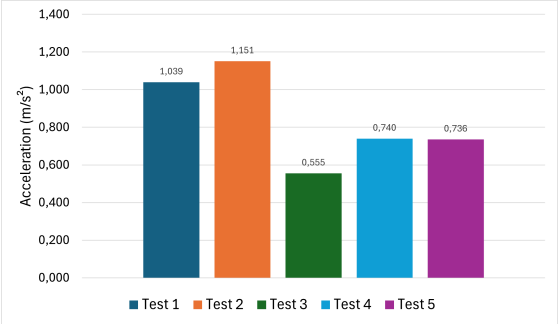
accelerations, representing an efficient cut without compromising stability. At last, test 5 showed an increase in Y and Z axes but still lower than the reference trial.



(a) Y-axis.



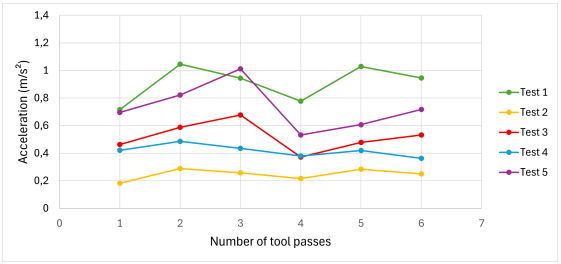
(b) Z-axis.



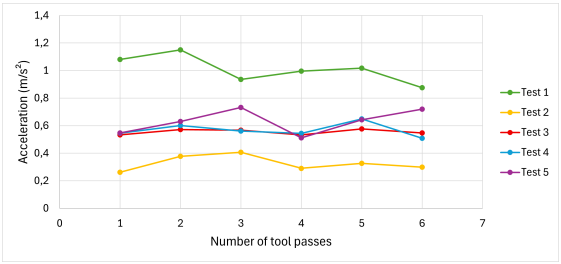
(c) X-axis.

Figure 4.58: Acceleration values in each individual axis- OP1.

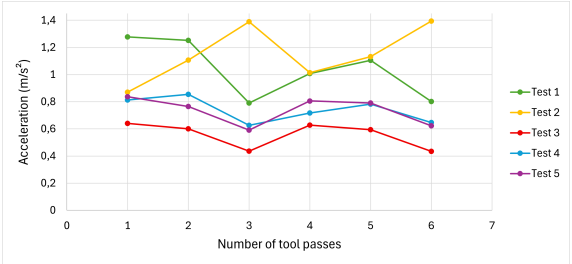
The acceleration values for each tool pass was also analysed in order to understand if this sensor, like the current clamps, is sensible to variations of the depth of cut. The results are demonstrated in Figure 4.59, where the evolution in each axis is distinguished.



(a) Y-axis.



(b) Z-axis.



(c) X-axis.

Figure 4.59: Acceleration values of each tool pass of the three axes of OP1.

The behaviour differs for each axis and, within the same direction, it varies from test to test. As such, it is harder to define a pattern with vibration signals. Nevertheless, there is a representation of acceleration changing with the different depths of cut, a_p. In both Y and Z axis, the vibration increases with the increase of a_p, while in X-axis there is a decrease (expect for test 2).

In addition to the individual analysis of axes, the resultant was also calculated. This variable is the combination of the three acceleration components, according to Equation 4.12.

$$a_R = \sqrt{a_x^2 + a_y^2 + a_z^2} \tag{4.12}$$

This approach allows to obtain a global scalar measure of the vibrations, particularly important to compare the global impact of different cutting parameters. The resultant facilitates the comparison between tests and detection of patterns. All the plots representing the evolution of the RMS resultant values, for all tests of OP1, can be consulted in Appendix F. The resultant values of each trial of operation one are represented in Figure 4.60. The results show that the reduction of f_z, test 3, and the increase of v_c, test 4, produce the highest decrease of vibration.

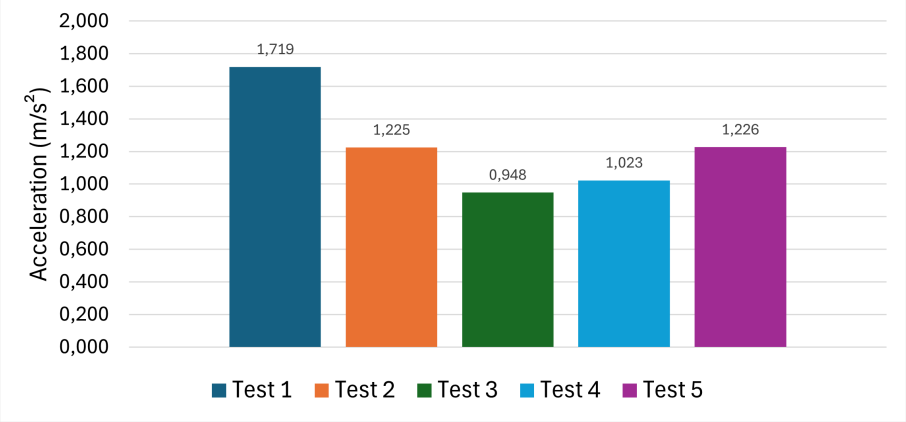


Figure 4.60: Acceleration values of the resultant of OP1.

The decrease of vibration with the increase of v_c is typically observed in chatter stability lobes, that have the goal of optimizing the maximum depth of cut, using the maximum spindle speed. The chatter typically represents the spindle speed, n, and the depth of cut, a_p, or chip width, b. Figure 4.61 exemplifies a common chatter stability, where the intersection between different lobes define a chatter line. Only points bellow this line are considered stable [82].

Cutting parameter variations create different stability lobes and the junction of several lobes define the limit between stable and unstable cutting conditions for different spindle speeds [50]. Vineet Paliwal et al. [50] showed that higher spindle speeds increase the critical depth of cut value where vibration does not occur. This phenomenon happened at 12000 rpm, where the stability zone shifted and higher a_p were sustained. This means that the stability of the process does not vary linearly with the increase of v_c. In fact, higher values can result in higher stability, as observed for OP1.

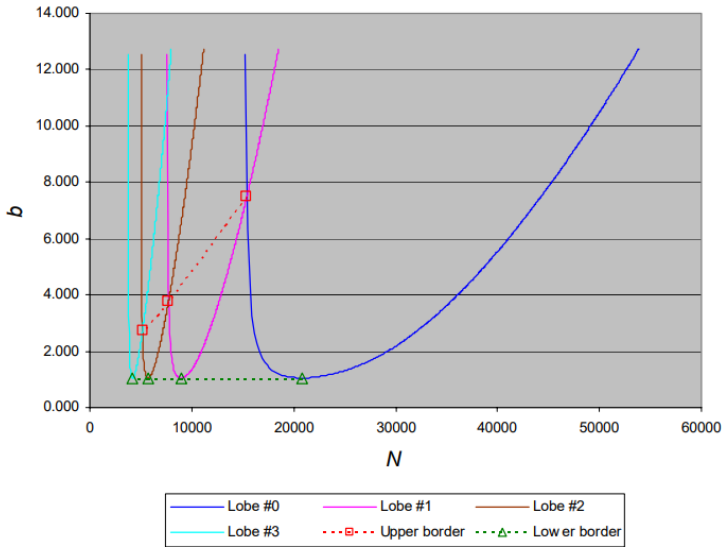


Figure 4.61: Example of a chatter stability lobe [82].

Each tool pass was also investigated and the corresponding evolution of vibration data is plotted in Figure 4.62, where all tests are compiled. Overall, the second and fifth passes produce the highest value of acceleration. Additionally, the behaviour is similar to the X-axis, reinforcing the conclusion that this is the direction prone to the most vibrations, while axes Y and Z maintain more stability. Tests 3 and 4 stand out as the most stable in a global view, while tests 1 and 2 have the highest fluctuations. As such, it can be affirmed that, in this operation, increasing v_c reduces vibrations.

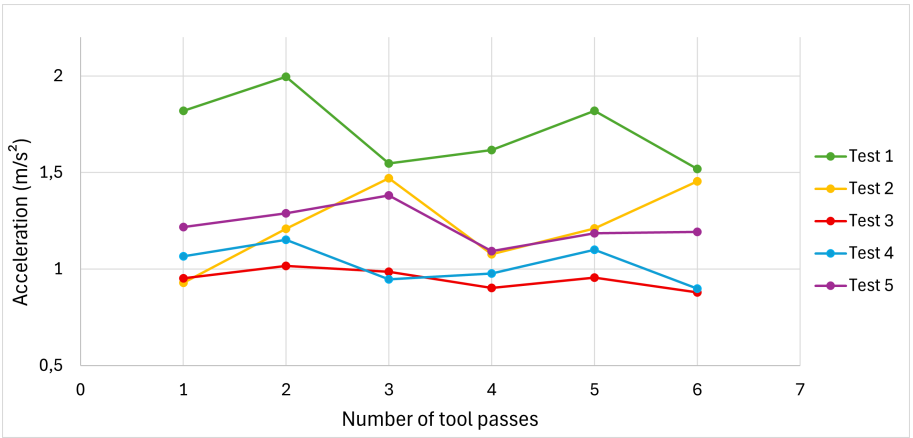


Figure 4.62: Variation of the resultant acceleration values for each tool pass and for all tests- OP1.

Another important analysis is to understand if the scalar of the axis X and Y produces higher vibration levels than axis Z. In most milling operations, the main load components are in the X and Y direction, corresponding to the perpendicular to the feed and main feed direction of the tool, respectively. As such, it is expect that these axes have more dynamic oscillations, as the Z direction is the spindle axis where the load is lower. Therefore, if the vibration measure in Z is

systematically higher than the scalar X + Y, it might indicate poor measurement of accelerations, wrong orientation of the accelerometer or noise. The results of the acceleration of the X and Y axes combined are represented in Figure 4.63 and compared with the values of the Z-axis.

With this representation, it is possible to conclude that the loads responsible for most of the dynamic excitations are, as predicted, in the direction of the feed and perpendicular to it. The lower vibration in the Z-axis indicates that axial forces are less significant and that the spindle remains relatively stable during the operation. It also confirms that the sensor is correctly placed and the acceleration signals are suitable to translate process vibrations.

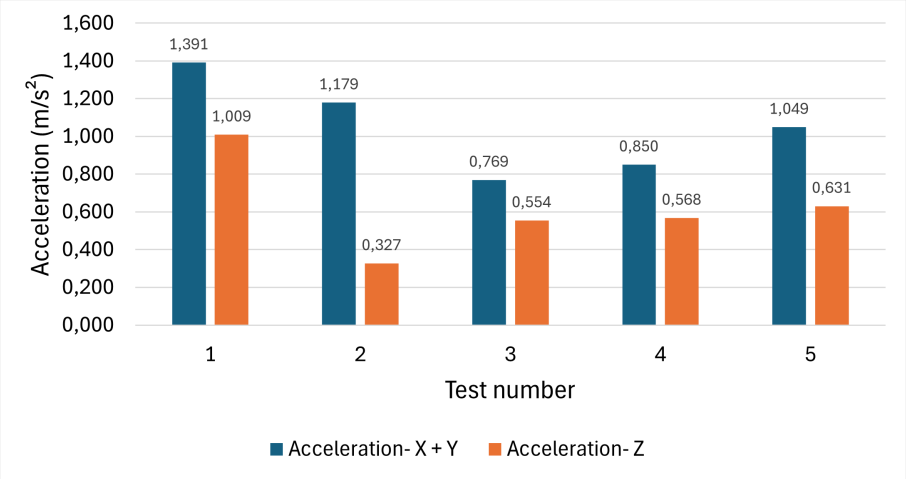


Figure 4.63: Comparison of the RMS acceleration values of the scalar X + Y with the Z axis- OP1.

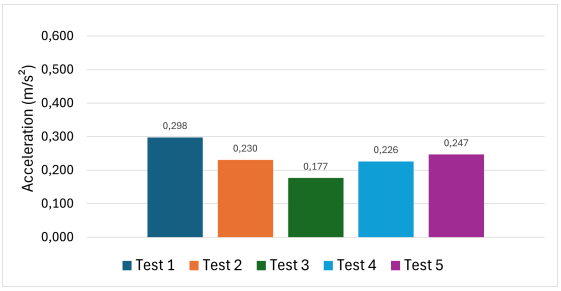
To sum up, the analysis of the individual acceleration components showed that the X-axis is the one that records the highest vibration levels during operation 1. This indicates that lateral forces are the main reason for the dynamic oscillation of the system, which can lead to tool bending. Evaluating the results of both individual axis and the corresponding resultant it can also be concluded that the reference test 1 is the most unstable and all the cutting parameters variation promoted a reduction of vibrations. However, the decrease of v_c led to a significant increase of vibration in the X-axis and showed the highest fluctuations during tool passes. As such, this is one of the most unstable conditions. On the other hand, tests 3 and 4 promote stability, resulting in decreased vibration levels and low variations in each tool pass.

4.2.2 Operation 13

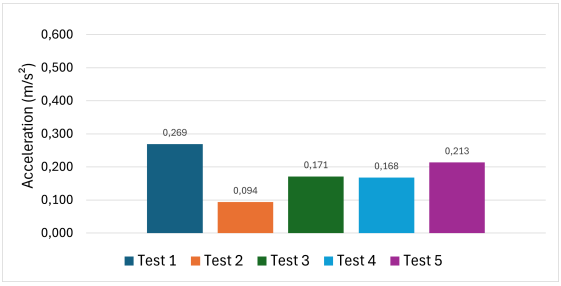
The same analysis methodology previously demonstrated was applied for this operation. The acceleration of each component (X,Y and Z) and the percentage variation are listed in Table 4.27 and a comparison of the results between trials is represented in Figure 4.64. All the RMS acceleration plots, of all tests of OP13, can be found in Appendix E.

Table 4.27: Acceleration RMS values and corresponding percentage variation in X, Y and Z axes for each test of OP13.

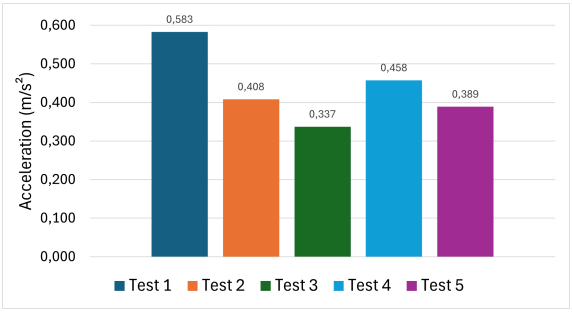
Test	RMS Y-axis (m/s^2)	RMS Z-axis (m/s^2)	RMS X-axis (m/s^2)	% Variation Y-axis	% Variation Z-axis	% Variation X-axis
1	0.298	0.269	0.583	0.00%	0.00%	0.00%
2	0.230	0.094	0.408	-22.61%	-65.12%	-29.96%
3	0.177	0.171	0.337	-40.73%	-36.41%	-42.14%
4	0.226	0.168	0.458	-24.10%	-37.61%	-21.51%
5	0.247	0.213	0.389	-17.22%	-20.74%	-33.26%



(a) Y-axis.



(b) Z-axis.



(c) X-axis.

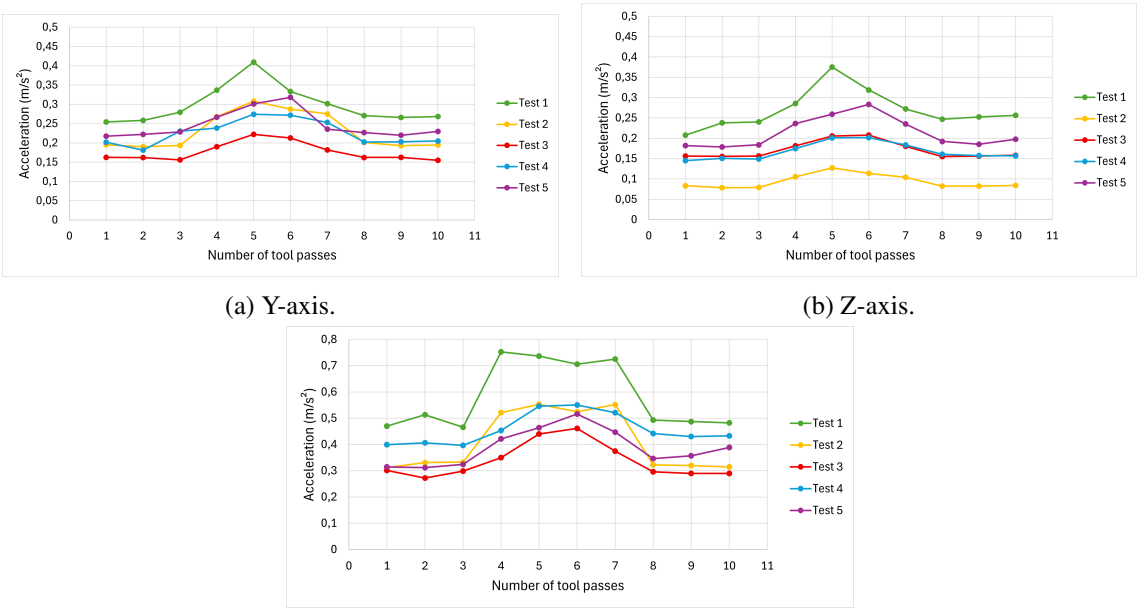
Figure 4.64: Acceleration values in each individual axis- OP13.

The orthogonal direction to the feed and tool axis, X, has the highest level of vibrations, where the reference test 1 is, once again, the most unstable. Axes Y and Z have similar results, with the first experiencing higher levels. This is what is expected since Z corresponds to the spindles axis, usually under lower cutting loads. Moreover, tests 2 and 4 produce higher acceleration values than tests 3 and 5. In this operation, the decrease and increase of v_c had similar impact on vibrations levels and the variation of f_z promoted stability.

During this operation, there is a time segment where the tool encounters a pre-drilled hole that caused a decrease of current. So, it is important to understand how the tool behaves in terms of vibration under this situation. The evolution of acceleration in each tool pass is represented in Figure 4.65, where all the tests are represented.

From passes 4 to 7 there is a general increase in vibration levels, particularly in the X direction, that translates this transition of full engagement with the material to void. This increase results from the loss of support material, which causes a sudden change in the cutting forces, enhancing dynamic excitation. In addition, there are some moments where only part of the cutting edge is in

contact with the material which causes load imbalance and, as consequence, increased vibration. These results demonstrate that the sensor is capable of detecting changes in tool engagement and efficiently translate the tool's response.



(a) Y-axis.

(b) Z-axis.

(c) X-axis.

Figure 4.65: Acceleration values of each tool pass of the three axes of OP13.

When evaluating the resultant, which is a global representation of vibration behaviour, the previous conclusions are reinforced. All the plots representing the evolution of the RMS resultant values, for all tests of OP13, can be consulted in Appendix F. As Figure 4.66 shows, the increase or decrease of v_c produce similar results. The decrease of f_z results in the lower vibration levels, followed by the decrease of v_c. Increasing v_c or f_z showcase higher acceleration values.

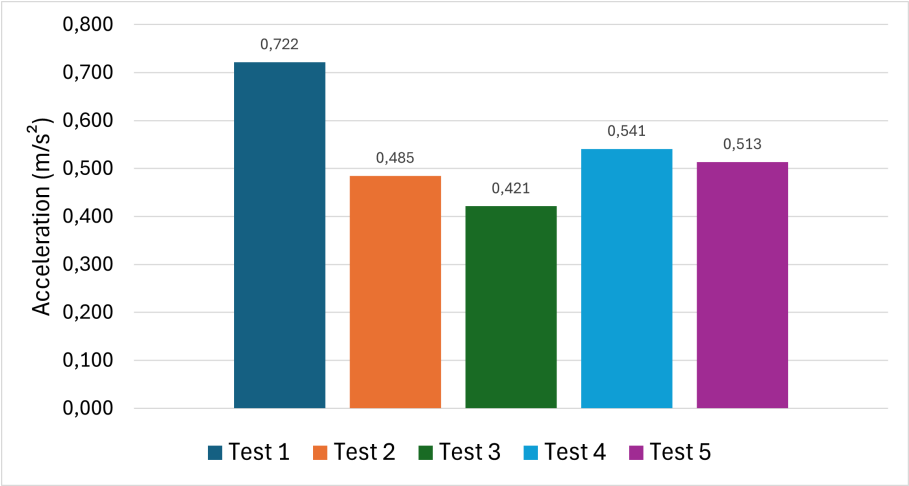


Figure 4.66: Acceleration values of each tool pass of the three axes of OP13.

Further analysing the acceleration values of the resultant- Figure 4.67- it can be observed that all trials present an increased vibration in passes 4 to 7, having a maximum peak in passes 5 or 6. This is directly related to the tool encounter with the pre-drilled hole. Test 1 has the highest values of dynamic excitation, while test 3 can be highlighted for its good stability.

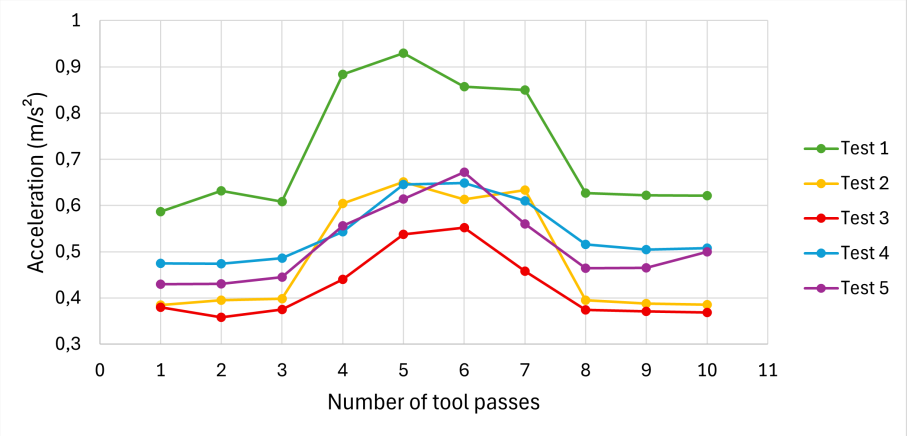


Figure 4.67: Variation of the resultant acceleration values for each tool pass and for all tests-OP13.

To confirm the data viability and confirm the forces that are mostly responsible for vibration, the resultant of the scalar X + Y, represented in Figure 4.68, was compared to the results of the Z direction. This graphic shows that the vibration levels of the Z direction are significantly lower. This means that the forces responsible for most of vibration levels are the tangential and radial forces. In this operation, there is no observation of excessive unbalance at the spindle (Z axis).

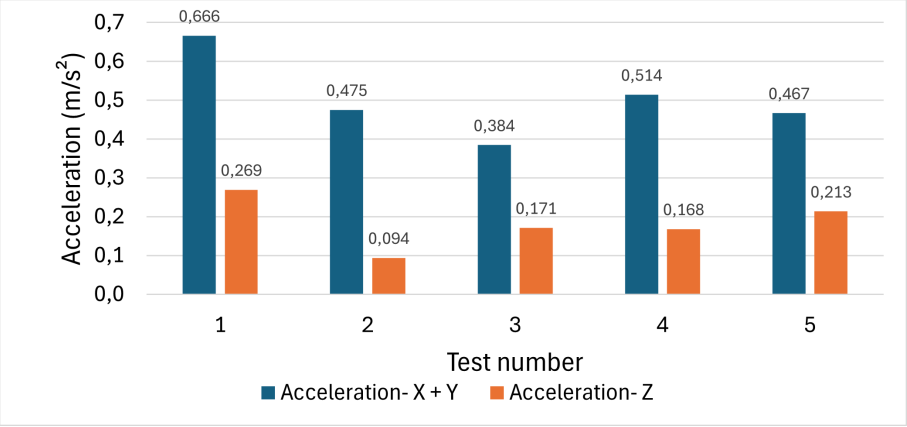


Figure 4.68: Comparison of the RMS acceleration values of the scalar X + Y with the Z axis-OP13.

In summary, the vibration analysis confirmed the ability of the sensor in detecting dynamic oscillations related to tool engagement, capturing an increase in vibration levels between passes 4 to 7 that coincides with the transition over a pre-drilled hole. Furthermore, the X-axis showed, in general, the highest RMS values of acceleration, where lateral forces are dominant. Among the cutting parameters variation, the reduction of f_z (test 3) demonstrated superior stability. The

resultant acceleration results are aligned with these observations, reinforcing the sensor's ability to reflect process stability and detect changes. Furthermore, comparing the scalar X + Y, it is possible to confirm that most of the dynamic excitations are from lateral cutting forces.

4.2.3 Operation 15

During the fifth trial of operation 15, the sensor began to froze. As such, the raw data of test number 5 only captured the begging of the operation which led to the disregard of this test. To sum up, in this operation only 4 tests are going to be studied. Moreover, the MEMS sensor captured both roughing and finishing passes, resulting in the registration of 15 passes in total.

Table 4.28 presents the results of the RMS values for each test of operation 15. In Appendix F, RMS acceleration plots of all tests of OP1 can be found.

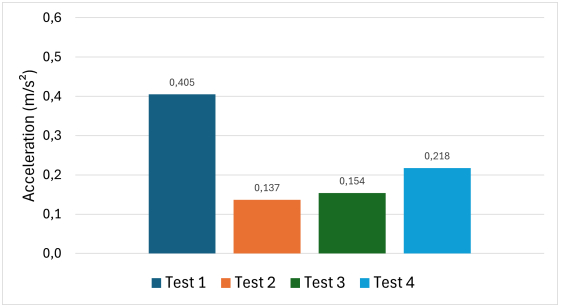
Table 4.28: Acceleration RMS values and corresponding percentage variation in X, Y and Z axes for each test of OP15.

Test	RMS Y-axis (m/s^2)	RMS Z-axis (m/s^2)	RMS X-axis (m/s^2)	% Variation Y-axis	% Variation Z-axis	% Variation X-axis
1	0.405	0.370	0.434	0.00%	0.00%	0.00%
2	0.137	0.125	0.419	-66.26%	-66.19%	-3.37%
3	0.154	0.214	0.328	-62.00%	-42.23%	-24.41%
4	0.218	0.223	0.530	-46.28%	-39.90%	+22.18%

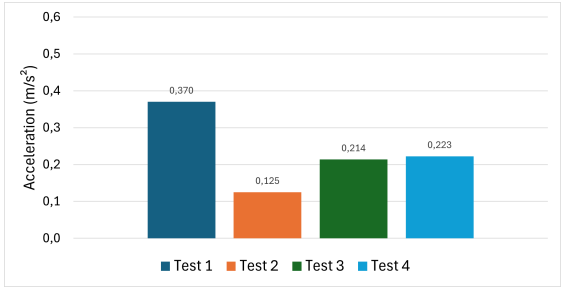
The comparison between tests is also plotted in Figure 4.69. These results indicate that the reduction of v_c significantly reduced vibrations in Y and Z directions, but did not provoke significant changes in the X direction. On the other hand, the increase of v_c increased the vibration levels in regards to the test of reference in the X-axis, while reducing dynamic excitations in the other directions. Test 3 had the least significant fluctuations between different axis.

In addition, the direction with the highest levels of vibrations corresponds, once more, to the X-axis. However, in this operation the difference of values between the different components is not as significant as observed for the other operations. The Y-axis followed and the Z-axis has, in general, the lowest results of vibration.

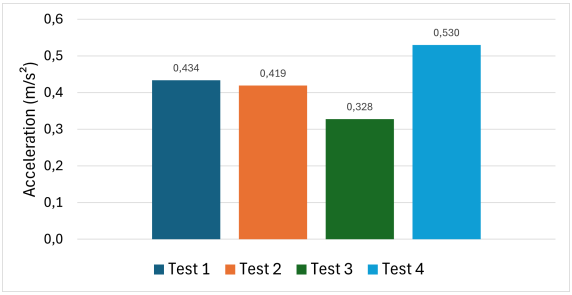
In this operation, there is also the interception of the tool and a pre-drilled hole. The sensor was capable of detecting this transition across all axes, as Figure 4.70 illustrates, marking an increase of vibration levels between passes 6 to 10, particularly in the Y axis. Z-axis appears, once again, as the most stable.



(a) Y-axis.

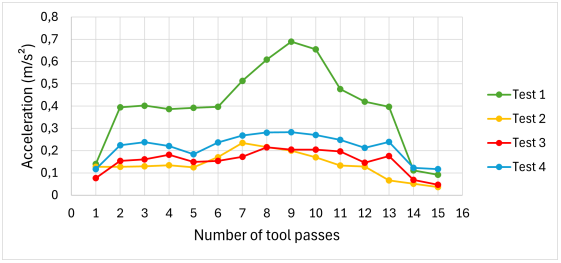


(b) Z-axis.

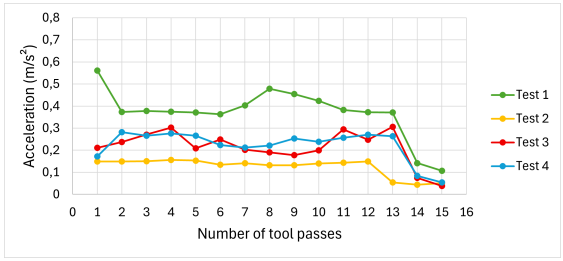


(c) X-axis.

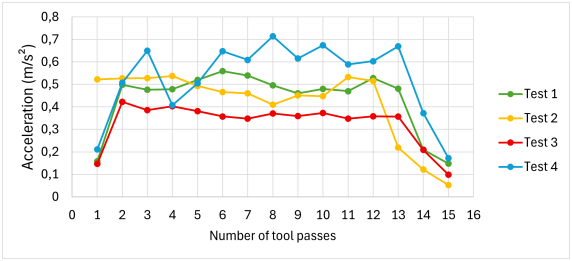
Figure 4.69: Acceleration values in each individual axis- OP15.



(a) Y-axis.



(b) Z-axis.



(c) X-axis.

Figure 4.70: Acceleration values of each tool pass of the three axes of OP13.

Analysing all the components combined in the resultant (Figure 4.71), it is possible to confirm the previous results. In this case, the increase of v_c led to a significant increase of vibrations while its reduction enhanced stability. The reduction of f_z also promotes stability. The plots of each test of OP15, representing the evolution of the RMS resultant values, can be consulted in Appendix F.

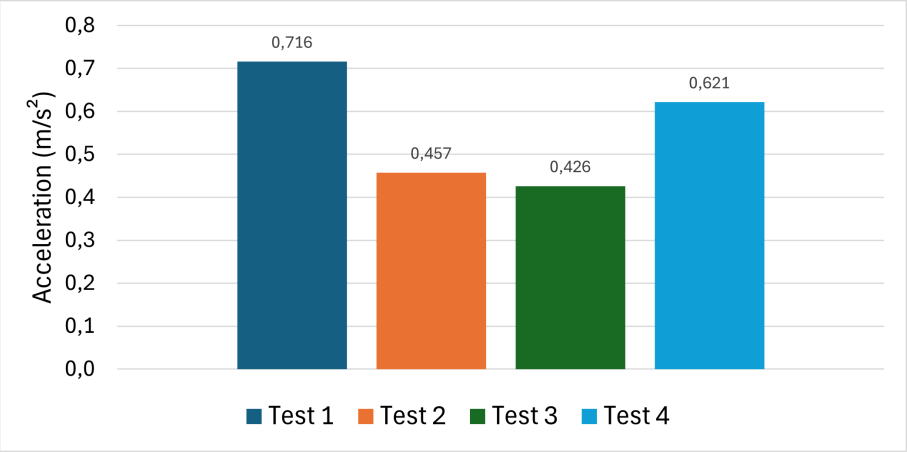


Figure 4.71: Acceleration values of the resultant of OP15.

Regarding tool passes, the plot of the resultant, demonstrated in Figure 4.72, indicates a more distinguishable pattern across tests, marking the intersection of the tool with void as an increase of vibration from passes 6 to 10. The decrease of f_z, test 3, did not show high fluctuations as the other tests, standing out as the most stable condition of all. Tests 1 and 4 are highlighted as the most prone to vibration.

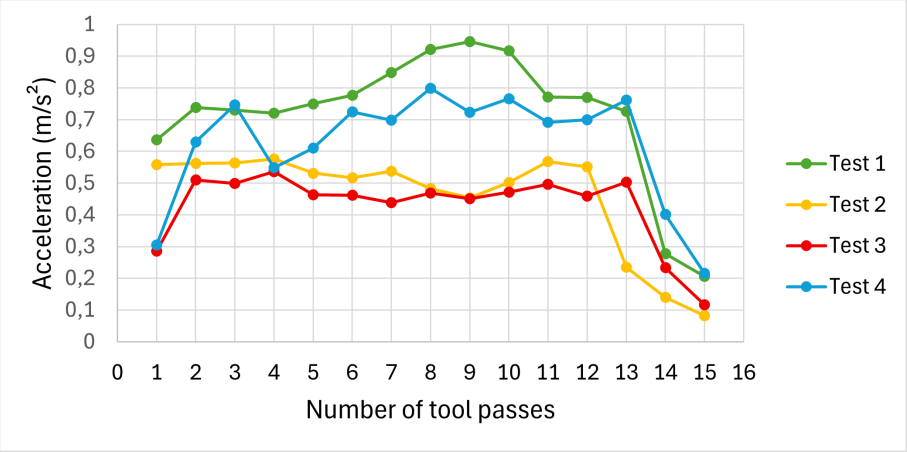


Figure 4.72: Variation of the resultant acceleration for each tool pass and for all tests- OP15.

To further investigate the dominant cutting forces components, a comparison between the scalar X and Y was compared to the spindle direction, Z. Figure 4.73 represents the graphic comparing both components. This plot shows that the scalar of X + Y has higher vibration levels than the Z direction, confirming that the dominant cutting forces, responsible for dynamic oscillations, are the tangential and radial directions. Z-axis, once again, remains more stable during testing.

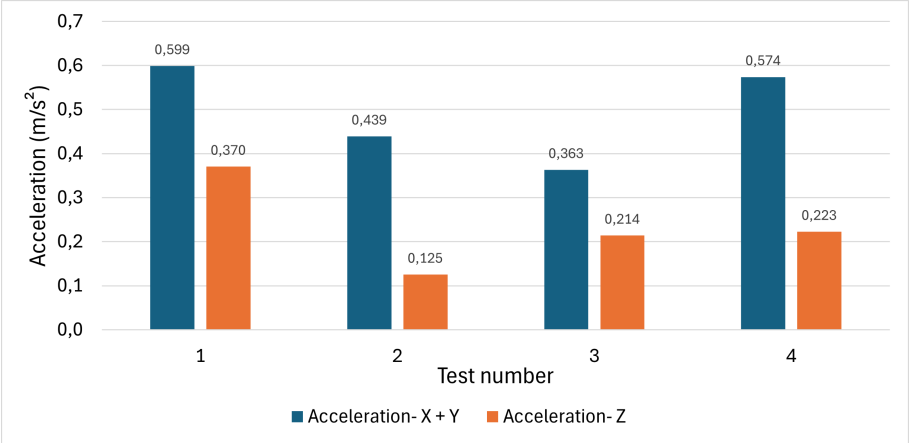


Figure 4.73: Comparison of the RMS acceleration values of the scalar X + Y with the Z axis- OP15.

Although this analysis was limited to four tests due to sensor failure, the recorded data revealed that the X-axis was the direction with the highest dynamic excitations. The reduction of v_c (test 2) significantly decrease vibration in the Y and Z axes, while increasing it in the X-axis. Moreover, the decrease of f_z can be highlighted as the most stable trial. There was also an increase in vibration levels between where the intersection of the tool with a pre-existing hole happened. Unlike the current signals, this sensor is capable of detecting finishing operations even though the acceleration values are smaller. Overall, this results reinforce the ability of this sensor to detect variations under different process conditions.

4.2.4 Comparison between operations

In order to compare the behaviour of the different tools in each operation, the values of acceleration of the resultant were compared- Figure 4.74. OP1 stood out as the operation with the highest vibration levels, which is expected since it is a demanding roughing operation with a longer tool that is, typically, more prone to vibration. The gradual increase of a_p also contributes to higher vibrations since the tool is under more demanding loads. OP13 and OP15 have similar levels of dynamic excitation, with the latest showing lower values overall. Moreover, higher number of tool steps also helps achieve a more uniform load distribution, which contributes to stability.

Test 1 exhibits the worst performance in terms of stability across all operations, while test 3 produces a reduction in vibration levels and provides the most stability. Typically, the decrease of v_c produces more dynamic excitations in the X-axis, reinforcing that the increasing speed does not necessarily increase vibration.

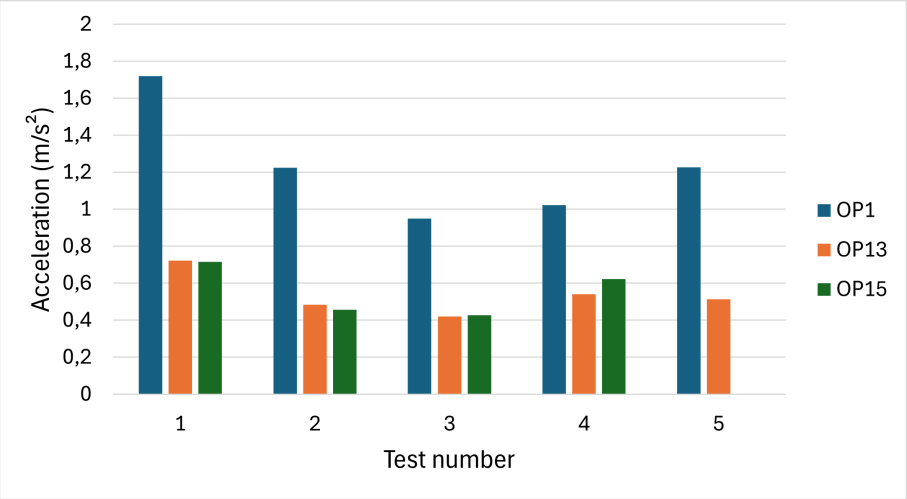


Figure 4.74: Comparison of the resultant acceleration values of all operations.

To sum up, this sensor is capable of translating process dynamic oscillations under different types of operations, tools and cutting parameters. It is also capable of distinguishing finishing operations, unlike the current signals. Additionally, it can represent different tool engagements and detect different fluctuations. From the different cutting data, the reduction of the feed per tooth is highlighted as the best adjustment to minimise vibration. However, when evaluating individual directions, it is harder to form a pattern and find a tendency of vibration evolution with different cutting parameters. The milling process is highly dynamic, and multiple variables can influence each axis differently. As a result, changes in cutting conditions may affect each vibration component in different ways, making it difficult to correlate parameter variations with specific directional responses.

In addition, the persistence of signal drift and offset despite calibration, along with the sensor's tendency to freeze throughout the tests, highlights the limitations of the used setup. These issues translate the need for more robust signal processing or alternative sensing hardware to ensure reliability and prevent compromising future trials and readings.

4.3 Quality Control

As part of the validation stage, quality control was performed to ensure the dimensional and geometrical accuracy of the machined parts. For this purpose, inspection reports for each test were generated, including deviation values relative to the nominal dimensions and roundness of the holes. The same features were measured across multiple planes to verify geometric consistency. This type of information enables the identification of deviations caused by tool wear, process instabilities or unsuitable strategies. All detailed reports can be found in Appendix G.

In this section, the analysis of the deviations for each monitored test, focusing on the features directly affected by the variation of parameters. Additionally, an overall evaluation of the workpiece is discussed, emphasising critical operations such as drilling.

Test number 7, involving the decrease of both v_c and f_z, is not included in the reports because the reamer broke inside the D3.28 hole, preventing the part to be submitted to the Machine Coordinate System. Instead, a manual evaluation using the caliper and the projector was conducted. The reamer had been previously used in several operations, so the likely cause of breakage was excessive tool wear rather than parameter variation.

An initial workpiece (number 0) was also produced to validate the machining strategy. Although not measured in the machine coordinate system due to equipment unavailability, quality control revealed that most dimensions were within tolerance, except for hole D4.04, where the No-Go gauge entered. The issue was most likely improper pilot drilling, that was not guiding the subsequent tool properly, resulting in a deviation of the main drill and enlarging of the hole. As a result, the pilot drill was removed from the process, and the strategy was adapted accordingly, as presented in Chapter 3.3.2. Additionally, the excessive accumulation of chips complicated inspection. To mitigate this problem, the chamfer was increased to 0.02, improving edge quality.

Table 4.29 shows the dimensional deviation of selected features for each test. These values represent the difference between measured and nominal dimensions. To assess overall performance, five metrics were calculated- mean, absolute mean, maximum, minimum and amplitude. The mean indicates the global tendency of deviation relative to the nominal reference (test 1). Positive results indicate that there is excess material removal, while negative values indicates under-machining. However, the presence of deviations with opposite signs can cancel each other out, resulting in an average close to zero, even if there are significant error.

To overcome this limitation, the absolute mean was calculated. This metric corresponds to the arithmetic mean of the absolute values of the deviations, regardless of positive or negative variation. This way, there is a more realistic reflection of the mean global error. The maximum and minimum represent the extreme deviations in each test and are useful to identify localised non-conformities. The difference between these variables determine the amplitude, that indications the extreme variation of deviations. At last, the standard deviation estimates the statistical variability of the measurements around the mean. It can be used as an indicator of process consistency.

As the results demonstrate, test 4 (increase of v_c) can be highlighted as the most dimensionally stable condition. It presents low amplitude (93 μm), which suggests low local non-conformities. It has the lowest absolute mean deviation (24.82 μm), which means it has a small average error regardless of direction. Additionally, it exhibits the lowest standard deviation (30.60 μm), indicating low dispersion of the deviations around the mean.

In contrast, test 7 (decrease of v_c and f_z) resulted in the lowest dimensional stability, presenting the highest amplitude, absolute mean and standard deviation (100 μm, 32.73 μm and 36.56 μm, respectively). These values indicate significant inconsistency, with localised non-conformities that require special attention.

In addition, tests 1 and 3 had small variations between measurements with standard deviations of 29.79 μm and 30.62 μm, respectively, suggesting a consistent performance. Test 5 showed higher amplitude (97 μm), but its mean was close to zero that does not clarify if it has a tendency to remove excess or insufficient amounts of material. Test 2 demonstrates larger dispersion with

an amplitude of 94 μm and absolute mean of 31.49 μm. Finally, test 6 had more fluctuation of the deviations around the mean, with a standard deviation result of 31.49 μm and the highest negative mean (-4.64 μm), indicating a tendency for under-machining.

Table 4.29: Dimensional deviation values (μm) for each test and corresponding statistical metrics.

Feature	**Test 1**	**Test 2**	**Test 3**	**Test 4**	**Test 5**	**Test 6**	**Test 7**
DIST 35 (OP1)	48.0	42.0	41.0	42.0	44.0	44.0	50.0
DIST 25 (OP13)	14.0	17.0	10.0	5.0	6.0	4.0	30.0
DIST 10 (OP13)	25.0	19.0	28.0	30.0	36.0	34.0	20.0
DIST 15 (OP13)	-40.0	-52.0	-51.0	-51.0	-53.0	-52.0	-50.0
R5_1 (OP13)	-30.0	-34.0	-32.0	-33.0	-27.0	-32.0	-20.0
R5_2 (OP13)	-33.0	-37.0	-41.0	-39.0	-37.0	-38.0	-30.0
DIST 10 (OP15)	36.0	36.0	24.0	34.0	33.0	32.0	30.0
DIST 4 (OP15)	-12.0	-10.0	-10.0	-9.0	-9.0	-9.0	-50.0
R3_1 (OP15)	21.0	22.0	19.0	8.0	10.0	4.0	40.0
R3_2 (OP15)	8.0	9.0	9.0	-7.0	10.0	-23.0	20.0
DIST 9 (OP15)	-16.0	-20.0	-21.0	-15.0	-14.0	-15.0	-20.0
Maximum	48.00	42.00	41.00	42.00	44.00	44.00	50.00
Minimum	-40.00	-52.00	-51.00	-51.00	-53.00	-52.00	-50.00
Amplitude	88.00	94.00	92.00	93.00	97.00	96.00	100.00
Mean	1.91	-0.73	-2.18	-3.18	-0.09	-4.64	1.82
Absolute Mean	25.73	27.09	26.00	24.82	25.36	26.09	32.73
Standard Deviation	29.79	31.62	30.62	30.60	31.21	31.49	36.56

Regarding drilling operations, all quality control reports showed that the Hole D4.04 consistently exceeded tolerance limits at the entry side, as shown in Table 4.30. Although the removal of pilot drill was implemented to correct this problem, deviations and roundness still occurred. Roundness (RN) is a critical indicator of hole quality as it is quantifies how close the shape of a hole is to a perfect circle. Even if the diameter is correct, the hole might not be exactly round. With tight tolerances, if the roundness is significant, it may no longer guarantee a proper fit. While the exit side roundness was, in general, acceptable (around 1 μm), the RN at the entry reached up to 20 μm, indicating instability.

Table 4.30: Dimensional and geometric deviations measured at entry and exit sides of the D4,04 hole.

	Entry			**Exit**		
	Measured value (mm)	**Deviation (µm)**	**RN (µm)**	**Measured value (mm)**	**Deviation (µm)**	**RN (µm)**
0	4.055	15,0	3,0	4.056	16,0	1,0
1	4.089	49,0	15,0	4.057	17,0	1,0
2	4.093	53,0	13,0	4.055	15,0	2,0
3	4.088	48,0	14,0	4.054	14,0	3,0
4	4.084	44,0	20,0	4.056	16,0	0,0
5	4.082	42,0	15,0	4.054	14,0	1,0
6	4.085	45,0	15,0	4.054	14,0	1,0

In addition to all this, all parts met the perpendicularity tolerance, confirming that the hole axis remained aligned and that the peck drilling strategy was effective. Since the geometric deviation was localised at the entry side, it is likely due to the long cutting edge of the drill being in constant contact with the material, which can lead to uncontrolled material removal and diameter enlargement. It is important to note that this phenomenon was not corrected along the tests because the time window for machining was small, not allowing an interruption of the trials to further study this deviation.

To mitigate this issue in future operations, it would be better to use a different strategy- similar to the one applied to the 3.28 mm hole. That is, start with a smaller drill (for example, diameter of 4.00 mm) and then finish the hole using a reamer with the final dimension (4.04 mm). This gives better control over the final dimension and helps to reduce shape errors at the entry. Moreover, a different drill with a higher point angle can be used to prevent constant tool contact. Another point that can be explored is the pressure of the internal cooling system. It would be interesting to increase the pressure levels and try to perform the operation in one pass. From all the alternatives, the one that is most likely to enhance stability and surface finish is the usage of a reamer.

Chapter 5

Conclusion and Future Works

5.1 Conclusion

In conclusion, the data obtained from the electrical current and vibration signals has proven to be a valuable approach for monitoring 5-axis CNC milling operations, The current signals demonstrated strong correlations with cutting power and material removal rate, with values of R^2 ranging from 0.74 to 0.92. These results indicate that this signal is a good indicator of energy consumption and cutting forces. However, it shows limited sensitivity under low cutting forces, being less effective in distinguishing finishing passes. Regarding cutting parameters effect, it was observed that the feed per tooth, f_z, had a significant influence on current consumption, due to its direct impact on the average chip thickness, h_m. In addition, the cutting speed, v_c, had a strong impact on idle current- with values of R^2 above 0.8- since higher rotation speeds require more energy consumption for the spindle to win over friction effects.

The accelerometer provided a vetorial insight into the dynamic evolution of process stability, where the lateral cutting forces were the main cause of vibrations. The X-axis consistently showed the highest levels of vibrations across the three operations. In addition, the impact of cutting speed, v_c, on vibration levels is not linear as the decrease of this variable produced a raise on dynamic excitations. The reduction of the feed per tooth was, in general, the condition that produced the best stability.

Current and vibration signals should be seen as independent sources of informations and used as a complement to each other. While current reflects the cutting forces and energy required for the process, vibration captures the dynamic behaviour, considering different directions. These two combined have the potential to be used as quality control and tool wear indicators in a series production, enhancing the efficiency in machining and tool performance.

Quality control results demonstrated that for the production of this test part, there is a considerable window of parameters that can be used without compromising dimensional accuracy. Even though all cutting data configurations, in global, verified the requirements, there are some variations that lead to higher deviations. As such, it is preferable to operate under more safe conditions that reach closer to the nominal value.

Overall, the sensor-based monitoring approach presented in this work creates a good foundation for future developments in process monitoring and optimization, with a great margin for improvement.

5.2 Future Works

Following the conclusion of this work and given the limitations found, there are several opportunities to further improve this work. Some ideas include the following:

- For higher statistical confidence, a larger number of trials should be executed. The ideal would be to perform a series production to further investigate the viability of current and vibrations signals to be used as indicators of tool wear and evaluate the impact of tool wear on cutting performance;
- Explore other sensing technology and hardware to improve the accuracy of the collected data. For example, to overcome the experimental accelerometer malfunction, it would be interesting to use a piezoelectric sensor to perform vibration analysis;
- Perform Design of Experiments or apply the Taguchi method to obtain a more structured evaluation on the impact of cutting parameters on the sensor signals and quality of the workpieces;
- Use of statistical analysis to identify the factors most related with the measured signals, such as ANOVA (Analysis of Variance);
- Obtain stability diagrams to investigate the sensitivity of vibrations to cutting parameters, providing further insight into process behaviour.

Appendix A

Cutting tools and tool holders nomenclature

Table A.1: End mill nomenclature.

Code	Description
FCH0.2	End mill with chamfer (creates a chamfer of 0.2 mm)
D10	Diameter value
Z4	Number of cutting edges
2.5XD	Cutting length (2.5 × 10 = 25 mm)
DE10	Shank diameter
REV	Coated
AD30	Usable length

Table A.2: Chamfer mill nomenclature.

Code	Description
FC	Chamfer mill
D4	Diameter value
Z4	Number of cutting edges
90	Cutting angle
DE4	Shank diameter
REV	Coated
MD	Tool material: hard metal

Table A.3: Drill code nomenclature.

Code	**Description**
B	Drill
D4.04	Diameter value
3XD	Cutting length
140	Tip angle
DE6	Shank diameter
MD	Tool material: hard metal
REF	Internal cooling

Table A.4: Face mill nomenclature.

Code	**Description**
FPA	Face mill
D40	Diameter value
R0.4	Corner radius
Z4	Number of inserts
AP8	Maximum depth of cut
90	Cutting angle

Table A.5: Reamer nomenclature.

Code	**Description**
M	Reamer
D3.28	Diameter value
CR	Straight flutes
DE3	Shank diameter
NREV	Not coated
MD	Tool material: hard metal

Table A.6: Tool holders nomenclature.

Code	**Description**
BBT30	Taper type (dual-contact cone)
PP	Clamping method (collets)
CP25	Type of collet pocket (Centro|P)
A=75	Projection length
DIR	Right-hand taper configuration
ER25	Type of collets
PR	Face mill holder
d16	Internal clamping diameter
D40	External cone diameter
REF	Internal cooling

This page was intentionally left blank

Appendix B

Cutting parameters comparison

Table B.1: Comparison between programmed and catalogue cutting parameters – Setup AP1.

Op.	Tool	Tool #	Programmed values				Catalog			
			v_c (m/min)	f_z (mm/tooth)	v_f (mm/min)	n (rpm)	v_c (m/min)	f_z (mm/tooth)	v_f (mm/min)	n (rpm)
1	FCH0.2 D10 Z4 2.5×D DE10 REV AD30	1	180	0.0449	1030	5730	180	0.076	1740	5730
2	FCH0.2 D10 Z4 2.5×D DE10 REV AD30	1	180	0.0449	1030	5730	180	0.076	1740	5730
3	FCH0.2 D10 Z4 2.5×D DE10 REV AD30	4	180	0.0449	1030	5730	180	0.090	2060	5730
4	FPA D40 R0.4 Z4 AP8 90	2	245	0.0513	400	1950	239	0.190	1445	1902
5	FC D4 Z4 90 DE4 REV MD	3	201	0.0117	750	16000	85	0.014	379	6760

Table B.2: Comparison between programmed and catalogue cutting parameters – Setup AP2.

Op.	Tool	Tool #	Programmed values				Catalog			
			v_c (m/min)	f_z (mm/tooth)	v_f (mm/min)	n (rpm)	v_c (m/min)	f_z (mm/tooth)	v_f (mm/min)	n (rpm)
1	FCH0.2 D10 Z4 2.5×D DE10 REV AD30	1	152	0.0438	850	4850	180	0.090	2060	5730
2	FCH0.2 D10 Z4 2.5×D DE10 REV AD30	1	152	0.0438	850	4850	180	0.090	2060	5730
3	FCH0.2 D10 Z4 2.5×D DE10 REV AD30	1	180	0.0449	1030	5730	180	0.0664	1520	5730
4	FCH0.2 D10 Z4 2.5×D DE10 REV AD30	4	126	0.0250	400	4000	180	0.0900	2060	5730
5	FPA D40 R0.4 Z4 AP8 90	2	245	0.0513	400	1950	247	0.2420	1903	1966
6	FCH0.2 D8 Z4 2.5×D DE8 REV AD25	5	146	0.0250	580	5800	180	0.0350	1000	7160
7	FCH0.03 D3 Z3 2×D DE6 REV	10	60	0.0194	370	6350	70	0.0200	446	7430
8	B D4.04 5×D 140 DE6 REV MD REF	7	44	0.0500	350	3500	120	0.0775	1466	9460
9	B 3.2 3×D 140 DE6 REV MD	8	35	0.0357	250	3500	105	0.1300	1359	10450
10	B 3.2 7×D 140 DE6 REV MD REF	9	30	0.0167	100	3000	120	0.0499	1194	11943
11	M D3.28 CR DE3 NREV MD	11	20	0.0132	150.39	1905	25	0.0149	219	2433
12	FCH0.2 D8 Z4 2.5×D DE8 REV AD25	5	146	0.0250	580	5800	180	0.0350	1000	7160
13	FCH0.2 D8 Z4 2.5×D DE8 REV AD25	5	146	0.0250	580	5800	180	0.0350	1000	7160
14	FCH0.2 D8 Z4 2.5×D DE8 REV AD25	5	146	0.0250	580	5800	180	0.0350	1000	7160
15	FCH0.1 D5 Z4 2.5×D DE6 REV AD19	12	86	0.0300	660	5500	180	0.0250	1150	11500
16	FCH0.2 D8 Z4 2.5×D DE8 REV AD25	13	146	0.0517	1200	5800	180	0.0350	1000	7160
17	FCH0.2 D8 Z4 2.5×D DE8 REV AD25	13	146	0.0517	1200	5800	180	0.0350	1000	7160
18	FCH0.2 D8 Z4 2.5×D DE8 REV AD25	13	146	0.0517	1200	5800	180	0.0350	1000	7160
19	FCH0.2 D8 Z4 2.5×D DE8 REV AD25	13	146	0.0517	1200	5800	180	0.0350	1000	7160
20	FC D4 Z4 90 DE4 REV MD	3	201	0.0055	350	16000	85	0.0140	379	6760
21	FC D4 Z4 90 DE4 REV MD	3	201	0.0055	350	16000	85	0.0140	379	6760
22	FC D4 Z4 90 DE4 REV MD	3	201	0.0055	350	16000	85	0.0140	379	6760
23	FC D4 Z4 90 DE4 REV MD	3	201	0.0055	350	16000	85	0.0140	379	6760
24	FC D4 Z4 90 DE4 REV MD	3	201	0.0055	350	16000	85	0.0140	379	6760
25	FC D4 Z4 90 DE4 REV MD	3	201	0.0055	350	16000	85	0.0140	379	6760
26	FC D4 Z4 90 DE4 REV MD	3	201	0.0055	350	16000	85	0.0140	379	6760
27	FC D4 Z4 90 DE4 REV MD	3	201	0.0055	350	16000	85	0.0140	379	6760

This page was intentionally left blank

Appendix C

Current clamps technical data



E25 & E27 AC/DC CURRENT CLAMPS

The current clamps in the E Series can be used to measure alternating and direct currents by means of Hall-effect technology. Their unique long, narrow shape facilitates measurement in confined spaces where access is difficult or when there are a large number of electrical cables and conductors present.

The clamps in the E Series are all equipped with an automatic DC Zero system and a deactivatable standby mode. They can be powered by a battery or a standard 5 VDC power pack (option) via their Micro USB connector.

They offer two different sensitivities and output an alternating and direct voltage signal (mVac+dc) which is a faithful image, in terms of the waveform and amplitude, of the current measured.

The E25 clamp, equipped with a cable terminated by 2 x Ø4 mm insulated male banana plugs, is the ideal complement for any multimeter or other measuring instrument.

The E27 clamp is an insulated current sensor whose wide bandwidth is useful for measuring and viewing complex AC+DC signals on an oscilloscope.

«Zero DC» control button
Control LED
ON/OFF and sensitivity selector switch

	E25	E27
	for multimeters	for oscilloscopes
Measurement range	5 mA .. 80 A DC / 60 A AC	100 mA .. 100 A peak
Bandwidth	20 kHz (-3 dB)	100 kHz (-3 dB)
Sensitivities (calibres)	1 mV/mA (1 V/A) 10 mV/A	100 mV/A 10 mV/A
Clamping diameter	11.8 mm	
Power supply	Internal: 9 V battery External: +5 VDC via female µUSB type B	
Output connections	2-wire cable 1.5 m long terminated by 2 x Ø4 insulated male banana plugs	Coaxial cable 2 m long terminated by 1 insulated BNC plug
Safety	IEC 61010-1 & IEC 61010-2-032 600V CAT III / 300V CAT IV	

Movable arm
Protective guard
Fixed jaw
11.8 mm clamping
Battery compartment
µUSB connector for external power supply
Ø 4 mm insulated male banana plugs
Movable jaw

To order

CLAMP E25 CVH 1-100/1 ..... P01120025
CLAMP E27 CVH OSCILLO P01120027
Delivered with 1 simplified user's manual, 1 safety datasheet, 1 verification certificate and a 9 V battery

Mains adapter 110-240V 50/60 Hz, USB 5 V 1 A P01651023
and USB type A/µUSB-B power and connection cable

Carrying bag P01298075
Dimensions 120 x 245 x 60 mm, compatible with MultiFix mounting system

FRANCE
Chauvin Arnoux
12 -16 rue Sarah Bernhardt
92600 Asnières-sur-Seine
Tél : +33 1 44 85 44 85
Fax : +33 1 46 27 73 89
info@chauvin-arnoux.fr
www.chauvin-arnoux.fr

UNITED KINGDOM
Chauvin Arnoux Ltd
Unit 1 Nelson Ct, Flagship Sq, Shaw Cross
Business Pk Dewsbury, West Yorkshire
WF12 7TH
Tel: +44 1924 460 494
Fax: +44 1924 455 328
info@chauvin-arnoux.co.uk

Middle East
Chauvin Arnoux Middle East
P.O. BOX 60-154
1241 2020 JAL EL DIB - LEBANON
Tel: +961 1 890 425
Fax: +961 1 890 424
camie@chauvin-arnoux.com

CHAUVIN ARNOUX GROUP

900211645 - Ed.1 - 04/2021 - LC - Non-contractual document - Specifications to be confirmed at time of order. Photo credits and diagrams Chauvin Arnoux

Figure C.1: E27 Current clamp from Chauvin Arnoux.

This page was intentionally left blank

Appendix D

RMS Current values over time

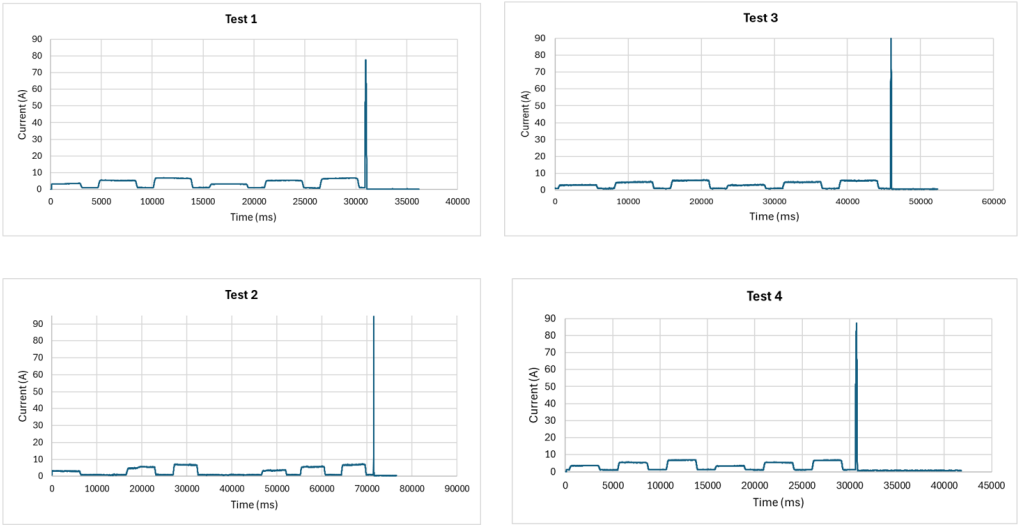


Figure D.1: RMS current values over time from tests 1 to 4 of OP1.

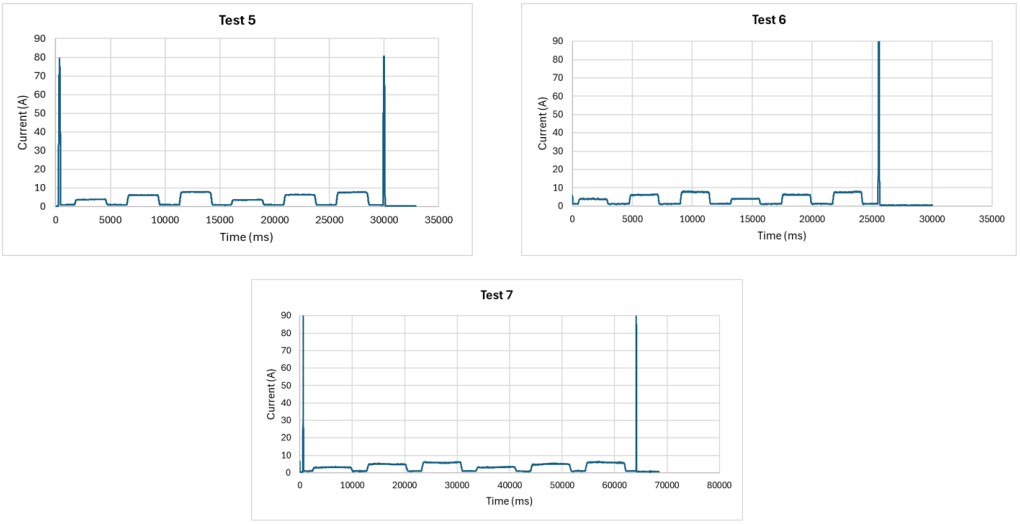


Figure D.2: RMS current values over time from tests 5 to 7 of OP1.

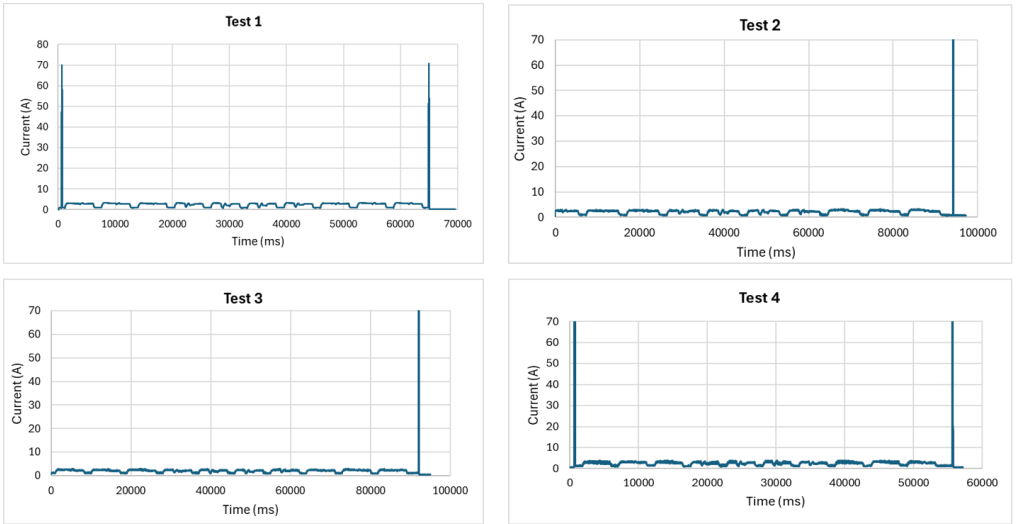


Figure D.3: RMS current values over time from tests 1 to 4 of OP13.

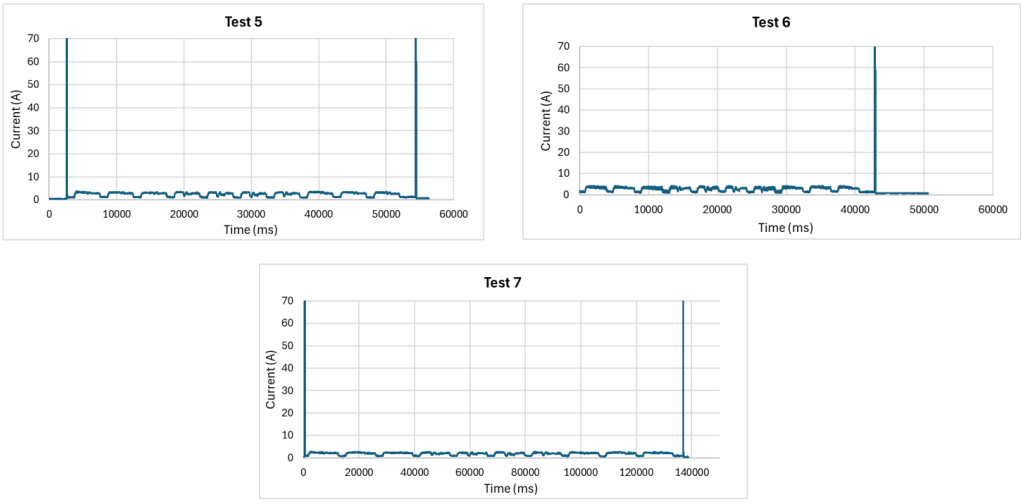


Figure D.4: RMS current values over time from tests 5 to 7 of OP13.

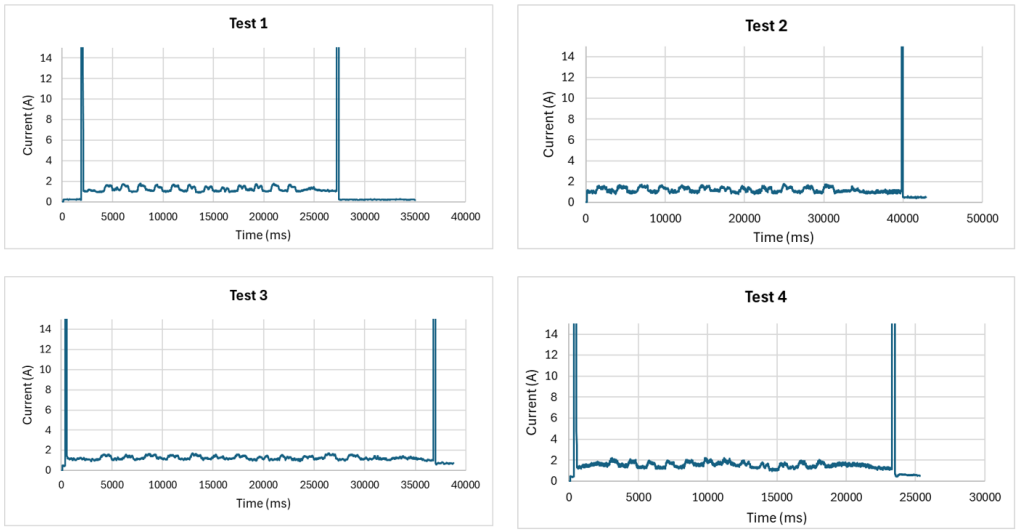


Figure D.5: RMS current values over time from tests 1 to 4 of OP15.

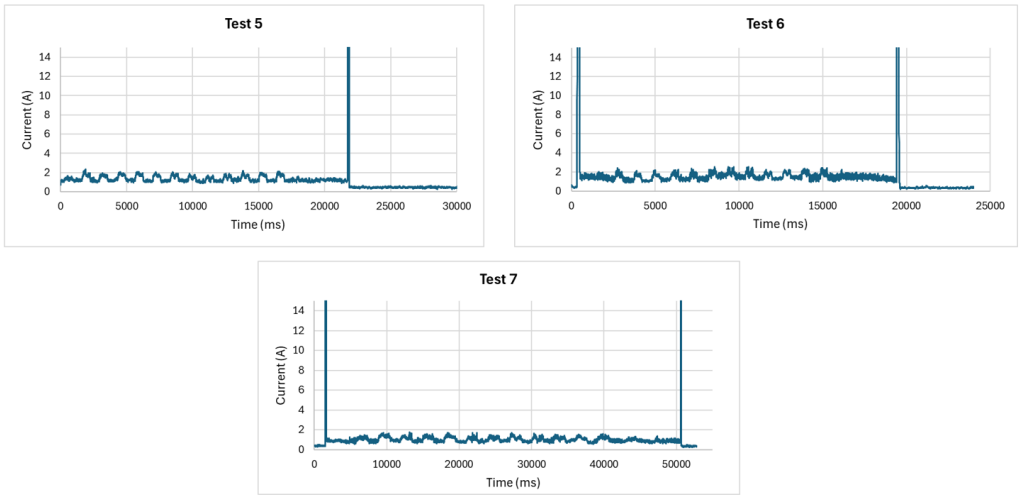


Figure D.6: RMS current values over time from tests 5 to 7 of OP15.

Appendix E

RMS acceleration plots of X, Y and Z axes

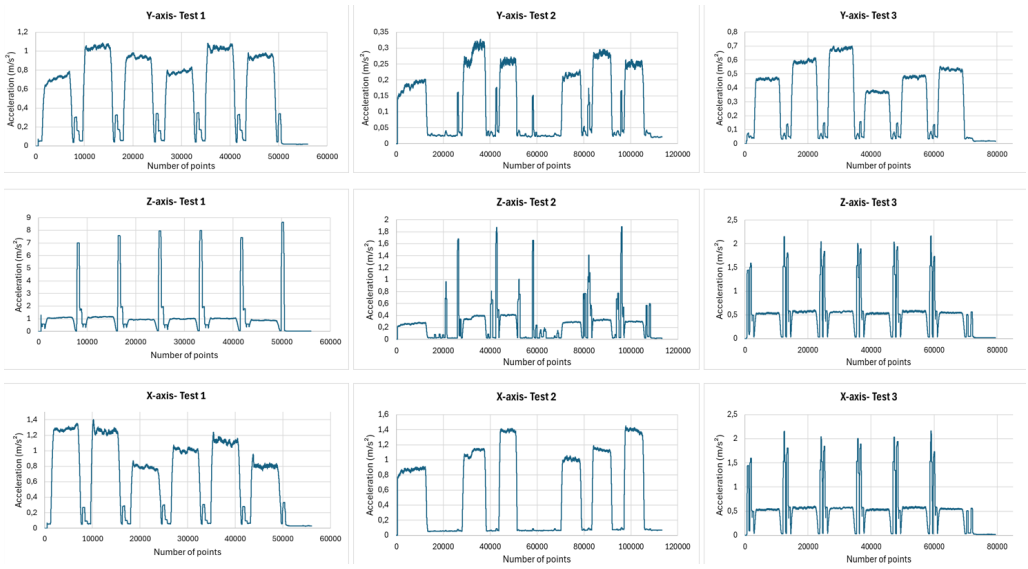


Figure E.1: RMS acceleration values from tests 1 to 3 of OP1.

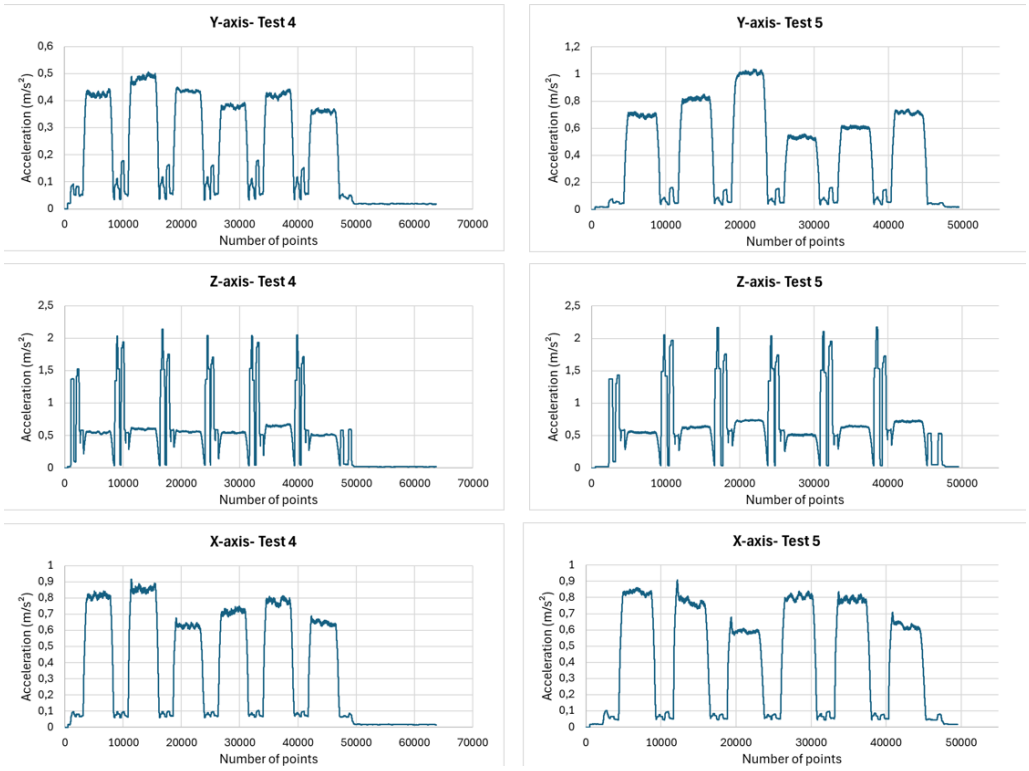


Figure E.2: RMS acceleration values from tests 4 and 5 of OP1.

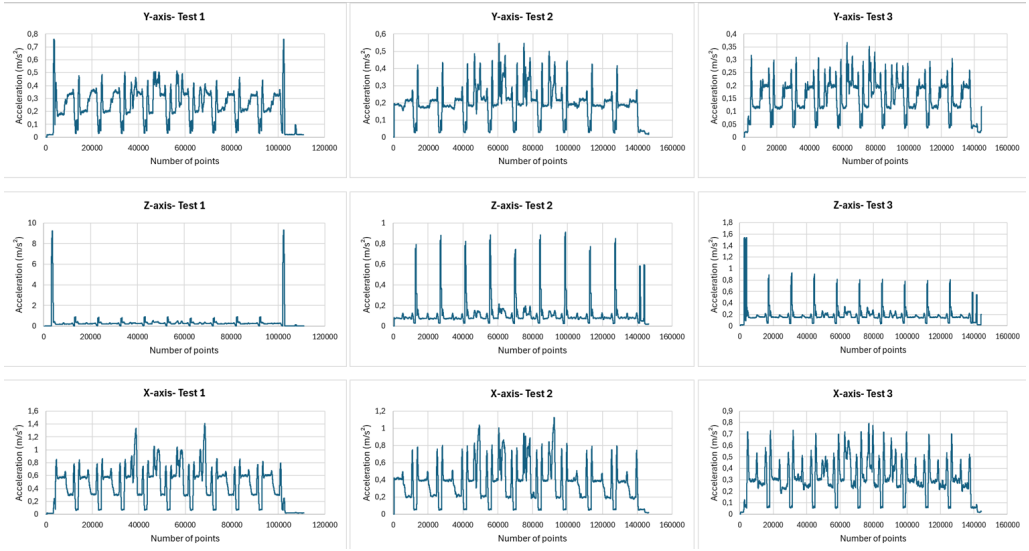


Figure E.3: RMS acceleration values from tests 1 to 3 of OP13.

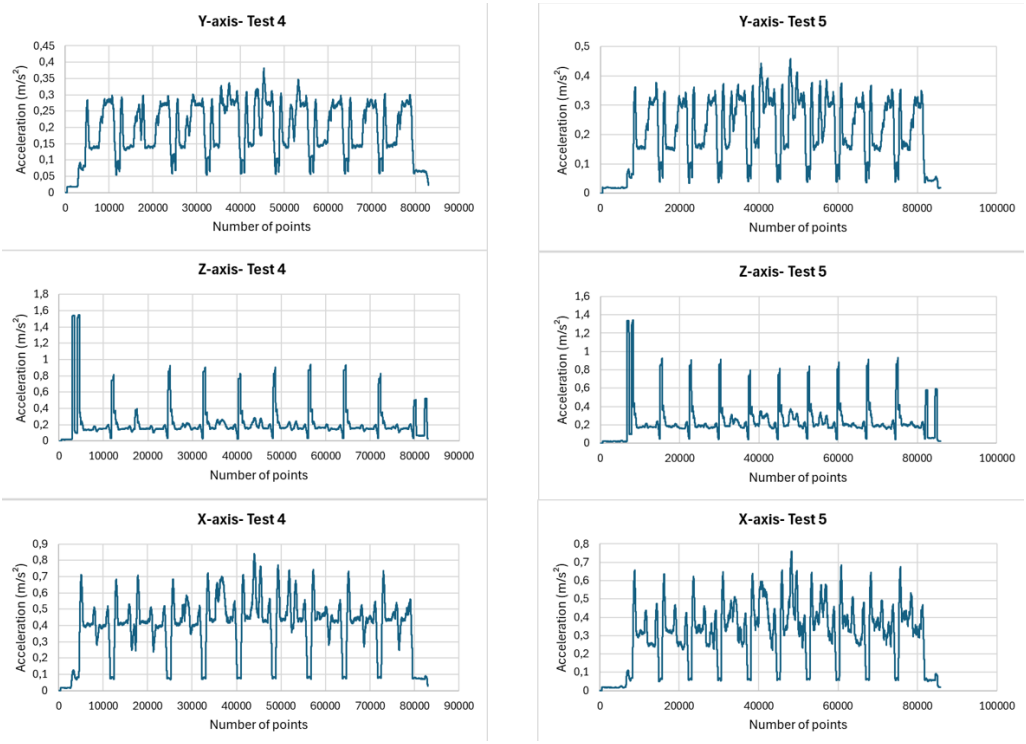


Figure E.4: RMS acceleration values from tests 4 and 5 of OP13.

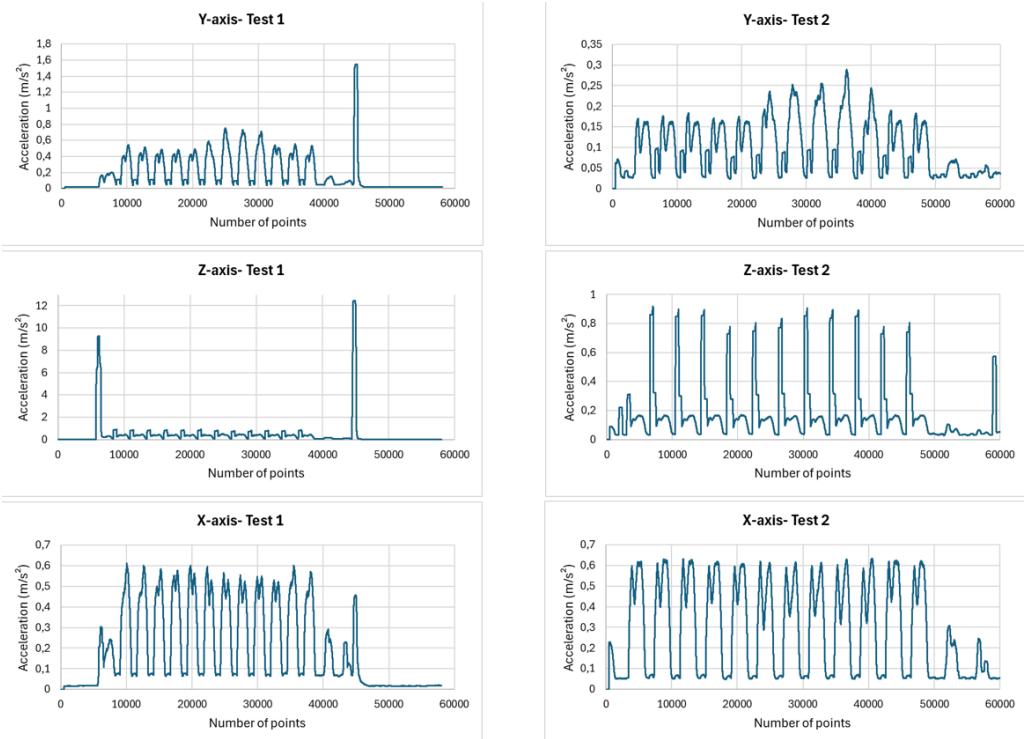


Figure E.5: RMS acceleration values from tests 1 and 2 of OP15.

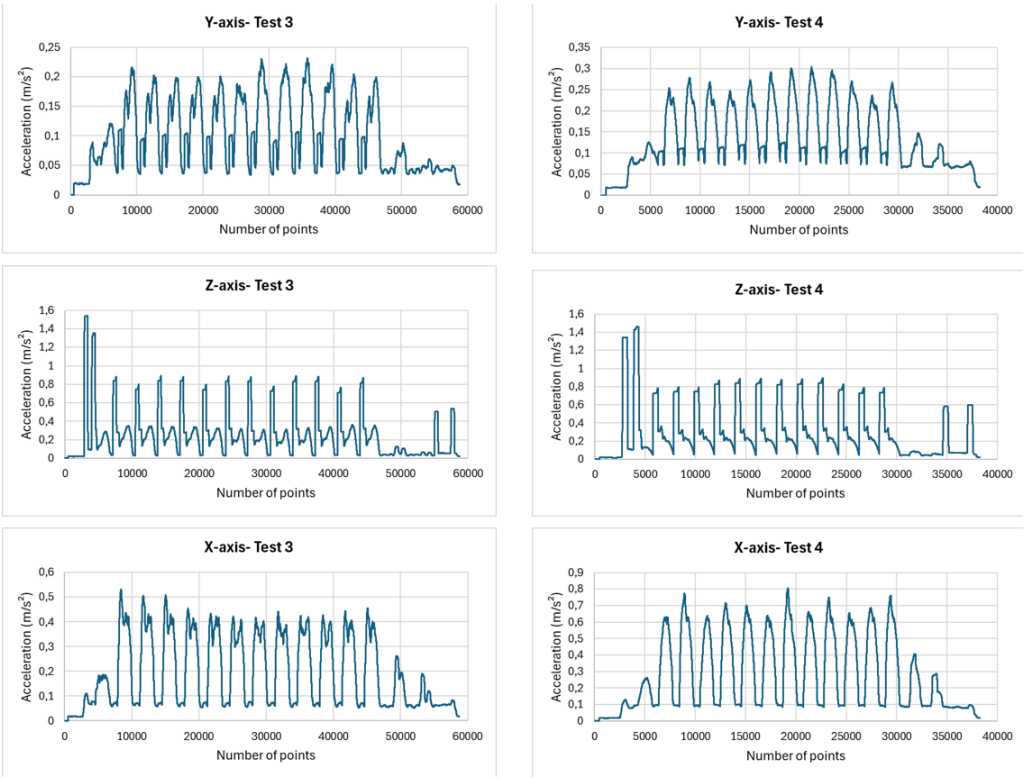


Figure E.6: RMS acceleration values from tests 3 and 4 of OP15.

Appendix F

RMS acceleration plots of the Resultant

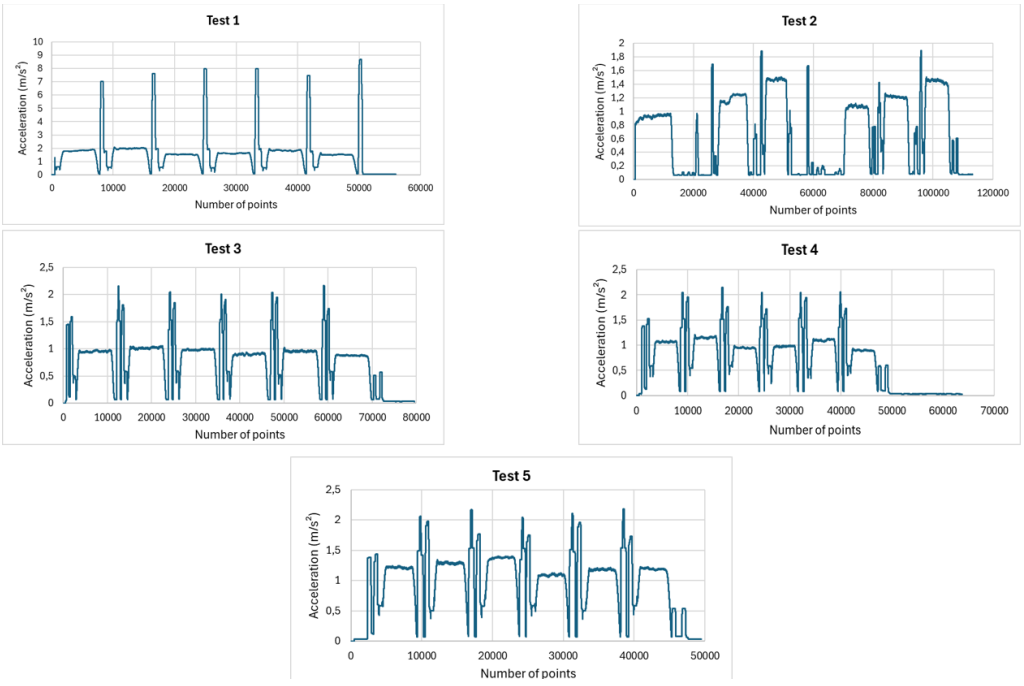


Figure F.1: RMS acceleration Resultant values of OP1.

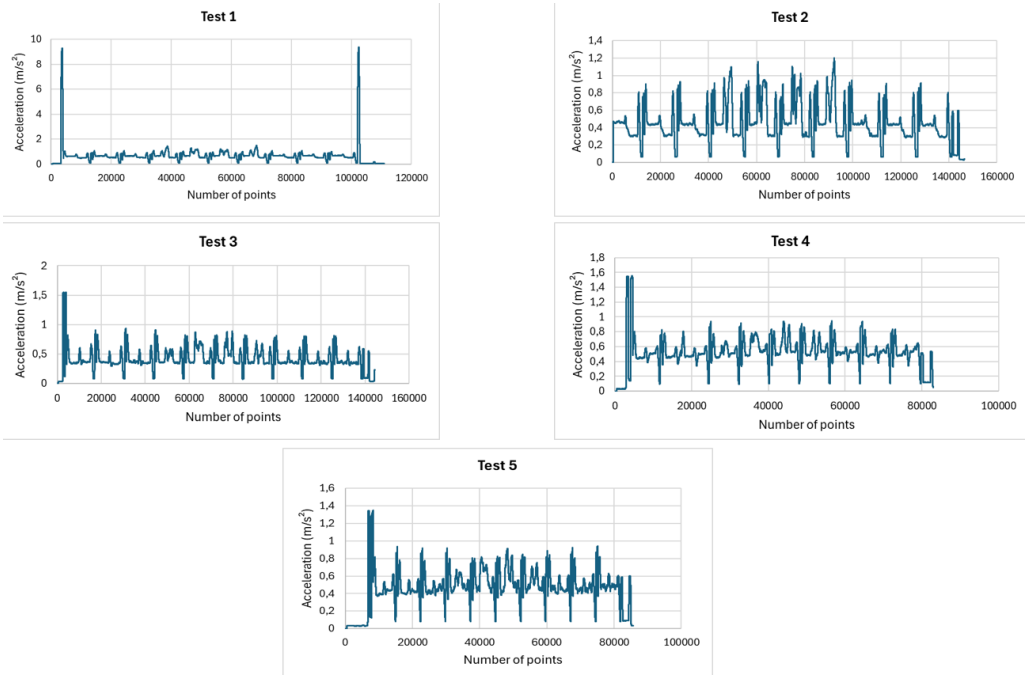


Figure F.2: RMS acceleration Resultant values of OP13.

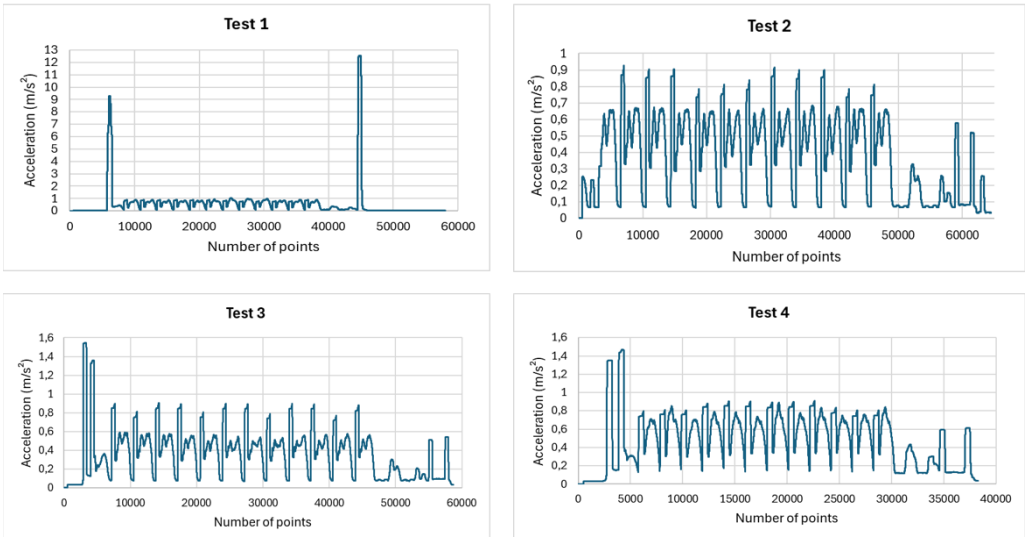
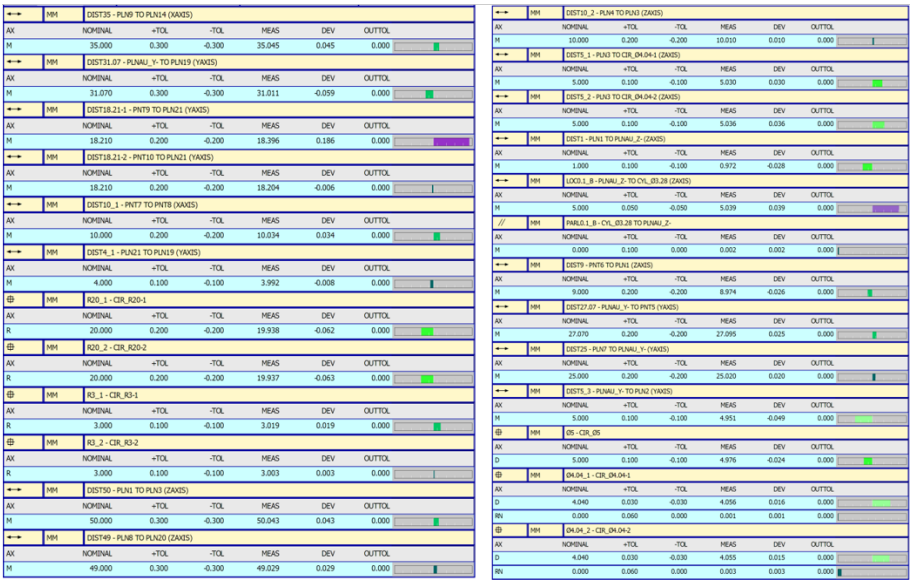


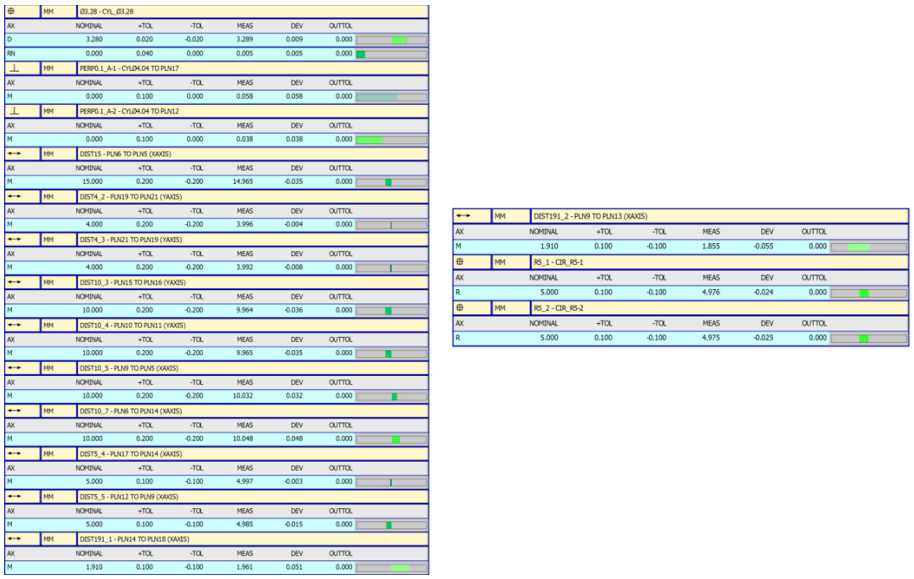
Figure F.3: RMS acceleration Resultant values of OP15.

Appendix G

Quality Control Reports

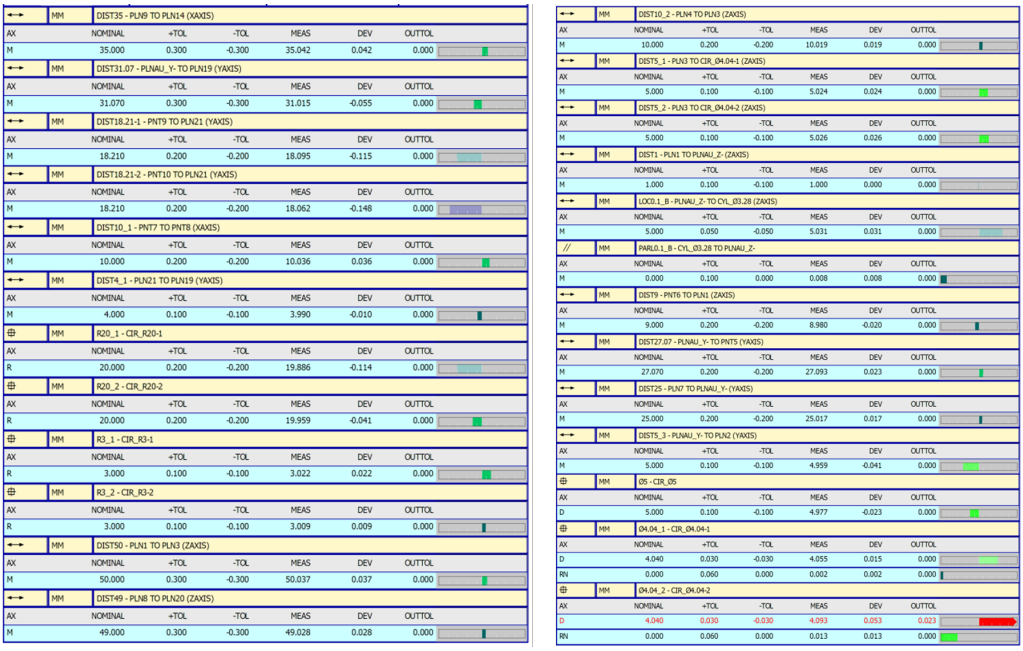


(a) Pages 1 (left) and 2 (right).



(b) Pages 3 (left) and 4 (right).

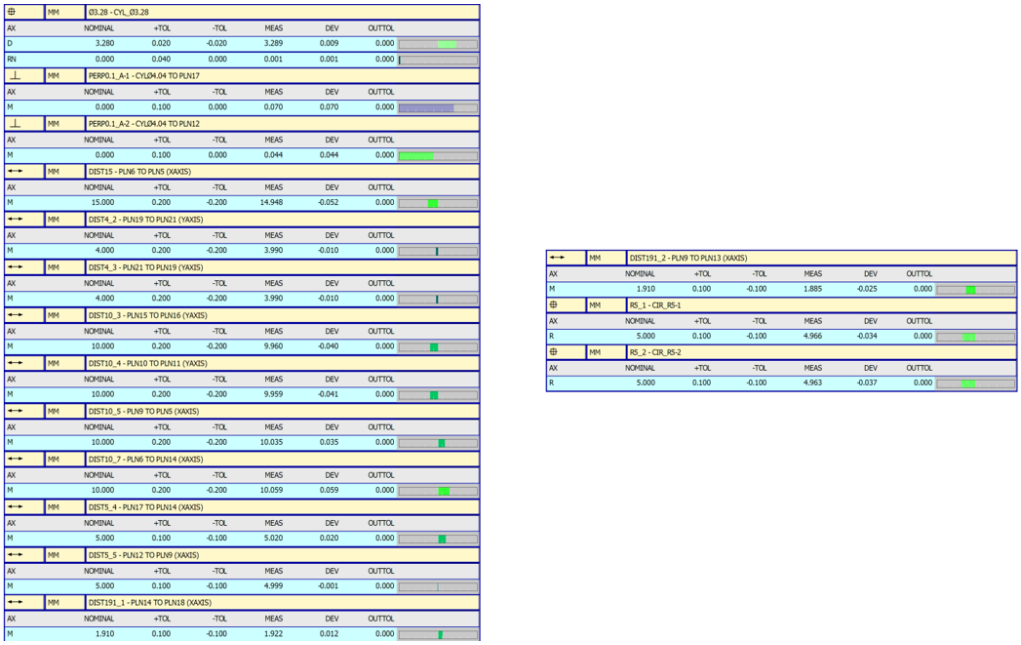
Figure G.1: Inspection report of workpiece number 1.



	MM	DIST35 - PLN9 TO PLN14 (XAXIS)					
AX		NOMINAL	+TOL	-TOL	MEAS	DEV	OUTTOL
M		35.000	0.300	-0.300	35.042	0.042	0.000
	MM	DIST31.07 - PLNAU_Y- TO PLN19 (YAXIS)					
AX		NOMINAL	+TOL	-TOL	MEAS	DEV	OUTTOL
M		31.070	0.300	-0.300	31.015	-0.055	0.000
	MM	DIST18.21-1 - PNT9 TO PLN21 (YAXIS)					
AX		NOMINAL	+TOL	-TOL	MEAS	DEV	OUTTOL
M		18.210	0.200	-0.200	18.095	-0.115	0.000
	MM	DIST18.21-2 - PNT10 TO PLN21 (YAXIS)					
AX		NOMINAL	+TOL	-TOL	MEAS	DEV	OUTTOL
M		18.210	0.200	-0.200	18.062	-0.148	0.000
	MM	DIST10_1 - PNT7 TO PNT8 (XAXIS)					
AX		NOMINAL	+TOL	-TOL	MEAS	DEV	OUTTOL
M		10.000	0.200	-0.200	10.036	0.036	0.000
	MM	DIST4_1 - PLN21 TO PLN19 (YAXIS)					
AX		NOMINAL	+TOL	-TOL	MEAS	DEV	OUTTOL
M		4.000	0.100	-0.100	3.990	-0.010	0.000
	MM	R20_1 - CIR_R20-1					
AX		NOMINAL	+TOL	-TOL	MEAS	DEV	OUTTOL
R		20.000	0.200	-0.200	19.886	-0.114	0.000
	MM	R20_2 - CIR_R20-2					
AX		NOMINAL	+TOL	-TOL	MEAS	DEV	OUTTOL
R		20.000	0.200	-0.200	19.959	-0.041	0.000
	MM	R3_1 - CIR_R3-1					
AX		NOMINAL	+TOL	-TOL	MEAS	DEV	OUTTOL
R		3.000	0.100	-0.100	3.022	0.022	0.000
	MM	R3_2 - CIR_R3-2					
AX		NOMINAL	+TOL	-TOL	MEAS	DEV	OUTTOL
R		3.000	0.100	-0.100	3.009	0.009	0.000
	MM	DIST50 - PLN1 TO PLN3 (ZAXIS)					
AX		NOMINAL	+TOL	-TOL	MEAS	DEV	OUTTOL
M		50.000	0.300	-0.300	50.037	0.037	0.000
	MM	DIST49 - PLN8 TO PLN20 (ZAXIS)					
AX		NOMINAL	+TOL	-TOL	MEAS	DEV	OUTTOL
M		49.000	0.300	-0.300	49.028	0.028	0.000

	MM	DIST10_2 - PLN4 TO PLN3 (ZAXIS)					
AX		NOMINAL	+TOL	-TOL	MEAS	DEV	OUTTOL
M		10.000	0.200	-0.200	10.019	0.019	0.000
	MM	DIST5_1 - PLN3 TO CIR_Ø4.04-1 (ZAXIS)					
AX		NOMINAL	+TOL	-TOL	MEAS	DEV	OUTTOL
M		5.000	0.100	-0.100	5.024	0.024	0.000
	MM	DIST5_2 - PLN3 TO CIR_Ø4.04-2 (ZAXIS)					
AX		NOMINAL	+TOL	-TOL	MEAS	DEV	OUTTOL
M		5.000	0.100	-0.100	5.026	0.026	0.000
	MM	DIST1 - PLN1 TO PLNAU_Z- (ZAXIS)					
AX		NOMINAL	+TOL	-TOL	MEAS	DEV	OUTTOL
M		1.000	0.100	-0.100	1.000	0.000	0.000
	MM	LOCO.1_B - PLNAU_Z- TO CYL_Ø3.28 (ZAXIS)					
AX		NOMINAL	+TOL	-TOL	MEAS	DEV	OUTTOL
M		5.000	0.050	-0.050	5.031	0.031	0.000
//	MM	PARLO.1_B - CYL_Ø3.28 TO PLNAU_Z-					
AX		NOMINAL	+TOL	-TOL	MEAS	DEV	OUTTOL
M		0.000	0.100	0.000	0.008	0.008	0.000
	MM	DIST9 - PNT6 TO PLN1 (ZAXIS)					
AX		NOMINAL	+TOL	-TOL	MEAS	DEV	OUTTOL
M		9.000	0.200	-0.200	8.980	-0.020	0.000
	MM	DIST27.07 - PLNAU_Y- TO PNT5 (YAXIS)					
AX		NOMINAL	+TOL	-TOL	MEAS	DEV	OUTTOL
M		27.070	0.200	-0.200	27.093	0.023	0.000
	MM	DIST25 - PLN7 TO PLNAU_Y- (YAXIS)					
AX		NOMINAL	+TOL	-TOL	MEAS	DEV	OUTTOL
M		25.000	0.200	-0.200	25.017	0.017	0.000
	MM	DIST5_3 - PLNAU_Y- TO PLN2 (YAXIS)					
AX		NOMINAL	+TOL	-TOL	MEAS	DEV	OUTTOL
M		5.000	0.100	-0.100	4.959	-0.041	0.000
	MM	Ø5 - CIR_Ø5					
AX		NOMINAL	+TOL	-TOL	MEAS	DEV	OUTTOL
D		5.000	0.100	-0.100	4.977	-0.023	0.000
	MM	Ø4.04_1 - CIR_Ø4.04-1					
AX		NOMINAL	+TOL	-TOL	MEAS	DEV	OUTTOL
D		4.040	0.030	-0.030	4.055	0.015	0.000
RN		0.000	0.060	0.000	0.002	0.002	0.000
	MM	Ø4.04_2 - CIR_Ø4.04-2					
AX		NOMINAL	+TOL	-TOL	MEAS	DEV	OUTTOL
D		4.040	0.030	-0.030	4.093	0.053	0.023
RN		0.000	0.060	0.000	0.013	0.013	0.000

(a) Pages 1 (left) and 2 (right).

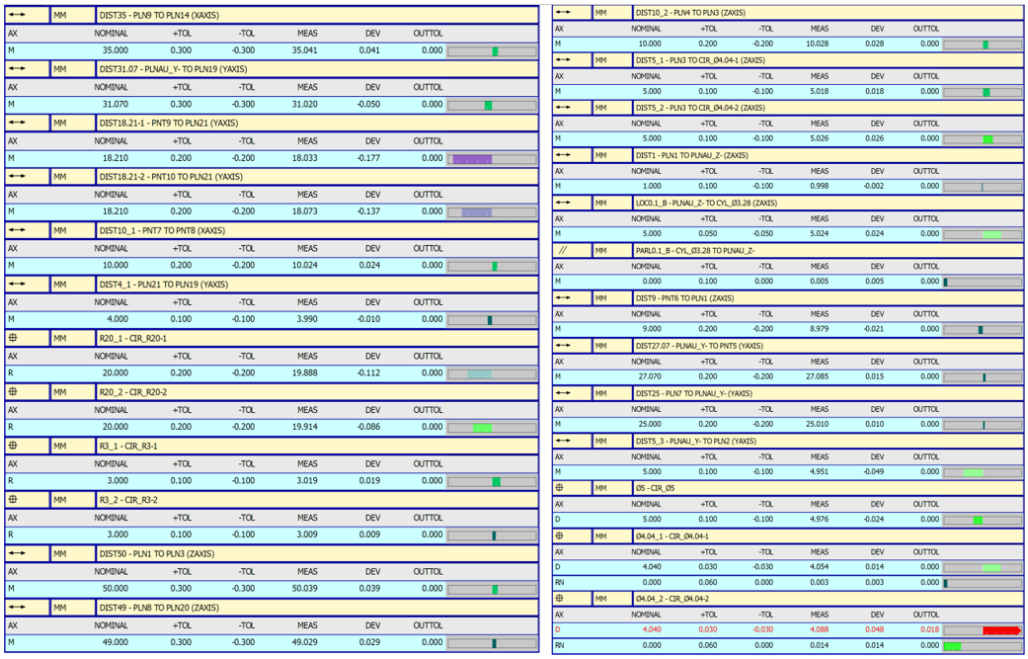


	MM	Ø3.28 - CYL_Ø3.28					
AX		NOMINAL	+TOL	-TOL	MEAS	DEV	OUTTOL
D		3.280	0.020	-0.020	3.289	0.009	0.000
RN		0.000	0.040	0.000	0.001	0.001	0.000
⊥	MM	PERPO.1_A-1 - CYLØ4.04 TO PLN17					
AX		NOMINAL	+TOL	-TOL	MEAS	DEV	OUTTOL
M		0.000	0.100	0.000	0.070	0.070	0.000
⊥	MM	PERPO.1_A-2 - CYLØ4.04 TO PLN12					
AX		NOMINAL	+TOL	-TOL	MEAS	DEV	OUTTOL
M		0.000	0.100	0.000	0.044	0.044	0.000
	MM	DIST15 - PLN6 TO PLN5 (XAXIS)					
AX		NOMINAL	+TOL	-TOL	MEAS	DEV	OUTTOL
M		15.000	0.200	-0.200	14.948	-0.052	0.000
	MM	DIST4_2 - PLN19 TO PLN21 (YAXIS)					
AX		NOMINAL	+TOL	-TOL	MEAS	DEV	OUTTOL
M		4.000	0.200	-0.200	3.990	-0.010	0.000
	MM	DIST4_3 - PLN21 TO PLN19 (YAXIS)					
AX		NOMINAL	+TOL	-TOL	MEAS	DEV	OUTTOL
M		4.000	0.200	-0.200	3.990	-0.010	0.000
	MM	DIST10_3 - PLN15 TO PLN16 (YAXIS)					
AX		NOMINAL	+TOL	-TOL	MEAS	DEV	OUTTOL
M		10.000	0.200	-0.200	9.960	-0.040	0.000
	MM	DIST10_4 - PLN10 TO PLN11 (YAXIS)					
AX		NOMINAL	+TOL	-TOL	MEAS	DEV	OUTTOL
M		10.000	0.200	-0.200	9.959	-0.041	0.000
	MM	DIST10_5 - PLN9 TO PLN5 (XAXIS)					
AX		NOMINAL	+TOL	-TOL	MEAS	DEV	OUTTOL
M		10.000	0.200	-0.200	10.035	0.035	0.000
	MM	DIST10_7 - PLN6 TO PLN14 (XAXIS)					
AX		NOMINAL	+TOL	-TOL	MEAS	DEV	OUTTOL
M		10.000	0.200	-0.200	10.059	0.059	0.000
	MM	DIST5_4 - PLN17 TO PLN14 (XAXIS)					
AX		NOMINAL	+TOL	-TOL	MEAS	DEV	OUTTOL
M		5.000	0.100	-0.100	5.020	0.020	0.000
	MM	DIST5_5 - PLN12 TO PLN9 (XAXIS)					
AX		NOMINAL	+TOL	-TOL	MEAS	DEV	OUTTOL
M		5.000	0.100	-0.100	4.999	-0.001	0.000
	MM	DIST191_1 - PLN14 TO PLN18 (XAXIS)					
AX		NOMINAL	+TOL	-TOL	MEAS	DEV	OUTTOL
M		1.910	0.100	-0.100	1.922	0.012	0.000

	MM	DIST191_2 - PLN9 TO PLN13 (XAXIS)					
AX		NOMINAL	+TOL	-TOL	MEAS	DEV	OUTTOL
M		1.910	0.100	-0.100	1.885	-0.025	0.000
	MM	R5_1 - CIR_R5-1					
AX		NOMINAL	+TOL	-TOL	MEAS	DEV	OUTTOL
R		5.000	0.100	-0.100	4.966	-0.034	0.000
	MM	R5_2 - CIR_R5-2					
AX		NOMINAL	+TOL	-TOL	MEAS	DEV	OUTTOL
R		5.000	0.100	-0.100	4.963	-0.037	0.000

(b) Pages 3 (left) and 4 (right).

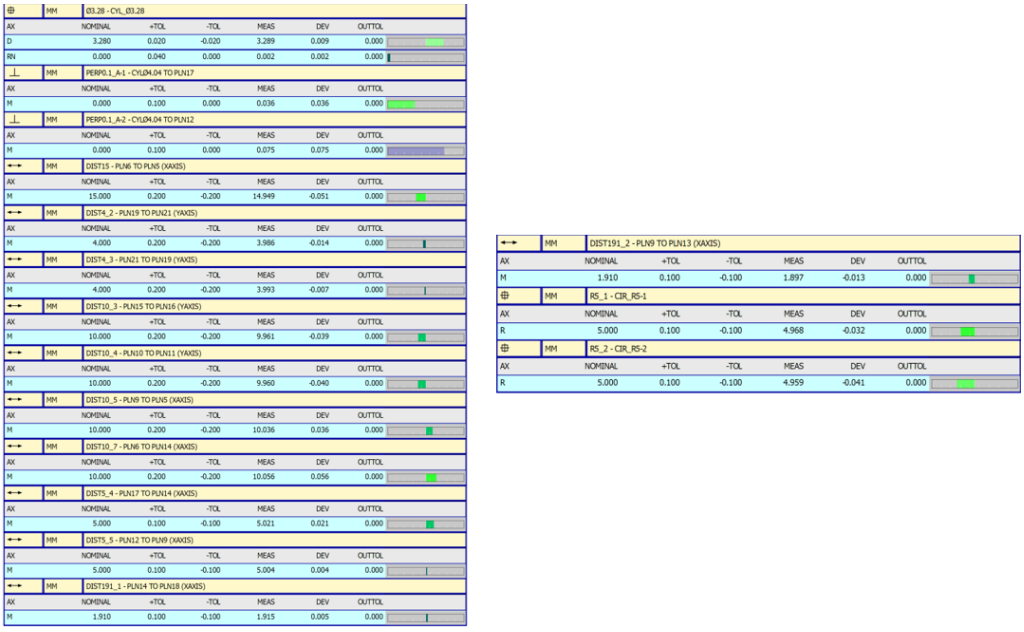
Figure G.2: Inspection report of workpiece number 2.



	MM	DIST35 - PLN9 TO PLN14 (XAXIS)					
AX		NOMINAL	+TOL	-TOL	MEAS	DEV	OUTTOL
M		35.000	0.300	-0.300	35.041	0.041	0.000
	MM	DIST31.07 - PLNAU_Y- TO PLN19 (YAXIS)					
AX		NOMINAL	+TOL	-TOL	MEAS	DEV	OUTTOL
M		31.070	0.300	-0.300	31.020	-0.050	0.000
	MM	DIST18.21-1 - PNT9 TO PLN21 (YAXIS)					
AX		NOMINAL	+TOL	-TOL	MEAS	DEV	OUTTOL
M		18.210	0.200	-0.200	18.033	-0.177	0.000
	MM	DIST18.21-2 - PNT10 TO PLN21 (YAXIS)					
AX		NOMINAL	+TOL	-TOL	MEAS	DEV	OUTTOL
M		18.210	0.200	-0.200	18.073	-0.137	0.000
	MM	DIST10_1 - PNT7 TO PNT8 (XAXIS)					
AX		NOMINAL	+TOL	-TOL	MEAS	DEV	OUTTOL
M		10.000	0.200	-0.200	10.024	0.024	0.000
	MM	DIST4_1 - PLN21 TO PLN19 (YAXIS)					
AX		NOMINAL	+TOL	-TOL	MEAS	DEV	OUTTOL
M		4.000	0.100	-0.100	3.990	-0.010	0.000
	MM	R20_1 - CIR_R20-1					
AX		NOMINAL	+TOL	-TOL	MEAS	DEV	OUTTOL
R		20.000	0.200	-0.200	19.888	-0.112	0.000
	MM	R20_2 - CIR_R20-2					
AX		NOMINAL	+TOL	-TOL	MEAS	DEV	OUTTOL
R		20.000	0.200	-0.200	19.914	-0.086	0.000
	MM	R3_1 - CIR_R3-1					
AX		NOMINAL	+TOL	-TOL	MEAS	DEV	OUTTOL
R		3.000	0.100	-0.100	3.019	0.019	0.000
	MM	R3_2 - CIR_R3-2					
AX		NOMINAL	+TOL	-TOL	MEAS	DEV	OUTTOL
R		3.000	0.100	-0.100	3.009	0.009	0.000
	MM	DIST50 - PLN1 TO PLN3 (ZAXIS)					
AX		NOMINAL	+TOL	-TOL	MEAS	DEV	OUTTOL
M		50.000	0.300	-0.300	50.039	0.039	0.000
	MM	DIST49 - PLN8 TO PLN20 (ZAXIS)					
AX		NOMINAL	+TOL	-TOL	MEAS	DEV	OUTTOL
M		49.000	0.300	-0.300	49.029	0.029	0.000

	MM	DIST10_2 - PLN4 TO PLN3 (ZAXIS)					
AX		NOMINAL	+TOL	-TOL	MEAS	DEV	OUTTOL
M		10.000	0.200	-0.200	10.028	0.028	0.000
	MM	DIST5_1 - PLN3 TO CIR_Ø4.04-1 (ZAXIS)					
AX		NOMINAL	+TOL	-TOL	MEAS	DEV	OUTTOL
M		5.000	0.100	-0.100	5.018	0.018	0.000
	MM	DIST5_2 - PLN3 TO CIR_Ø4.04-2 (ZAXIS)					
AX		NOMINAL	+TOL	-TOL	MEAS	DEV	OUTTOL
M		5.000	0.100	-0.100	5.026	0.026	0.000
	MM	DIST1 - PLN1 TO PLNAU_Z- (ZAXIS)					
AX		NOMINAL	+TOL	-TOL	MEAS	DEV	OUTTOL
M		1.000	0.100	-0.100	0.998	-0.002	0.000
	MM	LOC0.1_B - PLNAU_Z- TO CYL_Ø3.28 (ZAXIS)					
AX		NOMINAL	+TOL	-TOL	MEAS	DEV	OUTTOL
M		5.000	0.050	-0.050	5.024	0.024	0.000
//	MM	PARL0.1_B - CYL_Ø3.28 TO PLNAU_Z-					
AX		NOMINAL	+TOL	-TOL	MEAS	DEV	OUTTOL
M		0.000	0.100	0.000	0.005	0.005	0.000
	MM	DIST9 - PNT6 TO PLN1 (ZAXIS)					
AX		NOMINAL	+TOL	-TOL	MEAS	DEV	OUTTOL
M		9.000	0.200	-0.200	8.979	-0.021	0.000
	MM	DIST27.07 - PLNAU_Y- TO PNT5 (YAXIS)					
AX		NOMINAL	+TOL	-TOL	MEAS	DEV	OUTTOL
M		27.070	0.200	-0.200	27.085	0.015	0.000
	MM	DIST25 - PLN7 TO PLNAU_Y- (YAXIS)					
AX		NOMINAL	+TOL	-TOL	MEAS	DEV	OUTTOL
M		25.000	0.200	-0.200	25.010	0.010	0.000
	MM	DIST5_3 - PLNAU_Y- TO PLN2 (YAXIS)					
AX		NOMINAL	+TOL	-TOL	MEAS	DEV	OUTTOL
M		5.000	0.100	-0.100	4.951	-0.049	0.000
	MM	Ø5 - CIR_Ø5					
AX		NOMINAL	+TOL	-TOL	MEAS	DEV	OUTTOL
D		5.000	0.100	-0.100	4.976	-0.024	0.000
	MM	Ø4.04_1 - CIR_Ø4.04-1					
AX		NOMINAL	+TOL	-TOL	MEAS	DEV	OUTTOL
D		4.040	0.030	-0.030	4.054	0.014	0.000
RN		0.000	0.060	0.000	0.003	0.003	0.000
	MM	Ø4.04_2 - CIR_Ø4.04-2					
AX		NOMINAL	+TOL	-TOL	MEAS	DEV	OUTTOL
D		4.040	0.030	-0.030	4.088	0.048	0.018
RN		0.000	0.060	0.000	0.014	0.014	0.000

(a) Pages 1 (left) and 2 (right).

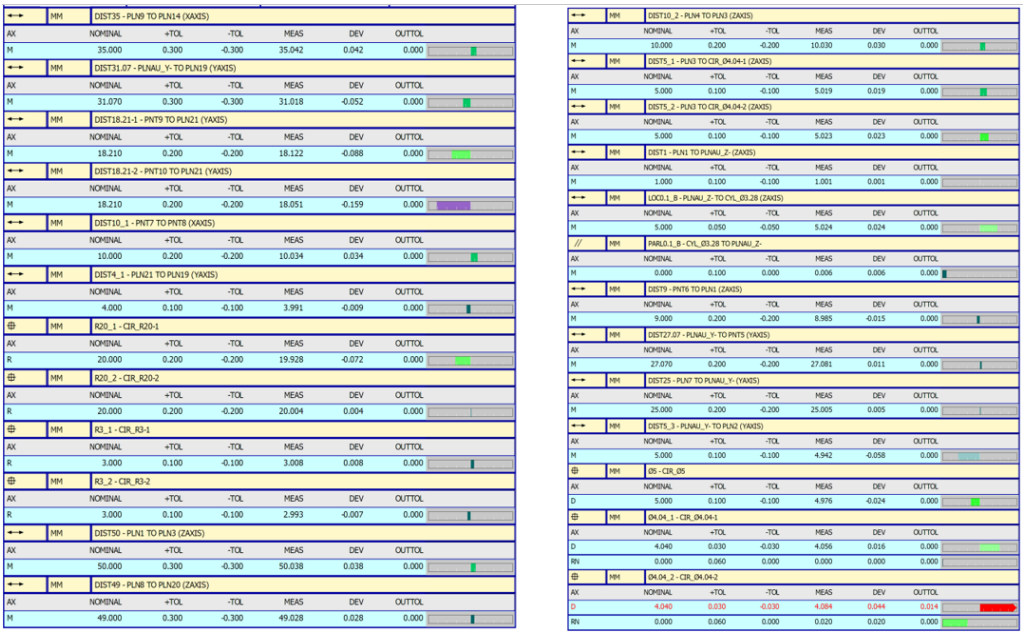


	MM	Ø3.28 - CYL_Ø3.28					
AX		NOMINAL	+TOL	-TOL	MEAS	DEV	OUTTOL
D		3.280	0.020	-0.020	3.289	0.009	0.000
RN		0.000	0.040	0.000	0.002	0.002	0.000
⊥	MM	PERP0.1_A-1 - CYLØ4.04 TO PLN17					
AX		NOMINAL	+TOL	-TOL	MEAS	DEV	OUTTOL
M		0.000	0.100	0.000	0.036	0.036	0.000
⊥	MM	PERP0.1_A-2 - CYLØ4.04 TO PLN12					
AX		NOMINAL	+TOL	-TOL	MEAS	DEV	OUTTOL
M		0.000	0.100	0.000	0.075	0.075	0.000
	MM	DIST15 - PLN6 TO PLN5 (XAXIS)					
AX		NOMINAL	+TOL	-TOL	MEAS	DEV	OUTTOL
M		15.000	0.200	-0.200	14.949	-0.051	0.000
	MM	DIST4_2 - PLN19 TO PLN21 (YAXIS)					
AX		NOMINAL	+TOL	-TOL	MEAS	DEV	OUTTOL
M		4.000	0.200	-0.200	3.986	-0.014	0.000
	MM	DIST4_3 - PLN21 TO PLN19 (YAXIS)					
AX		NOMINAL	+TOL	-TOL	MEAS	DEV	OUTTOL
M		4.000	0.200	-0.200	3.993	-0.007	0.000
	MM	DIST10_3 - PLN15 TO PLN16 (YAXIS)					
AX		NOMINAL	+TOL	-TOL	MEAS	DEV	OUTTOL
M		10.000	0.200	-0.200	9.961	-0.039	0.000
	MM	DIST10_4 - PLN10 TO PLN11 (YAXIS)					
AX		NOMINAL	+TOL	-TOL	MEAS	DEV	OUTTOL
M		10.000	0.200	-0.200	9.960	-0.040	0.000
	MM	DIST10_5 - PLN9 TO PLN5 (XAXIS)					
AX		NOMINAL	+TOL	-TOL	MEAS	DEV	OUTTOL
M		10.000	0.200	-0.200	10.036	0.036	0.000
	MM	DIST10_7 - PLN6 TO PLN14 (XAXIS)					
AX		NOMINAL	+TOL	-TOL	MEAS	DEV	OUTTOL
M		10.000	0.200	-0.200	10.056	0.056	0.000
	MM	DIST5_4 - PLN17 TO PLN14 (XAXIS)					
AX		NOMINAL	+TOL	-TOL	MEAS	DEV	OUTTOL
M		5.000	0.100	-0.100	5.021	0.021	0.000
	MM	DIST5_5 - PLN12 TO PLN9 (XAXIS)					
AX		NOMINAL	+TOL	-TOL	MEAS	DEV	OUTTOL
M		5.000	0.100	-0.100	5.004	0.004	0.000
	MM	DIST191_1 - PLN14 TO PLN18 (XAXIS)					
AX		NOMINAL	+TOL	-TOL	MEAS	DEV	OUTTOL
M		1.910	0.100	-0.100	1.915	0.005	0.000

	MM	DIST191_2 - PLN9 TO PLN13 (XAXIS)					
AX		NOMINAL	+TOL	-TOL	MEAS	DEV	OUTTOL
M		1.910	0.100	-0.100	1.897	-0.013	0.000
	MM	R5_1 - CIR_R5-1					
AX		NOMINAL	+TOL	-TOL	MEAS	DEV	OUTTOL
R		5.000	0.100	-0.100	4.968	-0.032	0.000
	MM	R5_2 - CIR_R5-2					
AX		NOMINAL	+TOL	-TOL	MEAS	DEV	OUTTOL
R		5.000	0.100	-0.100	4.959	-0.041	0.000

(b) Pages 3 (left) and 4 (right).

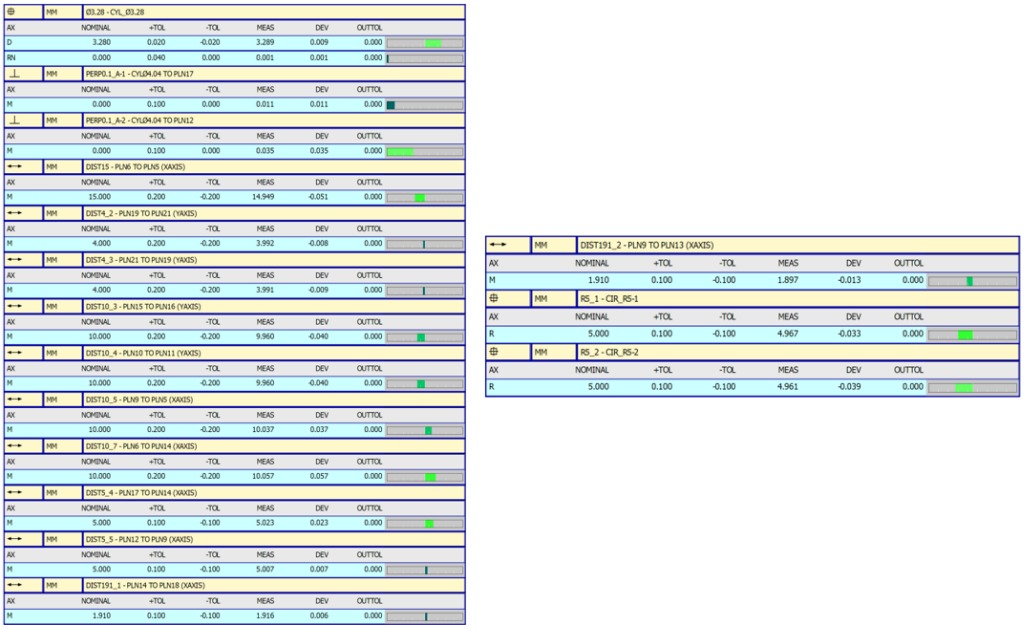
Figure G.3: Inspection report of workpiece number 3.



	MM	DIST35 - PLN9 TO PLN14 (XAXIS)					
AX		NOMINAL	+TOL	-TOL	MEAS	DEV	OUTTOL
M		35.000	0.300	-0.300	35.042	0.042	0.000
	MM	DIST31.07 - PLNAU_Y- TO PLN19 (YAXIS)					
AX		NOMINAL	+TOL	-TOL	MEAS	DEV	OUTTOL
M		31.070	0.300	-0.300	31.018	-0.052	0.000
	MM	DIST18.21-1 - PNT9 TO PLN21 (YAXIS)					
AX		NOMINAL	+TOL	-TOL	MEAS	DEV	OUTTOL
M		18.210	0.200	-0.200	18.122	-0.088	0.000
	MM	DIST18.21-2 - PNT10 TO PLN21 (YAXIS)					
AX		NOMINAL	+TOL	-TOL	MEAS	DEV	OUTTOL
M		18.210	0.200	-0.200	18.051	-0.159	0.000
	MM	DIST10_1 - PNT7 TO PNT8 (XAXIS)					
AX		NOMINAL	+TOL	-TOL	MEAS	DEV	OUTTOL
M		10.000	0.200	-0.200	10.034	0.034	0.000
	MM	DIST4_1 - PLN21 TO PLN19 (YAXIS)					
AX		NOMINAL	+TOL	-TOL	MEAS	DEV	OUTTOL
M		4.000	0.100	-0.100	3.991	-0.009	0.000
	MM	R20_1 - CIR_R20-1					
AX		NOMINAL	+TOL	-TOL	MEAS	DEV	OUTTOL
R		20.000	0.200	-0.200	19.928	-0.072	0.000
	MM	R20_2 - CIR_R20-2					
AX		NOMINAL	+TOL	-TOL	MEAS	DEV	OUTTOL
R		20.000	0.200	-0.200	20.004	0.004	0.000
	MM	R3_1 - CIR_R3-1					
AX		NOMINAL	+TOL	-TOL	MEAS	DEV	OUTTOL
R		3.000	0.100	-0.100	3.008	0.008	0.000
	MM	R3_2 - CIR_R3-2					
AX		NOMINAL	+TOL	-TOL	MEAS	DEV	OUTTOL
R		3.000	0.100	-0.100	2.993	-0.007	0.000
	MM	DIST50 - PLN1 TO PLN3 (ZAXIS)					
AX		NOMINAL	+TOL	-TOL	MEAS	DEV	OUTTOL
M		50.000	0.300	-0.300	50.038	0.038	0.000
	MM	DIST49 - PLN8 TO PLN20 (ZAXIS)					
AX		NOMINAL	+TOL	-TOL	MEAS	DEV	OUTTOL
M		49.000	0.300	-0.300	49.028	0.028	0.000

	MM	DIST10_2 - PLN4 TO PLN3 (ZAXIS)					
AX		NOMINAL	+TOL	-TOL	MEAS	DEV	OUTTOL
M		10.000	0.200	-0.200	10.030	0.030	0.000
	MM	DIST5_1 - PLN3 TO CIR_Ø4.04-1 (ZAXIS)					
AX		NOMINAL	+TOL	-TOL	MEAS	DEV	OUTTOL
M		5.000	0.100	-0.100	5.019	0.019	0.000
	MM	DIST5_2 - PLN3 TO CIR_Ø4.04-2 (ZAXIS)					
AX		NOMINAL	+TOL	-TOL	MEAS	DEV	OUTTOL
M		5.000	0.100	-0.100	5.023	0.023	0.000
	MM	DIST1 - PLN1 TO PLNAU_Z- (ZAXIS)					
AX		NOMINAL	+TOL	-TOL	MEAS	DEV	OUTTOL
M		1.000	0.100	-0.100	1.001	0.001	0.000
	MM	LOCO.1_B - PLNAU_Z- TO CYL_Ø3.28 (ZAXIS)					
AX		NOMINAL	+TOL	-TOL	MEAS	DEV	OUTTOL
M		5.000	0.050	-0.050	5.024	0.024	0.000
//	MM	PARL0.1_B - CYL_Ø3.28 TO PLNAU_Z-					
AX		NOMINAL	+TOL	-TOL	MEAS	DEV	OUTTOL
M		0.000	0.100	0.000	0.006	0.006	0.000
	MM	DIST9 - PNT6 TO PLN1 (ZAXIS)					
AX		NOMINAL	+TOL	-TOL	MEAS	DEV	OUTTOL
M		9.000	0.200	-0.200	8.985	-0.015	0.000
	MM	DIST27.07 - PLNAU_Y- TO PNT5 (YAXIS)					
AX		NOMINAL	+TOL	-TOL	MEAS	DEV	OUTTOL
M		27.070	0.200	-0.200	27.081	0.011	0.000
	MM	DIST25 - PLN7 TO PLNAU_Y- (YAXIS)					
AX		NOMINAL	+TOL	-TOL	MEAS	DEV	OUTTOL
M		25.000	0.200	-0.200	25.005	0.005	0.000
	MM	DIST5_3 - PLNAU_Y- TO PLN2 (YAXIS)					
AX		NOMINAL	+TOL	-TOL	MEAS	DEV	OUTTOL
M		5.000	0.100	-0.100	4.942	-0.058	0.000
	MM	Ø5 - CIR_Ø5					
AX		NOMINAL	+TOL	-TOL	MEAS	DEV	OUTTOL
D		5.000	0.100	-0.100	4.976	-0.024	0.000
	MM	Ø4.04_1 - CIR_Ø4.04-1					
AX		NOMINAL	+TOL	-TOL	MEAS	DEV	OUTTOL
D		4.040	0.030	-0.030	4.056	0.016	0.000
RN		0.000	0.060	0.000	0.000	0.000	0.000
	MM	Ø4.04_2 - CIR_Ø4.04-2					
AX		NOMINAL	+TOL	-TOL	MEAS	DEV	OUTTOL
D		4.040	0.030	-0.030	4.084	0.044	0.014
RN		0.000	0.060	0.000	0.020	0.020	0.000

(a) Pages 1 (left) and 2 (right).

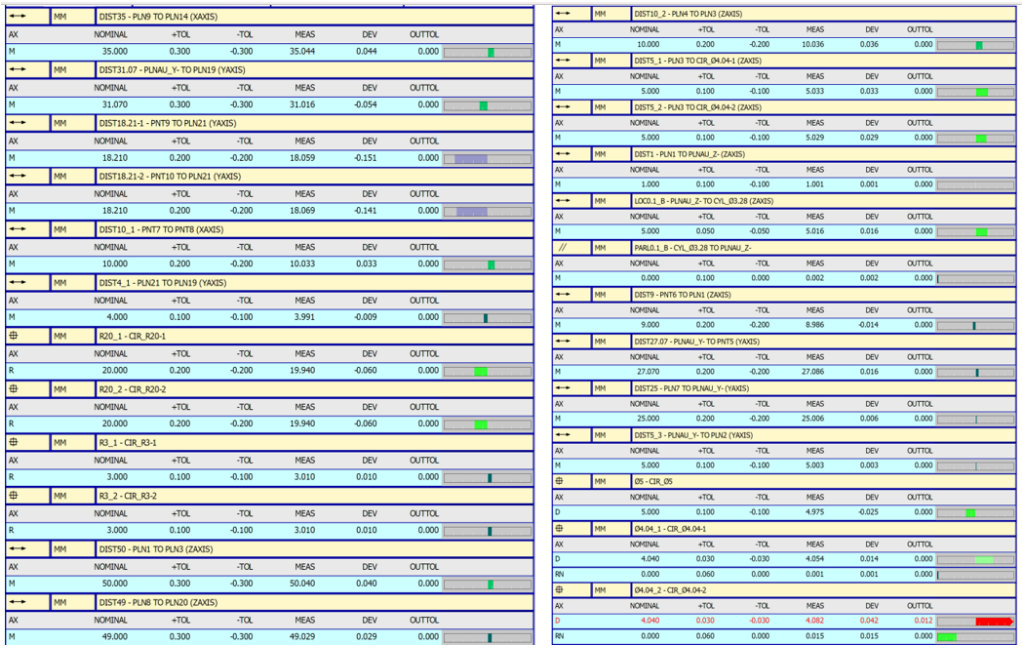


	MM	Ø3.28 - CYL_Ø3.28					
AX		NOMINAL	+TOL	-TOL	MEAS	DEV	OUTTOL
D		3.280	0.020	-0.020	3.289	0.009	0.000
RN		0.000	0.040	0.000	0.001	0.001	0.000
⊥	MM	PERP0.1_A-1 - CYL@4.04 TO PLN17					
AX		NOMINAL	+TOL	-TOL	MEAS	DEV	OUTTOL
M		0.000	0.100	0.000	0.011	0.011	0.000
⊥	MM	PERP0.1_A-2 - CYL@4.04 TO PLN12					
AX		NOMINAL	+TOL	-TOL	MEAS	DEV	OUTTOL
M		0.000	0.100	0.000	0.035	0.035	0.000
	MM	DIST15 - PLN6 TO PLN5 (XAXIS)					
AX		NOMINAL	+TOL	-TOL	MEAS	DEV	OUTTOL
M		15.000	0.200	-0.200	14.949	-0.051	0.000
	MM	DIST4_2 - PLN19 TO PLN21 (YAXIS)					
AX		NOMINAL	+TOL	-TOL	MEAS	DEV	OUTTOL
M		4.000	0.200	-0.200	3.992	-0.008	0.000
	MM	DIST4_3 - PLN21 TO PLN19 (YAXIS)					
AX		NOMINAL	+TOL	-TOL	MEAS	DEV	OUTTOL
M		4.000	0.200	-0.200	3.991	-0.009	0.000
	MM	DIST10_3 - PLN15 TO PLN16 (YAXIS)					
AX		NOMINAL	+TOL	-TOL	MEAS	DEV	OUTTOL
M		10.000	0.200	-0.200	9.960	-0.040	0.000
	MM	DIST10_4 - PLN10 TO PLN11 (YAXIS)					
AX		NOMINAL	+TOL	-TOL	MEAS	DEV	OUTTOL
M		10.000	0.200	-0.200	9.960	-0.040	0.000
	MM	DIST10_5 - PLN9 TO PLN5 (XAXIS)					
AX		NOMINAL	+TOL	-TOL	MEAS	DEV	OUTTOL
M		10.000	0.200	-0.200	10.037	0.037	0.000
	MM	DIST10_7 - PLN6 TO PLN14 (XAXIS)					
AX		NOMINAL	+TOL	-TOL	MEAS	DEV	OUTTOL
M		10.000	0.200	-0.200	10.057	0.057	0.000
	MM	DIST5_4 - PLN17 TO PLN14 (XAXIS)					
AX		NOMINAL	+TOL	-TOL	MEAS	DEV	OUTTOL
M		5.000	0.100	-0.100	5.023	0.023	0.000
	MM	DIST5_5 - PLN12 TO PLN9 (XAXIS)					
AX		NOMINAL	+TOL	-TOL	MEAS	DEV	OUTTOL
M		5.000	0.100	-0.100	5.007	0.007	0.000
	MM	DIST191_1 - PLN14 TO PLN18 (XAXIS)					
AX		NOMINAL	+TOL	-TOL	MEAS	DEV	OUTTOL
M		1.910	0.100	-0.100	1.916	0.006	0.000

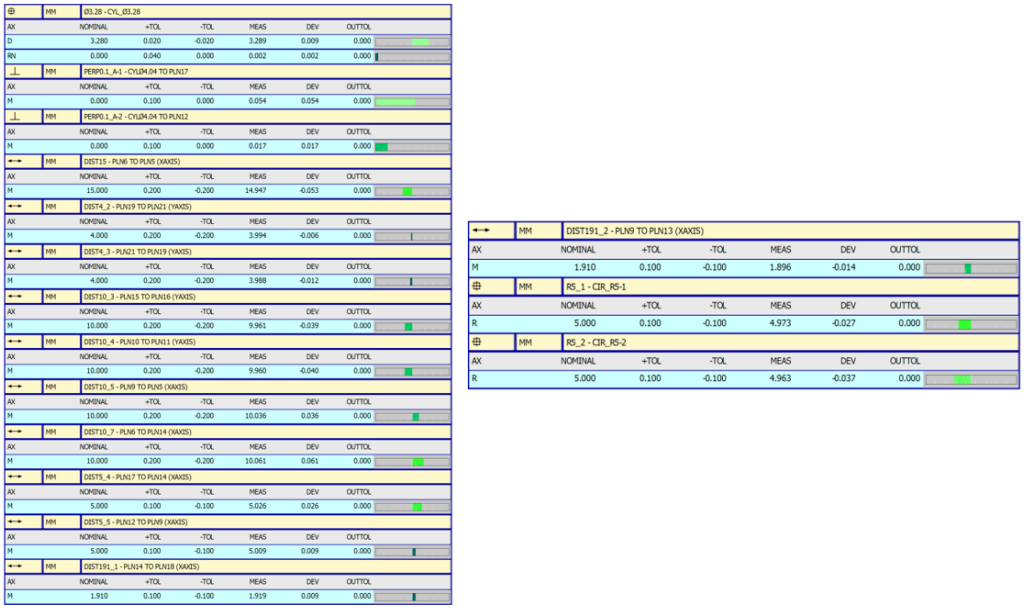
	MM	DIST191_2 - PLN9 TO PLN13 (XAXIS)					
AX		NOMINAL	+TOL	-TOL	MEAS	DEV	OUTTOL
M		1.910	0.100	-0.100	1.897	-0.013	0.000
	MM	R5_1 - CIR_R5-1					
AX		NOMINAL	+TOL	-TOL	MEAS	DEV	OUTTOL
R		5.000	0.100	-0.100	4.967	-0.033	0.000
	MM	R5_2 - CIR_R5-2					
AX		NOMINAL	+TOL	-TOL	MEAS	DEV	OUTTOL
R		5.000	0.100	-0.100	4.961	-0.039	0.000

(b) Pages 3 (left) and 4 (right).

Figure G.4: Inspection report of workpiece number 4.

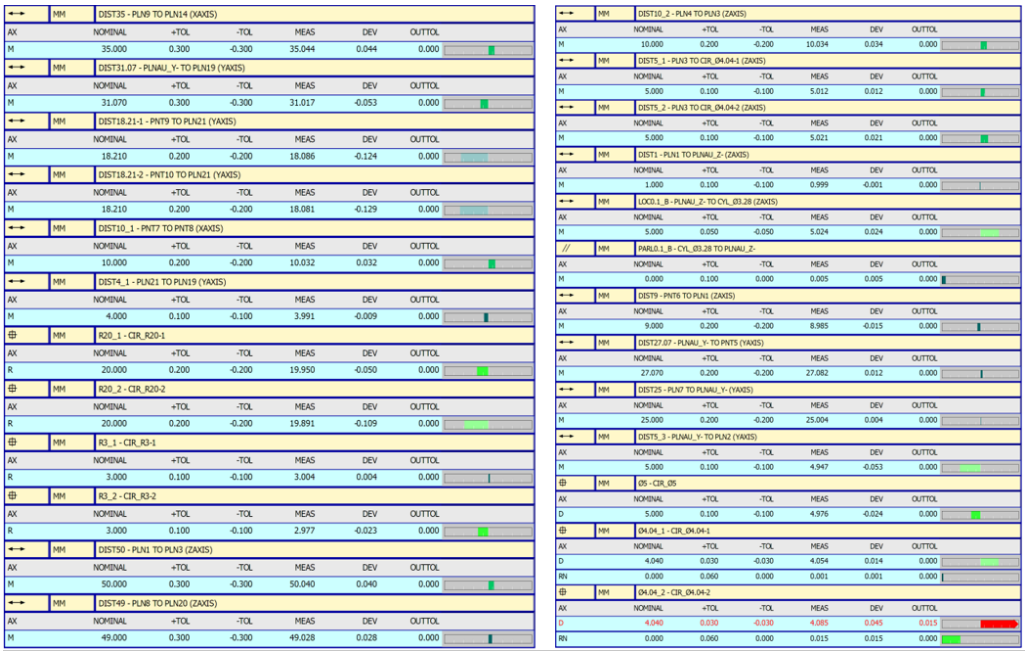


(a) Pages 1 (left) and 2 (right).



(b) Pages 3 (left) and 4 (right).

Figure G.5: Inspection report of workpiece number 5.



MM	DIST35 - PLN9 TO PLN14 (XAXIS)					
AX	NOMINAL	+TOL	-TOL	MEAS	DEV	OUTTOL
M	35.000	0.300	-0.300	35.044	0.044	0.000

MM	DIST31.07 - PLNAU_Y- TO PLN19 (YAXIS)					
AX	NOMINAL	+TOL	-TOL	MEAS	DEV	OUTTOL
M	31.070	0.300	-0.300	31.017	-0.053	0.000

MM	DIST18.21-1 - PNT9 TO PLN21 (YAXIS)					
AX	NOMINAL	+TOL	-TOL	MEAS	DEV	OUTTOL
M	18.210	0.200	-0.200	18.086	-0.124	0.000

MM	DIST18.21-2 - PNT10 TO PLN21 (YAXIS)					
AX	NOMINAL	+TOL	-TOL	MEAS	DEV	OUTTOL
M	18.210	0.200	-0.200	18.081	-0.129	0.000

MM	DIST10_1 - PNT7 TO PNT8 (XAXIS)					
AX	NOMINAL	+TOL	-TOL	MEAS	DEV	OUTTOL
M	10.000	0.200	-0.200	10.032	0.032	0.000

MM	DIST4_1 - PLN21 TO PLN19 (YAXIS)					
AX	NOMINAL	+TOL	-TOL	MEAS	DEV	OUTTOL
M	4.000	0.100	-0.100	3.991	-0.009	0.000

MM	R20_1 - CIR_R20-1					
AX	NOMINAL	+TOL	-TOL	MEAS	DEV	OUTTOL
R	20.000	0.200	-0.200	19.950	-0.050	0.000

MM	R20_2 - CIR_R20-2					
AX	NOMINAL	+TOL	-TOL	MEAS	DEV	OUTTOL
R	20.000	0.200	-0.200	19.891	-0.109	0.000

MM	R3_1 - CIR_R3-1					
AX	NOMINAL	+TOL	-TOL	MEAS	DEV	OUTTOL
R	3.000	0.100	-0.100	3.004	0.004	0.000

MM	R3_2 - CIR_R3-2					
AX	NOMINAL	+TOL	-TOL	MEAS	DEV	OUTTOL
R	3.000	0.100	-0.100	2.977	-0.023	0.000

MM	DIST50 - PLN1 TO PLN3 (ZAXIS)					
AX	NOMINAL	+TOL	-TOL	MEAS	DEV	OUTTOL
M	50.000	0.300	-0.300	50.040	0.040	0.000

MM	DIST49 - PLN8 TO PLN20 (ZAXIS)					
AX	NOMINAL	+TOL	-TOL	MEAS	DEV	OUTTOL
M	49.000	0.300	-0.300	49.028	0.028	0.000

MM	DIST10_2 - PLN4 TO PLN3 (ZAXIS)					
AX	NOMINAL	+TOL	-TOL	MEAS	DEV	OUTTOL
M	10.000	0.200	-0.200	10.034	0.034	0.000

MM	DIST5_1 - PLN3 TO CIR_Ø4.04-1 (ZAXIS)					
AX	NOMINAL	+TOL	-TOL	MEAS	DEV	OUTTOL
M	5.000	0.100	-0.100	5.012	0.012	0.000

MM	DIST5_2 - PLN3 TO CIR_Ø4.04-2 (ZAXIS)					
AX	NOMINAL	+TOL	-TOL	MEAS	DEV	OUTTOL
M	5.000	0.100	-0.100	5.021	0.021	0.000

MM	DIST1 - PLN1 TO PLNAU_Z- (ZAXIS)					
AX	NOMINAL	+TOL	-TOL	MEAS	DEV	OUTTOL
M	1.000	0.100	-0.100	0.999	-0.001	0.000

MM	LOC0.1_B - PLNAU_Z- TO CYL_Ø3.28 (ZAXIS)					
AX	NOMINAL	+TOL	-TOL	MEAS	DEV	OUTTOL
M	5.000	0.050	-0.050	5.024	0.024	0.000

MM	PARL0.1_B - CYL_Ø3.28 TO PLNAU_Z-					
AX	NOMINAL	+TOL	-TOL	MEAS	DEV	OUTTOL
M	0.000	0.100	0.000	0.005	0.005	0.000

MM	DIST9 - PNT6 TO PLN1 (ZAXIS)					
AX	NOMINAL	+TOL	-TOL	MEAS	DEV	OUTTOL
M	9.000	0.200	-0.200	8.985	-0.015	0.000

MM	DIST27.07 - PLNAU_Y- TO PNT5 (YAXIS)					
AX	NOMINAL	+TOL	-TOL	MEAS	DEV	OUTTOL
M	27.070	0.200	-0.200	27.082	0.012	0.000

MM	DIST25 - PLN7 TO PLNAU_Y- (YAXIS)					
AX	NOMINAL	+TOL	-TOL	MEAS	DEV	OUTTOL
M	25.000	0.200	-0.200	25.004	0.004	0.000

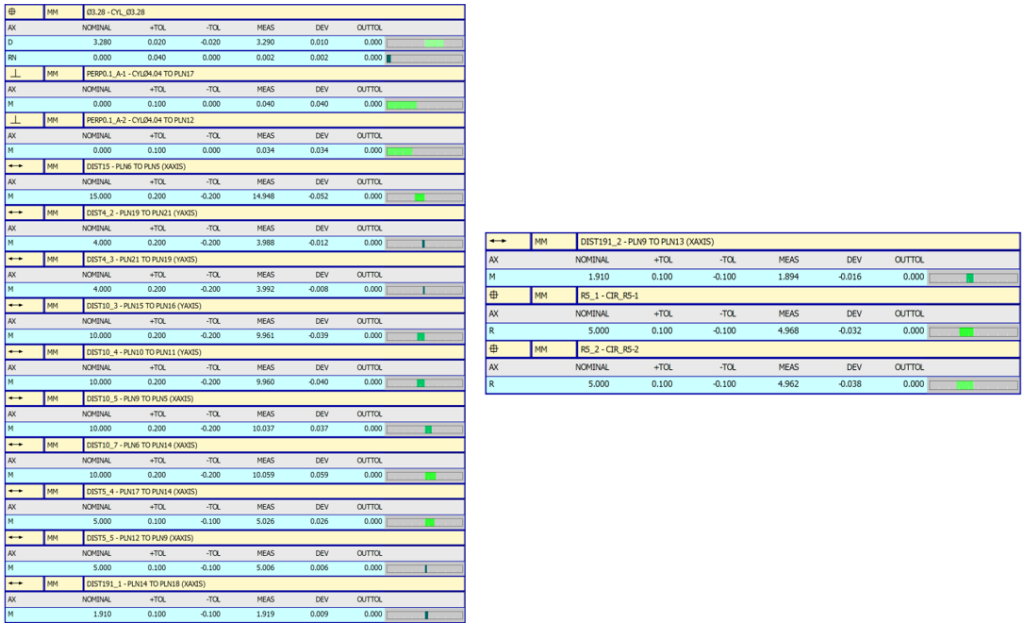
MM	DIST5_3 - PLNAU_Y- TO PLN2 (YAXIS)					
AX	NOMINAL	+TOL	-TOL	MEAS	DEV	OUTTOL
M	5.000	0.100	-0.100	4.947	-0.053	0.000

MM	Ø5 - CIR_Ø5					
AX	NOMINAL	+TOL	-TOL	MEAS	DEV	OUTTOL
D	5.000	0.100	-0.100	4.976	-0.024	0.000

MM	Ø4.04_1 - CIR_Ø4.04-1					
AX	NOMINAL	+TOL	-TOL	MEAS	DEV	OUTTOL
D	4.040	0.030	-0.030	4.054	0.014	0.000
RN	0.000	0.060	0.000	0.001	0.001	0.000

MM	Ø4.04_2 - CIR_Ø4.04-2					
AX	NOMINAL	+TOL	-TOL	MEAS	DEV	OUTTOL
D	4.040	0.030	-0.030	4.085	0.045	0.015
RN	0.000	0.060	0.000	0.015	0.015	0.000

(a) Pages 1 (left) and 2 (right).



MM	Ø3.28 - CYL_Ø3.28					
AX	NOMINAL	+TOL	-TOL	MEAS	DEV	OUTTOL
D	3.280	0.020	-0.020	3.290	0.010	0.000
RN	0.000	0.040	0.000	0.002	0.002	0.000

MM	PERP0.1_A-1 - CYLØ4.04 TO PLN17					
AX	NOMINAL	+TOL	-TOL	MEAS	DEV	OUTTOL
M	0.000	0.100	0.000	0.040	0.040	0.000

MM	PERP0.1_A-2 - CYLØ4.04 TO PLN12					
AX	NOMINAL	+TOL	-TOL	MEAS	DEV	OUTTOL
M	0.000	0.100	0.000	0.034	0.034	0.000

MM	DIST15 - PLN6 TO PLN5 (XAXIS)					
AX	NOMINAL	+TOL	-TOL	MEAS	DEV	OUTTOL
M	15.000	0.200	-0.200	14.948	-0.052	0.000

MM	DIST4_2 - PLN19 TO PLN21 (YAXIS)					
AX	NOMINAL	+TOL	-TOL	MEAS	DEV	OUTTOL
M	4.000	0.200	-0.200	3.988	-0.012	0.000

MM	DIST4_3 - PLN21 TO PLN19 (YAXIS)					
AX	NOMINAL	+TOL	-TOL	MEAS	DEV	OUTTOL
M	4.000	0.200	-0.200	3.992	-0.008	0.000

MM	DIST10_3 - PLN15 TO PLN16 (YAXIS)					
AX	NOMINAL	+TOL	-TOL	MEAS	DEV	OUTTOL
M	10.000	0.200	-0.200	9.961	-0.039	0.000

MM	DIST10_4 - PLN10 TO PLN11 (YAXIS)					
AX	NOMINAL	+TOL	-TOL	MEAS	DEV	OUTTOL
M	10.000	0.200	-0.200	9.960	-0.040	0.000

MM	DIST10_5 - PLN9 TO PLN5 (XAXIS)					
AX	NOMINAL	+TOL	-TOL	MEAS	DEV	OUTTOL
M	10.000	0.200	-0.200	10.037	0.037	0.000

MM	DIST10_7 - PLN6 TO PLN14 (XAXIS)					
AX	NOMINAL	+TOL	-TOL	MEAS	DEV	OUTTOL
M	10.000	0.200	-0.200	10.059	0.059	0.000

MM	DIST5_4 - PLN17 TO PLN14 (XAXIS)					
AX	NOMINAL	+TOL	-TOL	MEAS	DEV	OUTTOL
M	5.000	0.100	-0.100	5.026	0.026	0.000

MM	DIST5_5 - PLN12 TO PLN9 (XAXIS)					
AX	NOMINAL	+TOL	-TOL	MEAS	DEV	OUTTOL
M	5.000	0.100	-0.100	5.006	0.006	0.000

MM	DIST191_1 - PLN14 TO PLN18 (XAXIS)					
AX	NOMINAL	+TOL	-TOL	MEAS	DEV	OUTTOL
M	1.910	0.100	-0.100	1.919	0.009	0.000

MM	DIST191_2 - PLN9 TO PLN13 (XAXIS)					
AX	NOMINAL	+TOL	-TOL	MEAS	DEV	OUTTOL
M	1.910	0.100	-0.100	1.894	-0.016	0.000

MM	R5_1 - CIR_R5-1					
AX	NOMINAL	+TOL	-TOL	MEAS	DEV	OUTTOL
R	5.000	0.100	-0.100	4.968	-0.032	0.000

MM	R5_2 - CIR_R5-2					
AX	NOMINAL	+TOL	-TOL	MEAS	DEV	OUTTOL
R	5.000	0.100	-0.100	4.962	-0.038	0.000

(b) Pages 3 (left) and 4 (right).

Figure G.6: Inspection report of workpiece number 6.

This page was intentionally left blank

References

[1] Waleed Ahmed, Hussien Hegab, Atef Mohany, and Hossam Kishawy. Analysis and optimization of machining hardened steel aisi 4140 with self-propelled rotary tools. *Materials*, 14, 2021. doi: 10.3390/ma14206106.

[2] Stewart C. Black, Vic Chiles, A.J. Lissaman, and S.J. Martin. 11 - turning and milling. In Stewart C. Black, Vic Chiles, A.J. Lissaman, and S.J. Martin, editors, *Principles of Engineering Manufacture (Third Edition)*, pages 316–371. Butterworth-Heinemann, Oxford, third edition edition, 1996. doi: https://doi.org/10.1016/B978-034063195-9/50042-0.

[3] Josip Brnic, Goran Turkalj, Marko Canadija, Domagoj Lanc, and Marino Brcic. Study of the effects of high temperatures on the engineering properties of steel 42crmo4. *High Temperature Materials and Processes*, 34, 2015. doi: 10.1515/htmp-2014-0011.

[4] João Henrique Gregório Lopes Caxias, Luís Filipe Galrão dos Reis Vítor Manuel Rodrigues Anes Júri Presidente, Paulo Rui Alves Fernandes Orientador, Luís Filipe Galrão dos Reis Vogal, and Rui Fernando dos Santos Pereira Martins. Avaliação do dano acumulado em fadiga multiaxial aleatória engenharia mecânica. Technical report, Instituto Superior Técnico de Lisboa, 2017.

[5] Maheswara Rao Ch and Rajana Vara Prasad. Effect of milling process parameters on the multiple performance characteristics. Technical report, 2018. doi: = https://www.researchgate.net/publication/347306043.

[6] Kuang Hua Chang. *e-Design: Computer-aided engineering design*. 2015. doi: https://doi.org/10.1016/C2009-0-63076-2.

[7] Wen Lin Chu, Min Jia Xie, Qun Wei Chang, and Her Terng Yau. Research on the recognition of machining conditions based on sound and vibration signals of a cnc milling machine. *IEEE Sensors Journal*, 22, 2022. doi: 10.1109/JSEN.2022.3150751.

[8] Sandvik Coromant. *Manual Técnico*. AB Sandvik Coromant, 2010.

[9] L. Norberto López de Lacalle, Francisco J. Campa, and Aitzol Lamikiz. Chapter 3 : Milling. *Modern Machining Technology*, 2011. https://www.sciencedirect.com/science/article/pii/B9780857090997500034 (accessed March, 2025).

[10] Dormer. *Manual Técnico*. Dormer, 2005.

[11] Eugen Fahrion GmbH & Co. KG. *Tool Clamping Systems*. Eugen Fahrion GmbH & Co. KG, Kaisersbach, Germany. https://fahrion.blaetterkatalog.de/?catalog=FAHRION_EN_Tool_Clamping_Systems_2022 (accessed May, 2025).

[12] Eugen Fahrion GmbH & Co. KG. *Centro|P Premium*. Eugen Fahrion GmbH & Co. KG, Kaisersbach, Germany, 2024. https://fahrion.blaetterkatalog.de/?catalog=CENTRO_P_premium_2024_EN (accessed May, 2025).

[13] Muhamad Rausyan Fikri, Kushendarsyah Saptaji, and Fijai Naja Azmi. Wireless vibration monitoring system for milling process and analysis of the influence of processing parameters. *Journal of ICT Research and Applications*, 16:38–55, 4 2022. doi: 10.5614/itbj.ict.res.appl.2022.16.1.3.

[14] Domnita Fratila. Numerical and experimental approach of cutting temperatures to green turning of 42crmo4 steel. *Materials and Manufacturing Processes*, 31, 2016. doi: 10.1080/10426914.2015.1004708.

[15] Mohamad Hazwan Mohd Ghazali and Wan Rahiman. Vibration analysis for machine monitoring and diagnosis: A systematic review, 2021. doi: 10.1155/2021/9469318.

[16] Guhring GmbH. *Deep-Hole Drilling Technical Support*. Albstadt, Germany. https://guhring.com/Support/Technical/Deep-Hole-Drilling (accessed May, 2025).

[17] Deepam Goyal, Chirag Mongia, and Shankar Sehgal. Applications of digital signal processing in monitoring machining processes and rotary components: A review. *IEEE Sensors Journal*, 21, 2021. doi: 10.1109/JSEN.2021.3050718.

[18] Guhring GmbH & Co. KG. Centering and pilot drilling recommendations. https://guhring.com/media/support/Centering-And-Pilot-Drilling-Recommendations.pdf (accessed April, 2025).

[19] Guhring GmbH & Co. KG. Coating services. https://guhring.com/ProductsServices/CoatingServices (accessed May, 2025).

[20] Guhring GmbH & Co. KG. Deep hole solutions. https://guhring.com/media/catalogs/hbkbyevb0ee.pdf (accessed April, 2025).

[21] Sunčana Smokvina Hanza, Lovro Štic, Lovro Liverić, and Vedrana Špada. Corrosion behaviour of tempered 42crmo4 steel. *Materiali in Tehnologije*, 55:427–433, 2021. doi: 10.17222/mit.2021.014.

[22] George Haynes. *Milling Machines and Milling Operations-Second Edition: The Fundamentals of Conventional and CNC Milling*. Cyber Press, 2016.

[23] Panling Huang, Jianfeng Li, Jie Sun, and Jun Zhou. Vibration analysis in milling titanium alloy based on signal processing of cutting force. *International Journal of Advanced Manufacturing Technology*, 64, 2013. doi: 10.1007/s00170-012-4039-x.

[24] Mohamd Imad, Hossam A. Kishawy, Nima Z. Yussefian, and Ali Hosseini. Effect of cutting edge radius when milling hardened steels: a finite element analysis and surface integrity investigation. *Machining Science and Technology*, 26, 2022. doi: 10.1080/10910344.2022.2129986.

[25] Rahul Jain, Surjya K. Pal, and Shiv B. Singh. 5 - numerical modeling methodologies for friction stir welding process. In J. Paulo Davim, editor, *Computational Methods*

and Production Engineering, Woodhead Publishing Reviews: Mechanical Engineering Series, pages 125–169. Woodhead Publishing, 2017. doi: https://doi.org/10.1016/B978-0-85709-481-0.00005-7.

[26] Hao Jiang, Xinhua Long, and Guang Meng. Study of the correlation between surface generation and cutting vibrations in peripheral milling. *Journal of Materials Processing Technology*, 208, 2008. doi: 10.1016/j.jmatprotec.2007.12.127.

[27] Paulo Davim João. *Princípios da Maquinagem*. 2º edição edition, 2008.

[28] Tomas Kalvoda and Yean Ren Hwang. A cutter tool monitoring in machining process using hilbert-huang transform. *International Journal of Machine Tools and Manufacture*, 50, 2010. doi: 10.1016/j.ijmachtools.2010.01.006.

[29] Tae Yong Kim, Joongwon Woo, Dongwon Shin, and Jongwon Kim. Indirect cutting force measurement in multi-axis simultaneous nc milling processes. *International Journal of Machine Tools and Manufacture*, 39, 1999. doi: 10.1016/S0890-6955(99)00027-9.

[30] Kistler Group. Accelerometers – precise vibration measurement, 2024. https://www.kistler.com/INT/en/accelerometer/C00000091 (accessed March, 2025).

[31] Praveen Kumar and Geeta Agnihotri. Cold drawing process-a review. Technical report, 2013. https://www.researchgate.net/publication/285666312_Cold_drawing_process_-_A_review (accessed March, 2025).

[32] Gábor Kónya and Zsolt F. Kovács. Effects of machining parameters and tool reconditioning on cutting force, tool wear, surface roughness and burr formation in nickel-based alloy milling. *Materials*, 16, 2023. doi: 10.3390/ma16227140.

[33] L. N. López De Lacalle, A. Lamikiz, J. A. Sánchez, and I. Fernández De Bustos. Recording of real cutting forces along the milling of complex parts. *Mechatronics*, 16, 2006. doi: 10.1016/j.mechatronics.2005.09.001.

[34] M. Lamraoui, M. Thomas, and M. El Badaoui. Cyclostationarity approach for monitoring chatter and tool wear in high speed milling. *Mechanical Systems and Signal Processing*, 44, 2014. doi: 10.1016/j.ymssp.2013.05.001.

[35] C. H. Lauro, L. C. Brandão, D. Baldo, R. A. Reis, and J. P. Davim. Monitoring and processing signal applied in machining processes - a review. *Measurement: Journal of the International Measurement Confederation*, 58, 2014. doi: 10.1016/j.measurement.2014.08.035.

[36] C.H. Lauro, L.C. Brandão, and S.L.M. Ribeiro Filho. Monitoring the temperature of the milling process using infrared camera. *Scientific Research and Essays*, 8, 2013. doi: 10.5897/SRE12.579.

[37] Emilios Leonidas, Sabino Ayvar-Soberanis, Hatim Laalej, Stephen Fitzpatrick, and Jon R. Willmott. A comparative review of thermocouple and infrared radiation temperature measurement methods during the machining of metals, 2022. doi: 10.3390/s22134693.

[38] Denghui Li, Hongrui Cao, and Xuefeng Chen. Fuzzy control of milling chatter with piezoelectric actuators embedded to the tool holder. *Mechanical Systems and Signal Processing*, 148, 2021. doi: 10.1016/j.ymssp.2020.107190.

[39] Xiaoli Li, Gaoxiang Ouyang, and Zhenhu Liang. Complexity measure of motor current signals for tool flute breakage detection in end milling. *International Journal of Machine Tools and Manufacture*, 48, 2008. doi: 10.1016/j.ijmachtools.2007.09.008.

[40] W. Y.H. Liew. Low-speed milling of stainless steel with tialn single-layer and tialn/alcrn nano-multilayer coated carbide tools under different lubrication conditions. *Wear*, 269, 2010. doi: 10.1016/j.wear.2010.06.012.

[41] Changfu Liu, Bo Liu, Yang Zhou, Yan He, Dexia Chi, Xingjun Gao, and Qingkang Liu. A real-time cutting temperature monitoring of tool in peripheral milling based on wireless transmission. *International Journal of Thermal Sciences*, 186, 2023. doi: 10.1016/j.ijthermalsci.2022.108084.

[42] Alisson Rocha Machado, Leonardo Rosa Ribeiro da Silva, Danil Yu. Pimenov, Felipe Chagas Rodrigues de Souza, Mustafa Kuntoğlu, and Raphael Lima de Paiva. Comprehensive review of advanced methods for improving the parameters of machining steels. *Journal of Manufacturing Processes*, 125:111–142, 2024. doi: https://doi.org/10.1016/j.jmapro.2024.07.044.

[43] N K Mehta. *Metal Cutting and Design of Cutting Tools, Jigs & Fixtures*. McGraw Hill Education (India) Private Limited, 2015.

[44] A. J. Mian, N. Driver, and P. T. Mativenga. Identification of factors that dominate size effect in micro-machining. *International Journal of Machine Tools and Manufacture*, 51:383–394, 2011.

[45] Mitsubishi Materials Corporation. Drilling terminology – rotating tools technical information. https://www.mmc-carbide.com/us/technical_information/tec_rotating_tools/technical/tec_drilling_terminology (accessed April, 2025).

[46] Simões Morais. *Desenho Técnico Básico - 3*, volume 3. 26 edition, 2020.

[47] Van Hai Nguyen, Tien Thinh Le, Anh Tu Nguyen, X. T. Hoang, and Nhu Tung Nguyen. Multiobjective optimization of end milling parameters for enhanced machining performance on 42crmo4 using machine learning and nsga-iii. *Machining Science and Technology*, 2024. doi: 10.1080/10910344.2024.2381191.

[48] Van-Hai Nguyen, Tien-Thinh Le, Anh-Tu Nguyen, Xuan-Thinh Hoang, Nhu-Tung Nguyen, and Ngoc-Kien Nguyen. Optimization of milling conditions for aisi 4140 steel using an integrated machine learning-multi objective optimization-multi criteria decision making framework. *Measurement*, 242:115837, 2025. doi: https://doi.org/10.1016/j.measurement.2024.115837.

[49] Fernando Brandão De Oliveira, Alessandro Roger Rodrigues, Reginaldo Teixeira Coelho, and Adriano Fagali De Souza. Size effect and minimum chip thickness in micromilling. *International Journal of Machine Tools and Manufacture*, 89:39–54, 2015. doi: 10.1016/j.ijmachtools.2014.11.001.

[50] Vineet Paliwal and N. Ramesh Babu. Prediction of stability lobe diagrams in high-speed milling by operational modal analysis. volume 48, pages 283–293, 2020. doi: 10.1016/j.promfg.2020.05.049.

[51] Amitkumar Patil, Gunjan Soni, and Anuj Prakash. *Extremum center interpolation-based EMD approach for fault detection of reciprocating compressor*, pages 109–122. 2022. doi: 10.1016/B978-0-323-90789-7.00012-9.

[52] L Pejryd, M Eynian, and T Beno. Minimization of chatter in machining by the use of mobile platform technologies. Technical report, 2012. https://www.researchgate.net/publication/288008636.

[53] Marcin Plodzien, Jan Burek, Lukasz Zylka, and Pawel Sulkowicz. The influence of end mill helix angle on high performance milling process. *Journal of Mechanical Science and Technology*, 34, 2020. doi: 10.1007/s12206-020-0131-6.

[54] M Pop, D Frunza, F Popa, and A Neag. Aspects regarding the hot fracture behavior of 42crmo4 alloy. Technical report, 2016. https://rjp.nipne.ro/2017_62_5-6/RomJPhys.62.606.pdf.

[55] M. Postel, D. Aslan, K. Wegener, and Y. Altintas. Monitoring of vibrations and cutting forces with spindle mounted vibration sensors. *CIRP Annals*, 68, 2019. doi: 10.1016/j.cirp.2019.03.019.

[56] Marcin Płodzień, Łukasz Żyłka, Paweł Sułkowicz, Krzysztof Żak, and Szymon Wojciechowski. High-performance face milling of 42crmo4 steel: Influence of entering angle on the measured surface roughness, cutting force and vibration amplitude. *Materials*, 14, 2021. doi: 10.3390/ma14092196.

[57] Guillem Quintana and Joaquim Ciurana. Chatter in machining processes: A review, 2011. doi: 10.1016/j.ijmachtools.2011.01.001.

[58] Giorgio Rizzoni. *Fundamentals of Electrical Engineering*. McGraw-Hill Companies, Inc., first edition, 2009.

[59] H. Saglam and A. Unuvar. Tool condition monitoring in milling based on cutting forces by a neural network. *International Journal of Production Research*, 41, 2003. doi: 10.1080/0020754031000073017.

[60] Wisley Sales, Marcelo Becker, Clovis S. Barcellos, Janes Landre, John Bonney, and Emmanuel O. Ezugwu. Tribological behaviour when face milling aisi 4140 steel with minimum quantity fluid application. *Industrial Lubrication and Tribology*, 61, 2009. doi: 10.1108/00368790910940400.

[61] Sandvik Coromant. Milling knowledge. https://www.sandvik.coromant.com/en-us/knowledge/milling (accessed April, 2025).

[62] Sandvik Coromant. Specific cutting force. https://www.sandvik.coromant.com/en-us/knowledge/materials/specific-cutting-force (accessed June, 2025).

[63] Sandvik Coromant. Surface generation in milling. https://www.sandvik.coromant.com/en-us/knowledge/milling/surface-generation (accessed April, 2025).

[64] Sandvik Coromant. Workpiece materials. https://www.sandvik.coromant.com/en-us/knowledge/materials/workpiece-materials (accessed April, 2025).

[65] Tiago Silva. Module iii: Simulation of the metal cutting processes. Lecture slides, 2024. Advanced Manufacturing Technologies II, Master in Mechanical Engineering, Faculdade de Engenharia da Universidade do Porto.

[66] Graham T. Smith. *Cutting Tool Technology - Industrial Handbook*. Springer Verlag, 2008. doi: 10.1007/978-1-84800-205-0.

[67] Pinto Soares. *AÇOS- Características, Tratamentos*. 6º edição edition, 2009.

[68] Marco Antonio Stipkovic, Éd Claudio Bordinassi, Adalto De Farias, and Sergio Delijaicov. Surface integrity analysis in machining of hardened aisi 4140 steel. *Materials Research*, 20, 2017. doi: 10.1590/1980-5373-MR-2016-0420.

[69] Wuyang Sun, Ming Luo, and Dinghua Zhang. Machining vibration monitoring based on dynamic clamping force measuring in thin-walled components milling. *International Journal of Advanced Manufacturing Technology*, 107, 2020. doi: 10.1007/s00170-020-05153-9.

[70] R. Teti, K. Jemielniak, G. O'Donnell, and D. Dornfeld. Advanced monitoring of machining operations. *CIRP Annals - Manufacturing Technology*, 59, 2010. doi: 10.1016/j.cirp.2010.05.010.

[71] G Totis, Marco Sortino, E Kuljanic, and M Sortino. Vibrations and chatter in machining: State of the art and new approaches. Technical report, 2008. https://www.researchgate.net/publication/257444718 (accessed March, 2025).

[72] M. Q. Tran and M. K. Liu. Chatter identification in end milling process based on cutting force signal processing. In *IOP Conference Series: Materials Science and Engineering*, volume 654. Institute of Physics Publishing, 10 2019. doi: 10.1088/1757-899X/654/1/012001.

[73] Edward Trent and Paul Wright. *Metal Cutting*. Butterworth–Heinemann, fourth edition, 2000.

[74] Eckart Uhlmann and Tobias Holznagel. Acoustic emission-based process monitoring in the milling of carbon fibre-reinforced plastics. *CIRP Journal of Manufacturing Science and Technology*, 37, 2022. doi: 10.1016/j.cirpj.2022.02.024.

[75] J. Vivancos, C. J. Luis, L. Costa, and J. A. Ortíz. Optimal machining parameters selection in high speed milling of hardened steels for injection moulds. *Journal of Materials Processing Technology*, 155-156, 2004. doi: 10.1016/j.jmatprotec.2004.04.260.

[76] F. Vollertsen, D. Biermann, H. N. Hansen, I. S. Jawahir, and K. Kuzman. Size effects in manufacturing of metallic components. volume 58, pages 566–587. 2009. doi: 10.1016/j.cirp.2009.09.002.

[77] Walter AG. *Tiger·tec® Gold – The Benchmark in Steel Machining*. Walter AG, Tübingen, Germany, 2016. https://cdn.walter-tools.com/files/sitecollectiondocuments/downloads/global/brochures/en-us/flyer-tigertec-gold-us.pdf (accessed May, 2025).

[78] Bing Syun Wan, Ming Chyuan Lu, and Shean Juinn Chiou. Analysis of spindle ae signals and development of ae-based tool wear monitoring system in micro-milling. *Journal of Manufacturing and Materials Processing*, 6, 2022. doi: 10.3390/jmmp6020042.

[79] Wei Kang Wang, Min Wan, Wei Hong Zhang, and Yun Yang. Chatter detection methods in the machining processes: A review, 2022. doi: 10.1016/j.jmapro.2022.03.018.

[80] Baijun Xiao, Teng Fei Zhang, Zhu Guo, Zhou Li, Bin Fan, Ganxin Chen, Zhihong Xiong, and Qimin Wang. Mechanical, oxidation, and cutting properties of alcrn/altisin nano-multilayer coatings. *Surface and Coatings Technology*, 433, 2022. doi: 10.1016/j.surfcoat.2022.128094.

[81] I. Yesilyurt and H. Ozturk. Tool condition monitoring in milling using vibration analysis. *International Journal of Production Research*, 45, 2007. doi: 10.1080/00207540600677781.

[82] Jianping Yue. Creating a stability lobe diagram. In *Proceedings of the 2006 IJME–INTERTECH Conference*, pages 1–6. IJME, International Journal of Modern Engineering (IJME), 2006. https://ijme.us/cd_06/PDF/IT%20301-050.pdf.

[83] A. Zafra, L. B. Peral, J. Belzunce, and C. Rodríguez. Effect of hydrogen on the tensile properties of 42crmo4 steel quenched and tempered at different temperatures. *International Journal of Hydrogen Energy*, 43, 2018. doi: 10.1016/j.ijhydene.2018.03.158.

[84] Haimei Zhang. *Building Materials in Civil Engineering*. Woodhead Publishing, 2011. doi: 10.1533/9781845699567.

[85] Weiwu Zhong, Dongbiao Zhao, and Xi Wang. A comparative study on dry milling and little quantity lubricant milling based on vibration signals. *International Journal of Machine Tools and Manufacture*, 50, 2010. doi: 10.1016/j.ijmachtools.2010.08.011.

[86] Yuqing Zhou and Weifang Sun. Tool wear condition monitoring in milling process based on current sensors. *IEEE Access*, 8, 2020. doi: 10.1109/ACCESS.2020.2995586.

[87] A. Çalık, O. Dokuzlar, and N. Uçar. The effect of heat treatment on mechanical properties of 42crmo4 steel. *Journal of Achievements in Materials and Manufacturing Engineering*, 98, 2020. doi: 10.5604/01.3001.0014.0811.